Proceedings of the

4th WORKSHOP ON NEW ASPECTS AND PERSPECTIVES IN NUCLEAR PHYSICS

DEPARTMENT OF PHYSICS

THE UNIVERSITY OF IOANNINA

MAY 5-6, 2017

Edited by

A. Pakou ▪ C. Papachristodoulou

HELLENIC INSTITUTE OF NUCLEAR PHYSICS

HELLENIC INSTITUTE OF NUCLEAR PHYSICS

PROCEEDINGS

of the

4th WORKSHOP

on New Aspects and Perspectives in Nuclear Physics

(HINPW4)

DEPARTMENT OF PHYSICS

THE UNIVERSITY OF IOANNINA

MAY 5-6, 2017

ORGANISING COMMITTEE

X. Aslanoglou	University of Ioannina
D. Bonatsos	NCSR "Demokritos"
K. Ioannides	University of Ioannina
G.A. Lalazissis	Aristotle University of Thessaloniki
N.G. Nicolis	University of Ioannina
A. Pakou	University of Ioannina
C. Papachristodoulou	University of Ioannina
G. Souliotis	National and Kapodistrian University of Athens
K. Stamoulis	University of Ioannina

EDITORS

A. Pakou, C. Papachristodoulou

HINPW4 WEB-SITE

http://hinpw4.physics.uoi.gr/

WORKSHOP SPONSORS

University of Ioannina
www.uoi.gr

VECTOR Technologies Ltd
www.vectortechnologies.gr

FOREWORD

The 4th Workshop on new Aspects and Perspectives in Nuclear Physics (HINPW4) was held in Ioannina from May 5 to 6, 2017. This series of symposia, organized by the Hellenic Institute of Nuclear Physics since 2012, provides a lively forum not only for leading scientists of the Greek Universities and Institutes but also for fresheners in the field of Nuclear Physics to share the most recent advancements on various topics, thus offering a unique platform to exchange ideas and keep track of new aspects and perspectives in the area.

This year, there has been a very enthusiastic response, resulting in approximately 50 participants, mostly young scientists and post-graduate students. A total of 22 oral contributions were included in the agenda, in addition to 8 lectures delivered by distinguished colleagues invited from abroad. We are grateful to all the speakers and participants and especially to the invited speakers for their overwhelming response and participation in the Workshop.

The Workshop sessions covered the topics of Nuclear Structure and Nuclear Reactions, Hadron Physics and Environmental, Medical and Archaeometry Applications, with emphasis on Nuclear Reactions. All invited and contributed talks were of high quality and the articles based on the talks are collected together in the present volume.

We would like to thank the University of Ioannina for hosting the Workshop at the "Carolos Papoulias" Conference Center, and for providing accommodation of participants at the "Stavros Niarchos" guesthouse. Financial support by VECTOR Technologies LtD is warmly acknowledged. We also thank the Vice Rector of the University of Ioannina and the Dean of the School of Sciences for their kind presentations in the opening session. To O. Sgouros and V. Soukeras, PhD students of the University of Ioannina, we express our gratitude for providing us with the Workshop webpage and for their untiring efforts towards the successful organization of the Workshop. Last, but not least, I personally would like to cordially thank the President of HINP, G. Lalazissis, for his thoughtful gesture to honor me with a HINP plaque, as well as N. Alamanos for his touching farewell speech and accompanying letter, applauding my career so far and putting his trust in my future scientific work. These are included in the end of this volume.

Athena Pakou

on behalf of the Organizing Committee

Ioannina, August 2017

Contents

I N V I T E D   A N D   C O N T R I B U T E D   P A P E R S   (i n   p r o g r a m m e   o r d e r)

INVITED AND CONTRIBUTED PAPERS

(in programme order)

Covariant density functionals in nuclear physics and their microscopic origin

Peter Ring[1,2 a]

[1] Physics Department, Technical University of Munich, 85748 Garching, Germany
[2] School of Physics, Peking University, Beijing 100871, People's Republic of China

Abstract. Nuclear density functional theory provides a universal description of many nuclear properties all over the periodic table. However, at the moment, most of the successful functionals are completely phenomenological, dependent on up to a dozen parameters, which are adjusted to various experimental data in finite nuclei. The predictive power of such functionals is therefore under debate. Microscopic derivations, as they are possible nowadays in Coulombic systems are at their infancy. We discuss here several attempts to a better microscopic understanding of covariant density functional theory (a) by including in the fit ab-initio calculations for nuclear matter properties and reducing in this way the number of phenomenological parameters considerably and (b) by comparing the results of phenomenological results with those obtained by relativistic Brueckner-Hartree-Fock theory in finite nuclei, which is based on the G-matrix, a microscopically derived density dependent interaction.

PACS. PACS-key discribing text of that key – PACS-key discribing text of that key

1 Introduction

In recent years considerable progress has been achieved in ab-initio derivations of nuclear properties from bare nucleon-nucleon forces. For light nuclei it is possible to solve the exact nuclear many-body problem on the computer. For heavier nuclei approximate methods have been applied. The calculation of nuclear properties for the majority of nuclear systems, however, is left to density functional theory (DFT). Non-relativistic [1,2] and relativistic [3–7] versions enable an effective description of the nuclear many-body problem not only for bulk properties, such as binding energies and radii, but also for collective excitations such as rotations and giant resonances, and, by going beyond mean field, for complicated configurations [8–12] and for sophisticated low-lying spectra in transitional nuclei [13,14].

At present most of these functionals are purely phenomenological. Of course, one of the main goals in nuclear physics is to build a universal density functional theory based on microscopic calculations [15,16]. This functional should be able to explain as many as possible measured data within the same parameter set and to provide reliable predictions for properties of nuclei far from stability not yet or never accessible to experiments in the laboratory. It should be derived in a fully microscopic way from the interactions between bare nucleons. At present, however, attempts to derive such a density functional provide only qualitative results for two reasons: first, the three-body term of the bare interaction is not known well enough and, second, the methods to derive such a functional are not precise enough to achieve the required accuracy. Note that a 1 per mille error in the binding energy per particle of symmetric nuclear matter leads to an error of several MeV in the binding energy of heavy nuclei, an error which is an order of magnitude larger than required by astrophysical applications. From such considerations it is evident, that successful ab-inito functionals in nuclear physics, at least in foreseeable future will always depend on a very small number of phenomenological parameters for fine tuning. It is the number of final parameters which counts.

One of the underlying symmetries of QCD is Lorentz invariance and therefore covariant density functionals are of particular interest in nuclear physics. This symmetry not only allows to describe the spin–orbit coupling, which has an essential influence on the underlying shell structure, in a consistent way, but it also puts stringent restrictions on the number of parameters in the corresponding functionals without reducing the quality of the agreement with experimental data [17]. It is true, that the velocities of nucleons in the Fermi sea are relatively small and their kinetic energy is small compared to the rest mass. However, because of the large scalar field their effective Dirac mass is considerably reduced and the velocity dependent spin-orbit term is dramatically increased, such that even small velocities lead to large effects, which cannot be treat-

[a] Supported in part by the DFG cluster of excellence "Origin and Structure of the Universe" (www.universe-cluster.de)

ed by perturbation theory. Of course, a non-relativistic expansion is possible, but it leads to various correction terms at the cost of a lot of additional phenomenological parameters [18]. A well known example is the spin-orbit term in non-relativistic density functionals. Therefore we restrict ourselves in the following to covariant density functionals theory (CDFT).

2 Phenomenological covariant DFT's

In contrast to non-relativistic functionals of Skyrme [1] or Gogny [2] type, which start from the beginning with roughly a dozen parameters and a simple power-law of $\sim \rho^{1/3}$ for the density dependence, relativistic functionals, such as the Walecka model [3] start with only four parameters, the coupling constants for the three mesons g_σ, g_ω, g_ρ, and the mass m_σ of the σ-meson. These for parameters are clearly connected with basic properties of the effective nuclear force: medium range attraction (g_σ), short range repulsion (g_ω), isospin dependence (g_ω) and the range of the force (m_σ), which determines the surface properties, such as radii in finite nuclei. The details are, however more complicated. As Boguta and Bodmer [19] have pointed out already very early, this linear model fails to describe nuclear systems as for instance nuclear compressibility or nuclear deformations [20] . This was the birthday of covariant density functional theory and from that moment all the efforts of additional phenomenological parameters has been devoted to a better description of the density dependence. To keep the theory renormalizable Boguta et. al. used a ϕ^4-ansatz and introduced two additional parameters g_2 and g_3 for the cubic and quartic coupling of σ-mesons and therefore all the early successful parameter sets, such as for instance NL3 [21] or its modern version NL3* [22] had only 6 parameters.

In these and in many other relatively successful parameter sets the density dependence enters only in the isoscalar channel. This leads to rather large neutron skins at the upper end of the experimental error bars, to a neutron equation of state deviating considerably from theoretical predictions [23, 24] and to a rather stiff symmetry energy $S_2(\rho)$. The parameter $L = 3\rho dS_2/d\rho$ at saturation is larger then 120 MeV and far above the usual adopted value of $L \approx 50$ MeV. Since renormalizability plays no role in phenomenological density functional theory modern functionals, such as DD-ME2 [25] eliminate non-linear meson couplings and introduce density dependent coupling constants $g_\sigma(\rho)$, $g_\omega(\rho)$, and $g_\rho(\rho)$ with depend, apart from their values at saturation on additional four parameters which are fitted to finite nuclei. In particular they include also a density dependence in the isovector channel and this allows also a much better description of the EoS of neutron matter and of the symmetry energy.

Calculations with finite meson masses are still relatively complicated and therefore modern point-coupling functionals have been developed [26–28]. In the zero-range limit the meson exchange terms are replaced by contact terms of the proper spin- and isospin dependence and three coupling constants at saturation g_σ, g_ω, g_ρ are replaced by the coupling constants α_S, α_V, and α_{ST} and the finite mass m_σ leads to a derivative term in the scalar isoscalar channel with the strength δ_S. Again one has four parameters and their density dependence. All in all one has roughly 10 phenomenological parameters. This seems a similar number as in the non-relativistic case, but there is a difference: in the relativistic models most of the parameters (roughly 6) are used for a sophisticated description of the density dependence, where Skyrme or Gogny use only a power law ρ^α, and even that α is most cases chosen as fixed $\alpha = \frac{1}{3}$ or $\alpha = 1$

3 Semi-microscopic covariant DFTs

In Coulombic system an essential input for the derivation of microscopic functionals [29] is the exact numerical solution of the homogeneous electron gas at various densities. Starting from this energy functional $E[\rho]$ additional gradient terms and many other corrections have been added with great success.

Therefore it seems to be reasonable to apply a similar concept in nuclear physics. Of course, at present there are no exact solutions of the nuclear matter problem available. One has to rely on approximate solutions, such as sophisticated variational calculations [23] or modern Brueckner-Hartree-Fock methods [24]. The covariant point coupling functional DD-PC1 of the Munich-Zagreb group [28] used this microscopic input together with experimental masses of 64 heavy deformed nuclei in order to adjust 10 phenomenological parameters, the four coupling α_S, α_V, α_{ST}, and δ_S at saturation and six further parameters to describe the density dependence. The result is a semi-microscopic functional with an EoS nearly identical to the microscopic EoS of the Ilinois group [23], which can be used at higher densities in neutron stars with much more confidence than the extrapolations of phenomenological functionals adjusted only at saturation density and below.

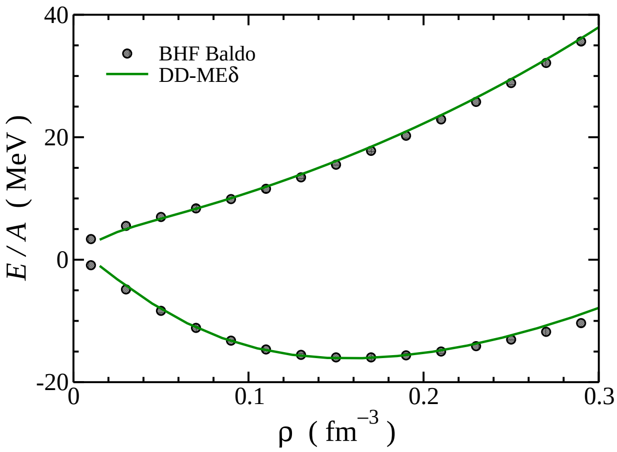

Fig. 1. Equation of state (EoS) for symmetric nuclear matter and for pure neutron matter as a function of the nucleon density. Details are given in the text (from Ref. [30].)

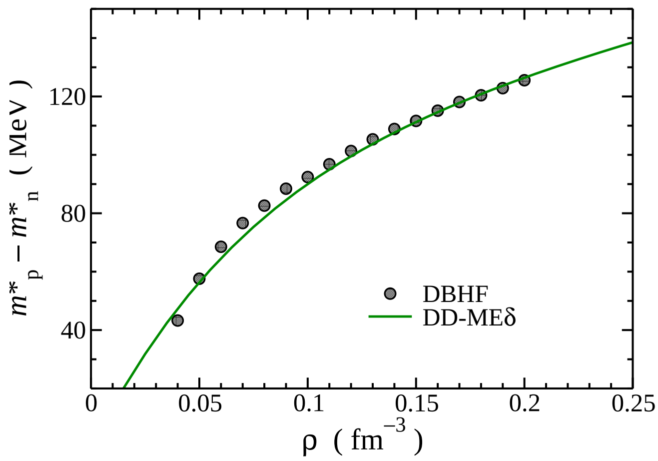

Fig. 2. Proton-neutron effective mass splitting as a function of the nucleon density in pure neutron matter (from Ref. [30])

Recently we went a step further [30]. We followed the spirit of the Barcelona group [31], who used Brueckner-Hartree-Fock calculations in nuclear matter (see Fig. 1) as a starting point for a semi-phenomenological non-relativistic potential, and derived in a similar way a relativistic functional DD-MEδ [30] with density dependent meson couplings. In contrast to the phenomenological covariant density functionals, where the isospin dependence is completely determined by the vector ρ-meson, microscopic Dirac-Brueckner-Hartree-Fock (DBHF) calculations [32] show very clearly that there is also a isospin dependence in the scalar channel described by the isovector δ-meson (sometimes called a_0). The density dependence of the meson nucleon coupling vertices in the new functional DD-MEδ [30] is derived from *ab-initio* DBHF calculations in nuclear matter. As shown in Fig. 1 the starting point forms the Equation of State (EoS) of symmetric nuclear matter and of neutron matter derived by Baldo et al. [24] in a state-of-the-art non-relativistic Brueckner-Hartree-Fock calculation including relativistic corrections and three-body forces. In addition the isovector part of the effective Dirac mass $m_p^* - m_n^*$, which is derived by the Tübingen group [32] using DBHF theory, determines the coupling constant of the δ-meson and its density dependence (see Fig. 2). Only four additional parameters the coupling constants g_σ, g_ω, g_ρ at saturation density and m_σ are used for a fine-tuning of binding energies and radii of finite nuclei.

In Fig. 3 we show in the upper panel, that for DD-MEδ the total symmetry energy is obtained as a sum of a nearly linear kinetic term and the a repulsive contribution from the ρ-meson and an attractive contribution from the δ-meson. Both cancel each other to a large extend. A nearly identical symmetry energy is obtained in the lower panel for DD-ME2 by the ρ-meson alone. Therefore it turns out that is very difficult to determine the strength of the δ-coupling from masses and radii of finite nuclei alone. In our calculations this strength has been determined by the isovector effective mass derived from the ab-inito calculations of Ref. [32].

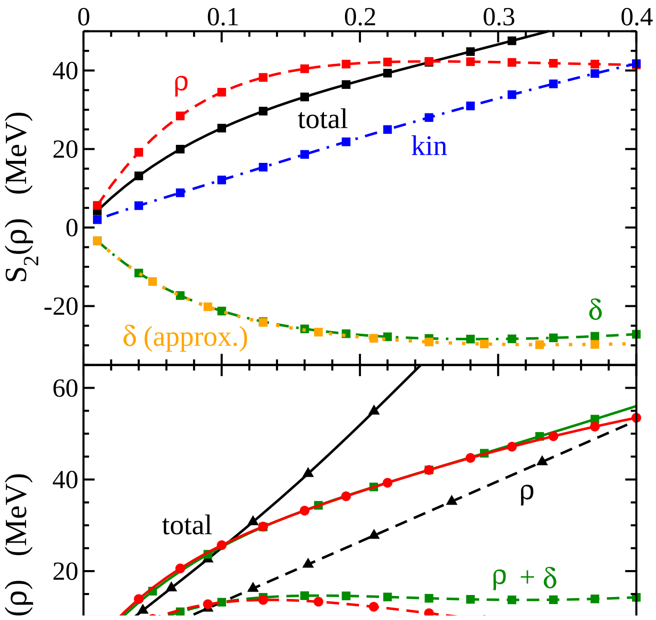

Fig. 3. Upper panel: the symmetry energy $S_2(\rho)$ (full in black) and its contributions as a function of the density. Lower panel: the symmetry energy $S_2(\rho)$ resulting from the parameter sets NL3 (triangles), DD-ME2(circles), and DD-MEδ (from Ref. [30])

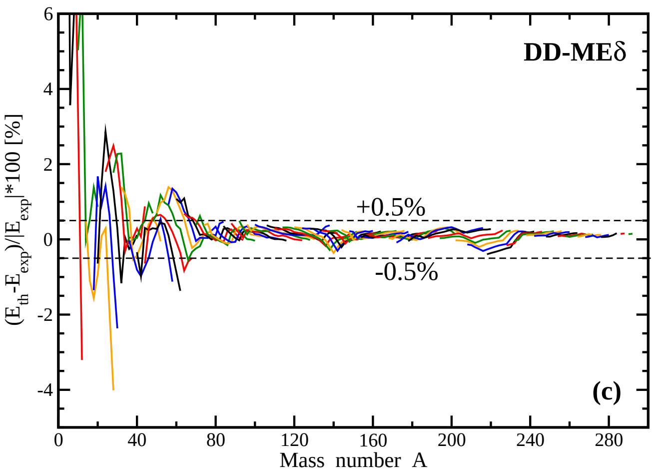

Fig. 4. The relative difference between theoretical and experimental masses of 835 even-even nuclei investigated in relativistic Hartree Bogoliubov (RHB) calculations with the set DD-MEδ If $E_{th} - E_{exp} < 0$, the nucleus is more bound in the calculations than in experiment. Dashed lines show the ± 0.5 % limit (from Ref. [33]).

Table 1. Various versions of covariant density functionals: number n of phenomenological parameters, rms deviations between theory and experiment for binding energies and charge radii. For further details see Ref. [33]. The rotational corrections E_{corr} for PC-PK1 are calculated without further phenomenological parameters in Ref. [35]

CEDF	n	ΔE_{rms} (MeV)	Δr_c^{rms} (fm)
NL3*	6	2.96	0.0283
DD-ME2	8	2.39	0.0230
DD-MEδ	4	2.29	0.0329
DD-PC1	10	2.01	0.0253
PC-PK1	10	2.58	-
PC-PK1 + E_{corr}	10	1.24	-

Extended applications of this functional on a global scale [33] have shown that it is comparable with all the modern relativistic high precision functionals containing considerably more phenomenological parameters. Fig. 4 shows that the deviations between theoretical and experimental binding energies are well below 0.5 %, with some exceptions for light nuclei.

In Table 1 we show for some characteristic covariant density functionals the number n of phenomenological parameters and the rms-deviations between theory and experiment for binding energies and radii of all even-even nuclei experimentally known. We find that for the best phenomenological models one does not go below 2 MeV for the rms-deviations of the binding energies. Only by including corrections beyond mean field, as for instance the rotational corrections one reaches values close to 1 MeV. All mass formulas going much beyond that limit (i.e. down to 500 keV) include phenomenological correction terms beyond mean field with up to 30 parameters [34]. It is interesting to see in Table 1, that the semi-microscopic functionals DD-PC1 (10 parameters) and in particular DD-MEδ (only 4 parameters) do as well as the others. This is no longer true for the charge radii. Here DD-MEδ with only 4 parameters does not as well as the others. We observe an 50 % increase of this quantity.

We can conclude that, at present, we are able to derive very successful semi-microscopic covariant density functionals [30,28] from ab-initio results for nuclear matter and neutron matter, containing only few remaining parameters for a fine tuning.

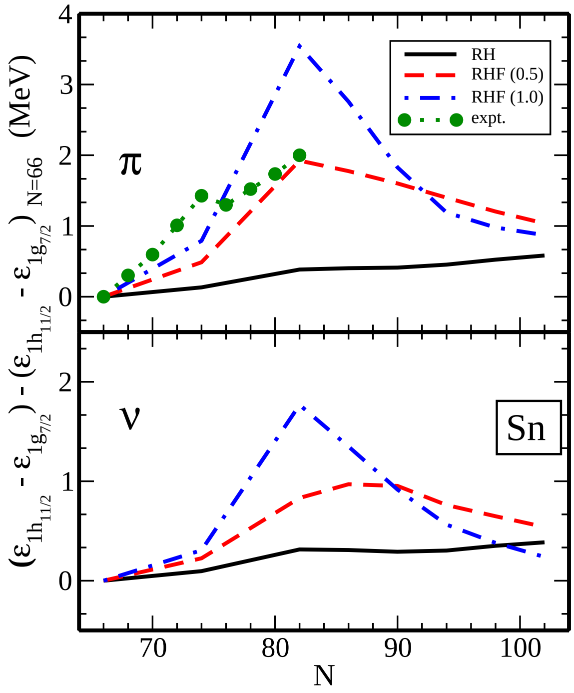

Fig. 5. The evolution of the $1h_{11/2}$ and $1g_{7/2}$ neutron and proton energy gap. The s.p levels of ^{116}Sn are taken as reference point. (right panel) χ^2 of the fit as function of the pion coupling constant in terms of the free pion coupling constant.(from Ref. [36]).

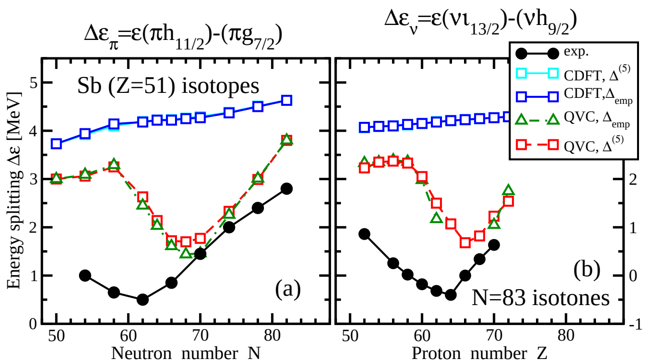

]

Fig. 6. The energy splittings between the indicated states obtained in experiment, covariant density functional theory (CDFT), and relativistic QVC calculations. The results of the calculations with two pairing schemes are shown (from Ref. [37]).

4 Remaining problems

However, we have to emphasize that all the microscopic input comes at this stage from ab-initio calculations in nuclear matter. On the other side, there are problems in finite nuclei, where simple density functionals of this type consistently fail. An example are single-particle energies and their distribution. This has been found in an indirect way by global investigations in the area of transitional nuclei, which depend in some cases in a sensitive way on the single particle structure (see the discussions in Refs. [33,38,39]), but also in experimental observations of systematic shifts of single particle energies in isotopic chains. A famous case is the splitting of $1h_{11/2}$ and $1g_{7/2}$ proton configurations in the Sn-region [40]. As it is shown in the left panel of Fig. 5, the experimental data can be reproduced by including the exchange term of a one-pion exchange using a strength parameter roughly one half of the experimental pion-nucleon coupling in the vacuum. It is impossible to determine the size of this parameter by fitting to bulk properties, such a masses and radii, because the best fit is obtained without pion contributions [36]. Similar results have also been found in density dependent Relativistic Hartree-Fock (RHF) theory [41].

On the other side, it is an open question, whether these shifts in observed single particle energies are an indication of the necessity of effective tensor forces in relativistic density functionals. It is also know, that present nuclear density functionals do not describe the exact solutions of the nuclear many-body problem. There are cases, which cannot be taken into account on the mean field level, and where one has to go beyond mean field. An example is particle vibrational coupling which has a considerable influence on the single particle energies. It can also be treated in covariant density functionals [8,42]. In fact, recently it has been shown by A. Afanasjev and E. Litvinova [37] that a large part of the shifting single particle spectra in the Sn region can be described with the simple functional NL3 including quasiparticle-vibrational coupling (QVC) (see Fig.6).

5 Microscopic calculations in finite nuclei

The concept to derive density functionals from properties of infinite nuclear matter, is very successful for general properties of these functionals. However, it cannot teach us too much when it comes to properties of the functionals, which do not show up in nuclear matter calculations as for instance the tensor term in spin non-saturated systems. Nuclear matter is usually spin-saturated and therefore the contributions of the tensor term in first order are small. In order to study such effects from ab-inito calculations, we have to carry out microscopic calculations in finite nuclei, in particular also in heavy nuclei, which are not spin-saturated.

An obvious way to carry out such investigations is Brueckner theory, the mother of modern density functional theory in nuclei [43,44]. The advantage of relativistic Brueckner theory is that one does not need three-body forces to get saturation in nuclear matter close to the experimental area. Therefore Dirac-Brueckner-Hartree-Fock (DBHF) theory has been used to describe also finite nuclei [45–48]. In most of these applications the local density approximation has been used, i.e. in a first step the self-energies are calculated in nuclear matter of various densities. In a second step the relativistic Hartree-Fock equations for Walecka-type functionals are solved in finite nuclei with density dependent coupling constants adjusted to the results of nuclear matter calculations at the corresponding density. This provides a mapping of the microscopically obtained nuclear matter results onto RHF-models of Walecka type.

Although such calculations are successful, they cannot reach the accuracy of present day phenomenological covariant density functionals. In particular, the mapping is not unique and therefore the results of different groups deviate form each other considerably. It is also clear that this concept is relatively useless for a microscopic study of the influence of the tensor force in finite non spin-saturated nuclei, because, as discussed above, nuclear matter is spin-saturated.

Table 2. Ground state properties of ^{16}O obtained with RBHF theory are compared various other approximations andwith experiment (from Ref. [51]).

	E (MeV)	r_c (fm)	$\Delta E^{ls}_{\pi 1p}$ (MeV)
Exp. [56,57]	−127.6	2.70	6.3
RBHF	−120.7	2.55	6.0
BHF [58]	−105.0	2.29	7.5
DDRH [59]	−106.4	2.72	–
DDRHF [59]	−142.6	2.62	4.5
NCSM [60]	−119.7	-	–
PKO1 [41]	−128.3	2.68	6.4

By this reason we started a new project to solve the DBHF equations in large finite basis. First we started in an oscillator basis [49], but then we found we found a large Dirac-Woods-Saxon (DWS) basis more appropriate [50]. There are basis states with positive and negative energies. and cut-off-parameters are introduced for the basis, such that convergence is achieved. For details see Ref. [51]

Within relativistic Brueckner-Hartree-Fock (RBHF) theory [52–55] the relativistic Hartree-Fock (RHF) equations are solved with an effective interaction in the nuclear medium, the so-called G-matrix. Its matrix elements $\langle ab|G(\omega)|cd\rangle$ are determined by the solution of the Bethe-Goldstone (BG) equation in the DWS basis

$$G(\omega) = \bar{V}^N + \bar{V}^N Q_F \frac{1}{\omega - H_0} Q_F G(\omega). \tag{1}$$

Here $\bar{V}^N$ are the anti-symmetrized matrix elements of the relativistic bare force, H_0 are the self-consistent two-particle energies $\epsilon_m + \epsilon_{m'}$ of the RHF-operator at each step of the iteration, and Q_F is the Pauli operator

$$Q_F = \sum_{m<m'} |mm'\rangle\langle mm'|. \tag{2}$$

summing over intermediate states m, m' above the Fermi surface. Of course, since the single particle energies ϵ_m and $\epsilon_{m'}$ refer to the eigenvalues of the RHF-operator, the Pauli operator (2) is defined in the corresponding relativistic Hartree-Fock basis. Therefore the full solution of this problem requires the transformation of the Pauli-operator from the RHF basis to the DWS basis and this is the final goal of such calculations. In a first step we applied the so-called *Dirac-Woods-Saxon* approximation for the Pauli operator, i.e. we use in Eq. (2) DWS states for the wave functions $|mm'\rangle$. On the other hand self-consistent RHF-energies $\epsilon_m + \epsilon_{m'}$ with the same number of radial nodes will be used for H_0. With a properly chosen DWS-basis this seems to be a reasonable approximation.

As an application we consider the nucleus ^{16}O. We use the realistic NN interaction Bonn A which has been adjusted to the NN scattering data in Ref. [61]. The ground-state properties are listed in Table 2: the total energy, the charge radius, and the proton spin-orbit splitting for the $1p$ shell. The results of our full RBHF calculation are compared with the corresponding experimental data and with several other calculations: BHF is a non-relativistic Brueckner calculation based on the interaction Bonn A. We also show results obtained in RHF-calculations with the phenomenological effective interaction PKO1, which has been fitted to binding energies and charge radii of a set of spherical nuclei. It is seen that the ground-state properties in RBHF theory are improved considerably as compared with the non-relativistic results. This energy of ^{16}O is also very close to the value of $E = -119.7$ MeV obtained in the No Core Shell Model (NCSM) calculation using the chiral NN interaction N^{3}LO [60]. Of course the results of the calculations with PKO1 which has been fitted to these data shows only a very small deviation from the experimental values

Next we compare in Fig. 7 our self-consistent results in finite nuclei with those obtained in Ref. [59] by two "*ab initio*" calculations based on the LDA. There the full RBHF equations are solved for nuclear matter at various densities

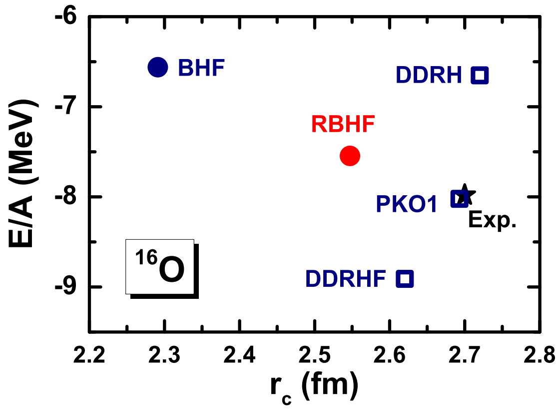

Fig. 7. Energy per particle and charge radius of ^{16}O by (relativistic) BHF theories compared with experimental data and other calculations. See text for details (from Ref. [51]).

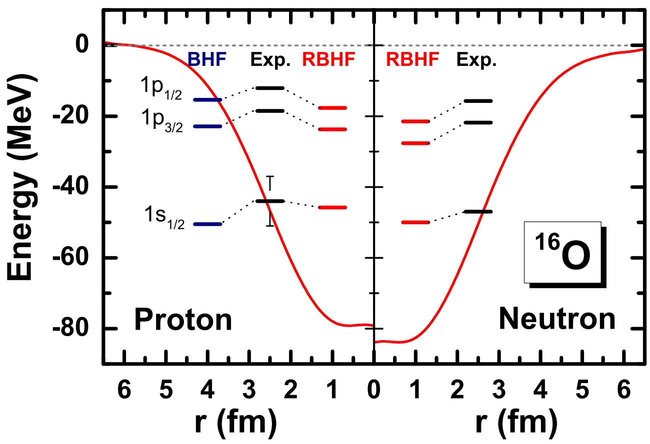

Fig. 8. Single-particle spectra for protons and neutrons obtained from the solution of the RHF-equation are compared with experimental values [57]. The red line corresponds to a local potential $V(r) + S(r)$ in a Dirac equation producing the same wave function and the same eigenvalue for the lowest $1s_{1/2}$ state as the full RBHF-equation (from Ref. [51]).

and the corresponding scalar and vector self-energies are derived. Then density-dependent coupling strengths for the exchange of various mesons in a relativistic Hartree (RH) or a RHF model have been adjusted to these results. In this case it is possible to investigate finite nuclei in an *ab inito* DDRH or DDRHF approach without any phenomenological parameters.

The single-particle energy levels of ^{16}O for protons and neutrons obtained from the full RBHF calculation are plotted in Fig. 8. They are compared with experimental data and (for the protons) with the results of non-relativistic BHF calculations.

6 Conclusions

In summary, the full relativistic Brueckner-Hartree-Fock (RBHF) equations have been solved in a Dirac-Woods-Saxon (DWS) basis. The relativistic structure of the two-body matrix elements as well as of the Pauli operator is fully taken into account. The only input is the bare NN-interaction Bonn A adjusted to the scattering phase shifts in Ref. [61]. No other parameter is used. Since nuclear matter calculations within the same framework produce results far away from the Coester line and close to the experimental values of saturation, we neglect at this stage three-body forces.

Despite the good agreement of these results, there is room for improvements. The RBHF-theory presented here is no exact solution of the nuclear many-body problem. So far, rearrangement terms are not taken into account and higher order diagrams in the hole-line expansion are not included. Those effects have been taken into account in some approximation in non-relativistic calculations [62], but for relativistic theories they are left for future investigations.

On the other side, our method has the potential to investigate heavier nuclei, where exact solutions are impossible, in particular systems without spin saturation and with large neutron excess. In this case we hope to be able to gain a parameter-free, microscopic understanding of open questions in modern phenomenological density functional theories, such as their isospin dependence or the importance of the tensor terms [36].

7 Aknowledgments

I would like to express my deep gratitude to all my collaborators, who contributed to the results presented in this contribution, in particular to Anatoli Afanasjev, George Lalazissis, Elena Litvinova, Jie Meng, Takaharu Otsuka, Xavier Roca-Maza, Shihang Shen, and Milena Serra†. This work was partly supported by the DFG cluster of excellence "Origin and Structure of the Universe" (www.universe-cluster.de).

References

1. D. Vautherin and D. M. Brink, Phys. Rev. C **5**, 626 (1972).

2. J. Dechargé and D. Gogny, Phys. Rev. C **21**, 1568 (1980).
3. B. D. Serot and J. D. Walecka, Adv. Nucl. Phys. **16**, 1 (1986).
4. P. G. Reinhard, Rep. Prog. Phys. **52**, 439 (1989).
5. P. Ring, Prog. Part. Nucl. Phys. **37**, 193 (1996).
6. D. Vretenar, A. V. Afanasjev, G. A. Lalazissis, and P. Ring, Phys. Rep. **409**, 101 (2005).
7. J. Meng, H. Toki, S. G. Zhou, S. Q. Zhang, W. H. Long, and L. S. Geng, Prog. Part. Nucl. Phys. **57**, 470 (2006).
8. E. Litvinova and P. Ring, Phys. Rev. C **73**, 044328 (2006).
9. E. Litvinova, P. Ring, and V. I. Tselyaev, Phys. Rev. C **75**, 064308 (2007).
10. E. Litvinova, P. Ring, and V. I. Tselyaev, Phys. Rev. C **78**, 014312 (2008).
11. E. Litvinova, P. Ring, and V. I. Tselyaev, Phys. Rev. Lett. **105**, 022502 (2010).
12. P. Ring and E. Litvinova, Phys. At. Nucl. **72**, 1285 (2009), translated from Yadernaya Fisika **72** (2009) No. 8, 1.
13. T. Niksic, D. Vretenar, and P. Ring, Prog. Part. Nucl. Phys. **66**, 519 (2011).
14. J. M. Yao, K. Hagino, Z. P. Li, J. Meng, and P. Ring, Phys. Rev. C **89**, 054306 (2014).
15. *Lecture Notes in Physics*, edited by G. A. Lalazissis, P. Ring, and D. Vretenar (Springer-Verlag, Heidelberg, 2004), Vol. 641.
16. J. Drut, R. Furnstahl, and L. Platter, Prog. Part. Nucl. Phys. **64**, 120 (2010).
17. *Relativistic Density Functional for Nuclear Structure*, edited by J. Meng (World Scientific, Singapore, 2016), Vol. 10.
18. P. Ring, in *Relativistic Density Functional for Nuclear Structure*, edited by J. Meng (World Scientific, Singapore, 2016), Vol. 10, Chap. 1, pp. 1–20.
19. J. Boguta and A. R. Bodmer, Nucl. Phys. A **292**, 413 (1977).
20. Y. K. Gambhir, P. Ring, and A. Thimet, Ann. Phys. (N.Y.) **198**, 132 (1990).
21. G. A. Lalazissis, J. König, and P. Ring, Phys. Rev. C **55**, 540 (1997).
22. G. A. Lalazissis, S. Karatzikos, R. Fossion, D. Peña Arteaga, A. V. Afanasjev, and P. Ring, Phys. Lett. B **671**, 36 (2009).
23. A. Akmal, V. R. Pandharipande, and D. G. Ravenhall, Phys. Rev. C **58**, 1804 (1998).
24. M. Baldo, C. Maieron, P. Schuck, and X. Viñas, Nucl. Phys. A **736**, 241 (2004).
25. G. A. Lalazissis, T. Nikšić, D. Vretenar, and P. Ring, Phys. Rev. C **71**, 024312 (2005).
26. T. Bürvenich, D. G. Madland, J. A. Maruhn, and P.-G. Reinhard, Phys. Rev. C **65**, 044308 (2002).
27. P. W. Zhao, Z. P. Li, J. M. Yao, and J. Meng, Phys. Rev. C **82**, 054319 (2010).
28. T. Niksic, D. Vretenar, and P. Ring, Phys. Rev. C **78**, 034318 (2008).
29. J. P. Perdew and S. Kurth, in *A Primer in Density Functional Theory*, edited by C. Fiolhais, F. Nogueira, and M. A. L. Marques (Springer Berlin Heidelberg, Berlin, 2003), Vol. 620, pp. 1–55.
30. X. Roca-Maza, X. Viñas, M. Centelles, P. Ring, and P. Schuck, Phys. Rev. C **84**, 054309 (2011).
31. M. Baldo, L. M. Robledo, P. Schuck, and X. Viñas, J. Phys. G **37**, 064015 (2010).
32. E. N. E. van Dalen, C. Fuchs, and A. Faessler, Eur. Phys. J. A **31**, 29 (2007).
33. S. E. Agbemava, A. V. Afanasjev, D. Ray, and P. Ring, Phys. Rev. C **89**, 054320 (2014).
34. S. Goriely, N. Chamel, and J. M. Pearson, Phys. Rev. C **82**, 035804 (2010).
35. Q.-S. Zhang, Z.-M. Niu, Z.-P. Li, J.-M. Yao, and J. Meng, Front. Phys. 529536 (2014).
36. G. A. Lalazissis, S. Karatzikos, M. Serra, T. Otsuka, and P. Ring, Phys. Rev. C **80**, 041301 (2009).
37. A. V. Afanasjev and E. Litvinova, Phys. Rev. C **92**, 044317 (2015).
38. A. V. Afanasjev, S. E. Agbemava, D. Ray, and P. Ring, Phys. Rev. C **91**, 014324 (2015).
39. S. E. Agbemava, A. V. Afanasjev, T. Nakatsukasa, and P. Ring, Phys. Rev. C **92**, 054310 (2015).
40. J. P. Schiffer, S. J. Freeman, J. A. Caggiano, C. Deibel, A. Heinz, C.-L. Jiang, R. Lewis, A. Parikh, P. D. Parker, K. E. Rehm, S. Sinha, and J. S. Thomas, Phys. Rev. Lett. **92**, 162501 (2004).
41. W.-H. Long, N. Van Giai, and J. Meng, Phys. Lett. B **640**, 150 (2006).
42. E. Litvinova and P. Ring, in *Relativistic Density Functional for Nuclear Structure*, edited by J. Meng (World Scientific, Singapore, 2016), Vol. 10, Chap. 11, pp. 469–516.
43. J. W. Negele, Phys. Rev. C **1**, 1260 (1970).
44. J. W. Negele and D. Vautherin, Phys. Rev. C **5**, 1472 (1972).
45. R. Brockmann and H. Toki, Phys. Rev. Lett. **68**, 3408 (1992).
46. R. Fritz, H. Müther, and R. Machleidt, Phys. Rev. Lett. **71**, 46 (1993).
47. R. Fritz and H. Müther, Phys. Rev. C **49**, 633 (1994).
48. H.-l. Shi, B.-q. Chen, and Z.-y. Ma, Phys. Rev. C **52**, 144 (1995).
49. P. Ring, J. Phys. Conf. Ser. **580**, 012005 (2015).
50. S.-G. Zhou, J. Meng, and P. Ring, Phys. Rev. C **68**, 034323 (2003).
51. S. Shen, J. Hu, H. Liang, J. Meng, P. Ring, and S. Zhang, Chin. Phys. Lett. **33**, 102103 (2016).
52. M. R. Anastasio, L. S. Celenza, W. S. Pong, and C. M. Shakin, Phys. Rep. **100**, 327 (1983).
53. R. Brockmann and R. Machleidt, Phys. Lett. B **149**, 283 (1984).
54. B. ter Haar and R. Malfliet, Phys. Rep. **149**, 207 (1987).
55. H. Müther, F. Sammarruca, and Z. Ma, Int. J. Mod. Phys. E **26**, 1730001 (2017).
56. I. Angeli and K. Marinova, At. Data Nucl. Data Tables **99**, 69 (2013).
57. L. Coraggio, N. Itaco, A. Covello, A. Gargano, and T. T. S. Kuo, Phys. Rev. C **68**, 034320 (2003).
58. H. Müther, R. Machleidt, and R. Brockmann, Phys. Rev. C **42**, 1981 (1990).
59. E. N. E. van Dalen and H. Müther, Phys. Rev. C **84**, 024320 (2011).
60. R. Roth, J. Langhammer, A. Calci, S. Binder, and P. Navrátil, Phys. Rev. Lett. **107**, 072501 (2011).
61. R. Machleidt, Adv. Nucl. Phys. **19**, 189 (1989).
62. J. Negele, Rev. Mod. Phys. **54**, 913 (1982).

Evolution of ideas in direct and fusion reactions

N. Alamanos

CEA-Saclay, DAPNIA-SPhN, Gif-sur-Yvette, France

Abstract. The evolution of our ideas in the domain of elastic and inelastic scattering as well as of direct and fusion reactions at near- and sub-barrier energies will be presented briefly. Start point will be our first attempts to describe elastic and inelastic scattering via the JLM model, without adjustable parameters, up to recent analyses using this model and aiming to obtain experimental matter radii. This new observable, "matter radii", will be compared to state-of-the-art ab-initio calculations and challenge their predictive strength. Fusion of very neutron-rich nuclei may be important to determine the composition and heating of the crust of accreting neutron stars. The evolution of our ideas in this domain will be discussed. Near- and sub-barrier fusion results will be compared to modern theoretical calculations (CDCC, density-constrained Hartree-Fock calculations). Personal ideas for both direct and sub- or near-barrier fusion reactions will be given, responding to the questions "where do we stand? What is next?".

Everything is coupled; reactions with weakly bound projectiles

K. Rusek

Heavy Ion Laboratory, University of Warsaw, Poland

Abstract. Weakly bound light nuclei are ideal to study the importance of coupling effects observed in experiments devoted to elastic scattering, transfer reactions and fusion. Dominant effects come from couplings to the breakup channels while the effects of transfer reactions are of less importance.

PACS. 25.45.De Elastic and inelastic scattering – 25.60.-t Reactions induced by unstable nuclei – 24.10.Eq Coupled-channel and distorted-wave models

1 Introduction

In nuclear physics we deal with real and virtual processes, allowed by quantum mechanics. As an example of a virtual process we may take the case where a projectile nucleus is raised to an excited state in the field of a target nucleus and then decays back to the ground state before it has traversed this field. It may also happen that instead of excitation, a nucleon is transfered back and forth when the two nuclei collide. At first glance such a process is indistinguishable from elastic scattering. However, it was demonstrated in experiments with polarized lithium isotopes that analysing powers are very sensitive to such couplings [1]. The elastic scattering cross section also shows sensitivity to coupling effects [2] while the influence of the direct reaction channels (mainly excitations of the nuclei involved) on the fusion cross section is the subject of a long lasting discussion [3].

2 Elastic scattering and couplings to the breakup and transfer channels

In experiments with a weakly bound projectile its desintegration in the field of the target nucleus is the dominant process at forward scattering angles, so couplings of the elastic scattering to the breakup channels must play a dominant role. In order to study these effects one needs a more microscopic model than the Optical Model (OM) usually applied to analyses of elastic scattering data. One of the best is the Continuum-Discretized Coupled-Channels (CDCC) model developed originally for d elastic scattering [4]. This is an extension of coupled channels technique to allow treatment of the couplings to resonant and non-resonant states from the continuum.

The coupling effect depends on energy and is pronounced at energies close to the Coulomb barrier. An example is shown in Fig. 1. In the upper panel the experimental data for ^{6}Li+^{28}Si elastic scattering taken at a bombarding energy slightly above the barrier are plotted. A standard analysis using the OM underestimates the data (dotted curve) while inclusion of couplings to the ^{6}Li $\rightarrow$ α+d breakup channels (CDCC method) improves significantly the description of the data (dashed curve). The couplings increase the differential cross sections, a general trend also observed for other scattering systems at energies from the vicinity of the Coulomb barrier. Such an increase could be simulated in OM calculations by a reduction of the real part of the OM potential. Thus, the couplings to the breakup channels correspond to a repulsive real term added to the standard OM potential, the so called Dynamic Polarization Potential (DPP). This conclusion is in agreement with many other observations reported previously for various scattering systems. At higher bombarding energies, well above the Coulomb barrier, the effective reduction of the real part of the OM potential by the breakup leads to another observation - the differential cross section for elastic scattering is supressed at forward scattering angles in comparison with the OM prediction [8]. This is due to the fact that at higher energies the scattering amplitude is dominated by the far-side component being reduced by weaker attraction in the field of the target [9].

The analysis by the CDCC method provides predictions for the breakup channel. They are plotted as the dashed curve in the lower panel of Fig. 1 and coincide well with the measured values of the breakup differential cross section (open dots).

Breakup is one of many processes that could be induced in the scattering of two nuclei, one of the most probable is transfer of neutrons. Indeed, in the ^{6}Li+^{28}Si experiment discussed here the largest cross section was measured for the one-neutron transfer reaction leading to many states in the final nucleus, ^{29}Si [7]. The effect of coupling to the transfer channels on the elastic scattering has

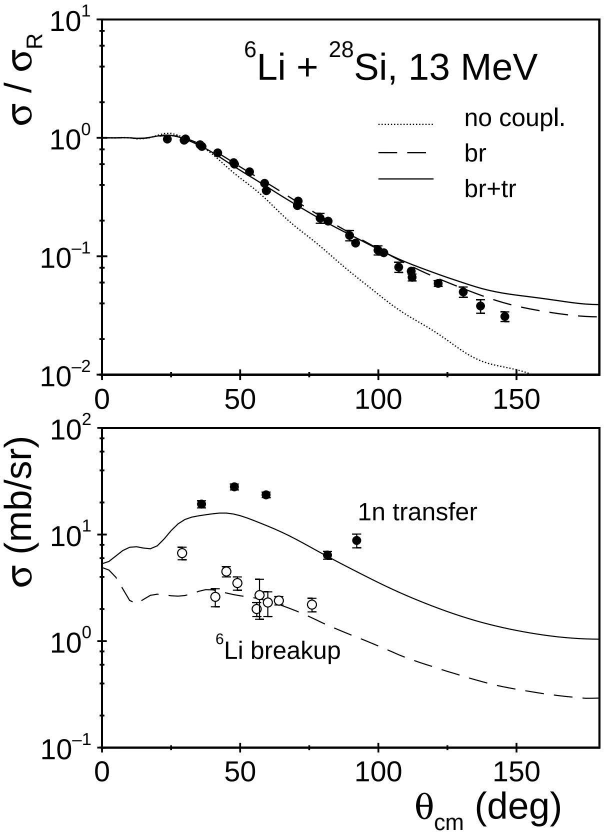

Fig. 1. Reactions induced by a 13 MeV lithium beam on a silicon target: elastic scattering (upper panel), one-neutron transfer and ^{6}Li breakup reactions (lower panel). Data are from [5–7]. For the curves see the text.

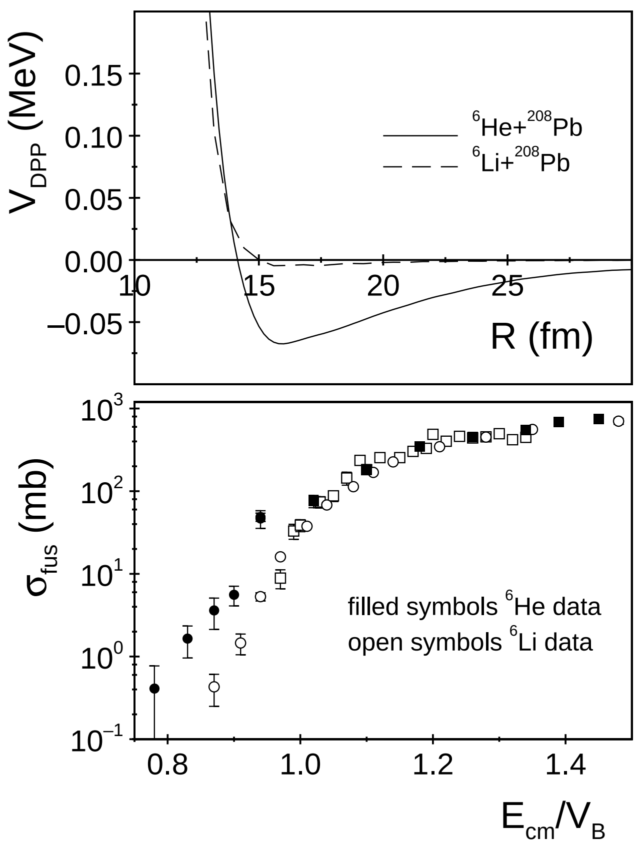

Fig. 2. Real parts of the DPP due to breakup for the two scattering systems (upper panel). Fusion cross sections for ^{6}Li and ^{6}He with lead and bismuth targets [10–13], lower panel.

not been investigated so intensively. Such a study requires another theoretical model, the method of Coupled Reaction Channels (CRC). The solid curve in the upper panel of the Fig. 1 shows the prediction of a CRC calculation for the ^{6}Li+^{28}Si elastic scattering. Inclusion of the one-neutron transfer reaction reduces the effect of breakup at more forward angles (around 50 deg) while at the very backward angles it enhances the cross section for the elastic scattering. The latter effect is much more visible at higher energies, well above the Coulomb barrier, as was recently reported for ^{6}Li+^{18}O [8].

Since the transfer cross section was also measured for the ^{6}Li+^{28}Si system (data plotted in the lower panel of Fig. 1), it could be compared with the results of the CRC calculation (solid curve in the lower panel of Fig. 1). The difference between the data and the calculations is due to the contribution of the compound nucleus reaction [7].

3 Fusion and direct reactions

Because of the very different time scale, the process of fusion can not be coupled to the direct channels in the way discussed in this contribution. Moreover, theoretical methods like CRC or CDCC are well suited to describe direct reaction channels but not fusion. The cross section for fusion is usually calculated by means of simple potential models, like the model of Wong [15]. Thus, in order to study the influence of direct reactions on the fusion cross section one has to find how the direct reactions contribute to the effective nucleus-nucleus potential or, in other words, study the DPPs corresponding to various direct channels.

For breakup, the DPPs have been studied for various scattering systems. It is well established that at energies well above the Coulomb barrier the real part of the DPP is repulsive while at energies close to the barrier it may become attractive and this attraction is due to the increasing importance of Coulomb couplings [16]. A typical example is plotted in the upper part of the Fig 2. The real part of the DPP obtained for ^{6}Li scattered from a lead target at an energy slighly above the Coulomb barrier is plotted by the dashed curve. The potential is repulsive at small projectile-target separations and its attractive component at large separations is negligible because the Coulomb couplings to the continuum for ^{6}Li are very weak

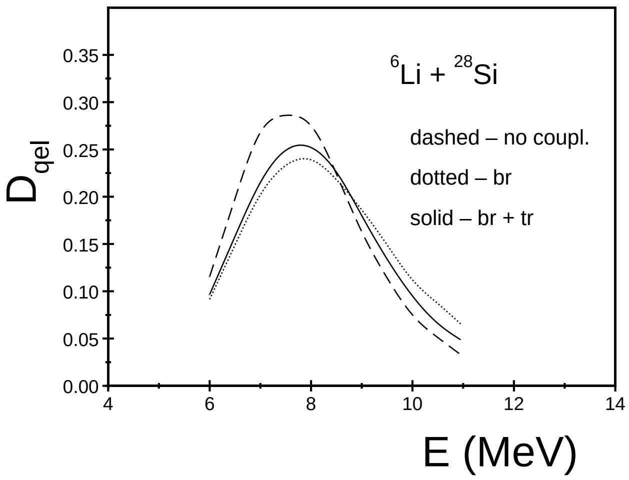

Fig. 3. Predicted Coulomb barrier distributions for ^{6}Li+^{28}Si. For comparison with the data see [14].

(no E1 excitations). For ^{6}He the dipole couplings to the $\alpha+2n$ continuum are strong and they generate the attractive component of the DPP (solid curve). Thus, one may expect that in low energy experiments, sensitive to the effective potential at large separations, the Coulomb barrier for ^{6}He+^{208}Pb is lower than that for ^{6}Li+^{208}Pb and, consequently, the fusion cross section for the latter system is reduced in comparison with the previous one. This speculation is in agreement with the experimental results plotted in the lower panel (fusion cross sections are plotted as a function of the energy divided by the nominal Coulomb barrier for the corresponding system).

For transfer reactions, much less is known about the DPPs generated by these channels. Complex analysis of ^{6}He+^{206}Pb experimental data [17] has shown that neutron-transfer reactions included in the CRC calculations led to a strong reduction of the imaginary part of the effective potential that became of the typical "short range" Woods-Saxon form, leaving the real part of the effective potential untouched.

4 Effect on the Coulomb barrier distribution

The problem of the influence of direct reaction channels on fusion cross section is related to investigations of Coulomb barrier distributions. The experimental studies rely mainly on measurements of the quasielastic scattering excitation function performed at backward scattering angles. Its first derivative (D_{qel}(E) in Fig. 3) reflects the Coulomb barrier distribution for a given scattering system [18] and it is dependent on couplings to the various direct reaction channels. The curves presented in Fig. 3 show the predictions for such a dependence resulting from CRC calculations for the ^{6}Li+^{28}Si system (for comparison with the data see [14]). As in the case of elastic scattering, coupling to the breakup channels has the dominant influence on the distribution while the one-neutron transfer reaction modifies this result only slightly.

5 Summary

Coupling to the breakup channels affects strongly the elastic scattering differential cross sections and contributes to the generation of analysing powers. Depending on the energy, this coupling may enhance or reduce the elastic cross section values with respect to "static" OM predictions. The effect of transfer reactions on the elastic scattering is especially important at backward scattering angles where an enhancement of the elastic scattering differential cross section due to transfer channels was reported.

Direct reaction channels may significantly affect fusion cross section predictions with respect to those based on a "static" potential model, e.g. enhance the predictions below the Coulomb barrier and supress them above it. In experiments investigating Coulomb barrier distributions breakup tends to broaden the distribution and to increase its average energy, while the role of the transfer is of less importance.

The best way to investigate coupling effects is to perform a series of complementary experiments and collect a variety of data. So far not many data sets exist that cover all posible reaction channels for a given pair of nuclei. However, one good example of such a set is the data for the ^{6}Li+^{28}Si system collected by Professor Athena Pakou and her team and discussed in this contribution.

All the calculations presented in this contribution were performed by means of the computer code FRESCO [19].

6 Aknowledgements

The author aknowledges financial support from the Ministry of Science and Higher Education of Poland and stimulating discussions with dr Nicholas Keeley.

References

1. D. Fick, G. Grawert and Irena M. Turkiewicz, Phys. Reports **214** (1992) 1.
2. N. Keeley et al., Eur. Phys. J. A **50**, 145 (2014).
3. J. J. Kolata et al., Eur. Phys. J. A **52**, 123 (2016).
4. G.H. Rawitsher, Phys. Rev. C **9**, 2210 (1974).
5. A. Pakou et al., Phys. Lett. **633**, 691 (2006).
6. A. Pakou et al., Phys. Rev. C **69**, 054602 (2004).
7. A. Pakou et al., Phys. Rev. C **76**, 054601 (2007).
8. K. Rusek et al., Phys. Rev. C **91**, 044612 (2015).
9. Y. Sakuragi, Phys. Rev. C **35**, 2161 (1987).
10. R. Wolski et al., Eur. Phys. J. A **47**, 111 (2011).
11. J.J. Kolata et al., Phys. Rev. Lett. **81**, 4580 (1998).
12. Y.W. Wu et al., Phys. Rev. C **68**, 044605 (2003).
13. M. Dasgupta et al., Phys. Rev. C **66**, 041602 (2002).
14. K. Zerva et al., Phys. Rev. C **82**, 044607 (2010).
15. C.Y. Wong, Phys. Rev. Lett. **31**, 766 (1973).
16. K. Rusek, Eur. Phys. J. A **41**, 399 (2009).
17. L. Standylo et al. Phys. Rev. C **87**, 064603 (2013).
18. J.P. Fernandez-Garcia et al., Phys. Rev. C **92**, 054602 (2015).
19. I.J. Thompson, Comput. Phys. Rep. **7**, 167 (1988).

Light charged particle production in reactions induced by weakly-bound projectiles: Still an open question.

N. Keeley

National Centre for Nuclear Research, ul. Andrzeja Sołtana 7, 05-400 Otwock, Poland

Abstract. It is often assumed that the large inclusive cross sections for production of alpha particles and other light fragments in reactions induced by weakly-bound projectiles are due to breakup. This is in spite of considerable evidence dating back over forty years that transfer reactions actually play the main rôle in most systems of this type. Some of the evidence available in the literature will be reviewed for the stable weakly-bound nuclei ^{6}Li and ^{7}Li as well as the rather more fragmentary data for radioactive beams like ^{6}He, ^{8}He, ^{8}B etc.

PACS. 24.50.+g Direct reactions – 25.60.-t Reactions induced by unstable nuclei

1 Introduction

Reactions induced by light weakly-bound nuclei produce large numbers of light charged particles (d, t, α, etc.) with atomic number less than that of the projectile. This phenomenon was first observed almost sixty years ago [1] and is still an active topic of research, see e.g. Ref. [2]. Given the low thresholds against breakup into two (or more) fragments of the projectiles involved it seems obvious that the large observed yields of light charged particles are due to breakup, so why the continued interest? We shall see that this simple but nevertheless attractive explanation had difficulties even from the very first studies and that the key to a full understanding is provided by *exclusive*, that is to say coincidence, measurements.

In the space available it is impossible to give more than a brief overview of the subject, since a complete survey would require a substantial review article. This contribution therefore represents a highly compressed summary and the choice of examples reflects the work with which the author is most familiar rather than a comprehensive reference list.

2 Breakup, or transfer, or . . .

The first experimental evidence of large yields of light charged charged particles of atomic numbers less than that of the projectile in a reaction induced by a weakly-bound heavy ion was presented in the contribution of C. E. Anderson to the Gatlinburg Conference in 1960 [1]. The reactions induced by beams of ^{6}Li nuclei incident on ^{197}Au targets were investigated and large inclusive yields of protons, deuterons and α particles were observed, see Fig. 1.

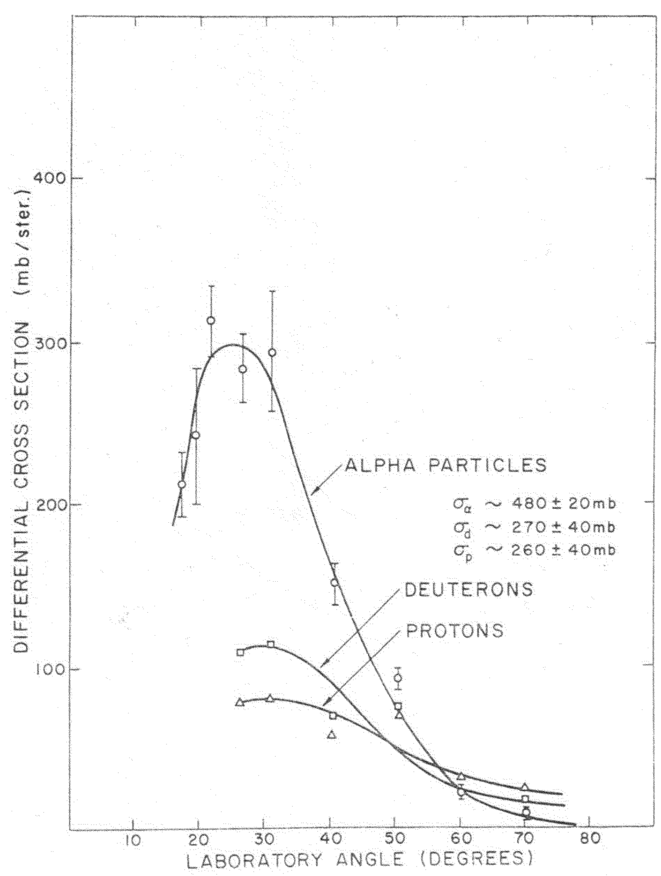

Fig. 1. Inclusive angular distributions for light charged particle production produced by 60.6 MeV ^{6}Li ions incident on a ^{197}Au target. Note that the data are in the *laboratory* frame. Taken from Ref. [1].

Leaving aside the protons for the moment, it is immediately obvious that the breakup hypothesis for the origin of these particles has a problem: approximately twice as many α particles as deuterons are observed. If the ^{6}Li $\rightarrow \alpha + d$ process were solely responsible then the inclusive α and d cross sections should be identical. The initial explanation proposed to overcome this difficulty was based on the observation that $\sigma_\alpha \approx \sigma_d + \sigma_p$; since the deuteron is itself weakly bound some of the deuterons produced in the initial ^{6}Li $\rightarrow \alpha + d$ breakup subsequently break up themselves, and/or part of the α yield comes from the ^{6}Li $\rightarrow \alpha + n + p$ four-body breakup (threshold 3.70 MeV compared to the 1.47 MeV of the ^{6}Li $\rightarrow \alpha + d$ three-body breakup).

This attractive explanation subsequently proved to be untenable. It was found [3] in exclusive measurements that much ($\sim 50\%$, as was later established) of the $\alpha + d$ coincidences were due to decay of the 2.19 MeV 3^+ resonance in ^{6}Li. The lifetime of the 3^+ (2.7×10^{-20} s) is such that on average it only decays into $\alpha + d$ at distances too far from the target for there to be much likelihood of the deuteron breaking up in its turn. It is also below the threshold for four-body breakup. Thus, for the explanation to hold much of the breakup via the non-resonant continuum would have to proceed either via four-body breakup or involve the subsequent breakup of the deuteron.

Ost *et al.* [3] also recorded significant numbers of $\alpha + p$ and $\alpha + \alpha$ coincidences in their measurements of the ^{6}Li + ^{208}Pb system. The projected $\alpha + p$ spectrum showed distinct peaks corresponding to levels in ^{209}Pb, proving that these coincidences came from the decay of ^{5}Li formed in the ^{208}Pb(^{6}Li,^{5}Li)^{209}Pb single neutron stripping reaction. The $\alpha + \alpha$ coincidences came from the decay of the ^{8}Be ground state formed in the ^{208}Pb(^{6}Li,^{8}Be)^{206}Tl deuteron pickup reaction. Their conclusion was that these transfer reactions could account for the observed excess of α particles over deuterons in the inclusive measurements.

This is a qualitatively satisfying explanation but can it provide a *quantitative* description? Signorini *et al.* [4] later performed quantitative inclusive and exclusive measurements for the ^{6}Li + ^{208}Pb system at a number of near-barrier energies, giving total *inclusive* α production and $\alpha + d$ and $\alpha + p$ coincidence cross sections. The $\alpha + d$ cross sections are well described by continuum discretised coupled channels (CDCC) calculations, as are the $\alpha + p$ coincidences by coupled reaction channels (CRC) calculations assuming a ^{208}Pb(^{6}Li,^{5}Li)^{209}Pb transfer mechanism, see Fig. 2. We thus have quantitative support for the conclusions of Ost *et al.* [3] regarding the origin of the $\alpha + p$ coincidences.

It will, however, be noted from Fig. 2 that the combined $\alpha + d$ and $\alpha + p$ coincidence cross sections are still considerably smaller than the inclusive α particle cross sections at all energies (also, that as the incident energy approaches the Coulomb barrier the inclusive α particle cross section trends towards saturating the total reaction cross section). Therefore, we are still some way from *proving* quantitatively that transfer reactions can account for

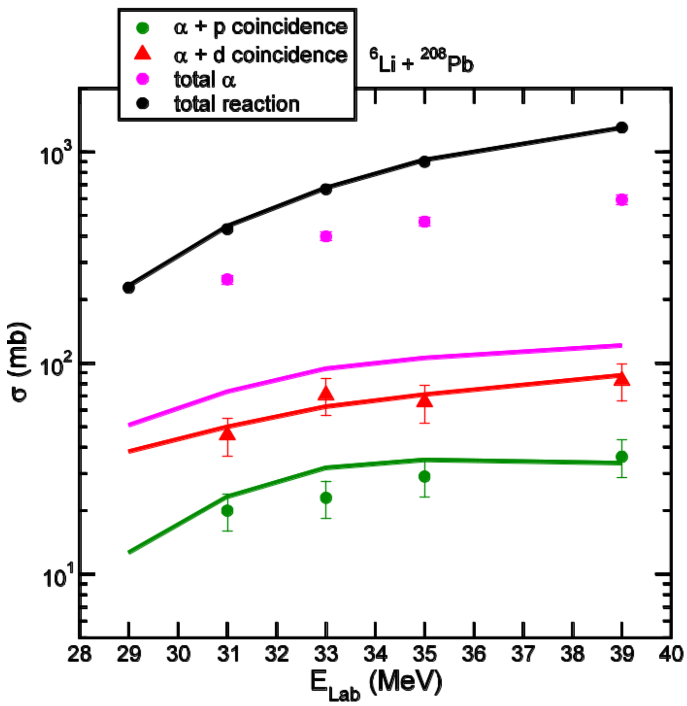

Fig. 2. Measured inclusive α production, $\alpha + d$ and $\alpha + p$ coincidence cross sections [4] and total reaction cross sections extracted from optical model fits to elastic scattering angular distributions [5]. Solid lines represent the results of combined CDCC/CRC calculations.

the excess of α particles over deuterons in systems of this type. Unfortunately it is not possible to perform a meaningful quantitative estimate of the contribution from the ^{208}Pb(^{6}Li,^{8}Be)^{206}Tl reaction since there are too many unknowns (the $\langle ^{208}\mathrm{Pb} \mid ^{206}\mathrm{Tl} + d \rangle$ spectroscopic factors and the exit channel optical potential). The Q-value window for this reaction is at least consistent with a possible significant contribution since it favours transfers to low-lying levels in ^{206}Tl.

Before moving on to other weakly-bound projectiles let us enumerate the sources of both α particles and deuterons in reactions induced by ^{6}Li beams:

1. ^{6}Li $\rightarrow \alpha + d$ breakup; produces equal quantities of both.
2. Fusion evaporation; more likely to produce α particles but not expected to contribute significantly for heavy targets.
3. (^{6}Li,^{5}Li) $\rightarrow$ ^{4}He + p.
4. (^{6}Li,^{5}He) $\rightarrow$ ^{4}He + n.
5. (^{6}Li,^{8}Be) $\rightarrow$ ^{4}He + ^{4}He.
6. (^{6}Li,^{4}He) (i.e. deuteron stripping).
7. (^{6}Li,^{6}Be) $\rightarrow$ ^{4}He + p + p.
8. (^{6}Li,^{6}He*) $\rightarrow$ ^{4}He + n + n.
9. (^{6}Li,^{7}Li*) $\rightarrow$ ^{4}He + ^{3}H.
10. (^{6}Li,^{7}Be*) $\rightarrow$ ^{4}He + ^{3}He.
11. (^{6}Li,d) (i.e. α stripping).

Admittedly reactions 7, 8, 9 and 10 are unlikely to contribute significantly but even disregarding them we see that there are four transfer reactions that can produce α

particles (one, reaction 5, with a multiplicity of 2) compared to just one that yields deuterons. This provides further qualitative support for what we may call the "transfer hypothesis". Of course, the relative importance of these reactions will depend very much on the target and incident energy since Q-value and L matching conditions and the availability of suitable states in the target-like residue will be critical to producing significant cross sections. The contribution of breakup will also depend on the target to some extent, since a higher Z implies more Coulomb breakup and thus a larger total breakup cross section. Finally, for lighter targets fusion-evaporation may be a major source of α particles and possibly also deuterons, further complicating matters.

The situation is similar for reactions induced by beams of ^{7}Li; many more α particles than tritons are observed in inclusive reactions for different targets over a wide mass range. In this case, four-body breakup of ^{7}Li and breakup of the triton following $^7\mathrm{Li} \to \alpha + t$ breakup may be ruled out as contributing factors to the lack of tritons. As an example we quote the study of the ^{7}Li + ^{197}Au system by Québert *et al.* [6]. Their measured singles (i.e. inclusive) yield for α particles was about a factor of 10 greater than the triton yield. In addition, they measured significant numbers of $\alpha + d$ coincidences coming from the (^{7}Li,^{6}Li*) single neutron stripping reaction to the 2.19 MeV 3^+ resonance of ^{6}Li.

3 Quantitative case studies

We have discussed qualitative support for a significant (and possibly dominant) contribution from transfer reactions to the α particle production in reactions induced by ^{6}Li and ^{7}Li but what quantitative support is there for this conclusion? In this section we present studies of two systems, ^{6}Li + ^{28}Si and ^{7}Li + ^{93}Nb where rather complete coincidence measurements have been made to disentangle the various production mechanisms.

In a series of papers [7–10] a group led by Prof. A. Pakou of the University of Ioannina made a complete study of the α particle production mechanism in the ^{6}Li + ^{28}Si system at near-barrier incident energies. Through coincidence measurements the dominant contribution of transfer reactions to the total cross section was determined, see Fig. 3. For this light target compound nucleus processes may make significant contributions which have to be estimated (using Hauser-Feshbach codes, for example) and subtracted from the data before comparing with direct reaction calculations. In this case the agreement of the DWBA calculations assuming nucleon stripping reactions is reasonable, the shapes of the angular distributions being well reproduced while the magnitudes are somewhat underestimated (but within the likely uncertainties of the calculations).

A recent study [11] of the ^{7}Li + ^{93}Nb system at energies approximately 2-3 times the Coulomb barrier measured significant cross sections for $\alpha + d$ and $\alpha + \alpha$ coincidences; the $\alpha + t$ coincidence from breakup were also recorded. A combination of CDCC and rather complete

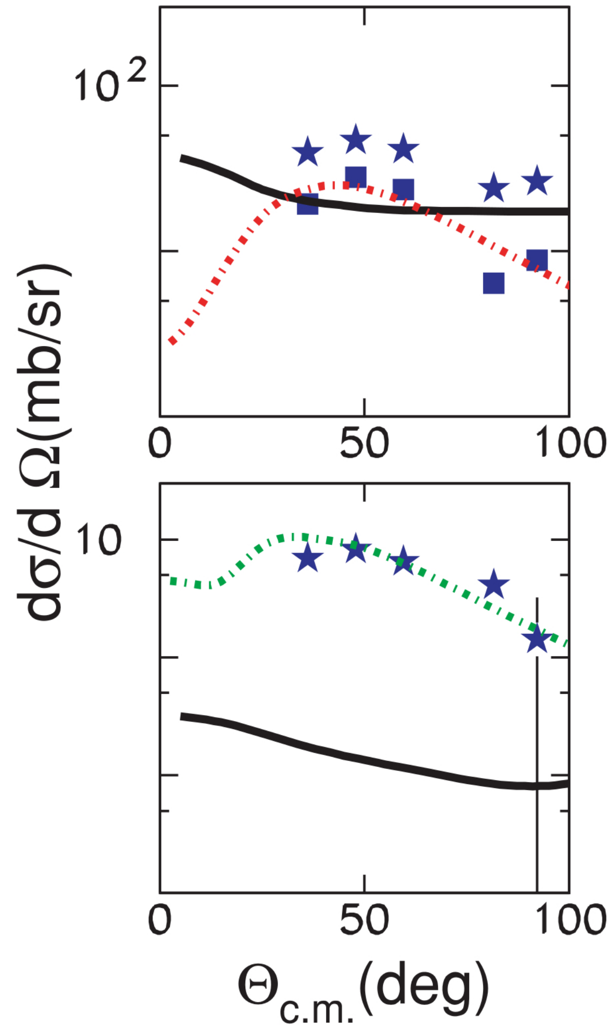

Fig. 3. Angular distributions for the ^{28}Si(^{6}Li,^{5}Li)^{29}Si (upper) and ^{28}Si(^{6}Li,^{5}He)^{29}P (lower) reactions at an incident ^{6}Li energy of 13 MeV obtained from $\alpha+\gamma$ coincidence measurements. The solid curves represent the calculated compound nucleus contributions, the stars the "raw" data and the squares the "direct" (with the compound contribution subtracted). The dot-dashed curves are the results of DWBA calculations for 1n and 1p stripping, multiplied by factors of 3.5 and 2.2 respectively. Adapted from Ref. [10].

CCBA calculations was able to describe very well the whole of the data (assuming neutron stripping to the 2.19 MeV 3^+ resonance of ^{6}Li and neutron pickup to the ground state of ^{8}Be) using structure information from the literature without the need for any renormalisation (this was helped by the fact that cuts were placed on the coincidence data to correspond exactly to the excitation energy ranges of the target-like residue states that it was possible to include in the CCBA calculations). Fig. 4 shows the results for an incident energy of 28 MeV.

We therefore see that there is quantitative proof of the importance of transfer mechanisms, at least for the α production in systems involving ^{6}Li and ^{7}Li projectiles.

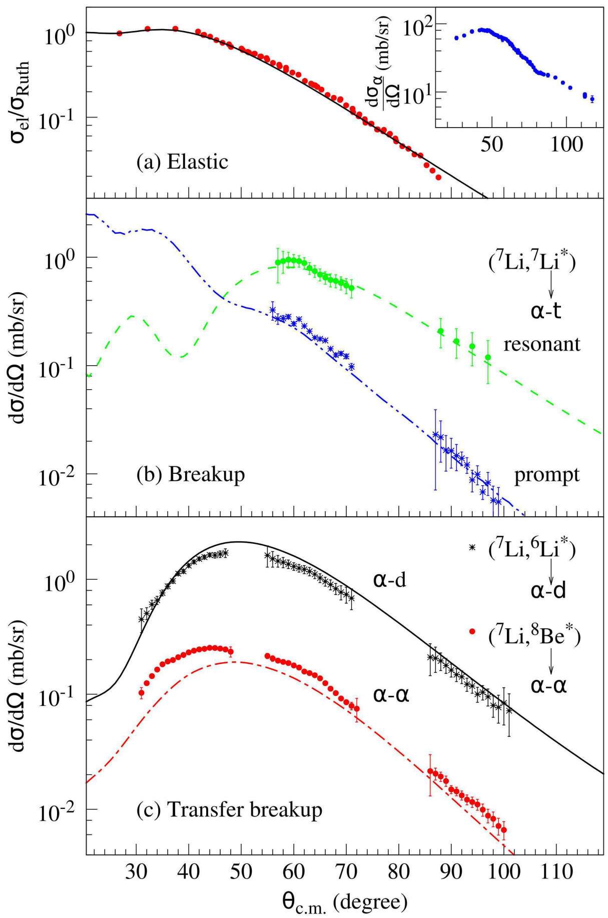

Fig. 4. Measured inclusive and exclusive cross sections for the ^{7}Li + ^{93}Nb system at 28 MeV. (a) Elastic scattering data and the CDCC calculation. Inset: the inclusive cross section for α production. (b) Prompt and resonant (the $7/2^-$ state) breakup of ^{7}Li, shown as asterisks and filled circles respectively. The CDCC results for prompt and resonant breakup are denoted by dot-dot-dashed and dashed lines respectively. (c) Exclusive data for $1p$ pickup to ^{8}Be(0_1^+) and $1n$ stripping to ^{6}Li(3_1^+) are presented as filled circles and asterisks respectively. The CCBA calculations for $1p$ pickup and $1n$ stripping are denoted by dot-dashed and solid lines respectively. Taken from Ref. [11].

However, as we found in the previous section for the ^{6}Li + ^{208}Pb system, it is still not always possible to account quantitatively for all of the observed inclusive α cross section in these stable beam systems. In the next section we shall examine the status of reactions induced by weakly-bound radioactive beams.

4 Radioactive beams

The situation becomes a little more complex in some respects when we turn to reactions induced by beams of light, weakly-bound radioactive nuclei. The range of light particles produced by breakup and/or transfer reactions increases, plus in many cases one or more neutrons may be

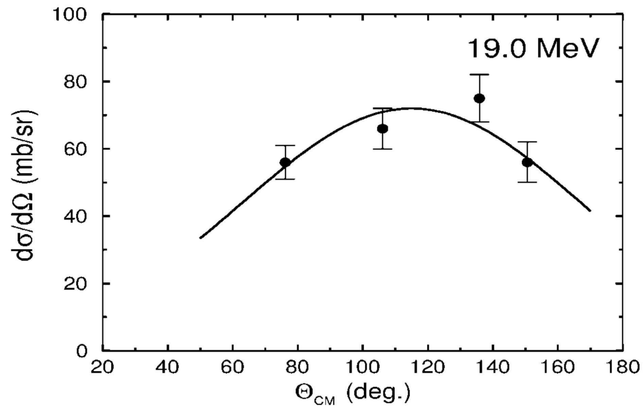

Fig. 5. Measured inclusive α particle angular distribution for the ^{6}He + ^{209}Bi system at an incident energy of 19.0 MeV. Taken from Ref. [13].

produced by breakup, complicating coincidence measurements. However, in the case of perhaps the best studied nucleus of this type, ^{6}He, the problem is actually simplified. The possible reactions leading to α particles are: ^{6}He breakup, $^6\text{He} \rightarrow \alpha + n + n$ and possibly $^6\text{He} \rightarrow {}^5\text{He} + n \rightarrow \alpha + n + n$; $1n$ stripping, (^{6}He,$^5\text{He} \rightarrow \alpha + n$); $2n$ stripping, (^{6}He,^{4}He); plus fusion evaporation for lighter targets.

The most complete data set is for the ^{6}He + ^{209}Bi system, measured at the TwinSol system of the University of Notre Dame. In a series of pioneering experiments basic elastic scattering angular distributions, fusion and inclusive α production excitation functions and α + n coincidence data were measured at near-barrier energies [12–16]. Very large inclusive α yields, much larger than measured fusion cross sections, were recorded. Their angular distributions suggested direct process(es), see Fig. 5. The cross section remains large at energies well below the barrier, implying that it is not dominated by breakup. In a series of α + n (+ n) coincidence measurements it was established that for a 22.5 MeV incident energy ^{6}He about 75% of the total α production cross section was due to the (^{6}He,^{5}He) and (^{6}He,^{4}He) transfer reactions (about 25% $1n$ stripping and 50% $2n$ stripping) with the remaining 25% due to breakup. Thus, it is something of a paradox that the α production is completely understood for the exotic ^{6}He nucleus but still not so in all cases for the stable ^{6}Li and ^{7}Li nuclei.

The situation is similar for ^{8}He, although a little more complicated since there is substantial ^{6}He production as well as ^{4}He and the available beam intensities are one to two orders of magnitude lower than for ^{6}He. Nevertheless, coincidence experiments have been performed for systems involving ^{8}He projectiles and it has been established that transfer reactions dominate the production mechanisms for ^{6}He and, for heavier targets, ^{4}He (for lighter mass targets the most important mechanism for ^{4}He production is fusion-evaporation), see e.g. Ref. [17].

Reactions induced by ^{7}Be appear to be similar to those induced by ^{6}Li and ^{7}Li projectiles in that there is an excess of α particles over ^{3}He in inclusive measurements, al-

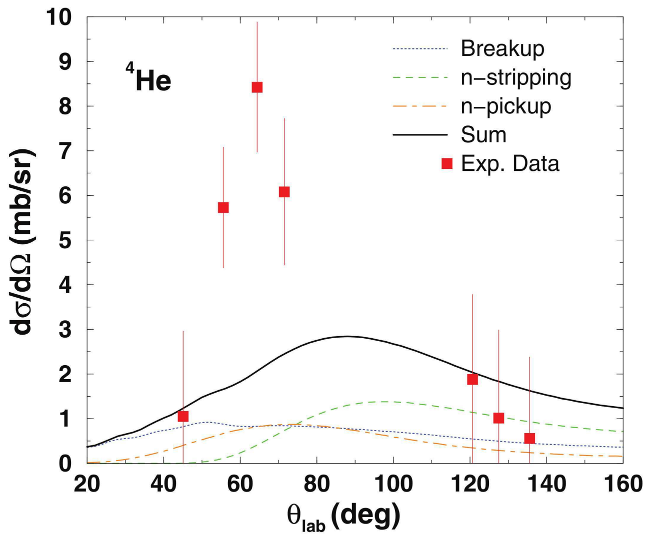

Fig. 6. Measured inclusive α particle angular distribution for the ^{7}Be + ^{58}Ni system at an incident energy of 22.0 MeV. The curves denote the various calculated contributions. The fusion-evaporation component has been subtracted from the data. Taken from Ref. [18].

though we still cannot be absolutely sure of all the production mechanisms. A recent study [18] examined the ^{7}Be + ^{58}Ni system at 22 MeV and found that while the ^{4}He production appears to be dominated by fusion-evaporation the ^{3}He are mainly produced by α particle stripping. The possible direct reactions that can lead to ^{3}He are only two in number, $^7\mathrm{Be} \rightarrow {}^4\mathrm{He} + {}^3\mathrm{He}$ breakup and the (^{7}Be,^{3}He) α transfer reaction. By contrast, ^{4}He can be produced by breakup, (^{7}Be,^{8}Be) $1n$ pickup, (^{7}Be,^{6}Be) $1n$ stripping and (^{7}Be,^{4}He) ^{3}He stripping in addition to fusion-evaporation.

The direct processes seem to contribute about equally to the ^{4}He production, but the (^{7}Be,^{4}He) contribution cannot be meaningfully calculated (the same applies to the (^{7}Be,^{3}He) contribution to the ^{3}He production), see Fig. 6.

Other weakly bound radioactive beams may behave differently. For example, it is fairly well established that breakup dominates the production of ^{7}Be and ^{16}O in reactions induced by ^{8}B and ^{17}F respectively. This may also be the case for ^{9}Li and ^{10}Be production in reactions induced by ^{11}Li and ^{11}Be beams. On the other hand, for ^{8}Li the ^{7}Li production is dominated by single neutron stripping. For ^{15}C the honours may be equal between breakup and transfer for the ^{14}C production, although this has yet to be measured. Of course, the exact trade-off between transfer and breakup for a given projectile may well depend critically on target and/or incident energy.

5 Conclusion

A brief survey of light charged particle production mechanisms in reactions induced by beams of stable and radioactive weakly bound nuclei has been given. In spite of almost sixty years of investigations into this topic there remain unanswered questions. Is ^{4}He (and d, t or ^{3}He) stripping in the conventional sense really important for light particle production in reactions induced by ^{6}Li, ^{7}Li and ^{7}Be or is the mechanism something else like "incomplete fusion" or "capture breakup"? Is it even meaningful to talk about different mechanisms in this context? All that can be said with any confidence is that, by some means or other, mass is transferred from the projectile to the target, whether this is transfer in the conventional nuclear reaction sense or some other mechanism.

It appears as something of a paradox that the mechanisms are better understood in the case of certain radioactive beams that is the case for their stable counterparts. This is due to the smaller number of mechanisms involved in these cases compared to the rather complex situation for ^{6}Li and ^{7}Li. In addition to ^{6}He we may cite the case of ^{15}C where only two mechanisms can contribute to the ^{14}C production, single neutron stripping and breakup. In this case we can also be sure that there will be no compound nucleus contribution.

There is thus still room for work in this area, and more exclusive (that is, coincidence) data are required to unravel this interesting problem.

References

1. C. E. Anderson, *Proc. 2nd Conf. on reactions between complex nuclei,* Gatlinburg, 1960, ed. A. Zucker, E. C. Halbert and F. J. Howard (Wiley, N.Y., 1960).
2. J. Lei and A. M. Moro, Phys. Rev. C **95**, 044605 (2017).
3. R. Ost, K. Bethge, H. Gemmeke, L. Lassen, and D. Scholz, Z. Phys. **266**, 369 (1974).
4. C. Signorini, A. Edifizi, M. Mazzocco, M. Lunardon, D. Fabris, A. Vitturi, P. Scopel, F. Soramel, L. Stroe, G. Prete, E. Fioretto, M. Cinausero, M. Trotta, A. Brondi, R. Moro, G. La Rana, E. Vardaci, A. Ordine, G. Inglima, M. La Commara, D. Pierroutsakou, M. Romoli, M. Sandoli, A. Diaz-Torres, I. J. Thompson, and Z. H. Liu, Phys. Rev. C **67**, 044607 (2003).
5. N. Keeley, S. J. Bennett, N. M. Clarke, B. R. Fulton, G. Tungate, P. V. Drumm, M. A. Nagarajan, and J. S. Lilley, Nucl. Phys. A **571**, 326 (1994).
6. J. L. Québert, B. Frois, L. Marquez, G. Sousbie, R. Ost, K. Bethge, and G. Gruber, Phys. Rev. Lett. **32**, 1136 (1974).
7. A. Pakou, N. Alamanos, A. Gillibert, M. Kokkoris, S. Kossionides, A. Lagoyannis, N. G. Nicolis, C. Papachristodoulou, D. Patiris, D. Pierroutsakou, E. C. Pollacco, and K. Rusek, Phys. Rev. Lett. **90**, 202701.
8. A. Pakou, K. Rusek, N. G. Nicolis, N. Alamanos, G. Doukelis, A. Gillibert, G. Kalyva, M. Kokkoris, A. Lagoyannis, A. Musumarra, C. Papachristodoulou, G. Perdikakis, D. Pierroutsakou, E. C. Pollacco, A. Spyrou and Ch. Zarkadas, J. Phys. G **31**, S1723 (2005).
9. A. Pakou, N. Alamanos, N. M. Clarke, N. J. Davis, G. Doukelis, G. Kalyva, M. Kokkoris, A. Lagoyannis, T. J. Mertzimekis, A. Musumarra, N. G. Nicolis, C. Papachristodoulou, N. Patronis, G. Perdikakis, D. Pierroutsakou, D. Roubos, K. Rusek, S. Spyrou, and Ch. Zarkadas, Phys. Lett. B **633**, 691 (2006).

10. A. Pakou, K. Rusek, N. Alamanos, X. Aslanoglou, S. Harissopulos, M. Kokkoris, A. Lagoyannis, T. J. Mertzimekis, A. Musumarra, N. G. Nicolis, C. Papachristodoulou, D. Pierroutsakou, and D. Roubos, Phys. Rev. C **76**, 054601 (2007).
11. S. K. Pandit, A. Shrivastava, K. Mahata, N. Keeley, V. V. Parkar, P. C. Rout, K. Ramachandran, I. Martel, C. S. Palshetkar, A. Kumar, A. Chatterjee, and S. Kailas, Phys. Rev. C **93**, 061602(R) (2016).
12. J. J. Kolata, V. Guimarães, D. Peterson, P. Santi, R. White-Stevens, P. A. DeYoung, G. F. Peaslee, B. Hughey, B. Atalla, M. Kern, P. L. Jolivette, J. A. Zimmerman, M. Y. Lee, F. D. Becchetti, E. F. Aguilera, E. Martinez-Quiroz, and J. D. Hinnefeld, Phys. Rev. Lett. **81**, 4580 (1998).
13. E. F. Aguilera, J. J. Kolata, F. M. Nunes, F. D. Becchetti, P. A. DeYoung, M. Goupell, V. Guimarães, B. Hughey, M. Y. Lee, D. Lizcano, E. Martinez-Quiroz, A. Nowlin, T. W. O'Donnell, G. F. Peaslee, D. Peterson, P. Santi, and R. White-Stevens, Phys. Rev. Lett. **84**, 5058 (2000).
14. J. P. Bychowski, P. A. DeYoung, B. B. Hilldore, J. D. Hinnefeld, A. Vida, F. D. Becchetti, J. Lupton, T. W. O'Donnell, J. J. Kolata, G. Rogachev, and M. Hencheck, Phys. Lett. B **596**, 26 (2004).
15. P. A. DeYoung, P. J. Mears, J. J. Kolata, E. F. Aguilera, F. D. Becchetti, Y. Chen, M. Cloughesy, H. Griffin, C. Guess, J. D. Hinnefeld, H. Jiang, S. R. Jones, U. Khadka, D. Lizcano, E. Martinez-Quiroz, M. Ojaniega, G. F. Peaslee, A. Pena, J. Rieth, S. VanDenDriessche, and J. A. Zimmerman, Phys. Rev. C **71**, 051601(R) (2005).
16. J. J. Kolata, H. Amro, F. D. Becchetti, J. A. Brown, P. A. DeYoung, M. Hencheck, J. D. Hinnefeld, G. F. Peaslee, A. L. Fritsch, C. Hall, U. Khadka, P. J. Mears, P. O'Rourke, D. Padilla, J. Rieth, T. Spencer, and T. Williams, Phys. Rev. C **75**, 031302(R) (2007).
17. A. Lemasson, A. Navin, M. Rejmund, N. Keeley, V. Zelevinsky, S. Bhattacharyya, A. Shrivastava, D. Bazin, D. Beaumel, Y. Blumenfeld, A. Chatterjee, D. Gupta, G. de France, B. Jacquot, M. Labiche, R. Lemmon, V. Nanal, J. Nyberg, R. G. Pillay, R. Raabe, K. Ramachandran, J. A. Scarpaci, C. Schmitt, C. Simenel, I. Stefan, and C. N. Timis, Phys. Lett. B **697**, 454 (2011).
18. M. Mazzocco, D. Torresi, D. Pierroutsakou, N. Keeley, L. Acosta, A. Boiano, C. Boiano, T. Glodariu, A. Guglielmetti, M. La Commara, J. A. Lay, I. Martel, C. Mazzocchi, P. Molini, C. Parascandolo, A. Pakou, V. V. Parkar, M. Romoli, K. Rusek, A. M. Sanchez-Benítez, M. Sandoli, O. Sgouros, C. Signorini, R. Silvestri, F. Soramel, V. Soukeras, E. Stiliaris, E. Strano, L. Stroe, and K. Zerva, Phys. Rev. C **92**, 024615 (2015).

The EXOTIC project at INFN-LNL

D. Pierroutsakou[1], A. Boiano[1], C. Boiano[2], M. La Commara[3,1], G. La Rana[3,1], M. Mazzocco[4,5], C. Parascandolo[1], C. Signorini[4,5], F. Soramel[4,5], and E. Strano[4,5]

[1] INFN - Sezione di Napoli, Via Cintia, I-80126 Napoli, Italy
[2] INFN - Sezione di Milano, Via Celoria 16, I-20133 Milano, Italy
[3] Dipartimento di Fisica, Università di Napoli, Via Cintia, I-80126 Napoli, Italy
[4] Dipartimento di Fisica e Astronomia, Università di Padova, Via Marzolo 8, I-35131 Padova, Italy
[5] INFN - Sezione di Padova, Via Marzolo 8, I-35131 Padova, Italy

Abstract. The low-energy light Radioactive Ion Beam in-flight facility EXOTIC and the associated experimental apparatus, installed at INFN-LNL and designed for nuclear physics and nuclear astrophysics measurements is presented.

PACS. 29.38.-c Radioactive beams – 29.40.Gx Tracking and position-sensitive detectors – 29.40.Cs Gas-filled counters – 29.40.Wk Solid-state detectors – 25.60.-t Reactions induced by unstable nuclei – 27.20.+n $6 \leq A \leq 19$

1 Introduction

The growing availability of Radioactive Ion Beams (RIBs) worldwide has opened up new scenarios and challenges in nuclear physics. Experiments with radioactive (exotic) nuclei allow to explore the properties of isotopes that have a proton-to-neutron ratio very different from the stable ones, measure cross sections of important reactions for the stellar nucleosynthesis occurring in explosive astrophysical environments, constrain the isospin-dependent nucleon-nucleon interaction in neutron-rich nuclei and in neutron stars, synthesize superheavy elements and test physics beyond the standard model.

While several large-scale RIB facilities are actually operating at RIKEN [1], NSCL/MSU [2], GANIL (France) [3], GSI [4], CERN (ISOLDE) [5], TRIUMF (ISAC) [6] and small-scale facilities like Twinsol in Notre Dame University (USA) [7], RIBRAS (Brasil) [8], JYFL (Jyvaskyla, Finland) [9], CRIB (Japan) [10–12], EXOTIC (LNL-INFN, Italy) [13–16], future infrastructures like SPES (LNL-INFN, Italy), SPIRAL2 (France), HIE-ISOLDE (CERN), FRIB (USA), FAIR (Germany), EURISOL (Europe) are aimed at delivering RIBs with the highest intensity and purity and with good ion optical quality for investigating unreachable parts of the nuclear chart.

Along with the construction of new RIB infrastructures, a continuous development of detection arrays is under way. Depending on the radioactive ion incident energy and on the class of reactions to be studied, different experimental set-ups were built for the detection of charged particles.

In this paper we describe the EXOTIC project, developed at the INFN Legnaro National Laboratories (LNL) and constisting of the EXOTIC RIB facility and the associated experimental apparatus.

2 EXOTIC facility

The EXOTIC facility is dedicated to the in-flight production of low-energy light RIBs, by inverse kinematics nuclear reactions using the intense heavy-ion beams from the LNL Tandem XTU accelerator hitting a light gas target (H_2, D_2, ^{3}He, ^{4}He). The main characteristics of the facility, displayed in Fig. 1, are a large RIB acceptance of the optics elements and a large capability to suppress all the unwanted scattered beams. It consists of: i) a production gas target that is a 5 cm-long cylindrical cell with entrance (ϕ=14 mm) and exit (ϕ=16 mm) windows made of 2.2 μm (1.83 mg/cm^2) thick HAVAR foil, operating at room or at liquid N_2 temperatures with an operational pressure up to 1 atm; ii) a beam selection and transport system consisting of: a triplet of large diameter quadrupole lenses (ϕ=160 mm), a 30° bending magnet, a Wien filter and a second triplet of quadrupole lenses placed before the reaction chamber. The Wien filter eliminates to a very large extent the tails of the primary beam that pass through the system with the same magnetic rigidity. In order to stop the RIB contaminants, different slit sets are installed along the beamline. All the slit sets are mounted on movable arms to be adjusted to the envelope of the considered RIB. The total length of the facility from the production target to the reaction target is 8.34 m. The beamline characteristics are the following: ΔE/E=±10%, Δp/p=±5%, $\Delta\theta$= ±50 mrad, $\Delta\phi$=±65 mrad, $\Delta\Omega$ ≈10 msr, Bρ=0.98 Tm.

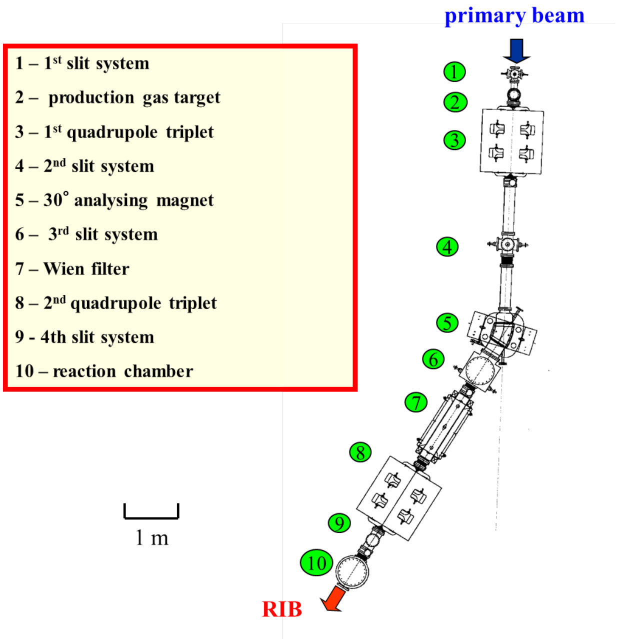

Fig. 1. (color online) Layout of the EXOTIC facility.

So far, RIBs of ^{7}Be, ^{8}B, ^{17}F, ^{15}O, ^{8}Li, ^{10}C and ^{11}C in the energy range 3-5 MeV/nucleon have been delivered with intensities about 10^6, 10^3, 10^5, $4*10^4$, 10^5, $5*10^3$ and $2*10^5$ pps, respectively, and with a high purity of 98-99% (apart from the ^{8}B that has a lower purity). This renders the EXOTIC facility competitive compared with other first generation small-scale in-flight facilities (for example the RIB facility at Argonne National Laboratory-USA [17], Twinsol in Notre Dame-USA or CRIB in Japan).

The envisioned experimental program at EXOTIC defines the requisites of the associated experimental apparatus and aims at:

1) studying reaction mechanisms induced by light exotic nuclei impinging on medium- and heavy-mass targets at incident energies near the Coulomb barrier. In this energy range, the peculiar features of exotic nuclei, such as excess of neutrons or protons, low binding energy, halo structure, neutron or proton dominated surface, influence the elastic scattering and the fusion process giving a picture that is rather different from that of well bound species (for a review see for instance [18]). Despite the efforts carried out so far, the understanding of nuclear reaction mechanisms in collisions involving exotic and weakly-bound nuclei is still a very challenging task. In the considered measurements the charged products emitted in direct nuclear reactions (elastic and inelastic scattering, nucleon transfer, breakup of the weakly bound projectile) and the light charged particles emitted in fusion-evaporation reactions should be charge and mass identified. A FWHM energy resolution of ∼ 250-400 keV is needed in the most demanding cases for discriminating the elastic from the inelastic scattering of the projectile from the target, depending on the considered colliding nuclei: ∼250 (400) keV for a ^{11}Be (^{17}F) projectile impinging on a ^{58}Ni or ^{208}Pb target. A large detection solid angle is requested to compensate the low RIB intensity, in the most favorable cases limited to a few orders of magnitude less than typical stable beams, and to allow detection of coincident breakup particles emitted at large relative angles while a high granularity would allow detection of coincident breakup particles emitted at small relative angles. A FWHM time resolution of ∼1-1.5 ns is sufficient for discriminating protons, α particles and heavy-ions for flight paths larger than 10 cm and for the event-by event rejection of contaminant beams. It has to be noticed here, that for nuclear reactions induced by in-flight produced RIBs, the overall experimental energy resolution is often limited by the energetic spread of the RIB and by the energy loss and energy straggling of the ions in the target that should be thick enough to compensate the low intensity of the beam;

2) studying α clustering phenomena in light exotic nuclei [19], employing the Thick Target Inverse Kinematic (TTIK) scattering technique [20], with the RIB impinging on a ^{4}He gas target. The pressure of the gas is tuned such that the RIB completely stops in the gas while the energetic recoiling light target nuclei, due to their low-rate of energy loss, can traverse the gas and be recorded by the detectors. The TTIK method is particularly useful for measurements with low-intensity RIBs since it allows to measure the elastic scattering excitation function over a wide energy range by using a single beam energy. The experimental requirements for the detection array are: a good energy resolution, high granularity to reconstruct the interaction point and the beam energy at the interaction point and light particle identification. A FWHM time resolution of ∼1-1.5 ns is enough for separating elastic scattering from other processes in most of the cases. It is worthnoting that the TTIK method helps improving the overall experimental energy resolution [21];

3) performing measurements of astrophysical interest with RIBs impinging on solid or gas light targets in inverse kinematics: among the different processes of stellar nucleosynthesis forming elements heavier than ^{9}Be, the rapid proton-capture and αp processes, occurring in explosive astrophysical environments such as novae, x-ray bursters and type Ia supernovae, are those than can be investigated by using the EXOTIC RIBs. Moreover, experiments based on the Trojan Horse Method (THM) [22] are considered. In the latter measurements, two among the three charged reaction products in the final state need to be detected with a ∼2% FWHM energy resolution and a FWHM angular resolution better than ∼1° [23].

4) performing measurements of fusion cross sections at near- and sub-barrier energies. In this kind of experiments, the EXOTIC facility designed for the in-flight production of low-energy light RIBs, is employed as a separator of evaporation residues from the incident beam (stable or

RIB). The evaporation residues are transported and detected at the focal plane of the facility.

3 Experimental set-up

The design of a high-performance detection system suitable for the above mentioned experiments must meet several requirements:

a) event-by-event beam tracking capabilities to account for the typical poor emittance of in-flight produced RIBs in conjuction with a good time resolution for Time of Flight (TOF) measurements and a fast signal for handling counting rates up to 10^6 Hz; b) charge and mass identification of the reaction products with the highest achievable energy resolution; c) a solid angle coverage as large as possible; d) high segmentation to achieve good angular resolution and for reducing pile up events and low-energy events coming from the radioactive decay of the elastically scattered projectiles; e) flexibility in order to be suitable for different experimental needs.

The experimental set-up [24] installed at the focal plane of the facility and displayed in Fig.2 consists of: (a) the RIB tracking system and (b) EXPADES, a new charged-particle telescope array. It satisfies the previously mentioned requisites for studies with low-energy light RIBs, moreover, it has the additional advantages of compactness and portability. The components of the EXPADES array can be easily reconfigured to suit many experiments while it can be used as an ancillary detection system with γ-ray and neutron arrays.

The two Parallel Plate Avalanche Counters (PPACs) of the tracking system, are position-sensitive, fast, high-transparency detectors, radiation hard which can sustain counting rates up to $\sim 10^6$ Hz. They are placed 909 mm (PPAC A) and 365 mm (PPAC B) upstream the reaction target (see Fig. 2). PPAC B is positioned at the entrance of the reaction chamber. The PPACs are filled with isobutane (C_4H_{10}) at a working pressure of 10-20 mbar and have entrance and exit windows that are made of 1.5 μm-thick mylar foil. The detector has a three-electrode structure: a central cathode and two anodes, placed symmetrically with respect to the cathode at a distance of 2.4 mm. The detector active area is 62 x 62 mm^2. The cathode is made of a 1.5 μm-thick stretched mylar foil while each anode is a mesh of 60 gold-plated tungsten 20 μm-thick wires in the x and y directions, with a spacing of 1 mm. The wires of the first anode are oriented horizontally and those of the second one vertically. The position information of a particle crossing the PPAC is extracted from the anode signals by using a delay-line readout. The FWHM 1 mm resolution of the two PPACs allows us to reconstruct the position of the event on the reaction target with a FWHM 2.3 mm position resolution. The cathode signal is used as a reference time for TOF measurements and for trigger purposes. The FWHM time resolution of a PPAC is about 0.9 ns.

EXPADES is an array of eight telescopes arranged in a cylindrical configuration around the reaction target (see Fig. 2). The telescope structure is flexible and is composed

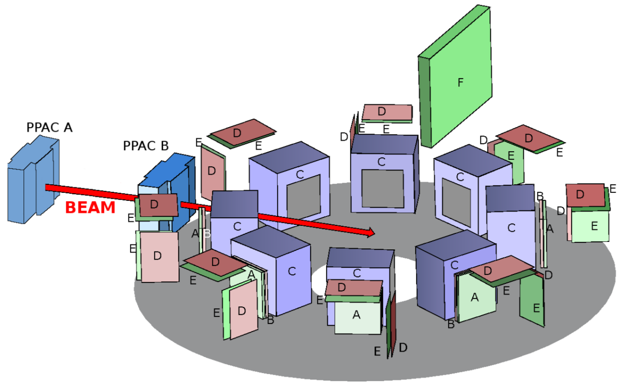

Fig. 2. (color online) Schematic view of: a) the event-by-event tracking system of the RIB in-flight facility EXOTIC, consisting of two PPACs: PPAC A and PPAC B, the second one being placed at the entrance of the reaction chamber; b) the EXPADES array telescopes arranged in the reaction chamber. Each telescope is made up of: **A)** 300 μm-thick DSSSD (E_{res} stage); **B)** 40 μm-thick DSSSD (ΔE stage); **C)** Ionization chamber (ΔE stage in experiments where the ions do not pass through the 40/60 μm DSSSD stage); **D)** Low-noise charge-sensitive preamplifier boards for the ΔE DSSSDs; **E)** Electronic boards for the E_{res} DSSSDs; **F)** Motherboard for the E_{res} DSSSD electronics. The beam enters in the reaction chamber from the left passing through PPAC A and PPAC B.

of two Double Side Silicon Strip Detectors (DSSSDs) and/or an Ionization Chamber (IC), depending on the experimental requests.

We use 40/60 μm-thick DSSSDs for the ΔE stage (elements B in Fig.2), whereas we adopt 300 μm-thick DSSSDs for the E_{res} layer (elements A in Fig.2), manufactured by Micron Semiconductor Ltd. [25]. Each DSSSD has 32 junction and 32 ohmic elements (strips). The strips are 64-mm long, with 2 mm pitch size and 40 μm inter-strip separation. The junction strips of the front (y) side are oriented orthogonally to the ohmic strips of the back (x) side, defining thus a $\sim 2 \times 2$ mm^2 pixel structure. For experiments requiring the detection of more energetic particles than those stopped in the E_{res} layer, few 1 mm-thick DSSSDs were recently purchased, to substitute the 300 μm-thick DSSSDs or to be used in addition to the previous stages.

The choice of the electronic front end of the DSSSDs was based on a compromise between the requirement for high granularity, good energy and good time resolution and that to maintain low the overall cost. Application Specific Integrated Circuit (ASIC)-based electronics was employed for the treatment of the E_{res} signals. ASIC electronics allows us to handle 32 energy signals of each side of the 300 μm-thick E_{res} DSSSD, ensuring a high granularity with a very low cost at the expense, however, of the possibility to perform TOF measurements with the requested time resolution (due to the lack of a constant fraction discriminator in the chip). To compensate the above drawback, for the signal readout of 40/60 μm DSSSD ΔE stage a compact low-noise electronics with an adequate dynamic range for the considered experiments ($\sim$ 100 MeV full range) and good energy and timing characteristics was developed by our collaboration.

In some experiments, the unambiguous identification by means of the ΔE-E_{res} technique of reaction products with range in silicon shorter than 40/60 μm might be of crucial relevance. A valid alternative to allow for ΔE-E_{res} identification of all the considered ions, is the use of an IC that can be handled easily, presents thickness uniformity, possibility to tune the effective thickness by changing the gas pressure, offers the chance of a large detection surface and does not present radiation damage problems. Thus, the construction of eight transverse-field ICs was undertaken. The ICs (elements C in Fig. 2) can be used as an alternative ΔE stage or to build up more complex triple telescopes. The IC is filled with carbon tetrafluoride (CF_4) at an operational gas pressure that can be varied up to 100 mbar, depending on the incident ion energy and on the species to be detected. It has 65 $\times$ 65 mm^2 entrance and exit windows made of 1.5 μm-thick mylar foil and an active depth along the ion direction of 61.5 mm.

The low-noise charge-sensitive preamplifiers for the ΔE DSSSDs (element D in Fig. 2), those of the ICs (not displayed in Fig. 2) as well as the boards containing the ASIC electronics (elements E in Fig. 2) for the E_{res} DSSSDs are placed under vacuum in the proximity of the array. This was done mainly for three reasons: 1) to have a compact set-up (detectors + electronics); 2) to minimize the internal and external connections and 3) to overcome the environmental noise at the EXOTIC beamline. In this way, we manage to keep as low as possible the DSSSDs electronic thresholds, typically 300-500 keV.

The distance of the EXPADES telescopes from the target can be varied continuously from a minimum value of 105 mm to a maximum of 225 mm, which corresponds to an angular resolution for a pixel from $\Delta\theta = 1^\circ$ to 0.5°. The maximum solid angle coverage (achieved in the configuration with only DSSSDs in use) is 2.72 sr ($\sim$ 22% of 4π sr). When all eight ICs are employed, the DSSSDs have to be placed at a minimum distance of 225 mm from the target position and the maximum solid angle coverage decreases to 0.64 sr ($\sim$ 5% of 4π sr).

The whole EXPADES array and the PPACB are housed in the reaction chamber, placed at the final focal plane of the EXOTIC facility. To allow the realization of experiments with RIBs impinging on both solid and gas reaction targets, a small chamber housing the PPAC B was built. When requested, this small chamber isolates, through a 2 μm-thick HAVAR window, the two PPACs and the beam line (held at vacuum) from the reaction chamber that is filled with gas at pressures ranging from 0.4 to 1 bar.

The low-energy RIBs of the EXOTIC facility and the above described experimental apparatus have been used so far, in the framework of international collaborations, for the study of nuclear reaction dynamics at Coulomb barrier energies [26–31] and α clustering phenomena in the light exotic nuclei ^{19}Ne [32] and ^{15}O [33]. Moreover, a first experiment of astrophysical interest was performed by means of the THM for the study of the ^{7}Be(n,α)^{4}He reaction [34].

4 Conclusion

The EXOTIC facility dedicated to the in-flight production of low-energy light RIBs and associated with a dedicated experimental set up is fully operational at INFN-LNL. Nuclear physics and nuclear astrophysics measurements can be carried out employing the produced RIBs, in the framework of international collaborations. Moreover, the facility can be used, besides for the RIB production, as a velocity filter to perform fusion-evaporation experiments at near- and sub-barrier energies with stable beams and also with the neutron-rich RIBs delivered by the SPES (Selective Production of Exotic Species) ISOL-type facility [35], in construction at INFN-LNL.

References

1. T. Kubo et al., Nucl. Instr. and Meth. B **70** (1992) 309; T. Suda J. Phys.: Conf. Ser. **267** (2011) 012008
2. The K500-K1200, A Coupled Cyclotron Facility at the NSCL, MSU, MSUCL-939, July 1994
3. W. Mittig, J. Phys. G: Nucl. Part. Phys. **24** (1998) 1331
4. H. Geissel et al., Nucl. Instr. and Meth. B **70** (1992) 286
5. A. Herlert, Nucl. Phys. News **20** (2010) 5
6. G. C. Ball et al., J. Phys. G: Nucl. Part. Phys. **38** (2011) 024003
7. A. Aprahamian and M. Wiescher, Nucl. Phys. News **12** (2002) 5
8. R. Lichtenthäler et al., Nucl. Phys. News **15** (2005) 25
9. J. Äystö et al., Eur. Phys. J. A **48** (2012) 42
10. S. Kubono et al., Eur. Phys. J. A **13** (2002) 217
11. Y. Yanagisawa et al., Nucl. Instr. and Meth. A **539** (2005) 74
12. H. Yamaguchi et al., Nucl. Instr. and Meth. **589** (2008) 150
13. V.Z. Maidikov et al., Nucl. Phys. A **746** (2004) 389c
14. D. Pierroutsakou et al., Eur. Phys. J. Special Topics **150** (2007) 47
15. F. Farinon et al., Nucl. Instr. and Meth. B **266** (2008) 4097
16. M. Mazzocco et al., Nucl. Instr. and Meth. B **266** (2008) 4665; Nucl. Instr. and Meth. B **317** (2013) 223
17. B. Harss et al., Rev. Sci. Instrum. **71** (2000) 380
18. L.F. Canto et al., Phys. Rep. **424** (2006) 1; Phys. Rep. **596** (2015) 1
19. M. Freer, Rep. Prog. Phys. **70** (2007) 21492210
20. K. Artemov et al., Sov. J. Nucl. Phys. **52** (1990) 408-411 ISSN 0038-5506
21. J. Walshe et al., J. Phys.: Conf. Ser. **569** (2014) 012052
22. G. Baur, Phys. Lett. B **178** (1986) 135; R. E. Tribble et al., Rep. Prog. Phys. **77** (2014) 106901
23. S. Cherubini et al., Phys. Rev. C **92** (2015) 015805
24. D. Pierroutsakou et al., Nucl. Instr. and Meth. A **834** (2016) 46
25. http://www.micronsemiconductor.co.uk/pdf/cat.pdf
26. C. Signorini et al., Eur. Phys. J. A **44** (2010) 63

27. M. Mazzocco et al., Phys. Rev. C **82** (2010) 054604; Phys. Rev. C **92** (2015) 024615; EPJ Web of Conferences **117** (2016) 06006
28. N. Patronis et al., Phys. Rev. C **85** (2012) 024609
29. A. Pakou et al., Phys. Rev. C **87** (2013) 014619; Eur. Phys. J. A (2015) 51: 55; Eur. Phys. J. A (2015) 51: 90
30. E. Strano et al., Phys. Rev. C **94** (2016) 024622
31. O. Sgouros et al., Phys. Rev. C **94** (2016) 044623; Phys. Rev. C **95** (2017) 054609
32. D. Torresi et al., EPJ Web of Conferences **117** (2016) 08027
33. D. Torresi et al., to be published
34. L. Lamia et al., to be published
35. https://web.infn.it/spes/.

NUMEN project @ LNS: Status and perspectives

F. Cappuzzello[1,2 a], C. Agodi[1 a], E. Aciksoz[15], L. Acosta[12], N. Auerbach[17], J. Bellone[1,2], S. Bianco[4], R. Bijker[12], D. Bonanno[3], V. Branchina[3], D. Bongiovanni[3], T. Borello[8], I. Boztosun[15], M. P. Bussa[4], L. Busso[4], S. Calabrese[1,2], L. Calabretta[1], A. Calanna[1], D. Carbone[1], M. Cavallaro[1], D. Calvo[4], E.R. Chávez Lomelí[12], M. Colonna[1], G. D' Agostino[1,2], N. Deshmukh[1], P.N. de Faria[9], C. Ferraresi[4], J.L. Ferreira[9], M. Fisichella[4], A. Foti[2,3], P. Finocchiaro[1], G. Gallo[1,2], U. Garcia[5], G. Giraudo[4], V. Greco[1], A. Hacisalihoglu[15], J. Kotila[18], F. Iazzi[4,6], R. Introzzi[4,6], G. Lanzalone[1,7], A. Lavagno[4], F. La Via[1,13], J.A. Lay[1], H. Lenske[14], R. Linares[9], G. Litrico[1], F. Longhitano[3], D. Lo Presti[2,3], J. Lubian[9], N. Medina[8], D. R. Mendes[9], A. Muoio[1], J.R.B. Oliveira[8], A. Pakou[10], L. Pandola[1], H. Petrascu[17], F. Pinna[4,6], F. Pirri[4], S. Reito[3], D. Rifuggiato[1], M.R.D. Rodrigues[8], A. D. Russo[1], G. Russo[2,3], G. Santagati[1], E. Santopinto[5], O. Sgouros[10], S.O. Solakci[15], G. Souliotis[11], V. Soukeras[10], D. Torresi[1], S. Tudisco[1], R.I.M. Vsevolodovna[5], R.J. Wheadon[4], and V. Zagatto[8]

[1] Istituto Nazionale di Fisica Nucleare, Laboratori Nazionali del Sud, Catania, Italy
[2] Dipartimento di Fisica e Astronomia, Università di Catania, Italy
[3] Istituto Nazionale di Fisica Nucleare, Sezione di Catania
[4] Istituto Nazionale di Fisica Nucleare, Sezione di Torino
[5] Istituto Nazionale di Fisica Nucleare, Sezione di Genova
[6] Politecnico di Torino, Italy
[7] Università degli Studi di Enna "Kore", Enna, Italy
[8] Universidade de Sao Paulo, Brazil
[9] Universidade Federal Fluminense, Niteroi, Brazil
[10] University of Ioannina and HINP, Ioannina, Greece
[11] University of Athens and HINP, Athens, Greece
[12] Universidad Nacional Autónoma de México
[13] CNR-IMM, Sezione di Catania, Italy
[14] University of Giessen, Germany
[15] Akdeniz University, Antalya, Turkey
[16] School of Physics and Astronomy Tel Aviv University, Israel
[17] IFIN-HH, Romania
[18] University of Jyväskylä, Jyväskylä, Finland

Abstract. The NUMEN project aims at accessing experimentally driven information on Nuclear Matrix Elements (NME) involved in the half-life of the neutrinoless double beta decay ($0v\beta\beta$), by high-accuracy measurements of the cross sections of Heavy Ion (HI) induced Double Charge Exchange (DCE) reactions. Particular attention is given to the (^{18}O,^{18}Ne) and (^{20}Ne,^{20}O) reactions as tools for $\beta^+\beta^+$ and $\beta^-\beta^-$ decays, respectively. First evidence of the possibility to get quantitative information about NME from experiments is found for both kind of reactions. In the experiments, performed at INFN - Laboratory Nazionali del Sud (LNS) in Catania, the beams are delivered by the Superconducting Cyclotron (CS) and the reaction products are detected by the MAGNEX magnetic spectrometer. The measured cross sections are challengingly low, limiting the present exploration to few selected isotopes of interest in the context of typically low-yield experimental runs. A major upgrade of the LNS facility is foreseen in order to increase the experimental yield of at least two orders of magnitude, thus making feasible a systematic study of all the cases of interest. Frontiers technologies are going to be developed to this purpose for the accelerator and the detection systems. In parallel, advanced theoretical models will be developed in order to extract the nuclear structure information from the measured cross sections.

1 Introduction

The $0v\beta\beta$ decay, besides establishing the Majorana nature of neutrinos, has the potential to shed light on the absolute neutrino mass and hierarchy. To this purpose,

[a] Spokespersons: F. Cappuzzello (cappuzzello@lns.infn.it) and C. Agodi (agodi@lns.infn.it)

it is critical that the associated Nuclear Matrix Elements (NME) are reliably known. From an updated comparison of the results of NME calculations, obtained within various nuclear structure frameworks [1–3], significant differences are found, which makes the present situation still not satisfactory. In addition, some assumption common to different competing calculations, like the unavoidable truncation of the many body wave-function, could cause overall systematic uncertainties.

In order to access quantitative information, relevant for 0v$\beta\beta$ decay NME, the NUMEN project proposes to use HI-DCE reactions as a tool. These reactions are characterized by the transfer of two charge units, leaving the mass number unchanged, and can proceed by a sequential nucleon transfer mechanism or by meson exchange. Despite 0v$\beta\beta$ decay and HI-DCE reactions are mediated by different interactions, they present a number of similarities. Among that, the key aspects are that initial and final nuclear states are the same and the transition operators in both cases present a superposition of isospin, spin-isospin and rank-two tensor components with a relevant momentum (100 MeV/c or so) available.

In a pioneering experiment, performed at the INFN-LNS laboratory, we studied the DCE reaction ^{40}Ca(^{18}O,^{18}Ne)^{40}Ar at 270 MeV, with the aim to measure the cross section at zero degrees [4]. In the experiment an advantageous condition was set, using a beam of ^{18}O and a double magic target as ^{40}Ca and choosing the bombarding energy in such a way to mismatch the competing transfer reactions leading to the same outgoing channel [5]. The key tools in the experiment were the high resolution CS beams and the MAGNEX spectrometer, a modern high resolution and large acceptance magnetic system characterized by high resolution in energy, mass and angle [6, 7]. The high-order solution of the equation of motion is the key feature of MAGNEX, which guarantees the above mentioned performances and its relevance in the research of heavy-ion physics [8,9]. In the "pilot experiment" we have shown that high resolution and statistically significant experimental data can be measured for DCE processes and that precious information towards NME determination could be at our reach. To move towards candidate nuclei for 0v$\beta\beta$ decay important experimental limits need to be overcome [10–12]. The challenge is to measure a rare nuclear transition under a very high rate of heavy ions produced by the beam-target interaction. We should consider that:

(a) About one order of magnitude more yield would have been necessary for the reaction studied in Ref. [4], especially at the largest angles where sizeable amounts of linear momentum (100-200 MeV/c) are transferred;
(b) The Q-value for DCE reactions on nuclei of interest for 0v$\beta\beta$ is normally more negative (typically -8 ÷ -10 MeV) than in the case of ^{40}Ca explored in Ref. [4] (Q = -5.9 MeV). This could strongly reduce the cross section at very forward angles, especially for L = 0 transitions.
(c) The (^{18}O,^{18}Ne) reaction is particularly advantageous, due to the large value of both the B[GT;^{18}O$_{gs}(0^+) \rightarrow$ ^{18}F$_{gs}(1^+)$] and B[GT;^{18}F$_{gs}(1^+) \rightarrow$ ^{18}Ne$_{gs}(1^+)$] strengths and to the concentration of the GT strength in the ^{18}F(1^+) ground state. However, this reaction is of $\beta^+\beta^+$ kind, while most of the research on 0v$\beta\beta$ is in the opposite direction;
(d) None of the reactions of $\beta^-\beta^-$ kind looks like as favorable as the (^{18}O,^{18}Ne). For example, the (^{18}Ne,^{18}O) requires a radioactive beam, which cannot be available with comparable intensity. The proposed (^{20}Ne,^{20}O) or the (^{12}C,^{12}Be) have smaller B(GT), so a sensible reduction of the yield is foreseen in these cases;
(e) In some case gas or implanted targets are necessary, e.g. ^{136}Xe or ^{130}Xe, which are normally much thinner than solid state ones, with a consequent reduction of the collected yield;
(f) In some case the energy resolution we can provide (about half MeV) is not enough to separate the ground state from the excited states in the final nucleus. In these cases the coincident detection of γ-rays from the de-excitation of the populated states is mandatory, but at the price of the collected yield.

As a consequence the present limits of beam power (~100 W) for the CS accelerator and acceptable rate for the MAGNEX focal plane detector (few kHz) must be sensibly overcome. For a systematic study of the many "hot" cases of $\beta\beta$ decays an upgraded set-up, able to work with at least two orders of magnitude more luminosity than the present, is thus necessary. This goal can be achieved by a substantial change in the technologies used in the beam extraction and in the detection of the ejectiles. For the accelerator the use of a stripper induced extraction is an adequate choice [13]. For the spectrometer the main foreseen upgrades are:

1. The substitution of the present focal plane detector gas tracker, based on multiplication wire technology with a tracker system based on micro patterned gas detector [14];
2. The substitution of the wall of silicon pad stopping detectors with SiC detectors [15] or similar [16];
3. The introduction of an array of detectors for measuring the coincident γ-rays;
4. The development of suitable front-end and read-out electronics, capable to guarantee a fast read-out of the detector signals, still preserving a high signal to noise ratio [17];
5. Develop a suitable architecture for data acquisition, storage and data treatment, including accurate detector response simulations
6. The enhancement of the maximum magnetic rigidity, preserving the geometry of the magnetic field [18–21];
7. The installation of a beam dump to stop the high power beams, keeping the generated radioactivity under control.

In addition, we are developing the technology for producing and cooling isotopically enriched thin films able to resist to the high intensity beams.

Finally, NUMEN is fostering the development of a specific theory program to allow an accurate extraction of nuclear structure information from the measured cross sections. Relying on the use of the DWBA approximation for the cross section, the theory is focused on the development of microscopic models for DCE reactions, employing several approaches (QRPA, shell model, IBM) for inputs connected to nuclear structure quantities. We are also investigating the possible link between the theoretical description of the 0v$\beta\beta$ decay and DCE reactions.

The project is divided into four different phases, covering at least a decade time horizon.

Phase1: the experiment feasibility

The pilot experiment: the ^{40}Ca(^{18}O,^{18}Ne)^{40}Ar reaction at 270 MeV, with the first experimental data on heavy-ion DCE reactions in a wide range of transferred momenta, was already explored. The results demonstrate the technical feasibility.

Phase2: toward "hot" cases, optimizing experimental conditions and getting first results

The necessary work for the upgrade of both the accelerator and MAGNEX will be carried out still preserving the access to the present facility. Due to the relevant technological challenges, the Phase2 is foreseen to have a duration of a 3-4 years. In the meanwhile, experiments with integrated charge of tens of mC (about one order of magnitude more than that collected in the pilot experiment) will be performed. These will require several weeks (4-8 depending on the case) data taking for each reaction, since thin targets (a few 10^{18} atoms/cm^2) are used in order to achieve enough energy and angular resolution in the energy spectra and angular distributions. The attention will be focused on a few favorable cases, like for example the ^{116}Sn(^{18}O,^{18}Ne)^{116}Cd, ^{106}Cd(^{18}O,^{18}Ne)^{106}Pd as $\beta\beta^{++}$ like reactions and the ^{116}Cd (^{20}Ne,^{20}O)^{116}Sn, ^{130}Te (^{20}Ne,^{20}O)^{130}Xe, ^{76}Ge(^{20}Ne,^{20}O)^{76}Se as $\beta\beta^{--}$ like reactions, with the goal to achieve valuable results for them.

Phase3: the facility upgrade

Once all the building block for the upgrade of the accelerator and spectrometer facility will be ready at the LNS a Phase3, connected to the disassembling of the old set-up and re-assembling of the new will start. An estimate of about 18-24 months is considered.

Phase4: the experimental campaign

The Phase4 will consist of a series of experimental campaigns at high beam intensities (some pμA) and long experimental runs. The goal is to reach integrated charges of hundreds of mC up to C, for the experiments in coincidences, spanning all the variety of candidate isotopes for 0v$\beta\beta$ decay, like: ^{48}Ca, ^{76}Ge, ^{82}Se, ^{96}Zr, ^{100}Mo, ^{110}Pd, ^{124}Sn, ^{128}Te, ^{130}Te, ^{136}Xe, ^{148}Nd, ^{150}Nd, ^{154}Sm, ^{160}Gd, ^{198}Pt.

References

1. J. D. Vergados, H. Ejiri, and F. Simkovic, Reports on Progress in Physics, **75**, no. 10, Article ID 106301, (2012).
2. P. Vogel, Journal of Physics G: Nuclear and Particle Physics, **39**, no. 12, Article ID 124002, (2012).
3. J. Engel and J. Menéndez Rep. Prog. Phys. **80**, 046301 (2017).
4. F. Cappuzzello, M. Cavallaro, C. Agodi et al., Eur. Phys. J. A **51**, 145 (2015).
5. D. M. Brink, et al., Phys. Lett. B **40**, 3 (1972).
6. F. Cappuzzello, C. Agodi, D. Carbone et al., Eur. Phys. J. A **52**, 167 (2016).
7. F. Cappuzzello et al., Nucl. Instr. Methods A **763**, 314 (2014).
8. F. Cappuzzello, D. Carbone, M. Cavallaro et al., NATURE COMMUNICATIONS **6**, 6743 (2015).
9. D. Pereira et al., Phys. Lett. B **710**, 426 (2012).
10. C. Agodi, F. Cappuzzello et al., Nuclear and Particle Physics Proceedings**265**,28 (2015).
11. C. Agodi et al., AIP Conference Proceedings **1686**,Article Number: 020001(2015).
12. F. Cappuzzello et al., J. Phys.: Conf. Ser. **630**, 12018 (2015).
13. L. Calabretta et al., Modern Physics Letters A, **32**, No. 17 (2017).
14. M. Cortesi, S. Rost, W. Mittig, et al., Review of Scientific Instruments **88**, Article Number: 013303 (2017).
15. A. Muoio, C. Agodi, D. Bonanno, et al., Eur. Phys. J. Web of Conferences Volume: **117** Article Number: 10006 (2016).
16. D. Carbone, M. Cavallaro, C. Agodi, F. Cappuzzello, L. Cosentino, P. Finocchiaro for the NUMEN collaboration, Results in Physics **6**, 863 (2016).
17. G. De Geronimo et al., IEEE Transactions On Nuclear Science **60**, 2314 (2013).
18. A. Lazzaro, F. Cappuzzello, A. Cunsolo et al., Nucl. Instr. Methods A **591**, 394 (2008).
19. A. Lazzaro, F. Cappuzzello, A. Cunsolo et al., Nucl. Instr. Methods A **585**, 136 (2008).
20. A. Lazzaro, F. Cappuzzello, A. Cunsolo et al., Nucl. Instr. Methods A **570**, 192 (2007).
21. A. Lazzaro, F. Cappuzzello, A. Cunsolo et al., Nucl. Instr. Methods A **602**, 494 (2009).

Speed of sound bounds, tidal polarizability and gravitational waves from neutron stars

Ch.C. Moustakidis, T. Gaitanos, Ch. Margaritis, and G.A. Lalazissis

Department of Theoretical Physics, Aristotle University of Thessaloniki,
54124 Thessaloniki, Greece

Abstract. The accurate determination of the maximum mass of the neutron stars is one of the most important tasks in astrophysics. It is directly related to the identification of the black holes in the universe, the production of neutron stars from the supernovae explosion, and the equation of state (EoS) of dense matter. However, not only the EoS is directly connected with neutron star masses, but also the speed of sound in dense matter is a crucial quantity which characterizes the stiffness of the EoS. Recent observations, of binary neutron star systems, offer the possibility of measuring with high accuracy both the mass and the tidal polarizability of the stars. We study possible effects of the upper bound of the speed of sound on the upper bound of the mass and the tidal polarizability. We conclude that these kinds of measurements, combined with recent observations of neutron stars with masses close to $2M_\odot$, will provide robust constraints on the equation of state of hadronic matter at high densities.

PACS. 26.60.-c, 21.30.Fe, 21.65.Cd, 26.60.Kp

1 Introduction

The determination of the maximum mass of a neutron star (NS) (rotating and nonrotating) is one of the long-standing subjects in astrophysics (for a comprehensive introduction dedicated to this problem see Ref. [1]). In particular, the identification of a black hole requires the knowledge of the maximum mass of a neutron star. The maximum neutron star mass is of considerable interest in the study of the production of neutron stars and black holes in the dynamics of supernovae explosion. Moreover, the experimental observations of neutron star masses have imposed strong constraints on the hadronic equation of state (EoS) of superdense matter (see also the references about the neutron star mass distribution [2,3]). The most famous examples are the recent discoveries of massive neutron stars with gravitational masses of $M = 1.97 \pm 0.04\ M_\odot$ (PRS J1614-2230 [4]) and $M = 2.01 \pm 0.04\ M_\odot$ (PSR J0348+0432 [5]).

From a theoretical point of view, it is well known that the exact value of the maximum mass $M_{\rm max}$ of an NS depends strongly on the EoS of β-stable nuclear matter [6, 7]. Despite intensive investigations, the upper bound of neutron stars remains up to present uncertain [8–13]. One possibility of proceeding with an estimate of $M_{\rm max}$ is based on the pioneering idea of Rhoades and Ruffini [8], where an optimum upper bound of mass of non-rotating neutron stars was derived using a variational technique. An issue was raised recently concerning the high-density upper bound of the speed of sound. The speed of sound v_s, because of the causality, should not exceed that of light. Recently, Bedaque and Steiner [14] have provided simple arguments that support the limit $c/\sqrt{3}$ in non-relativistic and/or weakly coupled theories. The authors pointed out that the existence of neutron stars with masses about two solar masses combined with the knowledge of the EoS of hadronic matter at low densities is not consistent with this bound. The main motivation of the present paper is to study in detail the limiting cases of the upper bound of the speed of sound and their effects on the bulk neutron star properties. We calculate maximum neutron star masses in relation to various scenarios for the upper bound of the speed of sound. We use a class of equation of states, which have been extensively employed in the literature and mainly have the advantage to predict neutron star masses close or higher to the experimentally observed value of $2M_\odot$ [4,5]. We also extend our study to the analysis of the tidal polarizability (deformability), which can be estimated experimentally. The theoretical results for the tidal polarizability are discussed and analyzed in comparison with the corresponding observations of the Advanced LIGO and the Einstein Telescope.

2 Nuclear equation of state and the maximum mass configuration

It is known that no bounds can be determined for the mass of non-rotating neutron stars without some assumptions concerning the properties of neutron star matter [1].

In this study, following the work of Sabbadini and Hartle [16] we consider the following four assumptions: (i) the matter of the neutron star is a perfect fluid described by a one-parameter equation of state between the pressure P and the energy density $\mathcal{E}$, (ii) the energy density $\mathcal{E}$ is non-negative (because of the attractive character of gravitational forces), (iii) the matter is microscopically stable, which is ensured by the conditions $P \geq 0$ and $dP/d\mathcal{E} \geq 0$ and (iv) below a critical baryon density n_0 the equation of state is well known. Furthermore, we introduce two regions for specifying more precisely the EoS. The radius R_0 at which the pressure is $P_0 = P(n_0)$, divides the neutron star into two regions. The core, where $r \leq R_0$ and $n \geq n_0$ and the envelope where $r \geq R_0$ and $n \leq n_0$. The adiabatic speed of sound is defined as [17]

$$\frac{v_s}{c} = \sqrt{\left(\frac{\partial P}{\partial \mathcal{E}}\right)_S}, \qquad (1)$$

where S is the entropy per baryon. In the present work we consider the following three upper bounds for the speed of sound:

1. $\frac{v_s}{c} \leq 1$: causality limit from special relativity (see [1] and reference therein)
2. $\frac{v_s}{c} \leq \frac{1}{\sqrt{3}}$: from QCD and other theories (see [14] and reference therein)
3. $\frac{v_s}{c} \leq \left(\frac{\mathcal{E} - P/3}{P + \mathcal{E}}\right)^{1/2}$: from relativistic kinetic theory (see [15] and reference therein)

We construct the maximum mass configuration by considering the following structure for the neutron star EoS

$$P(\mathcal{E}) = \begin{cases} P_{crust}(\mathcal{E}), & \mathcal{E} \leq \mathcal{E}_{\text{c-edge}} \\ P_{NM}(\mathcal{E}), & \mathcal{E}_{\text{c-edge}} \leq \mathcal{E} \leq \mathcal{E}_0 \\ \left(\frac{v_S}{c}\right)^2 (\mathcal{E} - \mathcal{E}_0) + P_{NM}(\mathcal{E}_0), & \mathcal{E}_0 \leq \mathcal{E}. \end{cases} \qquad (2)$$

According to Eq. (2), the EoS yielding the maximum mass of neutron stars, is divided into three regions. In particular, above the critical energy density $\mathcal{E}_0$ the EoS is maximally stiff with the speed of sound $\sqrt{\left(\frac{\partial P}{\partial \mathcal{E}}\right)_S}$ fixed in the interval $\left(1/\sqrt{3} - 1\right) c$. In the intermediate region $\mathcal{E}_{\text{c-edge}} \leq \mathcal{E} \leq \mathcal{E}_0$ we employed a specific EoS which is used for various nuclear models (see below for more details), while for $\mathcal{E} \leq \mathcal{E}_{\text{c-edge}}$ we used the equation of Feynman, Metropolis and Teller [18] and also of Baym, Bethe, and Sutherland [19]. The crust-core interface energy density $\mathcal{E}_{\text{c-edge}}$, between the liquid core and the solid crust is determined by employing the thermodynamical method [20].

We use the following notations and specifications for the results of the theoretical calculations: a) the case where the critical (fiducial) density is $n_0 = 1.5 n_s$ and for $n \geq n_0$ the speed of sound is fixed to the value $v_s = c$ (EoS/maxstiff), b) the case where the fiducial density is $n_0 = 1.5 n_s$ and for $n \geq n_0$ the speed of sound is fixed to the value $v_s = c/\sqrt{3}$ (EoS/minstiff), and c) the case where the for $n \geq n_{c-crust}$ we simple employ the selected EoS without constraints (EoS/normal).

3 The Nuclear Models

In the present work we employed various relativistic and non-relativistic nuclear models, which are suitable to reproduce the bulk properties of nuclear matter at low densities, close to saturation density as well as the maximum observational neutron star mass (Refs. [4,5]).

3.0.1 The MDI model

The momentum-dependent interaction(MDI) model used here, was already presented and analyzed in a previous paper [21]. The MDI model is designed to reproduce the results of the microscopic calculations of both nuclear and neutron-rich matter at zero temperature and can be extended to finite temperature. The energy per baryon at $T = 0$, is given by

$$\begin{aligned} E(n,I) &= \frac{3}{10} E_F^0 u^{2/3} \left[(1+I)^{5/3} + (1-I)^{5/3}\right] \\ &+ \frac{1}{3} A \left[\frac{3}{2} - (\frac{1}{2} + x_0) I^2\right] u \\ &+ \frac{\frac{2}{3} B \left[\frac{3}{2} - (\frac{1}{2} + x_3) I^2\right] u^{\sigma}}{1 + \frac{2}{3} B' \left[\frac{3}{2} - (\frac{1}{2} + x_3) I^2\right] u^{\sigma - 1}} \\ &+ \frac{3}{2} \sum_{i=1,2} \left[C_i + \frac{C_i - 8 Z_i}{5} I\right] \left(\frac{\Lambda_i}{k_F^0}\right)^3 \\ &\times \left(\frac{((1+I)u)^{1/3}}{\frac{\Lambda_i}{k_F^0}} - \tan^{-1} \frac{((1+I)u)^{1/3}}{\frac{\Lambda_i}{k_F^0}}\right) \\ &+ \frac{3}{2} \sum_{i=1,2} \left[C_i - \frac{C_i - 8 Z_i}{5} I\right] \left(\frac{\Lambda_i}{k_F^0}\right)^3 \\ &\times \left(\frac{((1-I)u)^{1/3}}{\frac{\Lambda_i}{k_F^0}} - \tan^{-1} \frac{((1-I)u)^{1/3}}{\frac{\Lambda_i}{k_F^0}}\right), \end{aligned} \qquad (3)$$

where $u = n/n_s$, with n_s denoting the equilibrium symmetric nuclear matter density, $n_s = 0.16$ fm^{-3}. The parameters A, B, σ, C_1, C_2 and B' employed to determine the properties of symmetric nuclear matter at saturation density n_s. By suitably choosing the parameters x_0, x_3, Z_1, and Z_2, it is possible to obtain different forms for the density dependence of the symmetry energy as well as on the value of the slope parameter L and the value of the symmetry energy at the saturation density [22].

3.0.2 Momentum-dependent relativistic mean-field model

The relativistic formulation of the nuclear matter problem is based on the well-known quantum hadrodynamics

(QHD) [23–26]. Here we adopt an RMF approach with non-linear derivative interactions, the so-called non-linear derivative (NLD) model; see Ref. [27,28] for details. It is suitable for applications in systems beyond saturation density, because it contains explicitly the momentum dependence of the interaction.

The energy density in NLD is obtained from the time-like 00-component of the energy-momentum tensor and it reads

$$\mathcal{E} = \sum_{i=p,n} \frac{k}{(2\pi)^3} \int_{|\mathbf{p}|\geq p_{F_i}} d^3p E(\mathbf{p}) + \frac{1}{2}\left(m_\sigma^2\sigma^2 + 2U(\sigma) - m_\omega^2\omega^2 - m_\rho^2\rho^2\right) . \quad (4)$$

The first term in Eq. (4) is the kinetic contribution, while the other terms appear because of the in-medium interaction, mediated by the three virtual σ, ω and ρ mesons with masses m_σ, m_ω and m_ρ, respectively. The additional contribution $U(\sigma)$ includes the conventional non-linear self-interactions of the σ field.

3.0.3 The HLPS model

Recently, Hebeler *et al.* [29,30] performed microscopic calculations based on chiral effective field theory interactions to constrain the properties of neutron-rich matter below nuclear densities. It explains the massive neutron stars of $M = 2M_\odot$. In this model the energy per particle is given by [30] (hereafter HLPS model)

$$\begin{aligned}\frac{E(u,x)}{T_0} &= \frac{3}{5}\left(x^{5/3} + (1-x)^{5/3}\right)(2u)^{2/3} \\ &- \left[(2\alpha - 4\alpha_L)x(1-x) + \alpha_L\right]u \\ &+ \left[(2\eta - 4\eta_L)x(1-x) + \eta_L\right]u^\gamma, \end{aligned} \quad (5)$$

where $T_0 = (3\pi^2 n_0/2)^{2/3}\hbar^2/(2m) = 36.84$ MeV. The parameters α, η, α_L and η_L are determined by combining the saturation properties of symmetric nuclear matter and the microscopic calculations for neutron matter [29,30]. The parameter γ is used to adjust the values of the incompessibility K and influences the range on the values of the symmetry energy and its density derivative.

3.0.4 The H-HJ model

Heiselberg and Hjorth-Jensen [31] adopted the following simple form for the energy per particle in nuclear matter (hereafter H-HJ model)

$$E = E_0 u \frac{u-2-d}{1+du} + S_o u^\gamma (1-2x)^2, \quad (6)$$

where $E_0 = -15.8$ MeV. The parameters d and γ are fixed to the EoS of Akmal et al. [32], both for pure neutron matter and symmetric nuclear matters. However, the high-density extrapolation is questionable, because the EoS of Akmal *et al.* [32] becomes superluminal.

3.0.5 The Skyrme models

Finally, we also perform calculations using the well-known Skyrme parametrization. The energy per baryon of asymmetric matter is given by [33,34]

$$\begin{aligned} E(n,I) &= \frac{3}{10}\frac{\hbar^2c^2}{m}\left(\frac{3\pi^2}{2}\right)^{2/3} n^{2/3} F_{5/3}(I) \\ &+ \frac{1}{8}t_0 n \left[2(x_0+2) - (2x_0+1)F_2(I)\right] \\ &+ \frac{1}{48}t_3 n^{\sigma+1}\left[2(x_3+2) - (2x_3+1)F_2(I)\right] \\ &+ \frac{3}{40}\left(\frac{3\pi^2}{2}\right)^{2/3} n^{5/3} \\ &\times \Big[\left(t_1(x_1+2) + t_2(x_2+2)\right)F_{5/3}(I) \\ &+ \frac{1}{2}\left(t_2(2x_2+1) - t_1(2x_1+1)\right)F_{8/3}(I)\Big] , \end{aligned} \quad (7)$$

where $F_m(I) = \frac{1}{2}\left[(1+I)^m + (1-I)^m\right]$. The parametrization is given in Refs. [33,34].

3.1 The relativistic kinetic theory

The relativistic kinetic theory also predicts an upper bound of the speed of sound, which differs from unity. This was achieved by Olson using a Grad method of moments [15, 36,37], in the framework of the Israel-Stewart theory [36, 37]. In the low temperature limit $1/kT \longrightarrow \infty$ the conditions are given by the following inequalities (for more details of the derivations of the inequalities see Ref. [38])

$$\mathcal{E}, P \geq 0,\ (P+\mathcal{E})\left(\frac{v_s}{c}\right)^2 \geq 0,\ \left(\frac{v_s}{c}\right)^2 \leq \frac{\mathcal{E} - P/3}{P+\mathcal{E}},\ P \leq 3\mathcal{E}. \quad (8)$$

The conditions in Eqs. (8) impose stringent constraints on the high-density equation of state and thus, stringent constraints on the maximum neutron star mass. The requirement of these conditions implies that the maximally stiff equation of state fulfills the following expression:

$$\left(\frac{v_s}{c}\right)^2 = \frac{\mathcal{E} - P/3}{P+\mathcal{E}}. \quad (9)$$

Equation (9) can be easily solved and leads to

$$\mathcal{E}(n) = \mathcal{C}_1 n^{a_1} + \mathcal{C}_2 n^{a_2},\ a_1 = (1+\sqrt{13})/3,\ a_2 = (1-\sqrt{13})/3, \quad (10)$$

and also

$$P(n) = \mathcal{C}_1 n^{a_1}(a_1 - 1) + \mathcal{C}_2 n^{a_2}(a_2 - 1). \quad (11)$$

The values of the constants $\mathcal{C}_1$ and $\mathcal{C}_2$ are determined with the help of the critical density n_0. Now, the total equation of state, suitably to describe the maximum mass configuration of a neutron matter, is given by the ansatz [see again Eq. (2)]

$$P(n) = \begin{cases} P_{crust}(n), & n \le n_{\text{c-edge}} \\ P_{NM}(n), & n_{\text{c-edge}} \le n \le n_0 \\ \mathcal{C}_1 n^{a_1}(a_1-1) + \mathcal{C}_2 n^{a_2}(a_2-1), & n_0 \le n. \end{cases} \quad (12)$$

For the equation of sate in the interval $n_{\text{c-edge}} \le n \le n_0$ we employed the MDI model with $L = 110$ MeV.

4 Tidal Polarizability

Gravitational waves from the final stages of inspiraling binary neutron stars are expected to be one of the most important sources for ground-based gravitational wave detectors [39–43]. Flanagan and Hinderer [39] have recently pointed out that tidal effects are also potentially measurable during the early part of the evolution when the waveform is relatively clean. The tidal fields induce quadrupole moments on the neutron stars. The response of the neutron star is described by the dimensionless so-called Love number k_2, which depends on the neutron star structure and consequently on the mass and the EoS of the nuclear matter. The tidal Love numbers k_2 is obtained from the ratio of the induced quadrupole moment Q_{ij} to the applied tidal field E_{ij}:

$$Q_{ij} = -k_2 \frac{2R^5}{3G} E_{ij} \equiv -\lambda E_{ij}, \quad (13)$$

where R is the neutron star radius and $\lambda = 2R^5 k_2/3G$ is the tidal polarizability. The tidal Love number k_2 is given by [39,40]

$$\begin{aligned} k_2 = & \frac{8\beta^5}{5}(1-2\beta)^2 \left[2 - y_R + (y_R-1)2\beta\right] \\ & \times \Big[2\beta\left(6 - 3y_R + 3\beta(5y_R - 8)\right) \\ & + 4\beta^3 \left(13 - 11y_R + \beta(3y_R-2) + 2\beta^2(1+y_R)\right) \\ & + 3(1-2\beta)^2 \left[2 - y_R + 2\beta(y_R-1)\right] \ln(1-2\beta) \Big]^{-1} \end{aligned} \quad (14)$$

where $\beta = GM/Rc^2$ the compactness parameter. The tidal Love number k_2 depends on the compactness parameter β and the quantity y_R. Actually, y_R is determined by solving the following differential equation for y

$$r\frac{dy(r)}{dr} + y^2(r) + y(r)F(r) + r^2 Q(r) = 0,\ y(0) = 2,\ y_R \equiv y(R) \quad (15)$$

where $F(r)$ and $Q(r)$ are functionals of $\mathcal{E}(r)$, $P(r)$ and $M(r)$ [42]. Equation (15) must be integrated with the TOV equations using the boundary conditions $y(0) = 2$, $P(0) = P_c$ and $M(0) = 0$. The solution of the TOV equations provides the mass M and radius R of the neutron star, while the corresponding solution of the differential Eq. (15) provides the value of $y_R = y(R)$. This together with the quantity β are the basic ingredients of the tidal Love number k_2 [Eq. (14)].

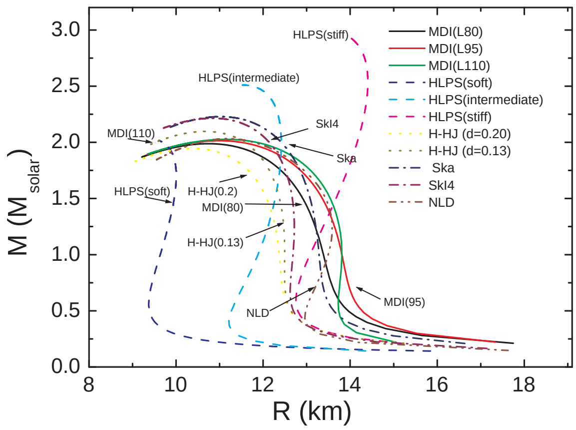

Fig. 1. Mass-radius diagram for the equations of state used in the present work.

In addition, the combined tidal effects of two neutron stars in a circular orbits are given by a weighted average of the quadrupole responses [39,42],

$$\tilde{\lambda} = \frac{1}{26}\left[\frac{m_1 + 12m_2}{m_1}\lambda_1 + \frac{m_2 + 12m_1}{m_2}\lambda_2\right], \quad (16)$$

where $\lambda_1 = \lambda_1(m_1)$ and $\lambda_2 = \lambda_2(m_2)$ are the tidal deformabilities of the two neutron stars and $M = m_1 + m_2$ the total mass. The symmetric mass ratio is defined as $h = m_1 m_2/M^2$. As pointed out in Ref. [42], the universality of the neutron star EoS allows one to predict the tidal phase contribution for a given binary system from each EoS. In this case the weighted average $\tilde{\lambda}$ is usually plotted as a function of chirp mass $\mathcal{M} = (m_1 m_2)^{3/5}/M^{1/5}$ for various values of the ratio h.

5 Results and Discussion

We start the discussion with Fig. 1. It shows the radius-mass relation of neutron stars using various EoS without any restriction on the speed of sound (except the relativistic one). One can see, that all hadronic models can reproduce the recent observation of two-solar massive neutron stars. In general, the stiffer EoS (at high densities) the higher the maximum neutron star mass. Before starting to analyze the effects of the speed of sound limits on the EoS, we show in Fig. 2 the density dependence of this quantity for the various EoSs used here. It is obvious that almost all the EoSs are causal even for high values of the pressure (the only exception is the case HLPS (stiff) where the v_c exceed the c for relative low pressure). However, it is worth mentioning that in all hadronic models, used in the present study, the speed of sound v_s reaches

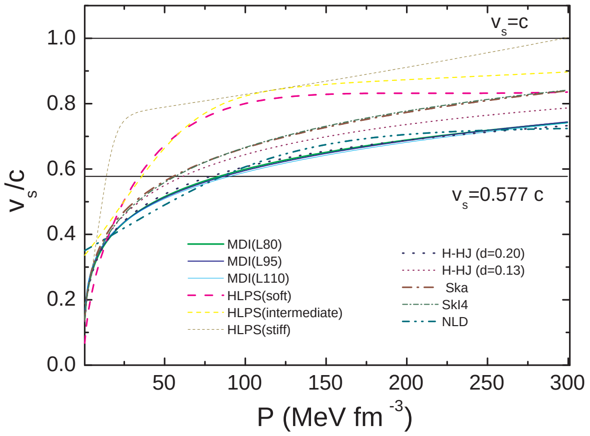

Fig. 2. The speed of sound dependence on the pressure for the EoSs used in the paper. The two specific upper bounds considered in the present work $v_s = c$ and $v_s = c/\sqrt{3} \simeq 0.577c$ are also indicated.

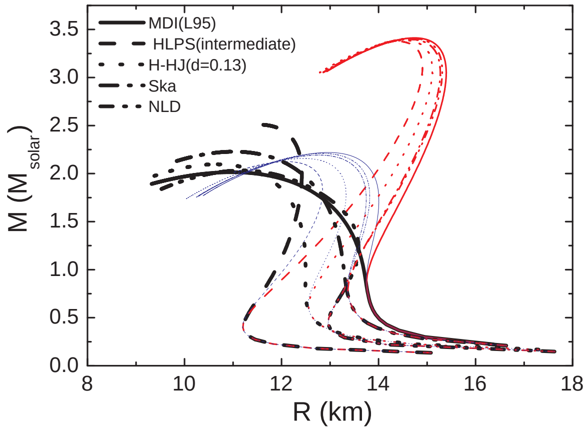

Fig. 3. The mass-radius diagram for five EoSs (EoS/normal case, line with thick width) in comparison with the corresponding maximum mass configuration results of the EoS/minstiff case (line with medium width) and and EoS/maxstiff case (line with thin width).

the bound limit $c/\sqrt{3}$ at relative low values of the pressure (for $P \leq 100$ MeV $\cdot$ fm^{-3}). This feature has dramatic effect on the maximum mass configuration. This is now discussed in Fig. 3. The neutron star configurations with the five selected EoSs in the normal case (no constraints on v_s except the conventional $v_s < c$) are also shown for comparison. It is seen that the upper bound limit of the speed of sound imposes essential changes to the neutron star structure. The higher the limit after the fiducial density, the stiffer the corresponding EoS. This results to a higher value for the maximum neutron star mass. By setting the upper limit to $v_s = c/\sqrt{3}$ the stiffness of the EoS weakens at higher densities and consequently the neutron star mass reduces to lower values.

To further clarify the critical density dependence on $M_{\rm max}$, we display in Fig. 4 the dependence of the maximum mass for the chosen EoS, on the fiducial density n_0. We considered three upper bounds for the speed of sound: $v_s = c$, $v_s = c/\sqrt{3}$, and the bound originated from the kinetic theory [see Eq. (9)]. First, one sees an overall reduction of the neutron star mass with increasing critical density. Using the density behavior of the $v_s = c/\sqrt{3}$ constraint in the calculations, the neutron star mass first decreases and then approaches a constant value, which is characteristic for each EoS. It is remarkable that in all cases the neutron star mass drops below the experimental value of two solar masses (the only exception is the stiff case of the HLPS model). Therefore, the assumption of $v_s = c/\sqrt{3}$ value as the upper limit for the speed of sound in compressed matter would exclude particular EOSs which contradict with recent astrophysical observation of massive neutron stars. Our results are similar to those of Bedaque and Steiner [14]. On the other hand, when the causality limit $v_s = c$ is imposed, the upper bound on the maximum mass significantly increases as is

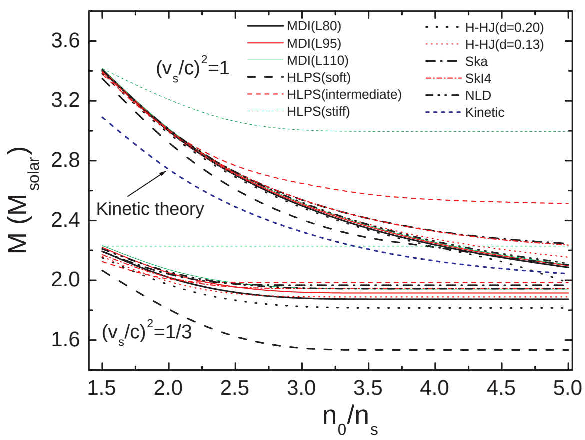

Fig. 4. The maximum mass of neutron stars as a function of the critical density n_0 for the two upper bounds for the speed of sound $v_s = c$ and $v_s = c/\sqrt{3}$. The case which corresponds to the upper bound for v_s, which is taken from the kinetic theory, is also indicated.

well known from previous studies and the relevant predictions (see Refs. [11,13] and references therein). The predictions of the kinetic theory for the $M_{\rm max}$ are lower but close to those of the causality limit and also in accordance with the observations. It is noted that recently an upper bound of neutron star masses was obtained from an analysis of short gamma-ray bursts [44]. Assuming that the rotation of the merger remnant is limited only by mass-shedding, then the maximum gravitational mass of a nonrotating neutron star is $M_{\rm max} = (2 - 2.2)\ M_\odot$ [44]. Furthermore, the authors of Ref. [45], using population studies, deter-

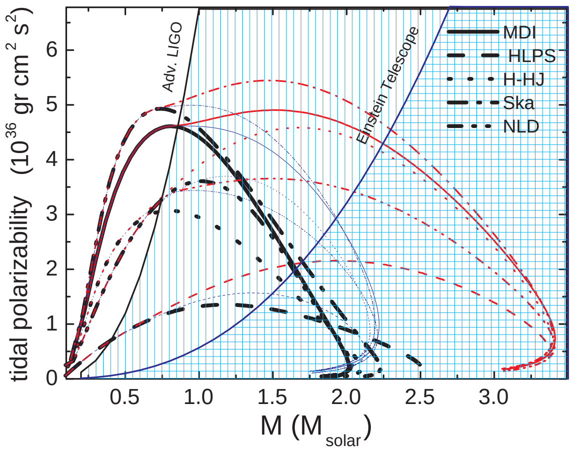

Fig. 5. The tidal polarizability λ of a single neutron star as a function of the mass for the five selected EoS's (EoS/normal case) in comparison with the corresponding maximum mass configurations results (EoS/minstiff and EoS/maxstiff cases). The notation is as in Fig. 3. The ability detection region of the Advanced LIGO is the unshaded region and the corresponding of the Einstein Telescope by the unshaded and light shaded region (see text for more details and also Ref. [42]).

mined the distribution of these compact remnants to compare with the observations. All these recent analyses, although dealing with the problem of the upper bound of neutron star mass in different ways, predict as an absolute upper limit for the maximum neutron star masses $M_{\rm max} \geq 2M_{\odot}$. This prediction is in accordance with the recent observations [4,5].

We propose now an additional approach to investigate the upper bound of v_s. It is well known that the influence of the star's internal structure on the waveform is characterized by the value of the tidal polarizability λ. It was found that λ is sensitive to the details of the equation of state. Furthermore, the tidal polarizability exhibits very strong dependence on the radius R and consequently on the details of the equation of state at low and high values of the baryons density.

The tidal polarizability is an important quantity, as it can be deduced from observations on neutron star binary systems. This is shown in Fig. 5. The *signature* of the maximum mass configuration on the values of λ is obvious. In particular, we found that λ takes a wide range of values ($\lambda \sim (1-5) \times 10^{36}$ gr cm^2 s^2) for the employed EoS (EoS/normal case). Because λ is sensitive to the neutron star radius, this quantity is directly affected by the EoS. An EoS leading to large neutron star radii will also give high values for the tidal polarizability λ (and vice versa). The constraints of the upper bound on the speed of sound (EoS/minstiff) lead to a non-negligible increase of λ for high values of neutron star mass. However, in the EoS/maxstiff case the corresponding increase of λ is substantial, compared to the EoS/normal case. Moreover, in this case the values of λ remain measurable even for very high values of the mass. This behavior results from the strong dependence of λ on the radius R. Specifically, the increase of the upper bound on the speed of sound influences significantly the maximum mass configuration in two ways. First, a dramatic increase of the upper bound of $M_{\rm max}$. Second, the neutron star radius is significantly increased. A radius increase by 10% leads already to a rise of the tidal polarizability λ by 60%.

In the same figure, the ability to measure the tidal polarizability from the Advanced LIGO and the Einstein Telescope is indicated. The region of possible observations with the Advanced LIGO is indicated by the unshaded region. The Einstein Telescope has larger ability and will be able to measure the tidal polarizability in the unshaded and light shaded region (see also Ref. [42]).

Note that the Einstein Telescope will be able to measure λ even for neutron stars with a masses up to 2.5 $M_{\odot}$ and consequently to constrain the stifness of the equation of state. To be more precise, from these observations one will be able to test the upper bound $v_s = c/\sqrt{3}$. The simultaneous measurements of neutron star masses M and tidal polarizabilities λ will definitely help to better clarify the stiffness limits of the equation of state. These features are shown in our calculations. For instance, the model within the EoS/normal case predicts values of the tidal polarizability λ, which are out of the detection region of the Einstein Telescope (see also the studies in Refs. [42]). On the other hand, the calculations with the EoS/minstiff model lead to λ values, which are just near that sensitivity region. The EoS/maxstiff results show a clear observable signature. In particular, for intermediate mass neutron stars $(1-2M_{\odot})$ with large values for the tidal polarizability λ the upper bound $v_s = c/\sqrt{3}$ seems to be violated. In view of the above analysis we conjecture that it is possible with the third-generations detectors to examine closely the extent of the stiffness of the neutron star EoS and the relative constraints on the upper bound on the speed of sound.

We now discuss the weighted tidal polarizability $\tilde{\lambda}$ as a function of the chirp mass $\mathcal{M}$ varying the symmetric ratio h, as shown in Fig. 6. We consider again the main three cases (EoS/normal, EoS/minstiff, and EoS/max stiff) where for the intermediate region of the density we employ the MDI model with the slope parameter $L = 95$ MeV. The three values of the symmetric ratio (0.25, 0.242, 0.222) correspond to the mass ratio m_2/m_1 (1.0, 0.7, 0.5) (for more details see also Ref. [42]). The uncertainty $\Delta\tilde{\lambda}$ in measuring $\tilde{\lambda}$ of the Advanced LIGO and the corresponding of the Einstein Telescope are also presented (see also Fig. 5 for more details). From Fig. 6 it is concluded that the upper bound of the speed of sound and consequently the maximum mass configuration affects appreciable the chirp mass-weighted tidal polarizability dependence. This effect is more pronounced for chirp masses $\mathcal{M} > 0.5\ M_{\odot}$. In particular, for high values of $\mathcal{M}$, the Einstein telescope has the sensibility to distinguish the mentioned dependence.

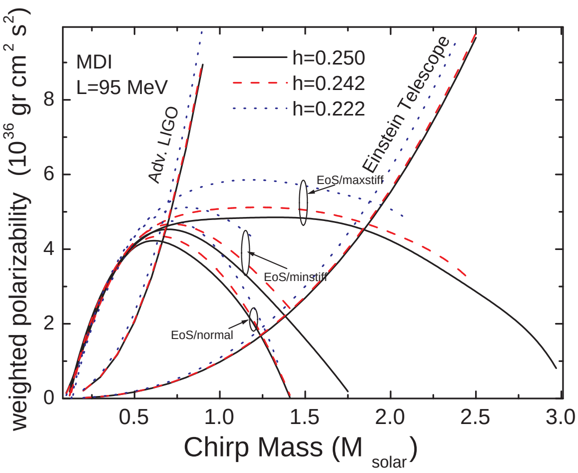

Fig. 6. The weighted tidal polarizability $\tilde{\lambda}$ as a function of the chirp mass $\mathcal{M}$ for various values of the symmetric ratio η for the three considered cases which correspond to the MDI (L95) EoS. The uncertainty $\Delta\tilde{\lambda}$ in the $\tilde{\lambda}$ measure of the Advanced LIGO and the corresponding of the Einstein Telescope are also indicated (for more details see text and also Ref. [42]).

We believe that the simultaneous measure of M and λ will help to better understand the stiffness limit of the equation of state. In particular, observations with third-generation detectors, will definitely provide constraints for the stiffness of the EoS at high density. This is expected to provide more information related to the upper bound of the speed of sound in hadronic matter. The accurate estimate of the upper bound of the speed of sound in hadronic matter is greatly important for a consistent prediction of the maximum mass of a neutron star. The future detection and analysis of gravitational waves in binary neutron star systems is expected to shed light on this problem.

References

1. J.B. Hartle, Phys. Rep. **46**, 201 (1978).
2. M. Coleman Miller and J.M. Miller, Phys. Rep. **548**, 1 (2015).
3. B. Kiziltan, A. Kottas, M.De Yoreo, and S.E. Thorsett, Astrophys. J. **778**, 66 (2013).
4. P. Demorest, T. Pennucci, S. Ransom, M. Roberts, and J. Hessels, Nature **467**, 1081 (2010).
5. J. Antoniadis, P.C. Freire, N. Wex, T.M. Tauris, R.S. Lynch, et al., Science **340**, 1233232 (2013).
6. S.L. Shapiro and S.A. Teukolsky, *Black Holes, White Dwarfs, and Neutron Stars* (John Wiley and Sons, New York, 1983).
7. N.K. Glendenning, *Compact Stars: Nuclear Physics, Particle Physics, and General Relativity*, (Springer, Berlin, 2000)
8. C.E. Rhoades and R. Ruffini, Phys. Rev. Lett. **32**, 324 (1974).
9. V. Kalogera and G. Baym, Astrophys. J. **470**, L61 (1996).
10. S. Koranda, N. Stergioulas, and J.L. Friedman, Astrophys. J. **488**, 799 (1997).
11. J.M. Lattimer and M. Prakash, *in From Nuclei to Stars*, (edited by S. Lee, (World Scientific, Singapore, 2011), p.275.
12. S. Gandolfi, J. Carlson, and S. Reddy, Phys. Rev. C **85**, 032801(R) (2012).
13. N. Chamel, P. Haensel, J.L. Zdunik, and A.F. Fantina, Int. J. Mod. Phys. E, **22** 1330018 (2013).
14. P. Bedaque and A.W. Steiner, Phys. Rev. Lett. **114**, 031103 (2015).
15. T.S. Olson, Phys. Rev. C **63**, 015802 (2000).
16. A.G. Sabbadini and J.B. Hartle, Ap. Space Sci., **25**, 117 (1973).
17. L.D. Landau an E.M. Lifshitz, *Fluid Mechanics* (Pergamonm Oxford, 1987), pages 251-254.
18. R. P. Feynman, N. Metropolis and E. Teller, Phys. Rev. **75**, 1561 (1949).
19. G. Baym, C. Pethik and P. Sutherland, Astrophys. J. **170**, 299 (1971).
20. Ch.C. Moustakidis, T. Niksic, G. A. Lalazissis, D. Vretenar, and P. Ring, Phys. Rev. C **81**, 065803 (2010).
21. Madappa Prakash, I. Bombaci, Manju Prakash, P. J. Ellis, J. M. Lattimer, and R. Knorren, Phys. Rep. 280, 1 (1997).
22. Ch.C. Moustakidis, Phys. Rev. C **91**, 035804 (2015).
23. H.-P. Duerr, Phys. Rev. **103**, 469 (1956).
24. J. Walecka, Annals Phys. **83**, 491 (1974).
25. B. D. Serot and J. D. Walecka, Int. J. Mod. Phys. E **6**, 515 (1997).
26. D. Vreternar, A.V. Afanasjev, G.A. Lalazissis, and P. Ring, Phys. Rep. 409, 101 (2005).
27. T. Gaitanos and M. M. Kaskulov, Nucl. Phys. A **899**, 133 (2013).
28. T. Gaitanos and M. Kaskulov, Nucl. Phys. A **940**, 181 (2015).
29. K. Hebeler, J.M. Lattimer, C.J. Pethick, and A. Schwenk, Phys. Rev. Lett. **105**, 161102 (2010).
30. K. Hebeler, J.M. Lattimer, C.J. Pethick, and A. Schwenk, Astrophys. J. **773**, 11 (2013).
31. H. Heiselberg and M. Hjorth-Jensen, Phys. Rep. **328**, 237 (2000).
32. A. Akmal, V.R. Pandharipande, D.G. Ravenhall, Phys. Rev. C **58**, 1804 (1998).
33. E. Chabanat, P. Bonche, P. Haensel, J. Meyer and R. Schaeffer, Nucl. Phys. A **627**, 710 (1997).
34. M. Farine, J.M. Pearson and F. Tondeur, Nucl. Phys. A **615**, 135 (1997).
35. F. Douchin and P. Haensel, A & A, **380**, 151 (2001).
36. W. Israel, Ann. Phys. (N.Y.) **100**, 310 (1976).
37. W. Israel and J.M. Stewart, Ann. Phys. (N.Y.) **118**, 341 (1979).
38. T.S. Olson and W.A. Hiscock, Phys. Rev. C **39**, 1818 (1989).
39. E.E. Flanagan and T. Hinderer, Phys. Rev. D **77**, 021502 (2008).
40. T. Hinderer, Astrophys. J. **677**, 1216 (2008).
41. T. Damour and A. Nagar, Phys. Rev. D **80**, 084035 (2009).
42. T. Hinderer, B.D. Lackey, R.N. Lang, and J.S. Read, Phys. Rev. D **81**, 1230161 (2010).
43. B.D. Lackey and L. Wade, Phys. Rev. D **91**, 043002 (2015).
44. S. Lawrence, J. G. Tervala, P. F. Bedaque and M.C. Miller, Astrophys. J. **808**, 186 (2015).
45. C.L. Freyer, K. Belczynski, E.R. Ruiz, S. Rosswong, G. Shen, A.W. Steiner, Astrophys. J. **812**, 24 (2015).

Momentum dependent mean-field dynamics for in-medium Y-interactions

T. Gaitanos and A. Violaris

Aristotle University of Thessaloniki, Physics Department, 54124 Thessaloniki, Greece

Abstract. We investigate the in-medium properties of hyperons (Y) at momenta far beyond the Fermi level. We use a covariant mean-field approach with momentum-dependent (MD) interactions. This is the non-linear derivative (NLD) model, in which the MD is modelled by non-linear derivative terms of infinite order. We extend the NLD model to the baryon-octet by including hyperons in the spirit of SU(3). It is shown that that the momentum-dependent cut-off induces a momentum dependence of hyperons, which is consistent with recent studies of chiral effective field theory. Such studies are important to understand better the still less known strangeness sector of the hadronic equation of state (EoS) and relevant for applications in nuclear astrophysics. The results can serve as predictions for the future experiments at FAIR (Facility for Antiproton and Ion Research, Darmstadt/Germany).

PACS. 21.65.Mn Equations of state of nuclear matter – 25.80.Pw Hyperon-induced reactions – 26.60.-c Nuclear matter aspects of neutron stars

1 Introduction

The recent astrophysical observations on compact neutron stars [1, 2] have driven the nuclear physics and astrophysics communities to detailed investigations of the nuclear equation of state (EoS) under conditions far beyond the ordinary matter [3]. Furthermore, theoretical and experimental studies on heavy-ion collisions over the last few decades concluded a softening of the high-density EoS in agreement with phenomenological and microscopic models [4–6]. However, the recent observations of two-solar mass pulsars [1,2] together with additional constraints on the high-density limit of the speed of sound [7] gave some controversial insights on the EoS of compressed baryonic matter. These observations provide the upper limit for the neutron star mass by excluding a soft EoS at high baryon densities.

Compressed baryonic matter consists not only of nucleons. It can include fractions of heavier baryons, since their production is energetically allowed. These are the hyperons Λ, Σ, Ξ and Ω as a part of the irreducible representations of SU(3). While the nucleon-nucleon (NN) interaction is fairly well known, the hyperon-nucleon (YN) interaction is still not fully understood. In fact, there are many experimental data for NN-scattering in free space and inside hadronic media (finite nuclei, heavy-ion collisions, hadron-induced reactions), which allow to determine the NN-parameters with high accuracy. On the other hand, the experimental access to the strangeness sector, that is the hyperon-nucleon (YN) interaction, is still scarce even for the free space scattering. As a consequence, theoretical predictions to the in-medium Y-interactions are considered as extrapolations to high densities. Note that the inclusion of strangeness degrees of freedom into dense nuclear matter leads to a dramatic softening of the EoS. This has made many successful nuclear models incompatible with the astrophysical observations of two-solar mass pulsars [1,2]. This is the so-called hyperon-puzzle [8].

We address here this issue by using an alternative approach based on the Relativistic Mean-Field (RMF) theory of Relativistic Hadrodynamics (RHD) [9]. The alternative model is formulated on the fact, that compressed matter consists of particles with high relative momenta. Thus, not only the density dependence, but also the momentum dependence of the in-medium interactions is of crucial importance. However, conventional RMF-models cannot explain the empirical saturation of the in-medium nucleon interaction at high momenta. Also in the case of in-medium antiprotons RMF leads to a divergent behaviour of the single-particle potential at high momenta [10]. For these reasons we have proposed the Non-Linear Derivative (NLD) model [10]. It is based on the simplicity of RMF, but it includes higher-order derivatives in the NN-interaction. It has been demonstrated that this Ansatz corrects the high-momentum behaviour of the interaction, makes the EoS softer at densities just above saturation, however, it reproduces the two-solar mass pulsars at densities far beyond saturation [10]. Here we extend the NLD approach by including strangeness into the nuclear matter and discuss the momentum dependence of the in-medium YN-potentials.

2 The NLD model

In this section we briefly introduce the non-linear derivative (NLD) model. A detailed desription can be found in Ref. [10]. Here we extend it to the baryonic octet by including nucleons

(N) and hyperons (Y) as degrees of freedom. These baryons interact through the exchange of virtual mesons in the spirit of the One-Boson-Exchange (OBE) approach to the NN-interaction [11]. The interaction involving hyperons is treated within the SU(6)-symmetry. Thus, the NLD-Lagrangian is given by

$$\begin{aligned}\mathcal{L} =& \frac{1}{2}\sum_B\left[\overline{\Psi}_B\gamma_\mu i\overrightarrow{\partial}^\mu\Psi_B - \overline{\Psi}_B i\overleftarrow{\partial}^\mu\gamma_\mu\Psi_B\right] - \sum_B m_B\overline{\Psi}_B\Psi_B \\ &-\frac{1}{2}m_\sigma^2\sigma^2 + \frac{1}{2}\partial_\mu\sigma\partial^\mu\sigma - U(\sigma) \\ &+\frac{1}{2}m_\omega^2\omega_\mu\omega^\mu - \frac{1}{4}F_{\mu\nu}F^{\mu\nu} \\ &+\frac{1}{2}m_\rho^2\boldsymbol{\rho}_\mu\boldsymbol{\rho}^\mu - \frac{1}{4}\boldsymbol{G}_{\mu\nu}\boldsymbol{G}^{\mu\nu} - \frac{1}{2}m_\delta^2\boldsymbol{\delta}^2 + \frac{1}{2}\partial_\mu\boldsymbol{\delta}\,\partial^\mu\boldsymbol{\delta} \\ &+\mathcal{L}_{int}^\sigma + \mathcal{L}_{int}^\omega + \mathcal{L}_{int}^\rho + \mathcal{L}_{int}^\delta \,. \end{aligned} \tag{1}$$

The sum over B runs over the baryonic octet

$$\Psi_B = (\Psi_N, \Psi_\Lambda, \Psi_\Sigma, \Psi_\Xi)^T \tag{2}$$

with

$$\Psi_N = (\psi_p, \psi_n)^T, \;\; \Psi_\Lambda = \psi_\Lambda \tag{3}$$

$$\Psi_\Sigma = (\psi_{\Sigma^+}, \psi_{\Sigma^0}, \psi_{\Sigma^-})^T, \;\; \Psi_\Xi = (\psi_{\Xi^0}, \psi_{\Xi^-})^T \tag{4}$$

for the isospin-doublets Ψ_N and Ψ_Ξ, isospin-triplet Ψ_Σ and the neutral Ψ_Λ. In a spirit of RHD, the interactions between the nucleon fields are described by the exchange of meson fields. These are the scalar σ and vector ω^μ mesons in the isoscalar channel, as well as the scalar $\boldsymbol{\delta}$ and vector $\boldsymbol{\rho}^\mu$ mesons in the isovector channel. Their corresponding Lagrangian densities are of the Klein-Gordon and Proca types, respectively. The term $U(\sigma) = \frac{1}{3}b\sigma^3 + \frac{1}{4}c\sigma^4$ contains the usual selfinteractions of the σ meson. The notations for the masses of fields in Eq. (1) are obvious. The field strength tensors are defined as $F^{\mu\nu} = \partial^\mu\omega^\nu - \partial^\nu\omega^\mu$, $\boldsymbol{G}^{\mu\nu} = \partial^\mu\boldsymbol{\rho}^\nu - \partial^\nu\boldsymbol{\rho}^\mu$ for the isoscalar and isovector fields, respectively.

The NLD interaction Lagrangians contain the conventional meson-nucleon RHD structures, however, they are extended by the inclusion of non-linear derivative operators into the meson-nucleon vertices. The NLD interaction Lagrangians followed here read

$$\mathcal{L}_{int}^\sigma = \sum_B \frac{g_{\sigma B}}{2}\left[\overline{\Psi}_B\overleftarrow{\mathcal{D}}_B\Psi_B\sigma + \sigma\overline{\Psi}_B\overrightarrow{\mathcal{D}}_B\Psi_B\right] , \tag{5}$$

$$\mathcal{L}_{int}^\omega = -\sum_B \frac{g_{\omega B}}{2}\left[\overline{\Psi}_B\overleftarrow{\mathcal{D}}_B\gamma^\mu\Psi_B\omega_\mu + \omega_\mu\overline{\Psi}_B\gamma^\mu\overrightarrow{\mathcal{D}}_B\Psi_B\right] , \tag{6}$$

for the isoscalar-scalar and isoscalar-vector vertices, respectively (the interactions for the isovector sector are of similar type). The arrows indicate the direction of the operator's action and the subindex the baryon type (nucleon and hyperons). As one can see, the only difference with respect to the conventional RHD interaction Lagrangian is the presence of additional operators $\overrightarrow{\mathcal{D}}_B$, $\overleftarrow{\mathcal{D}}_B$ which serve to regulate the high momentum component of the nucleon field. The hermiticity of the Lagrangian demands $\overleftarrow{\mathcal{D}}_B = \overrightarrow{\mathcal{D}}_B^\dagger$. The operator functions (regulators) $\overrightarrow{\mathcal{D}}_B$, $\overleftarrow{\mathcal{D}}_B$ are assumed to be generic functions of partial derivative operator and supposed to act on the nucleon spinors Ψ_B and $\overline{\Psi}_B$, respectively. Therefore, the formal Taylor expansion of the operator functions in terms of partial derivatives generates an infinite series of higher-order derivative terms

$$\overrightarrow{\mathcal{D}}_B := \mathcal{D}\left(\overrightarrow{\xi}_B\right) = \sum_{j=0}^{n\to\infty}\frac{\partial^j}{\partial\overrightarrow{\xi}_B^j}\mathcal{D}|_{\overrightarrow{\xi}_B\to 0}\frac{\overrightarrow{\xi}_B^j}{j!} , \tag{7}$$

$$\overleftarrow{\mathcal{D}}_B := \mathcal{D}\left(\overleftarrow{\xi}_B\right) = \sum_{j=0}^{n\to\infty}\frac{\overleftarrow{\xi}_B^j}{j!}\frac{\partial^j}{\partial\overleftarrow{\xi}_B^j}\mathcal{D}|_{\overleftarrow{\xi}_B\to 0} . \tag{8}$$

The expansion coefficients are given by the partial derivatives of $\mathcal{D}$ with respect to the operator arguments $\overrightarrow{\xi}_B$ and $\overleftarrow{\xi}_B$ around the origin. The operators are defined as $\overrightarrow{\xi}_B = -\zeta_B^\alpha i\overrightarrow{\partial}_\alpha$, $\overleftarrow{\xi}_B = i\overleftarrow{\partial}_\alpha\zeta_B^\alpha$ where the four vector $\zeta_B^\mu = v^\mu/\Lambda_B$ contains the cut-off Λ_B and v^μ is an auxiliary vector. The functional form of the regulators is constructed such that in the limit $\Lambda \to \infty$ ($\forall F$) the following limit holds $\overrightarrow{\mathcal{D}}(\overleftarrow{\mathcal{D}}) \to 1$. Therefore, in the limit $\Lambda \to \infty$ the original RHD Lagrangians are recovered.

The derivation of the equation of motion for the Dirac field follows the generalized Euler-Lagrange equations,

$$\frac{\partial\mathcal{L}}{\partial\varphi_r} + \sum_{i=1}^{n}(-)^i\partial_{\alpha_1\cdots\alpha_i}\frac{\partial\mathcal{L}}{\partial(\partial_{\alpha_1\cdots\alpha_i}\varphi_r)} = 0 , \tag{9}$$

for each baryon (nucleons and strangeness). Due to the absence of mixing terms the Dirac equations for N, Λ and Σ baryons are decoupled from each other, and the result reads as

$$\left[\gamma_\mu(i\partial^\mu - \Sigma_{B^i}^\mu) - (m_B - \Sigma_{sB^i})\right]\psi_{B^i} = 0 , \tag{10}$$

where the selfenergies $\Sigma_{B^i}^\mu$ and Σ_{sB^i} are given by

$$\Sigma_{B^i}^\mu = g_{\omega B}\omega^\mu\overrightarrow{\mathcal{D}}_B + g_{\rho B}\boldsymbol{\tau}_{B^i}\cdot\boldsymbol{\rho}^\mu\overrightarrow{\mathcal{D}}_B + \cdots , \tag{11}$$

$$\Sigma_{sB^i} = g_{\sigma B}\sigma\overrightarrow{\mathcal{D}}_B + g_{\delta B}\boldsymbol{\tau}_{B^i}\cdot\boldsymbol{\delta}\;\overrightarrow{\mathcal{D}}F + \cdots . \tag{12}$$

In above equations the subindices B and i denote the baryon type and its isospin state, respectively. Here the meson-nucleon couplings and regulators are isospin independent and both Lorentz-components of the selfenergy, Σ^μ and Σ_s, show an explicit linear behavior with respect to the meson fields σ, ω^μ, $\boldsymbol{\rho}^\mu$ and $\boldsymbol{\delta}$ as in the standard RMF. However, they contain an additional dependence on regulator functions.

The series of additional terms in Eqs. (11) and (12) containing the meson field derivatives are denoted by multiple dots. These derivative terms are irrelevant for proceeding applications to infinite nuclear matter and we do not show them here explicitly. Recall that in the mean-field approximation any kind of meson field derivatives vanish.

The derivation of the meson field equations of motion is straightforward, since here one has to use the standard Euler-Lagrange equations

$$\frac{\partial\mathcal{L}}{\partial\varphi_r} - \partial_\alpha\frac{\partial\mathcal{L}}{\partial(\partial_\alpha\varphi_r)} = 0 , \tag{13}$$

where now $r = \sigma, \omega, \rho$ and δ. The following Proca and Klein-Gordon equations are obtained

$$\partial_\alpha \partial^\alpha \sigma + m_\sigma^2 \sigma + \frac{\partial U}{\partial \sigma} = \frac{1}{2} \sum_B g_{\sigma B} \left[\overline{\Psi}_B \overleftarrow{\mathcal{D}}_B \Psi_B + \overline{\Psi}_B \overrightarrow{\mathcal{D}}_B \Psi_B \right] , \tag{14}$$

$$\partial_\mu F^{\mu\nu} + m_\omega^2 \omega^\nu = \frac{1}{2} \sum_B g_{\omega B} \left[\overline{\Psi}_B \overleftarrow{\mathcal{D}}_B \gamma^\nu \Psi_B + \overline{\Psi}_B \gamma^\nu \overrightarrow{\mathcal{D}}_B \Psi_B \right] , \tag{15}$$

and similar for the isovector channels. General expressions for the Noether-current and energy-momentum tensor can also be derived. We give them below in the RMF approximation.

We apply now the NLD formalism in the RMF approximation to infinite nuclear matter. In this case, the spatial components of the Lorentz-vector meson fields vanish, $\omega^\mu \to (\omega^0, \mathbf{0})$. Also in isospin space only the neutral component of the isovector fields survive, *i.e.*, $\boldsymbol{\rho}^\mu \to (\rho_3^0, \mathbf{0})$ and $\boldsymbol{\delta} \to \delta_3$. For simplicity, we denote in the following the third isospin components of the isovector fields as ρ and δ. We do not show the equations for the isovector channels for transparency, however, they are taken into account for asymmetric matter calculations.

The solutions of the RMF equations start with the usual plane wave *ansatz*

$$\psi_i(s, \boldsymbol{p}) = u_i(s, \boldsymbol{p}) e^{-ip^\mu x_\mu} , \tag{16}$$

where i stands for the various isospin states of the baryons. $p^\mu = (E, \boldsymbol{p})$ is the single baryon 4-momentum. The application of the non-linear derivative operator $\mathcal{D}$ to the plane wave *ansatz* of the spinor fields results in

$$\mathcal{D}(\overrightarrow{\xi}_B)\psi_i = \mathcal{D}_B(p)\, u_i(s, \boldsymbol{p}) e^{-ip^\mu x_\mu} , \tag{17}$$

$$\overline{\psi}_i \mathcal{D}(\overleftarrow{\xi}_B) = \mathcal{D}_B(p)\, \overline{u}_i(s, \boldsymbol{p}) e^{+ip^\mu x_\mu} , . \tag{18}$$

The regulators $\mathcal{D}_B$ are now functions of the scalar argument $\xi_B = -\frac{v_\alpha p^\alpha}{\Lambda_B}$. That is, they depend explicitly on the single baryon momentum p (with an appropriate choice of the auxiliary vector v^α) and on the cut-off Λ_B, which may be different for each baryon B.

With the help of Eqs. (16) and (17) one gets the Dirac equations for the baryons as in Eq. (10) with the corresponding explicitly momentum dependent selfenergies. For instance, the vector components are given by

$$\Sigma_{vp}^\mu = g_{\omega N}\, \omega^\mu\, \mathcal{D}_N + g_{\rho N}\, \rho^\mu\, \mathcal{D}_N , \tag{19}$$
$$\Sigma_{vn}^\mu = g_{\omega N}\, \omega^\mu\, \mathcal{D}_N - g_{\rho N}\, \rho^\mu\, \mathcal{D}_N , \tag{20}$$

$$\Sigma_{v\Lambda}^\mu = g_{\omega \Lambda}\, \omega^\mu\, \mathcal{D}_\Lambda , \tag{21}$$

$$\Sigma_{v\Sigma^+}^\mu = g_{\omega \Sigma}\, \omega^\mu\, \mathcal{D}_\Sigma + g_{\rho \Sigma}\, \rho^\mu\, \mathcal{D}_\Sigma , \tag{22}$$
$$\Sigma_{v\Sigma^-}^\mu = g_{\omega \Sigma}\, \omega^\mu\, \mathcal{D}_\Sigma - g_{\rho \Sigma}\, \rho^\mu\, \mathcal{D}_\Sigma , \tag{23}$$
$$\Sigma_{v\Sigma^0}^\mu = g_{\omega \Sigma}\, \omega^\mu\, \mathcal{D}_\Sigma , \tag{24}$$

$$\Sigma_{v\Xi^-}^\mu = g_{\omega \Xi}\, \omega^\mu\, \mathcal{D}_\Xi - g_{\rho \Xi}\, \rho^\mu\, \mathcal{D}_\Xi , \tag{25}$$
$$\Sigma_{v\Xi^0}^\mu = g_{\omega \Xi}\, \omega^\mu\, \mathcal{D}_\Xi + g_{\rho \Xi}\, \rho^\mu\, \mathcal{D}_\Xi , . \tag{26}$$

Similar are the expressions for the scalar selfenergies.

The solutions of the Dirac equation look similar as in the case of free space, i.e.,

$$u_{B^i}(s, \boldsymbol{p}) = N_{B^i} \begin{pmatrix} \varphi_s \\ \dfrac{\boldsymbol{\sigma} \cdot \boldsymbol{p}}{E^*_{B^i} + m^*_{B^i}} \varphi_s \end{pmatrix} , \tag{27}$$

but now for quasi-free particles with an in-medium energy

$$E^*_{B^i} := E - \Sigma^0_{vB^i}(p) , \tag{28}$$

and a Dirac mass

$$m^*_{B^i} := m_B - \Sigma_{sB^i}(p) . \tag{29}$$

For a given momentum the single particle energy E is obtained from the in-medium on-shell relation (28). Note again that the selfenergies are explicitly momentum dependent.

Proper normalization leads to the following 4-current

$$J^\mu = \frac{\kappa}{(2\pi)^3} \sum_{B^i} \int\limits_{|\boldsymbol{p}| \le p_{F_i}} d^3p\, \frac{\Pi^\mu_{B^i}}{\Pi^0_{B^i}} \tag{30}$$

with the generalized 4-momentum

$$\Pi^\mu_{B^i} = p^{*\mu}_{B^i} + m^*_{B^i} \Big(\partial^\mu_p \Sigma_{sB^i} \Big) - \Big(\partial^\mu_p \Sigma^\beta_{vB^i} \Big) p^*_{B^i\beta} \tag{31}$$

and the usual effective 4-momentum

$$p^{*\mu}_{B^i} = p^\mu - \Sigma^\mu_{vB^i} \tag{32}$$

The energy-momentum tensor in NLD is obtained by applying the Noether theorem for translational invariance. In nuclear matter the resummation procedure results in the following expression

$$T^{\mu\nu} = \sum_{B^i} \frac{\kappa}{(2\pi)^3} \int\limits_{|\boldsymbol{p}| \le p_{F_i}} d^3p\, \frac{\Pi^\mu_{B^i} p^\nu}{\Pi^0_{B^i}} - g^{\mu\nu} \langle \mathcal{L} \rangle , \tag{33}$$

from which the energy density $\varepsilon \equiv T^{00}$ and the pressure P can be calculated, *i.e.*,

$$\varepsilon = \sum_{B^i} \frac{\kappa}{(2\pi)^3} \int\limits_{|\boldsymbol{p}| \le p_{F_i}} d^3p\, E(\boldsymbol{p}) - \langle \mathcal{L} \rangle , \tag{34}$$

$$P = \frac{1}{3} \sum_{B^i} \frac{\kappa}{(2\pi)^3} \int\limits_{|\boldsymbol{p}| \le p_{F_i}} d^3p\, \frac{\boldsymbol{\Pi}_{B^i} \cdot \boldsymbol{p}}{\Pi^0_{B^i}} + \langle \mathcal{L} \rangle . \tag{35}$$

Above equations look similar as the familiar expressions of the usual RMF models. However, the NLD effects induced by the regulators show up through the generalized momentum Π^μ_i and through the dispersion relation for the single-particle energy $E(\boldsymbol{p})$.

Finally, the NLD meson-field equations in the RMF approach to nuclear matter read

$$m_\sigma^2 \sigma + \frac{\partial U}{\partial \sigma} = \sum_{B^i} g_{\sigma B} \left\langle \overline{\psi}_{B^i} \mathcal{D}_B \psi_{B^i} \right\rangle = \sum_{B^i} g_{\sigma B}\, \rho_{sB^i} \ , \tag{36}$$

$$m_\omega^2 \omega = \sum_{B^i} g_{\omega B} \left\langle \overline{\Psi}_{B^i} \gamma^0 \mathcal{D}_B \Psi_{B^i} \right\rangle = \sum_{B^i} g_{\omega B}\, \rho_{0B^i} \ , \tag{37}$$

with the scalar and vector densities

$$\rho_{sB^i} = \int\limits_{|\boldsymbol{p}|\le p_{F_i}} d^3p\, \frac{m^*_{B^i}}{\Pi^0_{B^i}}\, \mathcal{D}_B(p) \ , \tag{38}$$

$$\rho_{0B^i} = \int\limits_{|\boldsymbol{p}|\le p_{F_i}} d^3p\, \frac{E^*_{B^i}}{\Pi^0_{B^i}}\, \mathcal{D}_B(p) \, . \tag{39}$$

The isovector densities are calculated though the standard isospin relations. The meson-field equations of motion show a similar structure as those of the standard RMF approximation. For example, the scalar-isoscalar density ρ_s is suppressed with respect to the vector density ρ_0 by the factor m^*_i/Π^0_i, in a similar way as in the conventional Walecka models [9]. However, the substantial difference between NLD and conventional RMF appears in the source terms which now contain in addition the momentum-dependent regulator $\mathcal{D}$. This is a novel feature of the NLD model. The cut-off leads naturally to a particular suppression of the vector field at high densities or high Fermi-momenta in agreement with phenomenology. This feature is absent in conventional RHD approaches, except if one introduces by hand additional and complicated scalar/vector self-interactions.

Model	ρ_{sat} $[fm^{-3}]$	E_b $[\mathrm{MeV}/A]$	K $[\mathrm{MeV}]$	a_{sym} $[\mathrm{MeV}]$	Ref.
NLD	0.156	-15.30	251	30	this work
NL3*	0.150	-16.31	258	38.68	[12]
DD	0.149	-16.02	240	31.60	[13]
D^3C	0.151	-15.98	232.5	31.90	[14]
DBHF	0.185	-15.60	290	33.35	[15, 16]
	0.181	-16.15	230	34.20	[17]

Table 1. Bulk saturation properties of nuclear matter, i.e., saturation density ρ_{sat}, binding energy per nucleon E_b, compression modulus K and asymmetry parameter a_{sym} in the NLD model. Our results are compared with the non-linear parametrization NL3*, the density dependent DD and the derivative coupling D^3C models as well as with two versions of the microscopic DBHF approach. See Ref. [10] for more details.

Λ_{sN} $[\mathrm{GeV}]$	Λ_{vN} $[\mathrm{GeV}]$	$g_{\sigma N}$	$g_{\omega N}$	$g_{\rho N}$	b $[\mathrm{fm}^{-1}]$	c
0.95	1.125	10.08	10.13	3.50	15.341	-14.735

Table 2. The parameters of the NLD model. See Ref. [10] for details.

3 Results and discussion

For practical applications one needs a specific form of the regulator $\mathcal{D}(p)$. Various choices of the regulator functions are possible. We have done calculations for different forms of $\mathcal{D}(p)$ and found that the simplest momentum dependent monopole form factor provides the best description of the low and high density nuclear matter properties. In nuclear matter this results in

$$\mathcal{D}(p) = \frac{\Lambda^2}{\Lambda^2 + \boldsymbol{p}^2} \, . \tag{40}$$

This monopole form applies to nucleons and hyperons with cut-off parameters Λ_B. The nucleonic part was fitted to the bulk properties of ordinary nuclear matter. The results are shown in tables 1 and 2 for the extracted saturation properties and NLD parameters, respectively. It is seen that, the NLD model leads to a very good description of the empirical values. The NLD EoS is rather soft and similar to the density dependence of DBHF microscopic calculations. However, note that due to the non-linear effects, as induced by the regulators $\mathcal{D}(p_F)$, the NLD EoS becomes again stiff at very high densities. This is crucial for an appropriate description of neutron star masses [10]. In fact, the NLD model predicts a maximum mass of neutron stars of 2 (in units of the solar mass), even if the compression modulus is soft.

A novel feature of NLD is a simultaneously correct description of the Schroedinger-equivalent optical potential for in-medium protons and antiprotons, see Fig. 1. Note that in the fitting procedure two points for the proton optical potential were used only. The overall momentum dependence is a prediction of the NLD model, which is in very good agreement with the Dirac-phenomenology for in-medium protons (inserted panel in Fig. 1). The NLD calculations for the corresponding in-medium antiproton optical potential were performed by means of G-parity arguments only. That is, no additional parameters were used. Similar results are obtained for the imaginary part of the antiproton optical potential, as in detailed explained in Ref. [10]. In summary, the explicit momentum dependence of the NLD approach regulates not only the high momenta, but also the high Fermi-momenta (or the high density dependence) such that, it predicts a very reasonable descrip-

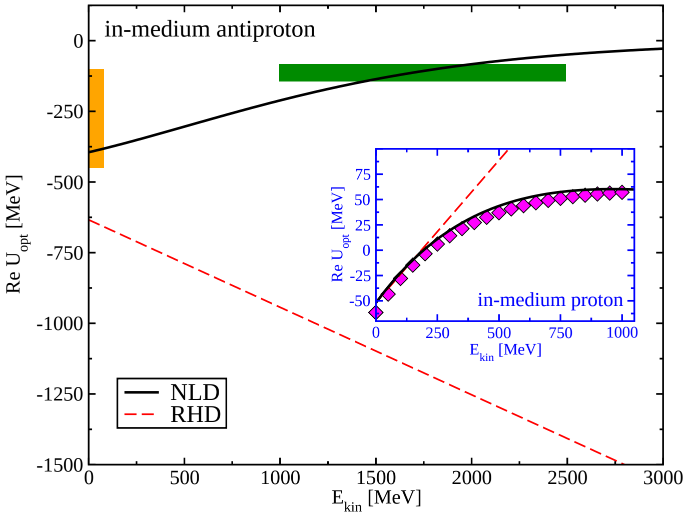

Fig. 1. Energy dependence of the real part of the Schroedinger-equivalent optical potential for antiprotons and protons, as indicated, in nuclear matter at saturation density. Calculations in the standard RHD model(dashed) and NLD approach (solid) are shown and compared with the Dirac-phenomenology (coloured bands, filled diamond symbols).

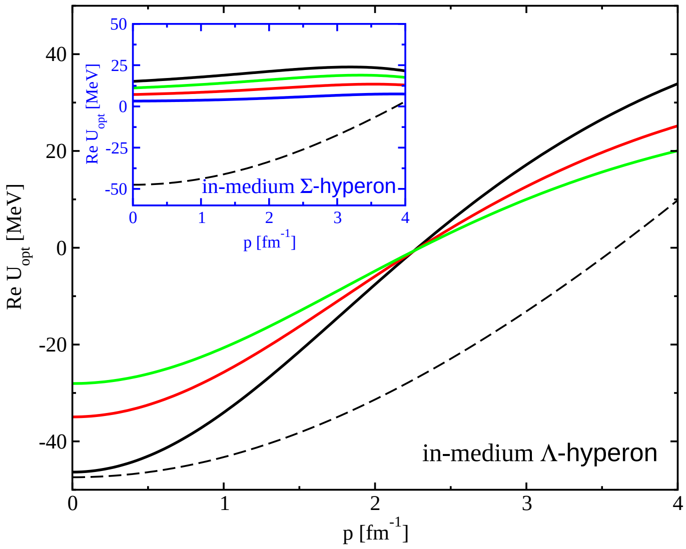

Fig. 2. Same as in Fig. 1, but now for Λ and Σ hyperons, as indicated, and as function of particle momentum relative to saturated nuclear matter at rest. The dashed curves show calculations in the standard RHD model. The coloured solid curves show NLD results by varying the cut-off regulator.

tion of all available empirical information for nuclear matter at saturation and beyond.

It is thus natural to extend the NLD formalism to hadronic systems by including the strangeness degrees of freedom, as discussed in the previous section. We have applied the NLD to in-medium hyperons inside nuclear matter and calculated the real part of the Schroedinger-equivalent optical potential for Λ and Σ hyperons. The results are shown in Fig. 2. The dashed curves show the calculations in the conventional RHD model. As in the case of in-medium (anti)protons, the momentum dependence divergences with increasing single-particle momentum (not shown in the figure).

The NLD calculations (solid curves in Fig. 2) predict a different behaviour in momentum. The momentum dependence of the in-medium Λ optical potential becomes stronger. At low momenta the Λ in-medium interaction is attractive, but it becomes repulsive at high momenta. This strong momentum dependence arises from the explicit momentum dependent non-linearities in the selfenergies and the appearance of the momentum dependent regulator in the source terms of the mesonic field equations. One should note that, the NLD behaviour here is consistent with recent microscopic calculations based on chiral effective field theory [18].

Microscopic studies, based on the chiral effective field theory [18] predict a weak and repulsive character for the Σ-hyperon potential in nuclear matter. Fig. 2 (inner panel) shows the momentum dependence of the in-medium optical potential for Σ hyperons. The conventional Walecka model (dashed curve) leads to a rather similar momentum behaviour as for the Λ optical potential and disagrees with the effective chiral models. Also here the optical potential will diverge with increasing Σ momentum. The situation is different in the NLD calculations (solid curves). The NLD model can predict a weak and repulsive Σ interaction in nuclear matter, in consistency with effective chiral field theory [18].

In the NLD calculations shown in Fig. 2 the various solid curves differ between each other in the choice of the hyperonic cut-offs Λ_Λ and Λ_Σ. In general, these cut-offs are of hadronic scale, that is $\Lambda_B \simeq 1$ GeV. The nucleonic regulators $\Lambda_{s,v}$ are fixed from empirical properties of ordinary nuclear matter. However, in the strangeness sector the experimental situation is still little understood. In particular, the hyperonic coupling constants $g_{\sigma Y}$ and $g_{\omega Y}$ are determined from the NN-couplings via SU(6) symmetry arguments. However, it is not obvious how to determine the strangeness regulators Λ_Λ and Λ_Σ in the absence of experimental information. This is also discussed within the chiral effective field theory, in which similar form-factors appear in their interaction kernels. In any case, since we are dealing with hadronic matter, values of hadronic scale in the range of 1 GeV for the NLD regulators seem to be an adequate choice.

A more clear picture to the in-medium strangeness interactions one expects at FAIR in the close future, when experimental data on multi-strangeness hypernuclei will be accessible. In particular, in the PANDA-experiment an abundant production of multi-strangeness bound clusters will be possible, as predicted by recent transport theoretical studies [19]. Therefore, hypernuclear spectroscopy will provide data on in-medium hyperons helping to determine better the hyperonic parameters. From the astrophysical side, neutron stars provide us with useful information of highly compressed hadronic matter. A precise knowledge of the maximum mass of these compact giants together with precise measurements of their still unknown radius will definitely help to better constrain the strangeness interactions in hadronic media. Indeed, the in-medium hyperonic potentials discussed here affect directly the production thresholds of the various hyperons, and thus they influence the high-density part of the hadronic equation of state. The application of the NLD approach with hyperons to neutron stars is in progress [20].

4 Summary and conclusions

We have investigated the properties of strangeness particles inside nuclear matter in the framework of the NLD approach. The NLD model is based on the simplicity of the relativistic mean-field theory, but it includes the missing momentum dependence in a manifestly covariant fashion. This is realized by the introduction of non-linear derivative series in the interaction Lagrangian. In momentum space this prescription leads to momentum dependent regulators, which are determined by a cut-off. The NLD approach does not only resolve the optical potential issues of protons and antiprotons at high momenta, but it affects the density dependence. That is, the cut-off regulators make the EoS softer at densities close to saturation and stiffer at very high densities relevant for neutron stars.

Because of the successful application of the NLD model to infinite nuclear matter (and to finite nuclei [21]), it is a natural desire to extend this approach to hadronic matter by taking strangeness degrees of freedom into account. This is realized in the spirit of SU(6) symmetry. We apply the NLD model to the description of in-medium hyperon interactions for ordinary nuclear matter. It is found that the strangeness cut-off regulates the momentum dependence of the optical potentials of hyperons in multiple ways. At first, the optical potentials do not diverge with increasing hyperon momentum. Furthermore, the NLD model predicts an attractive Λ-optical potential at low momenta, which becomes repulsive at high energies and finally saturates. As an important result, it is possible to predict a weak and repulsive in-medium interaction for Σ-hyperons inside nuclear matter at saturation density. These results are in consistent agreement with calculations based on the chiral effective field theory.

This study is relevant not only for hadron physics, but also for nuclear astrophysics. The application of the NLD approach to β-equilibrated compressed matter is under progress, in order to investigate the hyperon-puzzle in neutron stars. Another interesting application concerns the dynamics of neutron star binaries. To do so, an extension to hot and compressed hadronic matter is necessary and also under progress. Note that the NLD formalism is fully thermodynamically consistent, which is an important requirement before applying it to hot and dense systems. In summary, we conclude the relevance of our studies for future experiments at FAIR and for nuclear astrophysics.

References

1. P. Demorest, T. Pennucci, S. Ransom, M. Roberts, and J. Hessels, *Nature* **467** (2010) 1081.
2. J. Antoniadis *et al.*, Science **340** (2013) 6131.
3. J.M. Lattimer, A.W. Steiner, *Astrophys. J.* **784** (2014) 123.
4. T. Klähn, *et al.*, *Phys. Rev.* **C 74** (2006) 035802.
5. C. Fuchs, *Prog. Part. Nucl. Phys.* **56** (2006) 1.
6. C. Hartnack, *et al.*, *Phys. Rept.* **510** (2012) 119.
7. Ch. Moustakidis, T. Gaitanos, Ch. Margaritis, G.A. Lalazissis, *Phys. Rev.* **C 95** (2017) 045801.
8. I. Bombaci, arXiV:1601.05339 [nucl-th], D. Chatterjee, I. Vidana, *Eur. Phys. J.* **A 52** (2016) 29.
9. H.-P. Duerr, *Phys. Rev.* **103** (1956) 469, J.D. Walecka, *Ann. Phys.* **83** (1974) 491, J. Boguta, A. Bodmer, *Nucl. Phys.* **A 292** (1977) 413.
10. T. Gaitanos, M. Kaskulov, *Nucl. Phys.* **A 899** (2013) 133, T. Gaitanos, M. Kaskulov, *Nucl. Phys.* **A 940** (2015) 181.
11. R. Machleidt, K. Holinde, and C. Elster, *Phys. Rept.* **149** (1987) 1, K. Erkelenz, *Phys. Rept.* **13** (1974) 191.
12. G. Lalazissis *et al.*, *Phys. Lett.* **B 671** (2009) 36.
13. S. Typel and H. Wolter, *Nucl. Phys.* **A 656** (1999) 331.
14. S. Typel, *Phys. Rev.* **C 71** (2005) 064301.
15. G. Li, R. Machleidt, and R. Brockmann, Phys. Rev. **C45**, 2782 (1992).
16. R. Brockmann and R. Machleidt, Phys. Rev. **C42**, 1965 (1990).
17. T. Gross-Boelting, C. Fuchs, and A. Faessler, Nucl. Phys. **A648**, 105 (1999).
18. S. Petschauer, J. Haidenbauer, N. Kaiser, U. G. Meiner and W. Weise, *Eur. Phys. J.* **A 52** (2016) no.1, 15
19. T. Gaitanos, *Int. J. Mod. Phys.* **E 25** (2016) no.12, 1630008, T. Gaitanos, C. Moustakidis, G. A. Lalazissis and H. Lenske, *Nucl. Phys.* **A 954** (2016) 308.
20. A. Violaris, T. Gaitanos, in preparation.
21. S. Antic and S. Typel, *AIP Conf. Proc.* **1645** (2015) 276.

Spin-orbit splittings of neutron states in N = 20 isotones from covariant density functionals (CDF) and their extensions.

Konstantinos Karakatsanis[1], Georgios Lalazissis[1], Peter Ring[2], and Elena Litvinova[3]

[1] Physics Department, Aristotle University of Thessaloniki, Thessaloniki GR-54124, Greece
[2] Physik Department, Technische Universitat Munchen, D-85747 Garching, Germany
[3] Department of Physics, Western Michigan University, Kalamazoo MI 49008-5252 USA

Abstract. The spin-orbit splitting is an essential ingredient for our understanding of the shell structure in nuclei. One of the most important advantages of relativistic mean-field (RMF) models in nuclear physics is the fact that the large spin-orbit (SO) potential emerges automatically from the inclusion of Lorentz-scalar and -vector potentials in the Dirac equation. It is therefore of great importance to compare the results of such models with experimental data. We investigate the size of $2p$- and $1f$-splittings for the isotope chain ^{40}Ca, ^{38}Ar, ^{36}S, and ^{34}Si in the framework of various relativistic and non-relativistic density functionals. They are compared with the results of a recent experiment by Burgunder et al. [13].

PACS. 21.60.Cs, 21.10.Pc, 21.10.Ft

1 Introduction

Self-consistent mean field models in the framework of nuclear density functional theory provide a very successful way to study nuclear structure phenomena throughout the entire nuclear chart. The nucleons are treated as independent particles moving inside the nucleus under the influence of various potentials, derived from such functionals [2]. These methods are similar to those used in electronic systems where the form of the density functionals can be deduced *ab-initio* from the well known Coulomb force between the electrons [3,4]. Contrary to that, at present, the nuclear density functionals are constructed phenomenologically. The form of those functionals is motivated by the symmetries of the underlying basic theories. The parameters of the model, however, are adjusted to experimental data in finite nuclei.

Within the concept of density functional theory, the full quantum mechanical nuclear many-body problem is mapped onto a single particle problem, assuming that the exact ground state of the A-body system is determined by a Slater determinant and the corresponding single particle density matrix generated from the products of A single particle states. By imposing a variation principle on the energy functional with respect to this density one derives the equations of motion of the independently moving nucleons. The specific form of the phenomenological density functional leads to a certain form of the mean-field.

There are two general versions of this theory. The standard since almost fifty years ago, are non-relativistic functionals. The most widely known forms are the Skyrme type functionals, based on zero range interactions [5] and the Gogny type functionals of finite range interactions [6]. Later on covariant density functionals have been introduced. Their relativistic form is based on the simple model of Walecka [7,8] and its density dependence has been introduced by non-linear meson couplings by Boguta and Bodmer [9].

In all the conventional non-relativistic models the spin-orbit term is derived from a two-body spin-orbit interaction of zero range [5,6,11]. The corresponding Fock term leads to a strong isospin dependence of the spin-orbit splitting. This is the origin of the failure to reproduce the kink in the isotopic shifts mentioned above. In covariant models the spin-orbit splitting is a single-particle effect, derived directly from the Dirac equation. Its isospin dependence is given by the ρ-meson. Its strength is determined by the symmetry energy and it leads usually only to a weak isospin dependence [10,7]. The use of an additional scalar isovector δ-meson does not change very much this situation, because the contributions of the isovector mesons to the spin-orbit term are small as compared to the contributions of the isoscalar mesons [12].

There has been lately a renewed interest in experimental studies concerning the spin orbit part of the nuclear force. In particular two specific experiments [13,14] were recently published, where the structure of the $N = 20$ nucleus ^{34}Si nucleus is investigated. The reason why this particular nucleus was chosen is its unique bubble structure, unveiled in earlier theoretical calculations [15] using both relativistic and non-relativistic models.

Following, therefore, the identification of ^{34}Si as a bubble nucleus [15] a very specific experiment by Burgunder et.al. [13] was conducted attempting to set an additional constraint on the strength of the spin-orbit force. Comparing these results with earlier experiments of nuclei within the $N = 20$ isotone chain such as in [16,17], one is able to evaluate a reduction in the $2p_{3/2} - 2p_{1/2}$ splitting. This effect has been attributed to the occurrence of a bubble in the central proton density as one advances from ^{36}S to ^{34}Si.

We first neglect pairing correlations, as it has been done in the earlier non-relativistic work of Ref. [18] and calculate the single particle energies in the relativistic Hartree model (RH) based on several modern nonlinear and density dependent covariant density functionals. Afterwards we go beyond these investigations in various aspects: we study the influence of pairing correlations within the relativistic Hartree-Bogoliubov (RHB) scheme, we include tensor forces in relativistic Hartree-Fock (RHF) theory, and finally we go beyond mean field and include particle vibration coupling (PVC).

2 Results

As mentioned in the introduction we concentrate our study to the series of $N = 20$ isotones. We start with the nucleus ^{40}Ca with $Z = 20$ protons, where the last four protons fill the $1d_{3/2}$ orbit. By removing two protons we go to ^{38}Ar and by removing two more we reach ^{36}S which has its last two protons in the $2s_{1/2}$ orbit. The density distribution of this state is peaked in the center of the nucleus. and the removal of the two protons, as we go to ^{34}Si, leads to an occupation probability close to zero. Therefore we have a central depletion in the proton density and the formation of a dimple around the centre of the nuclear charge density. This is shown in Fig.1, where we have plotted the proton densities with respect to the nuclear radius. For the first three nuclei in this chain we can see clearly a peak of the proton density at the center of the nucleus whereas for ^{34}Si there is a dimple, (see also Ref. [15]). Experimental evidence of the existence of this bubble structure has been given very recently by Mutschler *et. al.* in Ref. [14], where the one-proton removal reaction ^{34}Si$(-1p)$ ^{33}Al has been studied. Even though the occupancy of a single-particle orbit is not a direct observable, its value can be calculated using experimental data. Therefore an occupancy of 0.17(3) has been deduced for the $2s_{1/2}$ proton state in ^{34}Si, which is only 10% of the 1.7(4) occupancy of the same state in ^{36}S, resulting in an occupancy change of $\Delta(2s1/2) = 1.53$. This result came in addition to the findings of the earlier experiment by Burgunder *et. al.* [13], where the energies and spectroscopic factors of the first $1f_{7/2}$, $2p_{3/2}$, $2p_{1/2}$ and $1f_{5/2}$ neutron states in the nucleus ^{35}Si were measured through a (d,p) transfer reaction. Together with the results of Refs. [16,17], it was discovered that the $2p = 2p_{1/2} - 2p_{3/2}$ spin-orbit splitting was considerably reduced as one goes from ^{36}S to ^{34}Si.

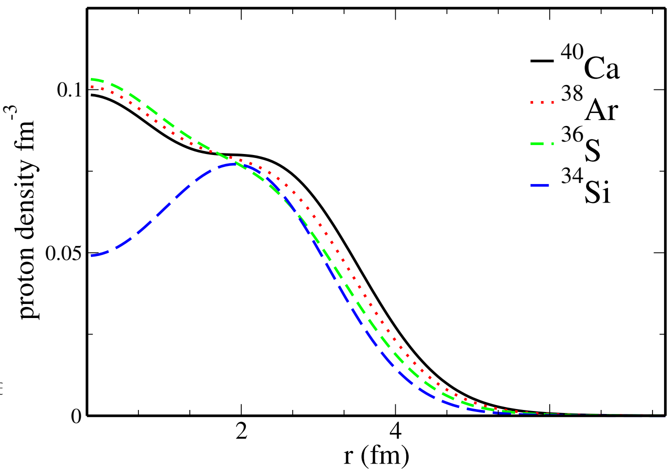

Fig. 1. (color online) Proton densities of the nuclei ^{40}Ca, ^{38}Ar, ^{36}S and ^{34}Si for the functional DD-ME2.

Table 1. Spin-orbit splittings in MeV (Upper part) and their relative reductions (Lower part) for f and p neutron states in the case of no pairing.

		^{40}Ca		^{38}Ar		^{36}S		^{34}Si	
	$\frac{W_1}{W_2}$	f	p	f	p	f	p	f	p
NL3	1.11	7.21	1.69	6.90	1.77	6.43	1.80	6.08	0.71
DD-ME2	1.07	7.40	1.71	7.04	1.72	6.52	1.65	6.12	0.87
DD-PC1	1.07	7.83	1.77	7.57	1.74	7.12	1.64	6.61	0.88
Exp.		6.98	1.66			5.61	1.99	5.5	1.13

	^{40}Ca $\to$ ^{36}S		^{36}S $\to$ ^{34}Si	
	f	p	f	p
NL3	11%	-6%	5%	61%
DD-ME2	12%	3%	6%	47%
DD-PC1	9%	8%	7%	46%
Exp.	20%	-20%	2%	43%

An important aspect of the spin-orbit force is its density and isospin dependence. It is clearly stated in Refs. [13, 14] that the results of these two experiments are ideal for a further theoretical investigation of the SO force deduced from the various nuclear density functionals. In particular, the extreme neutron-to-proton density asymmetry in the case of ^{34}Si and the subsequent large and abrupt reduction in the size of the p-spitting, can provide a better constraint of the SO force, since these results isolate the contributions coming mostly from its density and its isospin dependence.

As was noted in the introduction, the way the spin-orbit force is included in relativistic density functional theory is substantially different from the non-relativistic case.

2.1 Pure mean-field effects

We begin our investigations with simple mean field calculations without pairing: we solve the Relativistic Hartree equations and investigate the behaviour of the single-neutron

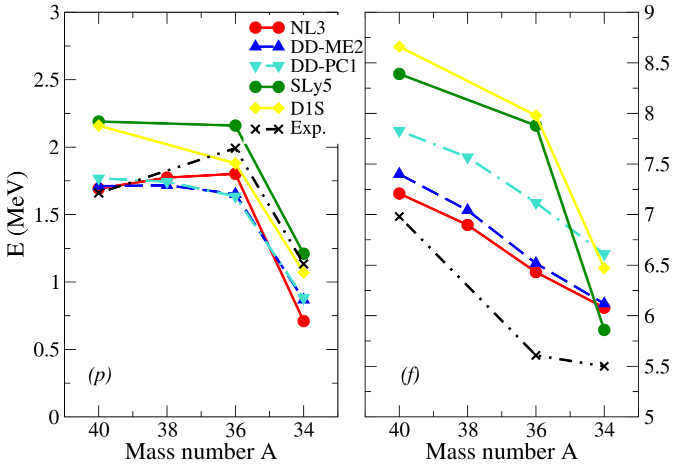

Fig. 2. (Color online) Evolution of spin-orbit splittings for the neutron levels p (left panel) and f (right panel) with respect to the mass number A, without pairing.

energies in the $N = 20$ isotone chain. In this case the single particle orbits are either fully occupied or completely empty. Thus the occupancy of the $2s_{1/2}$ proton state is 2 for the nuclei ^{40}Ca, ^{38}Ar, and ^{36}S and 0 for ^{34}Si. This will give us the pure relativistic mean field effect on the spin-orbit splittings.

The results for this case are given in Table 1. In the upper part we show the $f = 1f_{7/2} - 1f_{5/2}$ and $p = 2p_{3/2} - 2p_{1/2}$ energy splittings for each specific functional and for each of the nuclei ^{40}Ca, ^{38}Ar, ^{36}S, and ^{34}Si. In the lower part we present the relative reduction of the f and p splittings again for every functional, first as we move from ^{40}Ca to ^{36}S and then as we go from ^{36}S to ^{34}Si. We also show in the last row the experimental values of the splittings and the reductions for ^{40}Ca [16], ^{36}S [17], and ^{34}Si [13].

For ^{40}Ca we use the values of the centroids for the distribution of the respective fragments. These data can be compared directly with our theoretical results. In the other two cases this is not possible, because the experimental centroids are not known. Therefore for the $2p_{3/2} - 2p_{1/2}$ in both ^{36}S and ^{34}Si we use the major fragment of each state. For the $1f_{5/2}$ state in ^{36}S we use the major contribution that comes from three states centered at 5.61 MeV with a total spectroscopic factor $SF = 0.36$, and in ^{34}Si the broad structure around 5.5 MeV with a calculated $SF = 0.32$. Even though this is not directly comparable with our results, we use it as an indication of the size of the reduction we should expect.

A schematic representation of our results together with the results for the non-relativistic SLy5 and D1S models, is given in Fig. 2. For all the models we plot the evolution of the p and the f spin-orbit splittings as a function of the mass number A.

In this first approach we observe a gradual reduction in the f splittings of about 0.3-0.4 MeV at each step as we move down the chain of isotones. This is also apparent from the fact that the curves that show the evolution of the f-splitting in Fig. 2 have a similar slope for the different functionals. The total relative reduction is between 15-19% and around 5-7% at each step.

In contrast to the f-splittings, the p splittings change only slightly for the three first nuclei, the only exception being the functional DD-MEδ. Only when we move from ^{36}S to ^{34}Si we find a large reduction for the p splittings of the order of 40% to 60%. Qualitatively this picture is in line with the experiment. However, the absolute size of the p-splitting in ^{34}Si for most of our models is smaller than the respective experimental value. This leads in certain cases to an even larger relative reduction than what we should expect.

When we compare between relativistic and non-relativistic results we observe the following differences. In general the sizes of the splittings in all the relativistic models are smaller than the respective splittings in non-relativistic SLy5 and D1S models. More specifically in the nuclei ^{40}Ca and ^{36}S, where the proton density has the normal profile, i.e. no central depletion, the difference in the size of f-splittings is in the order of 1-2 MeV and the size of the p-splittings is around 0.5 MeV

In the interesting case of the bubble nucleus ^{34}Si, the f-splittings are in the same size because of the bigger relative reduction that appears in the non-relativistic case something not present in the relativistic models. However there is a difference in the p-splittings which are relatively small in size for all the relativistic functionals. This is translated into a relative reduction of the p-splitting when we go from ^{36}S to ^{34}Si, which is larger for most of the relativistic models as compared to the relative reduction for non-relativistic models.

2.2 The effect of pairing correlations

Pairing correlations and the related pairing gap can affect the size of the SO splittings. Already in Ref. [15] it was shown within the framework of Relativistic Hartree Bogoliubov (RHB) calculations that pairing correlations reduce the size of the bubble in ^{34}Si. According to this result and based on the previous discussion we expect to see a weakening of the bubble effect therefore larger absolute sizes and smaller relative reductions of the p-splitting, as compared to the pure Hartree-calculations without pairing.

Within the RHB for superfluid nuclei we deal with quasiparticles. The occupancy of each state is calculated self-consistently. It is determined by the strength of the pairing force. Subsequently, in the present work, we introduce pairing correlations in the proton subsystem and evaluate again the single-particle energies of the same neutron states as before. We also calculate the occupation probabilities of the proton $2s_{1/2}$ state for ^{36}S and ^{34}Si, since the bubble structure in ^{34}Si is created because of this state being almost empty.

In this context we use the TMR separable pairing force of Ref. [20] for the short range correlations. This kind of separable pairing force has been adjusted to reproduce the pairing gap of the Gogny force D1S in symmetric nuclear matter [20]. Both forces are of finite range and therefore

Table 2. Same as Table 1 but for the case of TMR pairing.

	^{40}Ca		^{38}Ar		^{36}S		^{34}Si	
	f	p	f	p	f	p	f	p
NL3	7.21	1.69	6.92	1.64	6.46	1.68	5.94	0.80
DD-ME2	7.40	1.71	7.08	1.64	6.55	1.57	6.00	0.94
DD-PC1	7.83	1.77	7.58	1.67	7.14	1.56	6.52	0.96
Exp.	6.98	1.66			5.61	1.99	5.5	1.13

	^{40}Ca $\rightarrow$ ^{36}S		^{36}S $\rightarrow$ ^{34}Si	
	f	p	f	p
NL3	10%	1%	8%	53%
DD-ME2	11%	8%	8%	40%
DD-PC1	9%	12%	9%	39%
Exp.	20%	-20%	2%	43%

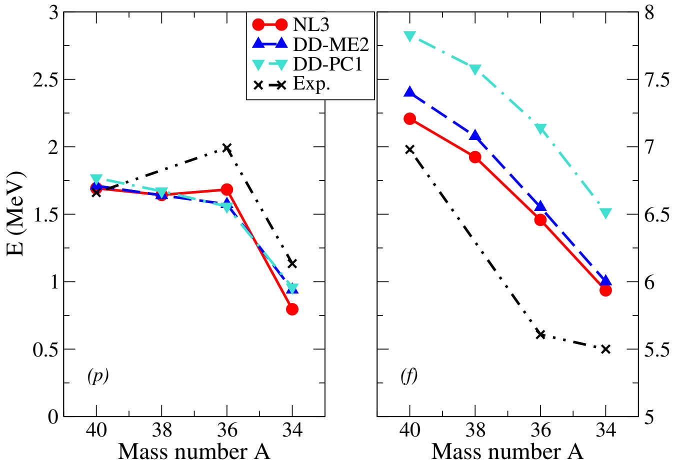

Fig. 3. Same as FIG. 2 but with TMR pairing.

they show no ultraviolet divergence and do not depend on a pairing cut- off. They provide a very reasonable description of pairing correlations all over the periodic table with a fixed set of parameters.

The SO splittings and the respective reductions found in these calculations are shown in Table 2. In Fig. 3 we present again a schematic representation of the evolution of SO splittings for all the forces with respect to the mass number.

Comparing the results of the calculations including pairing with the previous pure mean-field results we get the same qualitative picture. The f-splittings show again a gradual reduction as we go down the chain of isotones. The p-splittings stay roughly in the same size between the first three nuclei and are reduced dramatically for the last nucleus where there is the bubble structure. The inclusion of pairing correlation increases the f- splittings and reduces the p-splittings in ^{38}Ar and ^{36}S from the respective splittings in the pure mean field calculations. This change is very small for ^{38}Ar and slightly bigger for ^{36}S for the p-states and the other way around for the f- splittings, where in the case of ^{36}S they are practically unchanged. For the last nucleus ^{34}Si this picture is reversed and one gets smaller f-splittings and larger p-splittings again in

Table 3. Occupation probabilities of the $2s_{1/2}$ proton state in ^{36}S and ^{34}Si for the TMR pairing force.

	^{36}S	^{34}Si	$\Delta(2S_{1/2})$
NL3	1.83	0.20	1.62
DD-ME2	1.79	0.23	1.57
DD-PC1	1.77	0.30	1.47
Exp.[14]	1.64	0.17	1.56

the same order of magnitude of 0.1MeV. This last effect corrects for the enhanced effect of the bubble structure and the sudden reduction of the p-splitting as one goes from ^{36}S to ^{34}Si.

For a better understanding how pairing correlations lead to this differences we present in Table 3 the occupation factors of the $2s_{1/2}$ proton state in ^{36}S and ^{34}Si.

For ^{38}Ar, pairing affects mostly the *1d* proton orbit with its two last 2 protons in the $1d_{3/2}$ state. Here the surface density becomes more diffused and the spin-orbit force has a greater overlap with the f neutron states making the corresponding splittings slightly bigger. In the ^{36}S pairing influences the central densities reducing the size of the peak with a tendency to flatten it out. This can also be seen by the reduced occupancy of the $2s_{1/2}$ proton state which is now smaller than 2. This creates a less attractive SO force around the center and so the splittings of the neutron p states appear somewhat smaller.

For the case of ^{34}Si pairing reduces the dip at the center of the bubble as it has been noted already in Ref. [15]. This is caused by the increasing occupancy of the previously empty $2s_{1/2}$ proton state, as shown in Table 3. As we have seen, this reduction of the bubble leads to an increase of the p-splittings by almost 0.1 MeV. Together with the previous discussion about ^{36}S the relative reduction of this splitting comes closer to the experimental value deduced from the major fragments.

2.3 Extensions: Tensor Forces and Particle-VibrationCoupling

In this last part we extend the standard formulation of the covariant density functional models in two ways. First we include explicitly a tensor term. This extension remains on the mean-field level. In the second case we go beyond mean-field by taking into consideration the coupling of the single particle states to the low-lying surface modes in the nucleus.

2.3.1 The effect of the tensor force

As we have already stated the tensor part of the nuclear force plays an essential role in the description of the several nuclear properties. In our case it affects the single particle structure [21–23]. In conventional covariant density functional theory exchange terms are usually not taken into account, because the Fierz theorem shows that, for zero

Table 4. Spin-orbit splittings of f and p neutron states (upper part) and relative reductions (bottom part), for the case of tensor forces. For comparison we also show the results from Ref. [18].

	^{40}Ca		^{36}S		^{34}Si	
	f	p	f	p	f	p
NL3	7.21	1.69	6.44	1.68	5.56	0.74
NL3RHF0.5	7.87	1.74	5.80	1.64	5.12	0.66
SLy5$_{T-2013}$	6.77	1.76	5.53	1.07	4.41	0.61
D1ST$_{2c-2013}$	6.90	1.73	5.65	1.26	4.75	0.73
Exp.	6.98	1.66	5.61	1.99	5.5	1.13

	^{40}Ca $\to$ ^{36}S		^{36}S $\to$ ^{34}Si	
Splitting	f	p	f	p
NL3	10%	1%	14%	56%
NL3RHF0.5	26%	14%	12%	60%
SLy5$_{T-2013}$	18%	39%	20%	43%
D1ST$_{2c-2013}$	18%	27%	16%	42%
Exp.	20%	-20%	2%	43%

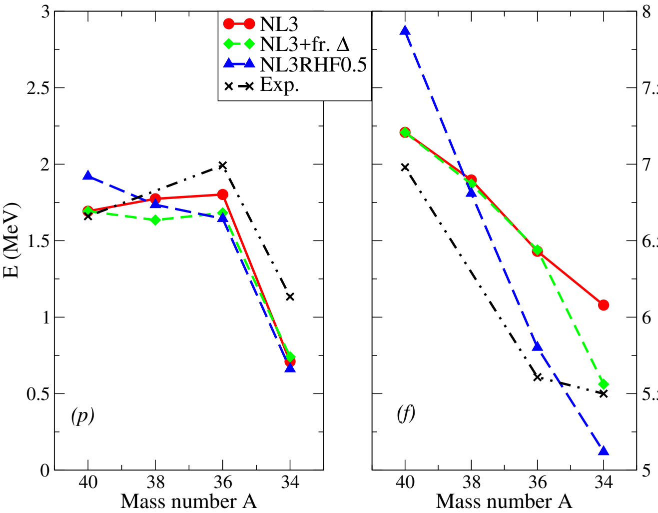

Fig. 4. Evolution of the p and f SO splittings for NL3

range forces, they can be rewritten in terms of direct terms by reshuffling the coupling constants of the various spin-isospin channels. Since the coupling constants are adjusted to experimental data anyhow, this seems to be reasonable approximation for the heavy mesons σ, ω, and ρ, which lead to forces of relatively short range. The direct term of the pion does not contribute because of parity conservation, but its mass is not small and therefore its exchange term should be taken into account explicitly. It leads to a tensor term in the functional. In the following we show results of relativistic Hartree-Fock calculations as discussed in Ref. [23].

In particular, we want to investigate in the specific case of the bubble nucleus ^{34}Si and the corresponding dramatic reduction in the p-splitting as compared with ^{36}S, whether the explicit inclusion of the tensor force changes the size of the splitting and the amount of the reduction.

In Table 4 we compare the results of the NL3RHF0.5 with calculation done with NL3 in the Hartree level with the same pairing scheme of frozen gap and to those of non-relativistic Skyrme and Gogny interactions SLy5$_{T-2013}$ and D1ST$_{2c-2013}$. These are modified versions of the functionals SLy5 and D1S, where tensor terms have been included and were adjusted together with the spin-orbit parameters. Details are given in Ref. [18]. We have to emphasize, however, that the tensor force used in the non-relativistic calculations in Ref. [18] is of zero range, whereas the tensor force in these relativistic calculations is of finite range because of the low mass of the pion. Finally in Fig. 4 we have plotted the evolution of the spin-orbit splittings as it is done in Fig. 2 and Fig. 3 but now just for the NL3 force in order to compare between the pure mean-field, pairing and the tensor effects.

We observe that the inclusion of the tensor force has a more pronounced effect in the transition from from ^{40}Ca to ^{36}S as to the transition from ^{36}S to ^{34}Si. Following the rule that we described in the beginning of the current section, we recognize that as we move from ^{40}Ca to ^{36}S and remove the four protons from the $j_<$ proton state $\pi 1d_{3/2}$, the attractive effect of the tensor interaction with the $j'_>$ neutron state $\nu 1f_{7/2}$ is reduced and thus this state is shifted upwards, from its starting point in ^{40}Ca. On the other side the $j'_<; \nu 1f_{5/2}$ which in ^{40}Ca is repelled by the protons of the $\pi 1d_{3/2}$ it is shifted downwards as we go to ^{36}S. The combination of all these effects leads to an enhanced quenching of the f-splitting as we go from ^{40}Ca to ^{36}S. This is also seen by the much steeper blue line that corresponds to NL3RHF0.5 case in the right panel in Fig. 4. The same behaviour can be observed also for the $j'_>; \nu 2p_{3/2}$ and the $j'_<; \nu 2p_{1/2}$ neutron states, although the effect on the absolute size of the splitting is smaller in those cases.

Finally, we have measured an occupancy of the $2s_{1/2}$ proton state of 0.18 with the NL3RHF0.5, which is larger than the 0.10 value in the case of NL3 in the RH level for the same pairing scheme. This indicates that the tensor force counteracts to some extent the effect of pairing that we described in the previous section and leads to smaller size, from 0.74 MeV to 0.66 MeV and slightly larger reduction from 56% to 60%, for the particular p-splitting.

2.3.2 The effect of particle vibration coupling

The coupling of the single particle states to low-lying phonons leads to a fragmentation of the single particle levels and therefore sometimes to considerable shifts of the major components, i.e. of the components with the largest spectroscopic factor. This is in particular important for states close to the Fermi surface. For our calculations we used the density functional NL3* [19] and a constant pairing gap of $\Delta = 2$ MeV.

After the solution of the Dyson equation we have the ability to isolate the major contributions to each s.p. state and compare its energy directly with the experimental results from Ref. [13], as shown in table 5. This is also done

Table 5. Comparison between the spin-orbit splittings (Upper part) and their relative reductions (Lower part) of the major fragments from PVC with the corresponding experimental results.

	^{36}S		^{34}Si	
Splitting	f	p	f	p
NL3* with PVC	6.3	2.28	5.28	1.4
Exp.	5.61	1.99	5.5	1.13

	$^{36}\mathrm{S} \rightarrow {}^{34}\mathrm{Si}$	
Splitting	f	p
NL3* with PVC	16%	39%
Exp.	2%	43%

schematically in fig. 5 where we compare the results of the PVC calculations for the nuclei ^{36}S and ^{34}Si with the experimental values of Ref. [13]. More specifically, we show the position of the major fragments and the splittings between the f and p states as well as their spectroscopic factors. The experimentally observed reduction of the spin-orbit splitting is 43% for the p states. It is in rather good agreement with the results obtained from the theoretical PVC calculations, which show a reduction of 39%. In both cases these are the splittings for the major fragments. Notice, that in the PVC calculations we have not included isospin-flip phonons as it is done, for instance, in Ref. [?]. It has been observed that the inclusion of such phonons causes an additional fragmentation and shifts of the dominant fragments, bringing the results to a better agreement with data. However, the latter approach is, so far, not yet adopted to the case of open-shell nuclei. It will be considered in the future.

In Fig. 5 we show the positions of the neutron states $2p_{1/2}$, $2p_{3/2}$ and $1f_{5/2}$ using the $1f_{7/2}$ as reference state for the nuclei ^{37}S (panel (a,b,c)) and ^{35}Si (panel (d,e,f)). The experimental data of Ref. [13] in panels (a) and (d) are compared with results of PVC-calculations with the density functional NL3* in panels (b) and (e). In this figure the experimental energies as well as the energies of the PVC-calculations correspond to the major components of the corresponding fragmented level. Only for the $1f_{5/2}$ orbits we show in panel (a) the experimental fragmentation and in panel (d) the area of the experimental fragmentation. In order to study the effect of particle vibrational coupling we show in panels (c) and (f) calculations with the same density functional without particle vibrational coupling.

We find that in both nuclei the SO-splitting of the $1f$-orbitals is reproduced relatively well. Particle vibrational coupling has only a small influence on this splitting. On the other side all $2p$-orbits are shifted downwards closer to the $1f_{7/2}$-orbit as it is also observed in the experiment. It is well known, that this effect is in particular large for levels close to the Fermi surface, i.e. larger for the $2p_{3/2}$-orbit than for the $2p_{1/2}$-orbit. As a result the SO-splitting of the $2p$ orbits is increased considerably by particle vibrational coupling. As compared to the much too small SO-splitting

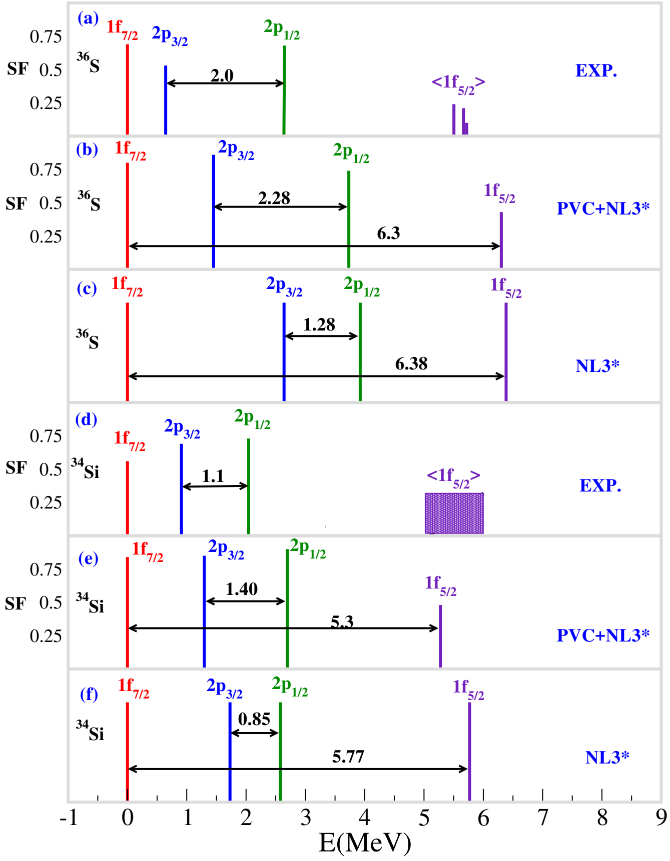

Fig. 5. Distribution of the major fragments of the single particle strengths of ^{37}S (panel (a)) and ^{35}Si (panel (d)) as given in Ref. [13] and the same distribution calculated with PVC for the force NL3* (panels (b) and (e)). Panels (c) and (f) show results obtained without particle vibrational coupling using the same density functional.

for the $2p$ orbits without PVC it is now much closer to the experimental value.

3 Conclusions

In this study we have calculated the single particle energies of the spin-orbit doublets $1f_{7/2}$-$1f_{5/2}$ and $2p_{3/2}$-$2p_{1/2}$ in order to investigate the spin-orbit splittings and their evolution as we move along the chain of isotones with N=20: ^{40}Ca, ^{38}Ar, ^{36}S, and ^{34}Si. We used several relativistic functionals of three different types: non-linear meson coupling, density dependent meson coupling and density dependent point coupling models. Furthermore, we used the separable TMR pairing force of finite range, which is essentially equivalent to the pairing part of the Gogny force D1S, in order to determine the effect of pairing on the size and on the reduction of the SO splittings. Finally, we considered specific extensions that go beyond the simple Hartree case, namely the inclusion of one-pion exchange which induces a tensor force and particle vibration coupling that takes into account correlations between single particle states going beyond the mean field approximation.

In general we observe a significant reduction of the $2p_{3/2} - 2p_{1/2}$ splitting for neutron states when we go from ^{36}S to ^{34}Si as it is observed in the experiment. In the pure mean-field level most of the forces show a relatively large reduction. When we include pairing this reduction is becomes less and less dramatic with increasing pairing correlations, because the occupation of the $2s_{1/2}$ proton-orbit changes less rapidly between ^{36}S and ^{34}Si. The isospin dependence of the effective spin-orbit force is weaker in the relativistic models and therefore the reduction is also less pronounced in these models.

Finally we went beyond the conventional Hartree level and included two effects, which have a strong influence on the single particle structure: We included tensor terms and particle vibrational coupling.

Here we found that the tensor term induced by the one pion-exchange force has a relatively small effect. It acts to some extent in the opposite direction of pairing. It increases the quenching of the spin-orbit distinctly for the f and to a smaller extent for p states when going from ^{40}Ca to ^{36}S, showing the tensor character of those reductions. On the other hand, for the transition from ^{36}S to ^{34}Si the size of the splittings are only slightly reduced for both nuclei and thus the relative reduction remains practically unchanged indicating that this comes purely from the spin-orbit interaction. Such an effect is also observed in the non-relativistic case [18] as it is seen in Table 4. On the other hand, particle vibrational coupling acts in the same direction as pairing. We find that the relative reduction of the splitting between $2p_{3/2}$ and $2p_{1/2}$ neutron states decreases. This is consistent with the general effect of PVC to produce a more dense spectrum near the Fermi surface. Finally this produces a reasonable agreement with the experimental data in the isotone chain with $N = 20$.

4 acknowledgments

This research is funded by the Greek State Scholarship Foundation (IKY), through the program "IKY Fellowships of excellence for postgraduate studies in Greece-SIEMENS program", by the DFG cluster of excellence "Origin and Structure of the Universe" (www.universe-cluster.de), and by US-NSF grant PHY-1404343.

References

1. G. Burgunder, O. Sorlin, F. Nowacki, S. Giron, F. Hammache, M. Moukaddam, N. de Séréville, D. Beaumel, L. Càceres, E. Clément, G. Duchêne, J. P. Ebran, B. Fernandez-Dominguez, F. Flavigny, S. Franchoo, J. Gibelin, A. Gillibert, S. Grévy, J. Guillot, A. Lepailleur, I. Matea, A. Matta, L. Nalpas, A. Obertelli, T. Otsuka, J. Pancin, A. Poves, R. Raabe, J. A. Scarpaci, I. Stefan, C. Stodel, T. Suzuki, and J. C. Thomas, Phys. Rev. Lett. **112**, 042502 (2014).
2. M. Bender, P.-H. Heenen, and P.-G. Reinhard, Rev. Mod. Phys. **75**, 121 (2003).
3. J. P. Perdew and S. Kurth, in *A Primer in Density Functional Theory*, edited by C. Fiolhais, F. Nogueira, and M. A. L. Marques (Springer Berlin Heidelberg, Berlin, 2003), Vol. 620, pp. 1–55.
4. R. J. Bartlett, Mol. Phys. **108**, 3299 (2010).
5. D. Vautherin and D. M. Brink, Phys. Rev. C **5**, 626 (1972).
6. J. Dechargé and D. Gogny, Phys. Rev. C **21**, 1568 (1980).
7. J. D. Walecka, Ann. Phys. (N.Y.) **83**, 491 (1974).
8. B. D. Serot and J. D. Walecka, Adv. Nucl. Phys. **16**, 1 (1986).
9. J. Boguta and A. R. Bodmer, Nucl. Phys. A **292**, 413 (1977).
10. H.-P. Dürr, Phys. Rev. **103**, 469 (1956).
11. M. Baldo, P. Schuck, and X. Viñas, Phys. Lett. B **663**, 390 (2008).
12. X. Roca-Maza, X. Viñas, M. Centelles, P. Ring, and P. Schuck, Phys. Rev. C
13. G. Burgunder, O. Sorlin, F. Nowacki, S. Giron, F. Hammache, M. Moukaddam, N. de Séréville, D. Beaumel, L. Càceres, E. Clément, G. Duchêne, J. P. Ebran, B. Fernandez-Dominguez, F. Flavigny, S. Franchoo, J. Gibelin, A. Gillibert, S. Grévy, J. Guillot, A. Lepailleur, I. Matea, A. Matta, L. Nalpas, A. Obertelli, T. Otsuka, J. Pancin, A. Poves, R. Raabe, J. A. Scarpaci, I. Stefan, C. Stodel, T. Suzuki, and J. C. Thomas, Phys. Rev. Lett. **112**, 042502 (2014).
14. A. Mutschler, A. Lemasson, O. Sorlin, D. Bazin, C. Borcea, R. Borcea, Z.
15. M. Grasso, L. Gaudefroy, E. Khan, T. Niksic, J. Piekarewicz, O. Sorlin, N. V.
16. Y. Uozumi, N. Kikuzawa, T. Sakae, M. Matoba, K. Kinoshita, S. Sajima, H. Ijiri,
17. G. Eckle, H. Kader, H. Clement, F. Eckle, F. Merz, R. Hertenberger, H. Maier,
18. M. Grasso and M. Anguiano, Phys. Rev. C **92**, 054316 (2015).
19. G. A. Lalazissis, S. Karatzikos, R. Fossion, D. Peña Arteaga, A. V. Afanasjev, and P. Ring, Phys. Lett. B **671**, 36 (2009).
20. Y. Tian, Z. Y. Ma, and P. Ring, Phys. Lett. B **676**, 44 (2009).
21. T. Otsuka, T. Suzuki, R. Fujimoto, H. Grawe, and Y. Akaishi, Phys. Rev. Lett.
22. T. Otsuka, T. Matsuo, and D. Abe, Phys. Rev. Lett. **97**, 162501 (2006).
23. G. A. Lalazissis, S. Karatzikos, M. Serra, T. Otsuka, and P. Ring, Phys. Rev. C **80**, 041301 (2009).

A symmetry for heavy nuclei: Proxy-SU(3)

Dennis Bonatsos[1], I. E. Assimakis[1], N. Minkov[2], Andriana Martinou[1], R. B. Cakirli[3], R. F. Casten[4,5], and K. Blaum[6]

[1] Institute of Nuclear and Particle Physics, National Centre for Scientific Research "Demokritos", GR-15310 Aghia Paraskevi, Attiki, Greece
[2] Institute of Nuclear Research and Nuclear Energy, Bulgarian Academy of Sciences, 72 Tzarigrad Road, 1784 Sofia, Bulgaria
[3] Department of Physics, University of Istanbul, Istanbul, Turkey
[4] Wright Laboratory, Yale University, New Haven, Connecticut 06520, USA
[5] Facility for Rare Isotope Beams, 640 South Shaw Lane, Michigan State University, East Lansing, MI 48824 USA
[6] Max-Planck-Institut für Kernphysik, Saupfercheckweg 1, D-69117 Heidelberg, Germany

Abstract. The SU(3) symmetry realized by J. P. Elliott in the sd nuclear shell is destroyed in heavier shells by the strong spin-orbit interaction. However, the SU(3) symmetry has been used for the description of heavy nuclei in terms of bosons in the framework of the Interacting Boson Approximation, as well as in terms of fermions using the pseudo-SU(3) approximation. We introduce a new fermionic approximation, called the proxy-SU(3), and we comment on its similarities and differences with the other approaches.

PACS. 21.60.Fw Models based on group theory – 21.60.Ev Collective models

1 Introduction

The SU(3) symmetry has been introduced in nuclear structure by J. P. Elliott [1,2], who considered the sd shell nuclei and showed the microscopic origins of the connection between the nuclear quadrupole deformation and SU(3). A generalization of the Elliott SU(3) scheme to more than one nuclear shell has been obtained in the framework of the microscopic symplectic model [3]. Since then the SU(3) symmetry has been used in the framework of various algebraic models, especially for the study of medium-mass and heavy deformed nuclei, where the LS coupling scheme of the Elliott model breaks down [4], while microscopic calculations are still out of reach. Descriptions in terms of bosons have been given in the frameowork of the Interacting Boson Model (IBM) [5] and of the Interacting Vector Boson Model (IVBM) [6], while fermionic descriptions have been provided by the Fermion Dynamical Symmetry Model (FDSM) [7]. It underlies also the pseudo-SU(3) scheme [8–14], which we will discuss below, as well as the quasi-SU(3) symmetry [15,16], in which an approximate restoration of LS coupling in heavy nuclei is obtained, based on the smallness of certain $\Delta j = 1$ matrix elements.

On the other hand, many properties of heavy deformed nuclei have been successfully described in detail in terms of the Nilsson model [17–19]. Nilsson states are labelled by $K[N n_z \Lambda]$, where N is the number of oscillator quanta, n_z is the number of quanta along the cylindrical symmetry axis, Λ is the projection of the orbital angular momentum along the symmetry axis, and K is the the projection of the total angular momentum along the symmetry axis, connected to Λ by $K = \Lambda + \Sigma$, where Σ is the the projection of the spin along the symmetry axis. For large deformations, the Nilsson wave functions reach the asymptotic limit, in which these quantum numbers become good quantum numbers, and they remain rather good even at intermediate deformation values [18].

Ben Mottelson has remarked [20] that the asymptotic quantum numbers of the Nilsson model can be seen as a generalization of Elliott's SU(3), applicable to heavy deformed nuclei. Working in this direction, we have shown [21,22] that a proxy-SU(3) symmetry of the Elliott type can be developed in heavy deformed nuclei. The development of the proxy-SU(3) scheme is based on the so-called 0[110] pairs of Nilsson orbits related by $\Delta K[\Delta N \Delta n_z \Delta \Lambda] = 0[110]$ [23]. These pairs, which are characterized by high overlaps [24], have been shown to play a key role in the onset and development of nuclear deformation in the rare earth region [23,24].

In the proxy-SU(3) scheme we also focus attention on Nilsson 0[110] pairs, but in a different way. Instead of taking advantage of proton-neutron pairs, we use proton-proton and neutron-neutron pairs. In this way we reveal an approximate SU(3) symmetry in heavy deformed nuclei, which can be used for predicting nuclear properties within the SU(3) symmetry using algebraic methods, as we shall see in Refs. [25,26].

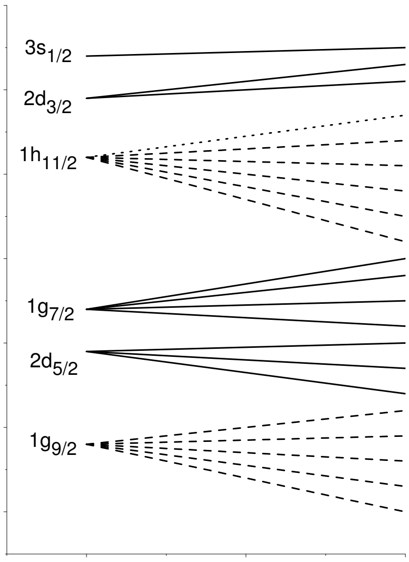

Fig. 1. Schematic representation of the 50–82 shell and the replacement leading to the proxy sdg shell.

2 The proxy-SU(3) model

We are going to explain the basic idea behind the proxy-SU(3) scheme by considering as an example the 50-82 major nuclear shell, shown in Fig. 1.

In the 50-82 major shell one finds the $3s_{1/2}$, $2d_{3/2}$, $2d_{5/2}$, and $1g_{7/2}$ orbitals (shown in Fig. 1 by solid lines). These are the pieces of the full sdg shell remaining after the desertion (because of the spin-orbit force) of the $1g_{9/2}$ orbitals (indicated by dashed lines) into the next shell below, i.e. into the 28-50 nuclear shell. In addition, the 50-82 major shell contains the $1h_{11/2}$ orbitals (shown by dashed lines plus one dotted line), which have invaded this shell from above, forced down and out of the pfh shell also by the spin-orbit force.

The deserter $1g_{9/2}$ orbital consists of the Nilsson orbitals 1/2[440], 3/2[431], 5/2[422], 7/2[413], 9/2[404]. These happen to be 0[110] partners of the $1h_{11/2}$ Nilsson orbitals 1/2[550], 3/2[541], 5/2[532], 7/2[523], 9/2[514], in the same order. Two orbitals being 0[110] partners possess exactly the same values of the projections of orbital angular momentum, spin, and total angular momentum, thus they are expected to exhibit identical behavior as far as properties related to angular momentum projections are concerned. 0[110] partners have been first used in relation to proton-neutron pairs [23], found to correspond to increased strength of the proton-neutron interaction, because of their large overlaps [24].

One can thus think of replacing all of the invading $1h_{11/2}$ orbitals (the upper group of dashed lines in Fig. 1), except the 11/2[505] orbital (the dotted line in Fig. 1) in the 50-82 shell by their deserting $1g_{9/2}$ counterparts (the lower group of dashed lines in Fig. 1), expecting nuclear properties related to angular momentum to be little affected, since angular momentum projections remain intact. However, one should take carefully into account that during this replacement the N and n_z quantum numbers have been changed by one unit each, thus changing the sign of the parity. These changes will obviously affect the selection rules of various relevant matrix elements, as well as the avoided crossings [27] in the Nilsson diagrams. Detailed calculations to be shown in Ref. [28] will demonstrate that the changes inflicted in the Nilsson diagrams by these modifications are indeed minimal.

The $1h_{11/2}$ 11/2[505] orbit has no 0[110] partner in the $1g_{9/2}$ shell, thus it has been excluded from this replacement. However, this orbit lies at the top of the 50-82 shell in the Nilsson diagrams [17,18], where it is unlikely to find nuclei with large deformations. The same remark applies to similar orbits in other shells such as the 13/2[606] orbit in the 82-126 shell.

After these two approximations have been performed, one is left with a collection of orbitals which form exactly the full sdg shell, which is known to possess a U(15) symmetry, having an SU(3) subalgebra [29]. However, in axially symmetric deformed nuclei the relevant symmetry is not spherical, but cylindrical [30]. As a consequence, the relevant algebras are not U(N) Lie algebras, but more complicated versions of deformed algebras [31–36]. Nevertheless, one can expect that some of the SU(3) features would appear within the approximate scheme.

Since the present approximation scheme is based on the replacement of the invading from above abnornal parity orbitals (except the one with highest angular momentum) by their 0[110] counterparts deserting to the lower shell, with the latter being used as proxies of the former in subsequent considerations, we are going to call this approximation the *proxy-SU(3)* model.

The same approximation can be made in the 28-50, 82-126, 126-184 shells, which thus become approximate pf, pfh, sdgi shells, respectivel. These shells are known to correspond to U(10), U(21), U(28) algebras having SU(3) subalgebras (see [29] and references therein).

3 The pseudo-SU(3) scheme

The present approach exhibits several similarities with and differences from the pseudo-SU(3) scheme, which has been extremely useful in the study of many properties of medium-mass and heavy nuclei away from closed shells. We list here some of these studies.

1) Yrast [10,11,37] and non-Yrast [38–43] bands of even-even deformed nuclei.

2) Normal parity bands and excited bands in odd-mass nuclei [44–48].

3) The scissors mode and magnetic dipole excitations [49–54].

4) Superdeformed bands [55,56].

5) Double-beta decay [57–59], neutrinoless double-beta decay [60], and double-electron capture [61].

6) It should be pointed out that in the case of pseudo-SU(3) a unitary transformation connecting the normal parity orbitals to the pseudo-SU(3) space is known [62, 63].

It is expected that using a large number of results regarding the study of fermionic systems by algebraic techniques, already developed and used in the pseudo-SU(3) framework, one would be able to perform further complementary studies using the proxy-SU(3) model.

4 Conclusions

A new approximate SU(3) symmetry applicable in heavy deformed nuclei has been suggested [21,22], called the proxy-SU(3) scheme. In Ref. [28] a detailed numerical study will demonstrate the validity of the approximation, while in Refs. [25,26] some first applications of the method in predicting nuclear properties will be described.

References

1. J. P. Elliott, Collective motion in the nuclear shell model I. Classification schemes for states of mixed configurations, Proc. Roy. Soc. Ser. A **245**, 128(1958).
2. J. P. Elliott, Collective motion in the nuclear shell model II. The introduction of intrinsic wave-functions, Proc. Roy. Soc. Ser. A **245**, 562 (1958).
3. G. Rosensteel and D. J. Rowe, On the algebraic formulation of collective models III. The symplectic shell model of collective motion, Ann. Phys. (NY) **126**, 343 (1980).
4. I. Talmi, *Simple models of complex nuclei: The shell model and the interacting boson model* (Harwood, Chur, 1993).
5. F. Iachello and A. Arima, *The Interacting Boson Model* (Cambridge University Press, Cambridge, 1987).
6. A. Georgieva, P. Raychev, and R. Roussev, Rotational limit of the interacting two-vector-boson model, J. Phys. G: Nucl. Phys. **9**, 521 (1983).
7. C.-L. Wu, D. H. Feng, X.-G. Chen, J.-Q. Chen, and M. W. Guidry, Fermion dynamical symmetry model of nuclei: Basis, Hamiltonian, and symmetries, Phys. Rev. C **36**, 1157 (1987).
8. R. D. Ratna Raju, J. P. Draayer, and K. T. Hecht, Search for a coupling scheme in heavy deformed nuclei: The pseudo SU(3) model, Nucl. Phys. A **202**, 433 (1973).
9. J. P. Draayer, K. J. Weeks, and K. T. Hecht, Strength of the $Q_\pi \cdot Q_\nu$ interaction and the strong-coupled pseudo-SU(3) limit, Nucl. Phys. A **381**, 1 (1982).
10. J. P. Draayer and K. J. Weeks, Shell-model description of the low-energy structure of strongly deformed nuclei, Phys. Rev. Lett. **51**, 1422 (1983).
11. J. P. Draayer and K. J. Weeks, Towards a shell model description of the low-energy structure of deformed nuclei I. Even-even systems, Ann. Phys. (N.Y.) **156**, 41 (1984).
12. C. Bahri, J. P. Draayer, and S. A. Moszkowski, Pseudospin symmetry in nuclear physics, Phys. Rev. Lett. **68**, 2133 (1992).
13. A. L. Blokhin, C. Bahri, and J. P. Draayer, Origin of pseudospin symmetry, Phys. Rev. Lett. **74**, 4149 (1995).
14. J. N. Ginocchio, Pseudospin as a relativistic symmetry, Phys. Rev. Lett. **78**, 436 (1997).
15. A. P. Zuker, J. Retamosa, A. Poves, and E. Caurier, Spherical shell model description of rotational motion, Phys. Rev. C **52**, R1741 (1995).
16. A. P. Zuker, A. Poves, F. Nowacki, and S. M. Lenzi, Nilsson–SU(3) self-consistency in heavy N=Z nuclei, Phys. Rev. C **92**, 024320 (2015).
17. S. G. Nilsson, Binding states of individual nucleons in strongly deformed nuclei, Mat. Fys. Medd. K. Dan. Vidensk. Selsk. **29**, no. 16 (1955).
18. S. G. Nilsson and I. Ragnarsson, Shapes and Shells in Nuclear Structure (Cambridge University Press, Cambridge, 1995).
19. I. Ragnarsson, S. G. Nilsson, and R. K. Sheline, Shell structure in nuclei, Phys. Reports **45**, 1 (1978).
20. B. Mottelson, The Nilsson Model and Sven Gösta Nilsson, Phys. Scr. **T125** (2006) editorial.
21. D. Bonatsos, I. E. Assimakis, N. Minkov, A. Martinou, R. B. Cakirli, R. F. Casten, and K. Blaum, Proxy-SU(3) symmetry in heavy deformed nuclei, Phys. Rev. C (2017) accepted, arXiv 1706.02282 [nucl-th].
22. D. Bonatsos, I. E. Assimakis, N. Minkov, A. Martinou, S. Sarantopoulou, R. B. Cakirli, R. F. Casten, and K. Blaum, Analytic predictions for nuclear shapes, prolate dominance and the prolate-oblate shape transition in the proxy-SU(3) model, Phys. Rev. C (2017) accepted, arXiv 1706.02321 [nucl-th].
23. R. B. Cakirli, K. Blaum, and R. F. Casten, Indication of a mini-valence Wigner-like energy in heavy nuclei, Phys. Rev. C **82**, 061304(R) (2010).
24. D. Bonatsos, S. Karampagia, R. B. Cakirli, R. F. Casten, K. Blaum, and L. Amon Susam, Emergent collectivity in nuclei and enhanced proton-neutron interactions, Phys. Rev. C **88**, 054309 (2013).
25. D. Bonatsos. I. E. Assimakis, N. Minkov, A. Martinou, S. Sarantopoulou, R. B. Cakirli, R. F. Casten, and K. Blaum, Parameter-independent predictions for shape variables of heavy deformed nuclei in the proxy-SU(3) model, in the Proceedings of the 4th Workshop of the Hellenic Institute of Nuclear Physics (HINPw4), ed. A. Pakou, http://hinpw4.physics.uoi.gr
26. D. Bonatsos. I. E. Assimakis, N. Minkov, A. Martinou, S. Sarantopoulou, R. B. Cakirli, R. F. Casten, and K. Blaum, Prolate dominance and prolate-oblate shape transition in the proxy-SU(3) model, in the Proceedings of the 4th Workshop of the Hellenic Institute of Nuclear Physics (HINPw4), ed. A. Pakou, http://hinpw4.physics.uoi.gr
27. P. Cejnar and P. Stránský, Quantum phase transitions in the collective degrees of freedom: nuclei and other many-body systems, Phys. Scripta **91**, 083006 (2016).
28. D. Bonatsos. I. E. Assimakis, N. Minkov, A. Martinou, R. B. Cakirli, R. F. Casten, and K. Blaum, Proxy-SU(3) symmetry in heavy nuclei: Foundations, in the Proceedings of the 4th Workshop of the Hellenic Institute of Nuclear Physics (HINPw4), ed. A. Pakou, http://hinpw4.physics.uoi.gr
29. D. Bonatsos and A. Klein, Exact boson mappings for nuclear neutron (proton) shell-model algebras having SU(3) subalgebras, Ann. Phys. (NY) **169**, 61 (1986).

30. Y. Takahashi, SU(3) shell model in a deformed harmonic oscillator basis, Prog. Theor. Phys. **53**, 461 (1975).
31. G. Rosensteel and J. P. Draayer, Symmetry algebra of the anisotropic harmonic oscillator with commensurate frequencies, J. Phys. A: Math. Gen. **22**, 1323 (1989).
32. W. Nazarewicz and J. Dobaczewski, Dynamical symmetries, multiclustering, and octupole susceptibility in superdeformed and hyperdeformed nuclei, Phys. Rev. Lett. **68**, 154 (1992).
33. W. Nazarewicz, J. Dobaczewski, and P. Van Isacker, Shell model calculations at superdeformed shapes, AIP Conf. Proc. **259**, 30 (1992).
34. D. Bonatsos, C. Daskaloyannis, P. Kolokotronis, and D. Lenis, The symmetry algebra of the N-dimensional anisotropic quantum harmonic oscillator with rational ratios of frequencies and the Nilsson model, arXiv: hep-th/9411218.
35. K. Sugawara-Tanabe and A. Arima, New dynamical SU(3) symmetry in deformed nuclei, Nucl. Phys. A **619**, 88 (1997).
36. A. Arima, Elliott's SU(3) model and its developments in nuclear physics, J. Phys. G: Nucl. Part. Phys. **25**, 581 (1999).
37. H. A. Naqvi and J. P. Draayer, Shell-model operator for K-band splitting, Nucl. Phys. A **516**, 351 (1990).
38. G. Popa, J. G. Hirsch, and J. P. Draayer, Shell model description of normal parity bands in even-even heavy deformed nuclei, Phys. Rev. C **62**, 064311 (2000).
39. G. Popa, A. Georgieva, and J. P. Draayer, Systematics in the structure of low-lying, nonyrast bandhead configurations of strongly deformed nuclei, Phys. Rev. C **69**, 064307 (2004).
40. C. E. Vargas and J. G. Hirsch, Pushing the pseudo-SU(3) model towards its limits: Excited bands in even-even Dy isotopes, Phys. Rev. C **70**, 064320 (2004).
41. G. Popa and A. Georgieva, Description of heavy deformed nuclei within the pseudo-SU(3) shell model, J. Phys.: Conf. Ser. **403**, 012009 (2012).
42. C. E. Vargas, V. Velázquez, and S. Lerma, Microscopic study of neutron-rich dysprosium isotopes, Eur. Phys. J. A **49**, 4 (2013).
43. C. E. Vargas, V. Velázquez, S. Lerma-Hernández, and N. Bagatella-Flores, Electromagnetic properties in $^{160-170}$Dy nuclei: A microscopic description by the pseudo-SU(3) shell model, Eur. Phys. J. A **53**, 73 (2017).
44. H. A. Naqvi and J. P. Draayer, Shell-model operator for K_J-band splitting in odd-A nuclei, Nucl. Phys. A **536**, 297 (1992).
45. C. Vargas, J. G. Hirsch, T. Beuschel, and J. P. Draayer, Shell model description of normal parity bands in odd-mass heavy deformed nuclei, Phys. Rev. C **61**, 031301(R) (2000).
46. C. E. Vargas, J. G. Hirsch, and J. P. Draayer, Preudo SU(3) shell model: Normal parity bands in odd-mass nuclei, Nucl. Phys. A **673**, 219 (2000).
47. C. E. Vargas, J. G. Hirsch, and J. P. Draayer, Interband $B(E2)$ transition strengths in odd-mass heavy deformed nuclei, Phys. Rev. C **64**, 034306 (2001).
48. C. E. Vargas, J. G. Hirsch, and J. P. Draayer, Excited bands in odd-mass rare-earth nuclei, Phys. Rev. C **66**, 064309 (2002).
49. O. Castaños, J. P. Draayer, and Y. Leschber, Towards a shell-model description of the low-energy structure of deformed nuclei II. Electromagnetic properties of collective M1 bands, Ann. Phys. (N.Y.) **180**, 290 (1987).
50. T. Beuschel, J. P. Draayer, D. Rompf, and J. G. Hirsch, Microscopic description of the scissors mode and its fragmentation, Phys. Rev. C **57**, 1233 (1998).
51. D. Rompf, T. Beuschel, J. P. Draayer, W. Scheid, and J. G. Hirsch, Towards understanding magnetic dipole excitations in deformed nuclei: Phenomenology, Phys. Rev. C **57**, 1703 (1998).
52. J. P. Draayer, T. Beuschel, and J. G. Hirsch, M1 strengths in deformed nuclei, J. Phys. G: Nucl. Part. Phys. **25**, 605 (1999).
53. T. Beuschel, J. G. irsch, and J. P. Draayer, Scissors mode and the pseudo-SU(3) model, Phys. Rev. C **61**, 054307 (2000).
54. C. E. Vargas, J. G. Hirsch, and J. P. Draayer, Microscopic description of the scissors mode in odd-mass heavy deformed nuclei, Phys. Lett. B **551**, 98 (2003).
55. J. Dudek, W. Nazarewicz, Z. Szymanski, and G. A. Leander, Abundance and systematics of nuclear superdeformed states; Relation to the pseudospin and pseudo-SU(3) symmetries, Phys. Rev. Lett. **59**, 1405 (1987).
56. W. Nazarewicz, P. J. Twin, P. Fallon, and J. D. Garrett, Natural-parity states in superdeformed bands and pseudo SU(3) symmetry at extreme conditions, Phys. Rev. Lett. **64**, 1654 (1990).
57. O. Castaños, J. G. Hirsch, O. Civitarese, and P. O. Hess, Double-beta decay in the pseudo-SU(3) scheme, Nucl. Phys. A **571**, 276 (1994).
58. J. G. Hirsch, O. Castaños, P. O. Hess, and O. Civitarese, Double-beta decay of ^{100}Mo: The deformed limit, Phys. Rev. C **51**, 2252 (1995).
59. J. G. Hirsch, O. Castaños, P. O. Hess, and O. Civitarese, Double-beta decay to excited states in ^{150}Nd, Nucl. Phys. A **589**, 445 (1995).
60. J. G. Hirsch, O. Castaños, and P. O. Hess, Neutrinoless double beta decay in heavy deformed nuclei, Nucl. Phys. A **582**, 124 (1995).
61. V. E. Ceron and J. G. Hirsch, Double electron capture in ^{156}Dy, ^{162}Er and ^{168}Yb, Phys. Lett. B **547**, 1 (1999).
62. O. Castaños, M. Moshinsky, and C. Quesne, Transformation to pseudo-SU(3) in heavy deformed nuclei, Phys. Lett. B **277**, 238 (1992).
63. O. Castaños, V. Velázquez A., P. O. Hess, and J. G. Hirsch, Transformation to pseudo-spin-symmetry of a deformed Nilsson hamiltonian, Phys. Lell. B **321**, 303 (1994).

Proxy-SU(3) symmetry in heavy nuclei: Foundations

Dennis Bonatsos[1], I. E. Assimakis[1], N. Minkov[2], Andriana Martinou[1], R. B. Cakirli[3], R. F. Casten[4,5], and K. Blaum[6]

[1] Institute of Nuclear and Particle Physics, National Centre for Scientific Research "Demokritos", GR-15310 Aghia Paraskevi, Attiki, Greece
[2] Institute of Nuclear Research and Nuclear Energy, Bulgarian Academy of Sciences, 72 Tzarigrad Road, 1784 Sofia, Bulgaria
[3] Department of Physics, University of Istanbul, Istanbul, Turkey
[4] Wright Laboratory, Yale University, New Haven, Connecticut 06520, USA
[5] Facility for Rare Isotope Beams, 640 South Shaw Lane, Michigan State University, East Lansing, MI 48824 USA
[6] Max-Planck-Institut für Kernphysik, Saupfercheckweg 1, D-69117 Heidelberg, Germany

Abstract. An approximate SU(3) symmetry appears in heavy deformed even-even nuclei, by omitting the intruder Nilsson orbital of highest total angular momentum and replacing the rest of the intruder orbitals by the orbitals which have escaped to the next lower major shell. The approximation is based on the fact that there is a one-to-one correspondence between the orbitals of the two sets, based on pairs of orbitals having identical quantum numbers of orbital angular momentum, spin, and total angular momentum. The accuracy of the approximation is tested through calculations in the framework of the Nilsson model in the asymptotic limit of large deformations, focusing attention on the changes in selection rules and in avoided crossings caused by the opposite parity of the proxies with respect to the substituted orbitals.

PACS. 21.60.Fw Models based on group theory – 21.60.Ev Collective models

1 Introduction

The proxy-SU(3) scheme [1,2], already described in Ref. [3], is a new approximate scheme applicable in medium-mass and heavy deformed nuclei, able to provide predictions for various nuclear properties, as it will be shown in Refs. [4,5]. In this contribution we are going to justify the relevant approximations by applying the proxy-SU(3) assumptions to the Nilsson model [6,7].

2 The Nilsson model

The Nilsson Hamiltonian [6,7] contains a harmonic oscillator with cylindrical symmetry,

$$H_{osc} = \frac{\mathbf{p}^2}{2M} + \frac{1}{2}M(\omega_z^2 z^2 + \omega_\perp^2 (x^2+y^2)), \qquad (1)$$

where M is the nuclear mass, $\mathbf{p}$ is the momentum, and the rotational frequencies ω_z and $\omega_\perp$ are related to the deformation parameter ϵ by

$$\omega_z = \omega_0 \left(1 - \frac{2}{3}\epsilon\right), \qquad \omega_\perp = \omega_0 \left(1 + \frac{1}{3}\epsilon\right), \qquad (2)$$

leading to

$$\epsilon = \frac{\omega_\perp - \omega_z}{\omega_0}, \qquad (3)$$

with $\epsilon > 0$ corresponding to prolate shapes and $\epsilon < 0$ corresponding to oblate shapes. In addition it contains a spin-orbit term and an angular momentum squared term, the total Hamiltonian having the form

$$H = H_{osc} + v_{ls}\hbar\omega_0(\mathbf{l}\cdot\mathbf{s}) + v_{ll}\hbar\omega_0(\mathbf{l}^2 - \langle \mathbf{l}^2\rangle_N), \qquad (4)$$

where $\mathbf{l}$ is the angular momentum, $\mathbf{s}$ is the spin,

$$\langle \mathbf{l}^2\rangle_N = \frac{1}{2}N(N+3) \qquad (5)$$

is the average of the square of the angular momentum $\mathbf{l}$ within the Nth oscillator shell, and v_{ls} and v_{ll} are constants determined from the available data on intrinsic nuclear spectra [8], their values being given in Table 5-1 of Ref. [8]. The eigenvalues of H_{osc} are

$$E_{osc} = \hbar\omega_0 \left(N + \frac{3}{2} - \frac{1}{3}\epsilon(3n_z - N)\right). \qquad (6)$$

3 Calculation of matrix elements

In order to simplify the calculation of matrix elements, one can choose a more convenient basis. Using the creation and annihilation operators $a_x^\dagger$, a_x, $a_y^\dagger$, a_y for the quanta of the harmonic oscillator in the Cartesian coordinates x and y, one can define creation and annihilation operators [7,9]

$$R^+ = \frac{1}{\sqrt{2}}(a_x^\dagger + i a_y^\dagger), \qquad R = \frac{1}{\sqrt{2}}(a_x - i a_y), \qquad (7)$$

$$S^+ = \frac{1}{\sqrt{2}}(a_x^\dagger - i a_y^\dagger), \qquad S = \frac{1}{\sqrt{2}}(a_x + i a_y). \quad (8)$$

These operators satisfy the commutation relations

$$[R, R^\dagger] = [S, S^\dagger] = 1. \quad (9)$$

In this way one goes over to a new basis, $|n_z r s \Sigma\rangle$, where r (s) is the number of quanta related to the harmonic oscillator formed by $R^\dagger$ and R ($S^\dagger$ and S). The following relations hold

$$n_\perp = r + s = N - n_z, \qquad \Lambda = r - s, \quad (10)$$

where $n_\perp$ is the number of quanta perpendicular to the z-axis.

It is then a straightforward task, described in detail in Ref. [7], to calculate the matrix elements of the $\mathbf{l}\cdot\mathbf{s}$ and $\mathbf{l}^2$ operators in the new basis.

The spin-orbit term, $\mathbf{l}\cdot\mathbf{s}$, has diagonal matrix elements

$$\langle n_z r s \Sigma | \mathbf{l}\cdot\mathbf{s} | n_z r s \Sigma\rangle = (r-s)\Sigma = \Lambda\Sigma, \quad (11)$$

as well as non-diagonal matrix elements

$$\langle n_z-1, r+1, s, \Sigma-1 | \mathbf{l}\cdot\mathbf{s} | n_z r s \Sigma\rangle = -\frac{1}{\sqrt{2}}\sqrt{n_z(r+1)}, \quad (12)$$

$$\langle n_z+1, r, s-1, \Sigma-1 | \mathbf{l}\cdot\mathbf{s} | n_z r s \Sigma\rangle = \frac{1}{\sqrt{2}}\sqrt{(n_z+1)s}, \quad (13)$$

$$\langle n_z+1, r-1, s, \Sigma+1 | \mathbf{l}\cdot\mathbf{s} | n_z r s \Sigma\rangle = -\frac{1}{\sqrt{2}}\sqrt{(n_z+1)r}, \quad (14)$$

$$\langle n_z-1, r, s+1, \Sigma+1 | \mathbf{l}\cdot\mathbf{s} | n_z r s \Sigma\rangle = \frac{1}{\sqrt{2}}\sqrt{n_z(s+1)}. \quad (15)$$

The orbital angular momentum term, $\mathbf{l}^2$, has diagonal matrix elements

$$\langle n_z r s \Sigma | \mathbf{l}^2 | n_z r s \Sigma\rangle = 2n_z(r+s+1) + (r+s) + (r-s)^2, \quad (16)$$

as well as non-diagonal matrix elements

$$\langle n_z+2, r-1, s-1, \Sigma | \mathbf{l}^2 | n_z r s \Sigma\rangle = -2\sqrt{(n_z+2)(n_z+1)rs}, \quad (17)$$

$$\langle n_z-2, r+1, s+1, \Sigma | \mathbf{l}^2 | n_z r s \Sigma\rangle = -2\sqrt{(n_z-1)n_z(r+1)(s+1)}. \quad (18)$$

4 Numerical results

Numerical results for the matrix elements of $\mathbf{l}\cdot\mathbf{s}$ for the 126-184 and sdgi shells are given in Table I, and those for the matrix elements of $\mathbf{l}^2$ for the same shells are given in Table II. Furthermore, numerical results for the full Hamiltonian for $\epsilon = 0.3$ for the 126-184 and sdgi shells are given in Table III, while Nilsson-like diagrams involving either just the diagonal terms of the Hamiltonian, or obtained through the diagonalization of the full Hamiltonian, are plotted for the same shells in Fig. 1. Many comments are in place.

In each of the Tables I, II, III, the upper table corresponds to the original Nilsson model 126-184 shell, while the lower table represents the proxy-SU(3) approximation to it, which is an sdgi shell. The lower table has one row and one column less than the upper table, since the orbital with the highest angular momentum in the 126-184 shell, 15/2[707], has no counterpart in the proxy-SU(3) sdgi shell. All tables are symmetric, thus only the upper half is shown.

All tables are divided into four blocks. The upper left block involves matrix elements among the normal parity orbitals, i.e. the orbitals which belong to the sdgi shell and remain in the 126-184 shell after the defection of the $1i_{13/2}$ orbital to the major shell below. Therefore the upper left blocks of the 126-184 and sdgi tables are identical.

The lower right block involves matrix elements among the abnormal orbitals, members of the $1j_{15/2}$ orbital which has invaded the sdgi shell coming from the major shell above. The 126-184 and sdgi results are either identical, or very similar, due to the fact that during the proxy-SU(3) approximation all angular momentum projections (orbital angular momentum, spin, total angular momentum) remain unchanged.

The upper right block of the 126-184 tables contains only vanishing matrix elements, since it connencts levels of opposite parity, namely positive parity sdgi orbitals to negative parity $1j_{15/2}$ orbitals. In the upper right block of the sdgi tables, though, a few non-vanishing matrix elements appear, connecting the original positive parity sdgi orbitals to the proxies of the $1j_{15/2}$ orbitals, which are positive parity $1i_{13/2}$ orbitals. These extra non-vanishing matrix elements represent the "damage" caused by the proxy-SU(3) approximation, i.e., by the replacement of the $1j_{15/2}$ orbitals (except the 15/2[707] one) by their $1i_{13/2}$ proxies.

The size of these extra non-vanishing matrix elements is comparable to the magnitude of the diagonal matrix elements in the case of the $\mathbf{l}\cdot\mathbf{s}$ and $\mathbf{l}^2$ operators, as one can see in Tables I and II. However, as one can see in Table III, the extra non-vanishing matrix elements are much smaller (by at least one order of magnitude) than the diagonal matrix elements. The reason behind this difference is the small values of the v_{ls} and v_{ll} coefficients (-0.127 and -0.0206 respectively, as given in Table 5-1 of Ref. [8]), by which the matrix elements of $\mathbf{l}\cdot\mathbf{s}$ and $\mathbf{l}^2$ are multiplied before entering Table III.

The smallness of the extra non-vanishing matrix elements means that the diagonalization of the Nilsson Hamiltonian for various values of the deformation ϵ will yield very similar results for the 126-184 and proxy-SU(3) sdgi shells, as seen in Fig. 1, indicating that the Nilsson diagrams are very little affected by these extra non-vanishing matrix elements and thus proving that the proxy-SU(3) approximation is a good one.

In a similar way one can see that good results are also obtained for the 28-50, 50-82, and 82-126 shells in comparison to their pf, sdg, and pfh proxy-SU(3) counterparts [1].

5 Conclusions

By applying the proxy-SU(3) assumptions to the Nilsson model, we prove that the Nilsson diagrams of the 126-184 shell and of its proxy-SU(3) sdgi counterpart are very similar, thus justifying the use of the proxy-SU(3) scheme, some applications of which for the calculation of nuclear properties will be discussed in Refs. [4, 5].

References

1. D. Bonatsos, I. E. Assimakis, N. Minkov, A. Martinou, R. B. Cakirli, R. F. Casten, and K. Blaum, Proxy-SU(3) symmetry in heavy deformed nuclei, Phys. Rev. C (2017) accepted, arXiv 1706.02282 [nucl-th].
2. D. Bonatsos, I. E. Assimakis, N. Minkov, A. Martinou, S. Sarantopoulou, R. B. Cakirli, R. F. Casten, and K. Blaum, Analytic predictions for nuclear shapes, prolate dominance and the prolate-oblate shape transition in the proxy-SU(3) model, Phys. Rev. C (2017) accepted, arXiv 1706.02321 [nucl-th].
3. D. Bonatsos. I. E. Assimakis, N. Minkov, A. Martinou, R. B. Cakirli, R. F. Casten, and K. Blaum, A new symmetry for heavy nuclei: Proxy-SU(3), in the Proceedings of the 4th Workshop of the Hellenic Institute of Nuclear Physics (HINPw4), ed. A. Pakou, http://hinpw4.physics.uoi.gr
4. D. Bonatsos. I. E. Assimakis, N. Minkov, A. Martinou, S. Sarantopoulou, R. B. Cakirli, R. F. Casten, and K. Blaum, Parameter-independent predictions for shape variables of heavy deformed nuclei in the proxy-SU(3) model, in the Proceedings of the 4th Workshop of the Hellenic Institute of Nuclear Physics (HINPw4), ed. A. Pakou, http://hinpw4.physics.uoi.gr
5. D. Bonatsos. I. E. Assimakis, N. Minkov, A. Martinou, S. Sarantopoulou, R. B. Cakirli, R. F. Casten, and K. Blaum, Prolate dominance and prolate-oblate shape transition in the proxy-SU(3) model, in the Proceedings of the 4th Workshop of the Hellenic Institute of Nuclear Physics (HINPw4), ed. A. Pakou, http://hinpw4.physics.uoi.gr
6. S. G. Nilsson, Binding states of individual nucleons in strongly deformed nuclei, Mat. Fys. Medd. K. Dan. Vidensk. Selsk. **29**, no. 16 (1955).
7. S. G. Nilsson and I. Ragnarsson, Shapes and Shells in Nuclear Structure (Cambridge University Press, Cambridge, 1995).
8. A. Bohr and B. R. Mottelson, Nuclear Structure, Vol. II: Nuclear Deformations (Benjamin, New York, 1975).
9. B. R. Mottelson and S. G. Nilsson, The shape of the nuclear photo-resonance in deformed nuclei, Nucl. Phys. **13**, 281 (1959).

TABLE I: $l \cdot s$ matrix elements for Nilsson orbitals in the 126–184 shell (upper part) and in the full sdgi shell (lower part).

	$\frac{1}{2}$[611]	$\frac{1}{2}$[600]	$\frac{3}{2}$[602]	$\frac{1}{2}$[631]	$\frac{3}{2}$[622]	$\frac{5}{2}$[613]	$\frac{1}{2}$[620]	$\frac{3}{2}$[611]	$\frac{5}{2}$[602]	$\frac{7}{2}$[604]	$\frac{1}{2}$[651]	$\frac{3}{2}$[642]	$\frac{5}{2}$[633]	$\frac{7}{2}$[624]	$\frac{9}{2}$[615]	$\frac{1}{2}$[640]	$\frac{3}{2}$[631]	$\frac{5}{2}$[622]	$\frac{7}{2}$[613]	$\frac{9}{2}$[604]	$\frac{11}{2}$[606]	$\frac{1}{2}$[770]	$\frac{3}{2}$[761]	$\frac{5}{2}$[752]	$\frac{7}{2}$[743]	$\frac{9}{2}$[734]	$\frac{11}{2}$[725]	$\frac{13}{2}$[716]	$\frac{15}{2}$[707]
1/2[611]	−0.5	1.225	0	0	0	0	−1.732	0	0	0	0	0	0	0	0	0	0	0	0	0	0	0	0	0	0	0	0	0	0
1/2[600]		0	0	0	0	0	0	0	0	0	0	0	0	0	0	0	0	0	0	0	0	0	0	0	0	0	0	0	0
3/2[602]			−1	0	0	0	0	−1.414	0	0	0	0	0	0	0	0	0	0	0	0	0	0	0	0	0	0	0	0	0
1/2[631]				−0.5	0	0	1.732	0	0	0	0	0	0	0	0	−2	0	0	0	0	0	0	0	0	0	0	0	0	0
3/2[622]					−1	0	0	1.414	0	0	0	0	0	0	0	0	−2.121	0	0	0	0	0	0	0	0	0	0	0	0
5/2[613]						−1.5	0	0	1	0	0	0	0	0	0	0	0	−2	0	0	0	0	0	0	0	0	0	0	0
1/2[620]							0	0	0	0	0	0	0	0	0	0	0	0	0	0	0	0	0	0	0	0	0	0	0
3/2[611]								0.5	0	0	0	0	0	0	0	0	0	0	0	0	0	0	0	0	0	0	0	0	0
5/2[602]									1	0	0	0	0	0	0	0	0	0	0	0	0	0	0	0	0	0	0	0	0
7/2[604]										−2	0	0	0	0	0	0	0	0	−1.581	0	0	0	0	0	0	0	0	0	0
1/2[651]											−0.5	0	0	0	0	1.581	0	0	0	0	0	0	0	0	0	0	0	0	0
3/2[642]												−1	0	0	0	0	1.414	0	0	0	0	0	0	0	0	0	0	0	0
5/2[633]													−1.5	0	0	0	0	1.225	0	0	0	0	0	0	0	0	0	0	0
7/2[624]														−2	0	0	0	0	1	0	0	0	0	0	0	0	0	0	0
9/2[615]															−2.5	0	0	0	0	0.707	0	0	0	0	0	0	0	0	0
1/2[640]																0	0	0	0	0	0	0	0	0	0	0	0	0	0
3/2[631]																	0.5	0	0	0	0	0	0	0	0	0	0	0	0
5/2[622]																		1	0	0	0	0	0	0	0	0	0	0	0
7/2[613]																			1.5	0	0	0	0	0	0	0	0	0	0
9/2[604]																				2	0	0	0	0	0	0	0	0	0
11/2[606]																					−3	0	0	0	0	0	0	0	0
1/2[770]																						0	0	0	0	0	0	0	0
3/2[761]																							0.5	0	0	0	0	0	0
5/2[752]																								1	0	0	0	0	0
7/2[743]																									1.5	0	0	0	0
9/2[734]																										2	0	0	0
11/2[725]																											2.5	0	0
13/2[716]																												3	0
15/2[707]																													3.5

	$\frac{1}{2}$[611]	$\frac{1}{2}$[600]	$\frac{3}{2}$[602]	$\frac{1}{2}$[631]	$\frac{3}{2}$[622]	$\frac{5}{2}$[613]	$\frac{1}{2}$[620]	$\frac{3}{2}$[611]	$\frac{5}{2}$[602]	$\frac{7}{2}$[604]	$\frac{1}{2}$[651]	$\frac{3}{2}$[642]	$\frac{5}{2}$[633]	$\frac{7}{2}$[624]	$\frac{9}{2}$[615]	$\frac{1}{2}$[640]	$\frac{3}{2}$[631]	$\frac{5}{2}$[622]	$\frac{7}{2}$[613]	$\frac{9}{2}$[604]	$\frac{11}{2}$[606]	$\frac{1}{2}$[660]	$\frac{3}{2}$[651]	$\frac{5}{2}$[642]	$\frac{7}{2}$[633]	$\frac{9}{2}$[624]	$\frac{11}{2}$[615]	$\frac{13}{2}$[606]
1/2[611]	−0.5	1.225	0	0	0	0	−1.732	0	0	0	0	0	0	0	0	0	0	0	0	0	0	0	0	0	0	0	0	0
1/2[600]		0	0	0	0	0	0	0	0	0	0	0	0	0	0	0	0	0	0	0	0	0	0	0	0	0	0	0
3/2[602]			−1	0	0	0	0	−1.414	0	0	0	0	0	0	0	0	0	0	0	0	0	0	0	0	0	0	0	0
1/2[631]				−0.5	0	0	1.732	0	0	0	0	0	0	0	0	−2	0	0	0	0	0	0	0	0	0	0	0	0
3/2[622]					−1	0	0	1.414	0	0	0	0	0	0	0	0	−2.121	0	0	0	0	0	0	0	0	0	0	0
5/2[613]						−1.5	0	0	1	0	0	0	0	0	0	0	0	−2	0	0	0	0	0	0	0	0	0	0
1/2[620]							0	0	0	0	0	0	0	0	0	0	0	0	0	0	0	0	0	0	0	0	0	0
3/2[611]								0.5	0	0	0	0	0	0	0	0	0	0	0	0	0	0	0	0	0	0	0	0
5/2[602]									1	0	0	0	0	0	0	0	0	0	0	0	0	0	0	0	0	0	0	0
7/2[604]										−2	0	0	0	0	0	0	0	0	−1.581	0	0	0	0	0	0	0	0	0
1/2[651]											−0.5	0	0	0	0	1.581	0	0	0	0	0	**−1.732**	0	0	0	0	0	0
3/2[642]												−1	0	0	0	0	1.414	0	0	0	0	0	**−2.236**	0	0	0	0	0
5/2[633]													−1.5	0	0	0	0	1.225	0	0	0	0	0	**−2.450**	0	0	0	0
7/2[624]														−2	0	0	0	0	1	0	0	0	0	0	**−2.450**	0	0	0
9/2[615]															−2.5	0	0	0	0	0.707	0	0	0	0	0	**−2.236**	0	0
1/2[640]																0	0	0	0	0	0	0	0	0	0	0	0	0
3/2[631]																	0.5	0	0	0	0	0	0	0	0	0	0	0
5/2[622]																		1	0	0	0	0	0	0	0	0	0	0
7/2[613]																			1.5	0	0	0	0	0	0	0	0	0
9/2[604]																				2	0	0	0	0	0	0	0	0
11/2[606]																					−3	0	0	0	0	0	**−1.732**	0
1/2[660]																						0	0	0	0	0	0	0
3/2[651]																							0.5	0	0	0	0	0
5/2[642]																								1	0	0	0	0
7/2[633]																									1.5	0	0	0
9/2[624]																										2	0	0
11/2[615]																											2.5	0
13/2[606]																												3

TABLE II: l^2 matrix elements for Nilsson orbitals in the 126–184 shell (upper part) and in the full sdgi shell (lower part).

	$\frac{1}{2}$[611]	$\frac{1}{2}$[600]	$\frac{3}{2}$[602]	$\frac{1}{2}$[631]	$\frac{3}{2}$[622]	$\frac{5}{2}$[613]	$\frac{1}{2}$[620]	$\frac{3}{2}$[611]	$\frac{5}{2}$[602]	$\frac{7}{2}$[604]	$\frac{1}{2}$[651]	$\frac{3}{2}$[642]	$\frac{5}{2}$[633]	$\frac{7}{2}$[624]	$\frac{9}{2}$[615]	$\frac{1}{2}$[640]	$\frac{3}{2}$[631]	$\frac{5}{2}$[622]	$\frac{7}{2}$[613]	$\frac{9}{2}$[604]	$\frac{11}{2}$[606]	$\frac{1}{2}$[770]	$\frac{3}{2}$[761]	$\frac{5}{2}$[752]	$\frac{7}{2}$[743]	$\frac{9}{2}$[734]	$\frac{11}{2}$[725]	$\frac{13}{2}$[716]	$\frac{15}{2}$[707]
1/2[611]	18	0	0	−12	0	0	0	0	0	0	0	0	0	0	0	0	0	0	0	0	0	0	0	0	0	0	0	0	0
1/2[600]		6	0	0	0	0	−8.485	0	0	0	0	0	0	0	0	0	0	0	0	0	0	0	0	0	0	0	0	0	0
3/2[602]			10	0	0	0	0	0	0	0	0	0	0	0	0	0	0	0	0	0	0	0	0	0	0	0	0	0	0
1/2[631]				28	0	0	0	0	0	0	−12.649	0	0	0	0	0	0	0	0	0	0	0	0	0	0	0	0	0	0
3/2[622]					28	0	0	0	0	0	0	0	0	0	0	0	0	0	0	0	0	0	0	0	0	0	0	0	0
5/2[613]						26	0	0	0	0	0	0	−9.798	0	0	0	0	0	0	0	0	0	0	0	0	0	0	0	0
1/2[620]							24	0	0	0	0	0	0	0	0	−13.856	0	0	0	0	0	0	0	0	0	0	0	0	0
3/2[611]								18	0	0	0	0	0	0	0	0	−12	0	0	0	0	0	0	0	0	0	0	0	0
5/2[602]									10	0	0	0	0	0	0	0	0	−8	0	0	0	0	0	0	0	0	0	0	0
7/2[604]										22	0	0	0	−6.325	0	0	0	0	0	0	0	0	0	0	0	0	0	0	0
1/2[651]											22	0	0	0	0	0	0	0	0	0	0	0	0	0	0	0	0	0	0
3/2[642]												30	0	0	0	0	0	0	0	0	0	0	0	0	0	0	0	0	0
5/2[633]													36	0	0	0	0	0	0	0	0	0	0	0	0	0	0	0	0
7/2[624]														40	0	0	0	0	1	0	0	0	0	0	0	0	0	0	0
9/2[615]															42	0	0	0	0	0	0	0	0	0	0	0	0	0	0
1/2[640]																26	0	0	0	0	0	0	0	0	0	0	0	0	0
3/2[631]																	28	0	0	0	0	0	0	0	0	0	0	0	0
5/2[622]																		28	0	0	0	0	0	0	0	0	0	0	0
7/2[613]																			26	0	0	0	0	0	0	0	0	0	0
9/2[604]																				22	0	0	0	0	0	0	0	0	0
11/2[606]																					42	0	0	0	0	0	0	0	0
1/2[770]																						14	0	0	0	0	0	0	0
3/2[761]																							26	0	0	0	0	0	0
5/2[752]																								36	0	0	0	0	0
7/2[743]																									44	0	0	0	0
9/2[734]																										50	0	0	0
11/2[725]																											54	0	0
13/2[716]																												56	0
15/2[707]																													56

	$\frac{1}{2}$[611]	$\frac{1}{2}$[600]	$\frac{3}{2}$[602]	$\frac{1}{2}$[631]	$\frac{3}{2}$[622]	$\frac{5}{2}$[613]	$\frac{1}{2}$[620]	$\frac{3}{2}$[611]	$\frac{5}{2}$[602]	$\frac{7}{2}$[604]	$\frac{1}{2}$[651]	$\frac{3}{2}$[642]	$\frac{5}{2}$[633]	$\frac{7}{2}$[624]	$\frac{9}{2}$[615]	$\frac{1}{2}$[640]	$\frac{3}{2}$[631]	$\frac{5}{2}$[622]	$\frac{7}{2}$[613]	$\frac{9}{2}$[604]	$\frac{11}{2}$[606]	$\frac{1}{2}$[660]	$\frac{3}{2}$[651]	$\frac{5}{2}$[642]	$\frac{7}{2}$[633]	$\frac{9}{2}$[624]	$\frac{11}{2}$[615]	$\frac{13}{2}$[606]
1/2[611]	18	0	0	−12	0	0	0	0	0	0	0	0	0	0	0	0	0	0	0	0	0	0	0	0	0	0	0	0
1/2[600]		6	0	0	0	0	−8.485	0	0	0	0	0	0	0	0	0	0	0	0	0	0	0	0	0	0	0	0	0
3/2[602]			10	0	0	0	0	0	0	0	0	0	0	0	0	0	0	0	0	0	0	0	0	0	0	0	0	0
1/2[631]				28	0	0	0	0	0	0	−12.649	0	0	0	0	0	0	0	0	0	0	0	0	0	0	0	0	0
3/2[622]					28	0	0	0	0	0	0	0	0	0	0	0	0	0	0	0	0	0	0	0	0	0	0	0
5/2[613]						26	0	0	0	0	0	0	−9.798	0	0	0	0	0	0	0	0	0	0	0	0	0	0	0
1/2[620]							24	0	0	0	0	0	0	0	0	−13.856	0	0	0	0	0	0	0	0	0	0	0	0
3/2[611]								18	0	0	0	0	0	0	0	0	−12	0	0	0	0	0	0	0	0	0	0	0
5/2[602]									10	0	0	0	0	0	0	0	0	−8	0	0	0	0	0	0	0	0	0	0
7/2[604]										22	0	0	0	−6.325	0	0	0	0	0	0	0	0	0	0	0	0	0	0
1/2[651]											22	0	0	0	0	0	0	0	0	0	0	0	0	0	0	0	0	0
3/2[642]												30	0	0	0	0	0	0	0	0	0	0	0	0	0	0	0	0
5/2[633]													36	0	0	0	0	0	0	0	0	0	0	0	0	0	0	0
7/2[624]														40	0	0	0	0	1	0	0	0	0	0	0	0	0	0
9/2[615]															42	0	0	0	0	0	0	0	0	0	0	0	0	0
1/2[640]																26	0	0	0	0	0	**−10.955**	0	0	0	0	0	0
3/2[631]																	28	0	0	0	0	0	**−12.649**	0	0	0	0	0
5/2[622]																		28	0	0	0	0	0	**−12**	0	0	0	0
7/2[613]																			26	0	0	0	0	0	**−9.798**	0	0	0
9/2[604]																				22	0	0	0	0	0	**−6.324**	0	0
11/2[606]																					42	0	0	0	0	0	0	0
1/2[660]																						**12**	0	0	0	0	0	0
3/2[651]																							**22**	0	0	0	0	0
5/2[642]																								**30**	0	0	0	0
7/2[633]																									**36**	0	0	0
9/2[624]																										**40**	0	0
11/2[615]																											**42**	0
13/2[606]																												**42**

TABLE III: H matrix elements for $\epsilon = 0.3$ for Nilsson orbitals in the 126–184 shell (upper part) and in the full sdgi shell (lower part).

	$\frac{1}{2}$[611]	$\frac{1}{2}$[600]	$\frac{3}{2}$[602]	$\frac{1}{2}$[631]	$\frac{3}{2}$[622]	$\frac{5}{2}$[613]	$\frac{1}{2}$[620]	$\frac{3}{2}$[611]	$\frac{5}{2}$[602]	$\frac{7}{2}$[604]	$\frac{1}{2}$[651]	$\frac{3}{2}$[642]	$\frac{5}{2}$[633]	$\frac{7}{2}$[624]	$\frac{9}{2}$[615]	$\frac{1}{2}$[640]	$\frac{3}{2}$[631]	$\frac{5}{2}$[622]	$\frac{7}{2}$[613]	$\frac{9}{2}$[604]	$\frac{11}{2}$[606]	$\frac{1}{2}$[770]	$\frac{3}{2}$[761]	$\frac{5}{2}$[752]	$\frac{7}{2}$[743]	$\frac{9}{2}$[734]	$\frac{11}{2}$[725]	$\frac{13}{2}$[716]	$\frac{15}{2}$[707]
1/2[611]	8.05	−0.16	0	0.25	0	0	0.22	0	0	0	0	0	0	0	0	0	0	0	0	0	0	0	0	0	0	0	0	0	0
1/2[600]		8.53	0	0	0	0	0.17	0	0	0	0	0	0	0	0	0	0	0	0	0	0	0	0	0	0	0	0	0	0
3/2[602]			8.58	0	0	0	0	0.18	0	0	0	0	0	0	0	0	0	0	0	0	0	0	0	0	0	0	0	0	0
1/2[631]				7.24	0	0	−0.22	0	0	0	0.26	0	0	0	0	0.25	0	0	0	0	0	0	0	0	0	0	0	0	0
3/2[622]					7.61	0	0	−0.18	0	0	0	0	0	0	0	0	0.27	0	0	0	0	0	0	0	0	0	0	0	0
5/2[613]						8.01	0	0	−0.13	0	0	0	0.20	0	0	0	0	0.25	0	0	0	0	0	0	0	0	0	0	0
1/2[620]							7.56	0	0	0	0	0	0	0	0	0.29	0	0	0	0	0	0	0	0	0	0	0	0	0
3/2[611]								7.92	0	0	0	0	0	0	0	0	0.25	0	0	0	0	0	0	0	0	0	0	0	0
5/2[602]									8.32	0	0	0	0	0	0	0	0	0.16	0	0	0	0	0	0	0	0	0	0	0
7/2[604]										8.46	0	0	0	0.13	0	0	0	0	0.20	0	0	0	0	0	0	0	0	0	0
1/2[651]											6.77	0	0	0	0	−0.20	0	0	0	0	0	0	0	0	0	0	0	0	0
3/2[642]												6.97	0	0	0	0	−0.18	0	0	0	0	0	0	0	0	0	0	0	0
5/2[633]													7.21	0	0	0	0	−0.16	0	0	0	0	0	0	0	0	0	0	0
7/2[624]														7.49	0	0	0	0	−0.13	0	0	0	0	0	0	0	0	0	0
9/2[615]															7.81	0	0	0	0	−0.09	0	0	0	0	0	0	0	0	0
1/2[640]																6.92	0	0	0	0	0	0	0	0	0	0	0	0	0
3/2[631]																	7.12	0	0	0	0	0	0	0	0	0	0	0	0
5/2[622]																		7.35	0	0	0	0	0	0	0	0	0	0	0
7/2[613]																			7.63	0	0	0	0	0	0	0	0	0	0
9/2[604]																				7.95	0	0	0	0	0	0	0	0	0
11/2[606]																					8.17	0	0	0	0	0	0	0	0
1/2[770]																						7.53	0	0	0	0	0	0	0
3/2[761]																							7.52	0	0	0	0	0	0
5/2[752]																								7.55	0	0	0	0	0
7/2[743]																									7.62	0	0	0	0
9/2[734]																										7.74	0	0	0
11/2[725]																											7.89	0	0
13/2[716]																												8.089	0
15/2[707]																													8.32

	$\frac{1}{2}$[611]	$\frac{1}{2}$[600]	$\frac{3}{2}$[602]	$\frac{1}{2}$[631]	$\frac{3}{2}$[622]	$\frac{5}{2}$[613]	$\frac{1}{2}$[620]	$\frac{3}{2}$[611]	$\frac{5}{2}$[602]	$\frac{7}{2}$[604]	$\frac{1}{2}$[651]	$\frac{3}{2}$[642]	$\frac{5}{2}$[633]	$\frac{7}{2}$[624]	$\frac{9}{2}$[615]	$\frac{1}{2}$[640]	$\frac{3}{2}$[631]	$\frac{5}{2}$[622]	$\frac{7}{2}$[613]	$\frac{9}{2}$[604]	$\frac{11}{2}$[606]	$\frac{1}{2}$[660]	$\frac{3}{2}$[651]	$\frac{5}{2}$[642]	$\frac{7}{2}$[633]	$\frac{9}{2}$[624]	$\frac{11}{2}$[615]	$\frac{13}{2}$[606]
1/2[611]	8.05	−0.16	0	0.25	0	0	0.22	0	0	0	0	0	0	0	0	0	0	0	0	0	0	0	0	0	0	0	0	0
1/2[600]		8.53	0	0	0	0	0.17	0	0	0	0	0	0	0	0	0	0	0	0	0	0	0	0	0	0	0	0	0
3/2[602]			8.58	0	0	0	0	0.18	0	0	0	0	0	0	0	0	0	0	0	0	0	0	0	0	0	0	0	0
1/2[631]				7.24	0	0	−0.22	0	0	0	0.26	0	0	0	0	0.25	0	0	0	0	0	0	0	0	0	0	0	0
3/2[622]					7.61	0	0	−0.18	0	0	0	0	0	0	0	0	0.27	0	0	0	0	0	0	0	0	0	0	0
5/2[613]						8.01	0	0	−0.13	0	0	0	0.20	0	0	0	0	0.25	0	0	0	0	0	0	0	0	0	0
1/2[620]							7.56	0	0	0	0	0	0	0	0	0.29	0	0	0	0	0	0	0	0	0	0	0	0
3/2[611]								7.92	0	0	0	0	0	0	0	0	0.25	0	0	0	0	0	0	0	0	0	0	0
5/2[602]									8.32	0	0	0	0	0	0	0	0	0.16	0	0	0	0	0	0	0	0	0	0
7/2[604]										8.46	0	0	0	0.13	0	0	0	0	0.20	0	0	0	0	0	0	0	0	0
1/2[651]											6.77	0	0	0	0	−0.20	0	0	0	0	0	**0.22**	0	0	0	0	0	0
3/2[642]												6.97	0	0	0	0	−0.18	0	0	0	0	0	**0.28**	0	0	0	0	0
5/2[633]													7.21	0	0	0	0	−0.16	0	0	0	0	0	**0.31**	0	0	0	0
7/2[624]														7.49	0	0	0	0	−0.13	0	0	0	0	0	**0.31**	0	0	0
9/2[615]															7.81	0	0	0	0	−0.09	0	0	0	0	0	**0.28**	0	0
1/2[640]																6.92	0	0	0	0	0	**0.23**	0	0	0	0	0	0
3/2[631]																	7.12	0	0	0	0	0	**0.26**	0	0	0	0	0
5/2[622]																		7.35	0	0	0	0	0	**0.25**	0	0	0	0
7/2[613]																			7.63	0	0	0	0	0	**0.20**	0	0	0
9/2[604]																				7.95	0	0	0	0	0	**0.13**	0	0
11/2[606]																					8.17	0	0	0	0	0	**0.22**	0
1/2[660]																						**7.40**	0	0	0	0	0	0
3/2[651]																							**7.44**	0	0	0	0	0
5/2[642]																								**7.51**	0	0	0	0
7/2[633]																									**7.62**	0	0	0
9/2[624]																										**7.78**	0	0
11/2[615]																											**7.97**	0
13/2[606]																												**8.21**

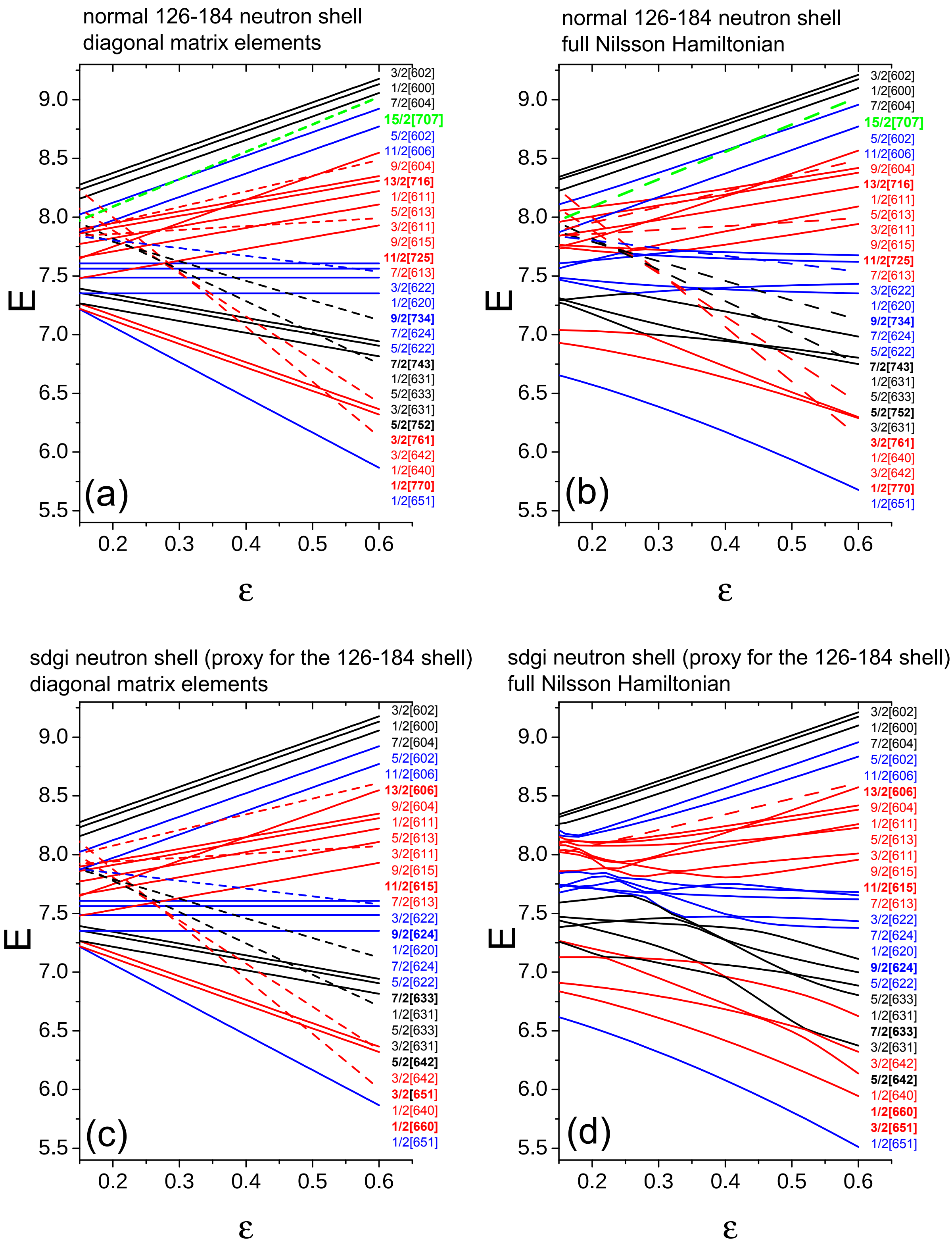

Fig. 1. Diagonal matrix elements (in units of $\hbar\omega_0$) of the Nilsson Hamiltonian for the 126-184 (a) and sdgi (c) neutron shells compared to the results of the full diagonalization for the 126-184 (b) and sdgi (d) neutron shells, as functions of the deformation parameter ϵ. The Nilsson parameters are taken from Table 5-1 of Ref. [8]. The $1j_{15/2}$ orbitals in (a) and (b), as well as the $1i_{13/2}$ orbitals in (c), are indicated by dashed lines. The $1j_{15/2}$ orbital labels in (a) and (b), as well as the $1i_{13/2}$ orbital labels in (c) and (d), appear in boldface. Orbitals are grouped in color only to facilitate visualizing the patterns of orbital evolution. Note that the Nilsson labels at the right are always in the same order as the energies of the orbitals as they appear at the right as well (largest deformation shown). Therefore, in some cases the order of the Nilsson orbitals changes slightly from panel to panel.

Parameter-independent predictions for shape variables of heavy deformed nuclei in the proxy-SU(3) model

Dennis Bonatsos[1], I. E. Assimakis[1], N. Minkov[2], Andriana Martinou[1], S. Sarantopoulou[1], R. B. Cakirli[3], R. F. Casten[4,5], and K. Blaum[6]

[1] Institute of Nuclear and Particle Physics, National Centre for Scientific Research "Demokritos", GR-15310 Aghia Paraskevi, Attiki, Greece
[2] Institute of Nuclear Research and Nuclear Energy, Bulgarian Academy of Sciences, 72 Tzarigrad Road, 1784 Sofia, Bulgaria
[3] Department of Physics, University of Istanbul, Istanbul, Turkey
[4] Wright Laboratory, Yale University, New Haven, Connecticut 06520, USA
[5] Facility for Rare Isotope Beams, 640 South Shaw Lane, Michigan State University, East Lansing, MI 48824 USA
[6] Max-Planck-Institut für Kernphysik, Saupfercheckweg 1, D-69117 Heidelberg, Germany

Abstract. Using a new approximate analytic parameter-free proxy-SU(3) scheme, we make predictions of shape observables for deformed nuclei, namely β and γ deformation variables, and compare these with empirical data and with predictions by relativistic and non-relativistic mean-field theories.

PACS. 21.60.Fw Models based on group theory – 21.60.Ev Collective models

1 Introduction

Proxy-SU(3) is a new approximate symmetry scheme applicable in medium-mass and heavy deformed nuclei [1, 2]. The basic features and the theoretical foundations of proxy-SU(3) have been described in Refs. [3,4], to which the reader is referred. In this contribution we are going to focus attention on the first applications of proxy-SU(3) in making predictions for the deformation variables of deformed rare earth nuclei.

2 Connection between deformation variables and SU(3) quantum numbers

A connection between the collective variables β and γ of the collective model [5] and the quantum numbers λ and μ characterizing the irreducible represention (λ, μ) of SU(3) [6,7] has long been established [8,9], based on the fact that the invariant quantities of the two theories should posses the same values.

The relevant equation for β reads [8,9]

$$\beta^2 = \frac{4\pi}{5}\frac{1}{(A\bar{r^2})^2}(\lambda^2 + \lambda\mu + \mu^2 + 3\lambda + 3\mu + 3), \qquad (1)$$

where A is the mass number of the nucleus and $\bar{r^2}$ is related to the dimensionless mean square radius [10], $\sqrt{\bar{r^2}} = r_0 A^{1/6}$. The constant r_0 is determined from a fit over a wide range of nuclei [11,12]. We use the value in Ref. [8], $r_0 = 0.87$, in agreement to Ref. [12]. The quantity in Eq. (1) is proportional to the second order Casimir operator of SU(3) [13],

$$C_2(\lambda, \mu) = \frac{2}{3}(\lambda^2 + \lambda\mu + \mu^2 + 3\lambda + 3\mu). \qquad (2)$$

The relevant equation for γ reads [8,9]

$$\gamma = \arctan\left(\frac{\sqrt{3}(\mu+1)}{2\lambda + \mu + 3}\right). \qquad (3)$$

3 Predictions for the β variable

The β deformation variable for a given nucleus can be obtained from Eq. (1), using the (λ, μ) values corresponding to the ground state band of this nucleus, obtained from Table 2 of Ref. [14].

A rescaling in order to take into account the size of the shell will be needed, as in the case of the geometric limit [15] of the Interacting Boson Model [13] in which a rescaling factor $2N_B/A$ is used, where N_B is the number of bosons (half of the number of the valence nucleons measured from the closest closed shell) in a nucleus with mass number A. In the present case one can see [2] that the β values obtained from Eq. (1) should be multiplied by a rescaling factor $A/(S_p + S_n)$, where S_p (S_n) is the size of the proton (neutron) shell in which the valence protons (neutrons) of the nucleus live. In the case of the rare earths considered here, one has $S_p = 82 - 50 = 32$ and $S_n = 126 - 82 = 44$, thus the rescaling factor is $A/76$.

Results for the β variable for several isotopic chains are shown in Fig. 1. These can be compared to Relativistic Mean Field predictions [16] shown in Fig. 2, as well as to empirical β values obtained from $B(E2)$ transition rates [17] shown in Fig. 3. Indeed such detailed comparisons for various series of isotopes are shown in Figs. 4-7. We remark that the proxy-SU(3) predictions are in general in very good agreement with both the RMF predictions and the empirical values. The sudden minimum developed in Fig. 1 at $N = 116$ could be related to the prolate-to-oblate shape/phase transition to be discussed in Ref. [14].

4 Predictions for the γ variable

The γ deformation variable for a given nucleus can be obtained from Eq. (3), using the (λ, μ) values corresponding to the ground state band of this nucleus, obtained from Table 2 of Ref. [14].

Results for the γ variable for several isotopic chains are shown in Figs. 8 and 9. In Fig. 9, predictions by Gogny D1S calculations [18] are also shown for comparison. The sharp jump of the γ variable from values close to 0 to values close to 60 degrees, seen in Fig. 9 close to $N = 116$, for both the proxy-SU(3) and the Gogny D1S predictions, can be related to the prolate-to-oblate shape/phase transition to be discussed in the next talk [14]. In contrast, in the series of isotopes shown in Fig. 8, γ is only raising at large neutron number N up to 30 degrees, indicating possible regions with triaxial shapes.

Minima appear in the proxy-SU(3) predictions for the neutron numbers for which the relevant SU(3) irrep, seen in Table 2 of Ref. [14], happens to possess $\mu = 0$, as one can easily see from Eq. (3). These oscillations could probably be smoothed out through a procedure of taking the average of neighboring SU(3) representations, as in Ref. [19].

Empirical values for the γ variable can be estimated from ratios of the γ vibrational bandhead to the first 2^+ state,

$$R = \frac{E(2_2^+)}{E(2_1^+)}, \tag{4}$$

through [20–22]

$$\sin 3\gamma = \frac{3}{2\sqrt{2}} \sqrt{1 - \left(\frac{R-1}{R+1}\right)^2}. \tag{5}$$

The proxy-SU(3) predictions for several isotopic chains are compared to so-obtained empirical values, as well as to Gogny D1S predictions where available, in Figs. 10 and 11. Again in general good agreement is seen.

5 Conclusions

The proxy-SU(3) symmetry provides predictions for the β collective variable which are in good agreement with RMF predictions, as well as with empirical values obtained from $B(E2)$ transition rates. Furthermore, the proxy-SU(3) symmetry provides predictions for the γ collective variable which are in good agreement with Gogny D1S predictions, as well as with empirical values obtained from the γ vibrational bandhead.

References

1. D. Bonatsos, I. E. Assimakis, N. Minkov, A. Martinou, R. B. Cakirli, R. F. Casten, and K. Blaum, Proxy-SU(3) symmetry in heavy deformed nuclei, Phys. Rev. C (2017) accepted, arXiv 1706.02282 [nucl-th].
2. D. Bonatsos, I. E. Assimakis, N. Minkov, A. Martinou, S. Sarantopoulou, R. B. Cakirli, R. F. Casten, and K. Blaum, Analytic predictions for nuclear shapes, prolate dominance and the prolate-oblate shape transition in the proxy-SU(3) model, Phys. Rev. C (2017) accepted, arXiv 1706.02321 [nucl-th].
3. D. Bonatsos. I. E. Assimakis, N. Minkov, A. Martinou, R. B. Cakirli, R. F. Casten, and K. Blaum, A new symmetry for heavy nuclei: Proxy-SU(3), in the Proceedings of the 4th Workshop of the Hellenic Institute of Nuclear Physics (HINPw4), ed. A. Pakou, http://hinpw4.physics.uoi.gr
4. D. Bonatsos. I. E. Assimakis, N. Minkov, A. Martinou, R. B. Cakirli, R. F. Casten, and K. Blaum, Proxy-SU(3) symmetry in heavy nuclei: Foundations, in the Proceedings of the 4th Workshop of the Hellenic Institute of Nuclear Physics (HINPw4), ed. A. Pakou, http://hinpw4.physics.uoi.gr
5. A. Bohr and B. R. Mottelson, Nuclear Structure, Vol. II: Nuclear Deformations (Benjamin, New York, 1975).
6. J. P. Elliott, Collective motion in the nuclear shell model I. Classification schemes for states of mixed configurations, Proc. Roy. Soc. Ser. A **245**, 128(1958).
7. J. P. Elliott, Collective motion in the nuclear shell model II. The introduction of intrinsic wave-functions, Proc. Roy. Soc. Ser. A **245**, 562 (1958).
8. O. Castaños, J. P. Draayer, and Y. Leschber, Shape variables and the shell model, Z. Phys. A **329**, 33 (1988).
9. J. P. Draayer, S. C. Park, and O. Castaños, Shell-model interpretation of the collective-model potential-energy surface, Phys. Rev. Lett. **62**, 20 (1989).
10. P. Ring and P. Schuck, *The Nuclear Many-Body Problem* (Springer, Berlin, 1980).
11. H. De Vries, C. W. De Jager, and C. De Vries, Nuclear charge-density-distribution parameters from elastic electron scattering, At. Data Nucl. Data Tables **36**, 495 (1987).
12. J. R. Stone, N. J. Stone, and S. Moszkowski, Incompressibility in finite nuclei and nuclear matter, Phys. Rev. C **89**, 044316 (2014).
13. F. Iachello and A. Arima, *The Interacting Boson Model* (Cambridge University Press, Cambridge, 1987).
14. D. Bonatsos. I. E. Assimakis, N. Minkov, A. Martinou, S. Sarantopoulou, R. B. Cakirli, R. F. Casten, and K. Blaum, Prolate dominance and prolate-oblate shape transition in the proxy-SU(3) model, in the Proceedings of the 4th Workshop of the Hellenic Institute of Nuclear Physics (HINPw4), ed. A. Pakou, http://hinpw4.physics.uoi.gr

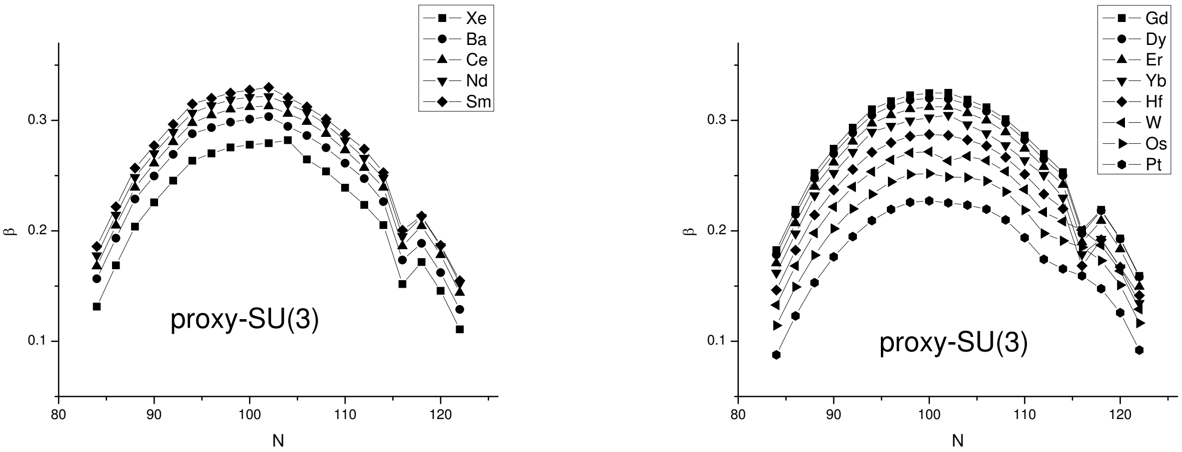

Fig. 1. Proxy-SU(3) predictions for β, obtained from Eq. (1).

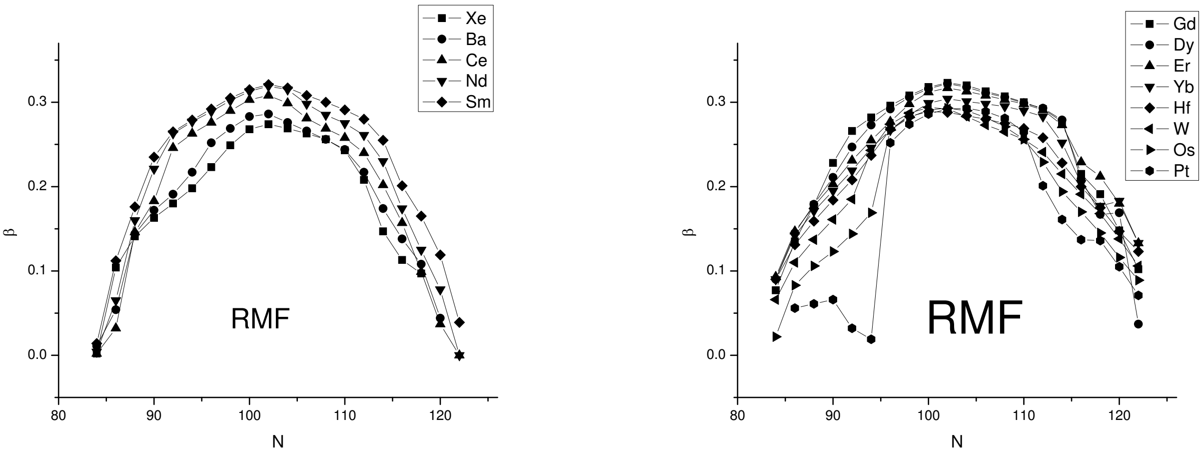

Fig. 2. RMF predictions for β, obtained from Ref. [16].

15. J. N. Ginocchio and M. W. Kirson, An intrinsic state for the Interacting Boson Model and its relationship to the Bohr–Mottelson model, Nucl. Phys. A **350**, 31 (1980).
16. G. A. Lalazissis, S. Raman, and P. Ring, Ground-state properties of even-even nuclei in the relativistic mean-field theory, At. Data Nucl. Data Tables **71**, 1 (1999).
17. S. Raman, C. W. Nestor, Jr., and P. Tikkanen, Transition probability from the ground to the first-excited 2^+ state of even-even nuclides, At. Data Nucl. Data Tables **78**, 1 (2001).
18. L. M. Robledo, R. Rodríguez-Guzmán, and P. Sarriguren, Role of triaxiality in the ground state shape of neutron rich Yb, Hf, W, Os and Pt isotopes, J. Phys. G: Nucl. Part. Phys. **36**, 115104 (2009).
19. K. H. Bhatt, S. Kahane, and S. Raman, Collective properties of nucleons in abnormal-parity states, Phys. Rev. C **61**, 034317 (2000).
20. A. S. Davydov and G. F. Filippov, Rotational states in even atomic nuclei, Nucl. Phys. **8**, 237 (1958).
21. R. F. Casten, *Nuclear Structure from a Simple Perspective* (Oxford University Press, Oxford, 2000).
22. L. Esser, U. Neuneyer, R. F. Casten, and P. von Brentano, Correlations of the deformation variables β and γ in even-even Hf, W, Os, Pt, and Hg nuclei, Phys. Rev. C **55**, 206 (1997).

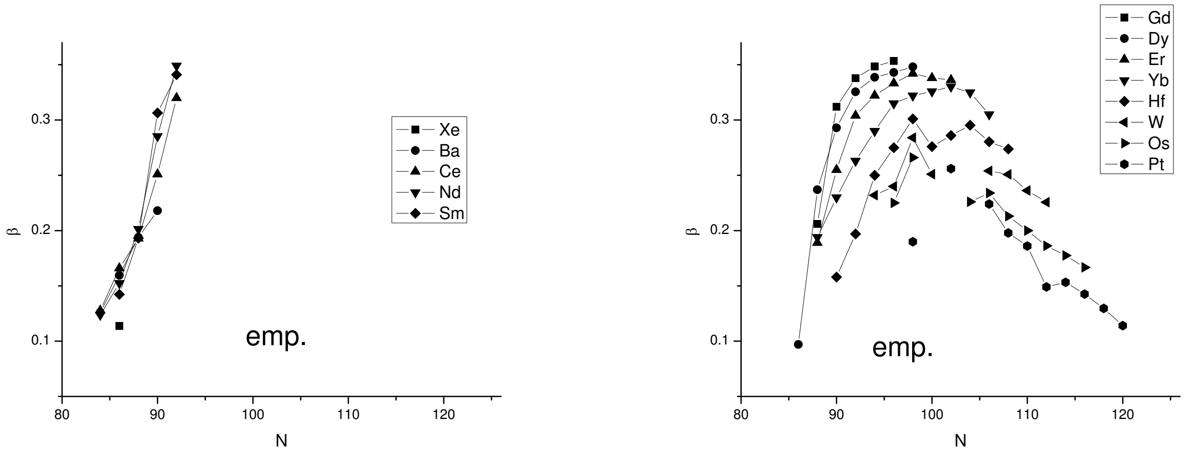

Fig. 3. Empirical predictions for β, obtained from Ref. [17].

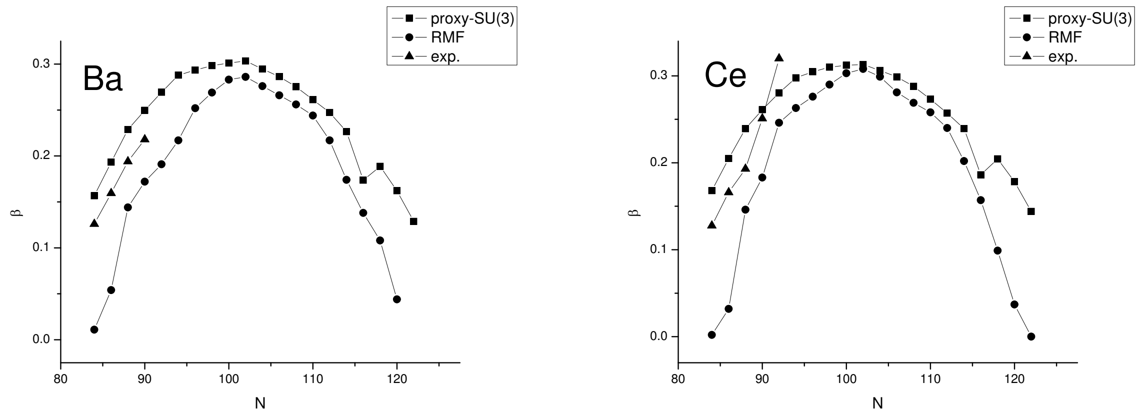

Fig. 4. Proxy-SU(3) predictions for β, obtained from Eq. (1), compared with tabulated β values [17] and also with predictions from relativistic mean field theory [16].

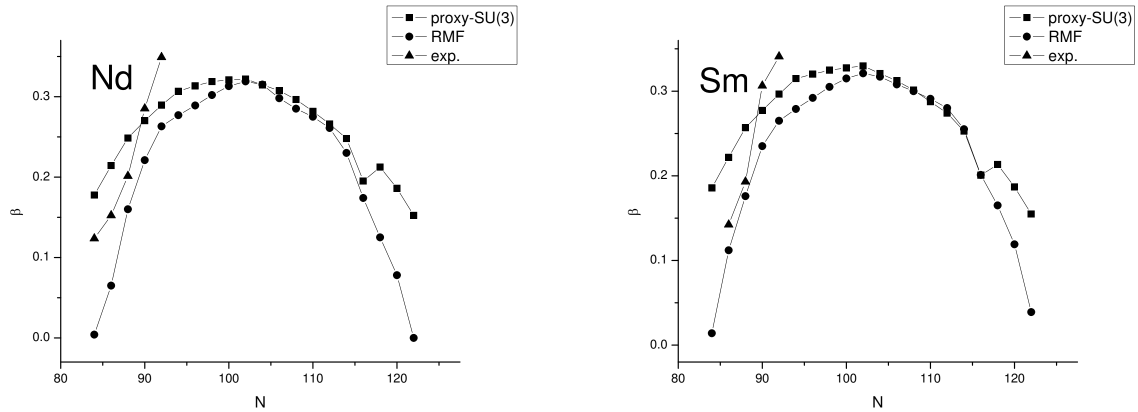

Fig. 5. Proxy-SU(3) predictions for β, obtained from Eq. (1), compared with tabulated β values [17] and also with predictions from relativistic mean field theory [16].

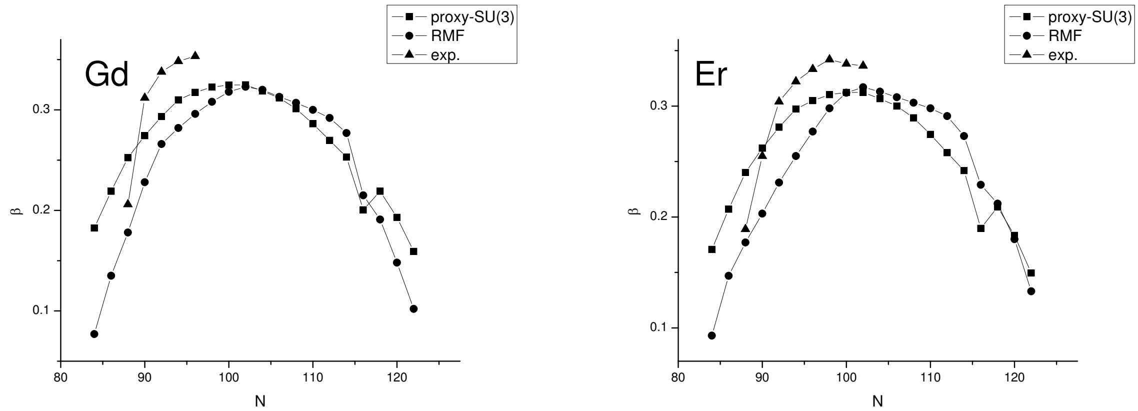

Fig. 6. Proxy-SU(3) predictions for β, obtained from Eq. (1), compared with tabulated β values [17] and also with predictions from relativistic mean field theory [16].

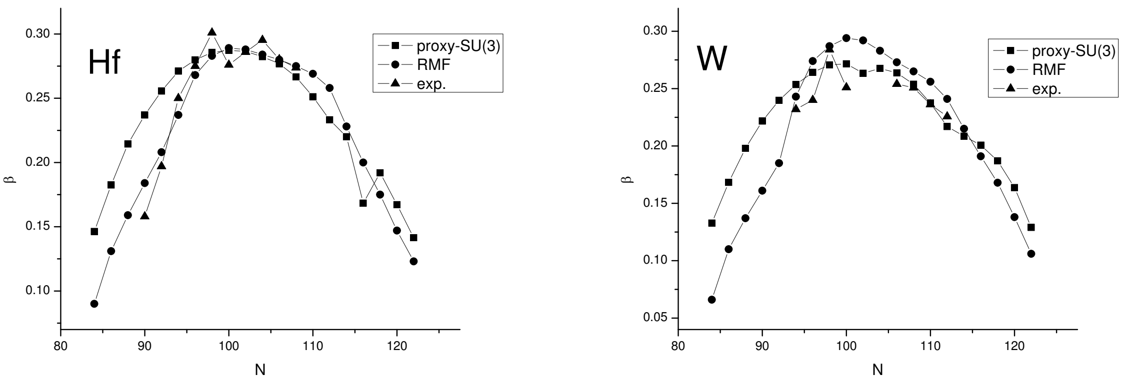

Fig. 7. Proxy-SU(3) predictions for β, obtained from Eq. (1), compared with tabulated β values [17] and also with predictions from relativistic mean field theory [16].

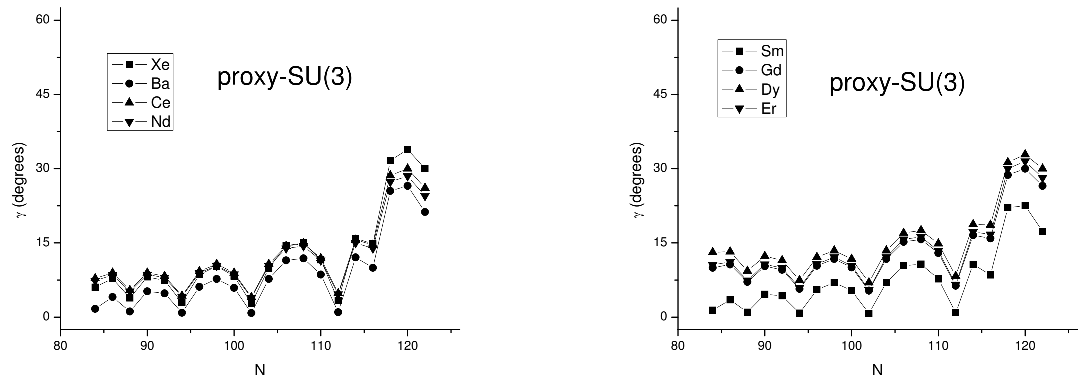

Fig. 8. Proxy-SU(3) predictions for γ, obtained from Eq. (3).

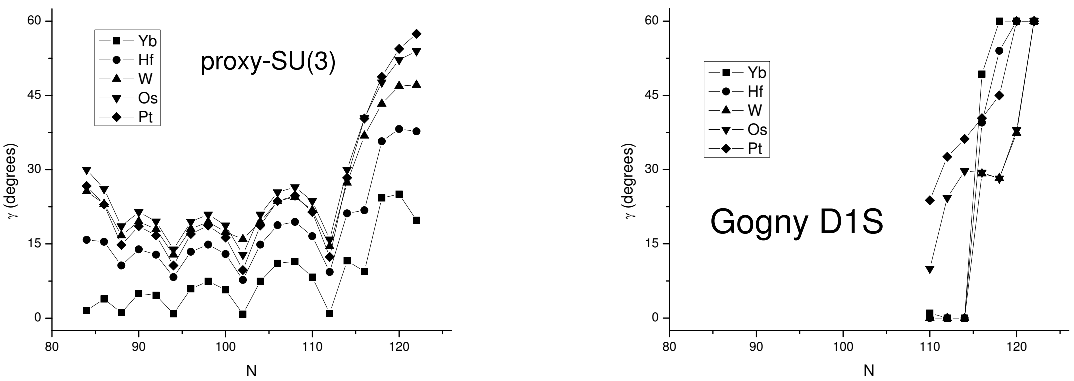

Fig. 9. Proxy-SU(3) predictions for γ, obtained from Eq. (3) and from Gogny D1S calculations [18].

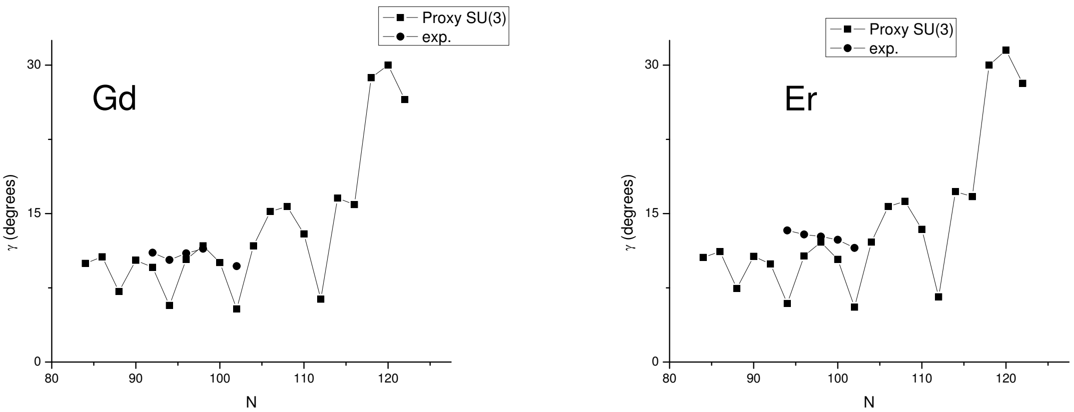

Fig. 10. Proxy-SU(3) predictions for γ, obtained from Eq. (3), compared with experimental values obtained from Eq. (5) [21, 22], as well as with predictions of Gogny D1S calculations [18].

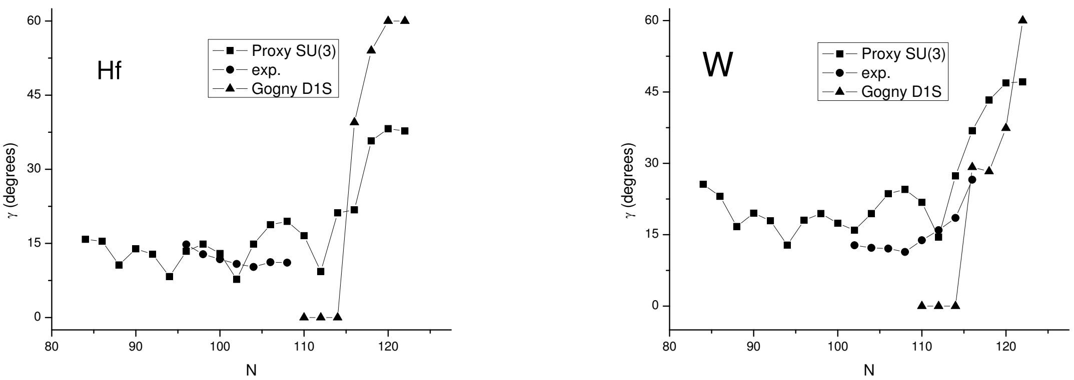

Fig. 11. Proxy-SU(3) predictions for γ, obtained from Eq. (3), compared with experimental values obtained from Eq. (5) [21, 22], as well as with predictions of Gogny D1S calculations [18].

Prolate dominance and prolate-oblate shape transition in the proxy-SU(3) model

Dennis Bonatsos[1], I. E. Assimakis[1], N. Minkov[2], Andriana Martinou[1], S. Sarantopoulou[1], R. B. Cakirli[3], R. F. Casten[4,5], and K. Blaum[6]

[1] Institute of Nuclear and Particle Physics, National Centre for Scientific Research "Demokritos", GR-15310 Aghia Paraskevi, Attiki, Greece
[2] Institute of Nuclear Research and Nuclear Energy, Bulgarian Academy of Sciences, 72 Tzarigrad Road, 1784 Sofia, Bulgaria
[3] Department of Physics, University of Istanbul, Istanbul, Turkey
[4] Wright Laboratory, Yale University, New Haven, Connecticut 06520, USA
[5] Facility for Rare Isotope Beams, 640 South Shaw Lane, Michigan State University, East Lansing, MI 48824 USA
[6] Max-Planck-Institut für Kernphysik, Saupfercheckweg 1, D-69117 Heidelberg, Germany

Abstract. Using a new approximate analytic parameter-free proxy-SU(3) scheme, we make simple predictions for the global feature of prolate dominance in deformed nuclei and the locus of the prolate-oblate shape transition and compare these with empirical data.

PACS. 21.60.Fw Models based on group theory – 21.60.Ev Collective models

1 Introduction

The dominance of prolate (rugby ball) over oblate (pancake) shapes in the ground states of even-even nuclei is still a puzzling open problem in nuclear structure [1]. Furthermore, there is experimental evidence for a prolate-to-oblate shape/phase transition in the rare earth region around neutron number $N = 116$ [2–6], in agreement with predictions by microscopic calculations [7–10]. We are going to consider these two issues in the framework of the proxy-SU(3) model, a new approximate symmetry scheme applicable in medium-mass and heavy deformed nuclei [11, 12]. The basic features and the theoretical foundations of proxy-SU(3), as well as some first applications for making predictions for ground state properties of even-even deformed nuclei, have been described in Refs. [13–15], to which the reader is referred.

2 Particle-hole symmetry breaking

We are going to show that the prolate vs. oblate dominance in the deformed shapes of even-even nuclei is rooted in the breaking of the particle-hole symmetry in the shell picture of the nucleus. A glance at the level schemes of the Nilsson model [16, 17] suffices in order to see that the first few orbitals lying in the beginning of a shell carry values of quantum numbers completely different from the last few orbitals at the end of the shell. In the neutron 50-82 major shell, for example, and at a moderate deformation $\epsilon = 0.3$, the three orbitals at the beginning of the shell are 1/2[431], 1/2[420], and 1/2[550], while the last three orbitals below the top of the shell are 11/2[505], 3/2[402], and 1/2[400], with the usual Nilsson notation $K[Nn_z\Lambda]$ being used, where N is the number of oscillator quanta, n_z is the number of oscillator quanta along the cylindrical symmetry axis z, Λ is the z-projection of the orbital angular momentum, and K is the z-projection of the total angular momentum.

In the framework of the proxy-SU(3) the particle-hole symmetry breaking can be seen in Table 1, in which the SU(3) irreducible representations (irreps) [18, 19] corresponding to the highest weight state for a given number of particles (protons or neutrons) are shown. The harmonic oscillator shell, possessing a U(N) symmetry, corresponding to each nuclear shell within the proxy-SU(3) scheme is also shown in Table 1. The highest weight states have been obtained by using the code UNTOU3 [20]. We see that the particle-hole symmetry is valid only up to 4 particles and 4 holes, while it is broken in the middle of each shell. In the *sd* shell however, the particle-hole symmetry breaking is absent for even particle numbers and it appears only for one odd particle number, due to the small size of the shell. It should be noticed that no particle-hole symmetry breaking occurs if, instead of the highest weight irreps, one considers the irreps possessing the highest eigenvalue of the second order Casimir operator of SU(3) [21]

$$C_2(\lambda, \mu) = \frac{2}{3}(\lambda^2 + \lambda\mu + \mu^2 + 3\lambda + 3\mu). \qquad (1)$$

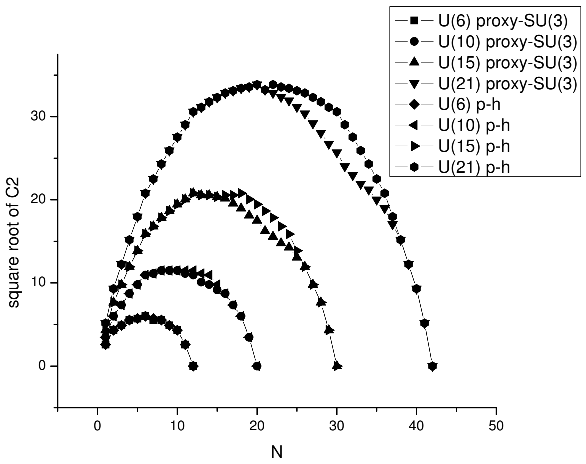

Fig. 1. Values of the square root of the second order Casimir operator of SU(3), obtained from Eq. (1), vs. particle number N, for different shells, obtained through proxy-SU(3) or through the particle-hole symmetry assumption.

The difference can be seen in Fig. 1, where the values of the square root of the Casimir operator are shown for the two cases in discussion. The particle-hole symmetry breaking can also be seen in Table 5 of Ref. [22], where the odd numbers of particles in the U(10) shell are reported.

3 Prolate over oblate dominance

Using the group theoretical results reported in Table 1 for the rare earths with 50-82 protons and 82-126 neutrons, one obtains for the highest weight irrep corresponding to each nucleus the irreps shown in Table 2. Similar results for rare earths with 50-82 protons and 50-82 neutrons are shown in Table 3.

As it was mentioned in Ref. [15], a connection between the collective variables β and γ of the collective model [24] and the quantum numbers λ and μ characterizing the irreducible represention (λ, μ) of SU(3) [18,19] is known [25,26], based on the fact that the invariant quantities of the two theories should posses the same values, the relevant equation for γ being [25,26]

$$\gamma = \arctan\left(\frac{\sqrt{3}(\mu+1)}{2\lambda+\mu+3}\right). \quad (2)$$

From this equation one easily sees that irreps with $\lambda > \mu$ correspond to prolate shapes with $0 < \gamma < 30^o$, while irreps with $\lambda < \mu$ correspond to oblate shapes with $30^o < \gamma < 60^o$.

As a result, in Table 2 we see that most nuclei possess prolate ground states, with the exception of a few nuclei appearing simultaneously just below the $Z = 82$ shell closure and just below the $N = 126$ shell closure. Similar conclusions are drawn from Table 3, where a few oblate nuclei are predicted just below the $Z = 82$ shell closure and just below the $N = 82$ shell closure.

4 The prolate-to-oblate shape/phase transition

In Table 2 it appears that a prolate-to-oblate shape/phase transition occurs at $N = 116$, while in Table 3 a similar transition is predicted at $N = 72$. The latter transition lies far away from the experimentally accessible region, but the first one is supported by existing experimental data. In particular

1) In the W series of isotopes, ^{190}W, which has $N = 116$, has been suggested as the lightest oblate isotope [2].

2) In the Os series of isotopes, ^{192}Os, which has $N = 116$, has been suggested as lying at the shape/phase transition point [3,4], with ^{194}Os [3,4] and ^{198}Os [5] found to possess an oblate character.

3) In the chain of even nuclei (differing by two protons or two neutrons) ^{180}Hf, $^{182-186}$W, $^{188-192}$Os, ^{194,196}Pt, ^{198,200}Hg, considered in Ref. [6], the collection of experimental data used suggests the the transition from prolate to oblate shapes occurs between ^{192}Os and ^{194}Pt, both of them possessing $N = 116$.

Furthermore, the present findings are in agreement with recent self-consistent Skyrme Hartree-Fock plus BCS calculations [7] and Hartree-Fock-Bogoliubov calculations [8–10] studying the structural evolution in neutron-rich Yb, Hf, W, Os, and Pt isotopes, reaching the conclusion that $N = 116$ nuclei in this region can be identified as the transition points between prolate and oblate shapes.

5 Conclusions

We have shown that the prolate over oblate dominance in the ground states of deformed even-even nuclei is predicted by the proxy-SU(3) scheme, based on the breaking of the particle-hole symmetry within each nuclear shell. Furthermore, we have seen that the proxy-SU(3) symmetry suggests $N = 116$ as the point of the prolate-to-oblate shape/phase transition, in agreement with existing expremental evidence [2–6] and microscopic calculations [7–10].

References

1. I. Hamamoto and B. Mottelson, Shape deformations in atomic nuclei, Scholarpedia **7(4)**, 10693 (2012).
2. N. Alkhomashi *et al.*, β-delayed spectroscopy of neutron-rich tantalum nuclei: Shape evolution in neutron-rich tungsten isotopes, Phys. Rev. C **80**, 064308 (2009).
3. R. F. Casten, A. I. Namenson, W. F. Davidson, D. D. Warner, and H. G. Borner, Low-lying levels in ^{194}Os and the prolateoblate phase transition, Phys. Lett. B **76**, 280 (1978).
4. C. Wheldon, J. Garcés Narro, C. J. Pearson, P. H. Regan, Zs. Podolyák, D. D. Warner, P. Fallon, A. O. Macchiavelli, and M. Cromaz, Yrast states in ^{194}Os: The prolate-oblate transition region, Phys. Rev. C **63**, 011304(R) (2000).

5. Zs. Podolyák *et al.,*, Weakly deformed oblate structures in $^{198}_{76}$Os$_{122}$, Phys. Rev. C **79**, 031305(R) (2009).
6. J. Jolie and A. Linnemann, Prolate-oblate phase transition in the Hf-Hg mass region, Phys. Rev. C **68**, 031301(R) (2003).
7. P. Sarriguren, R. Rodríguez-Guzmán, and L. M. Robledo, Shape transitions in neutron-rich Yb, Hf, W, Os, and Pt isotopes within a Skyrme Hartree-Fock + BCS approach, Phys. Rev. C **77**, 064322 (2008).
8. L. M. Robledo, R. Rodríguez-Guzmán, and P. Sarriguren, Role of triaxiality in the ground-state shape of neutron-rich Yb, Hf, W, Os and Pt isotopes, J. Phys. G: Nucl. Part. Phys. **36**, 115104 (2009).
9. K. Nomura, T. Otsuka, R. Rodríguez-Guzmán, L. M. Robledo, P. Sarriguren, P. H. Regan, P. D. Stevenson, and Zs. Podolyák, Spectroscopic calculations of the low-lying structure in exotic Os and W isotopes, Phys. Rev. C **83**, 054303 (2011).
10. K. Nomura, T. Otsuka, R. Rodríguez-Guzmán, L. M. Robledo, and P. Sarriguren, Collective structural evolution in neutron-rich Yb, Hf, W, Os, and Pt isotopes, Phys. Rev. C **84**, 054316 (2011).
11. D. Bonatsos, I. E. Assimakis, N. Minkov, A. Martinou, R. B. Cakirli, R. F. Casten, and K. Blaum, Proxy-SU(3) symmetry in heavy deformed nuclei, Phys. Rev. C (2017) accepted, arXiv 1706.02282 [nucl-th].
12. D. Bonatsos, I. E. Assimakis, N. Minkov, A. Martinou, S. Sarantopoulou, R. B. Cakirli, R. F. Casten, and K. Blaum, Analytic predictions for nuclear shapes, prolate dominance and the prolate-oblate shape transition in the proxy-SU(3) model, Phys. Rev. C (2017) accepted, arXiv 1706.02321 [nucl-th].
13. D. Bonatsos. I. E. Assimakis, N. Minkov, A. Martinou, R. B. Cakirli, R. F. Casten, and K. Blaum, A new symmetry for heavy nuclei: Proxy-SU(3), in the Proceedings of the 4th Workshop of the Hellenic Institute of Nuclear Physics (HINPw4), ed. A. Pakou, http://hinpw4.physics.uoi.gr
14. D. Bonatsos. I. E. Assimakis, N. Minkov, A. Martinou, R. B. Cakirli, R. F. Casten, and K. Blaum, Proxy-SU(3) symmetry in heavy nuclei: Foundations, in the Proceedings of the 4th Workshop of the Hellenic Institute of Nuclear Physics (HINPw4), ed. A. Pakou, http://hinpw4.physics.uoi.gr
15. D. Bonatsos. I. E. Assimakis, N. Minkov, A. Martinou, S. Sarantopoulou, R. B. Cakirli, R. F. Casten, and K. Blaum, Parameter-independent predictions for shape variables of heavy deformed nuclei in the proxy-SU(3) model, in the Proceedings of the 4th Workshop of the Hellenic Institute of Nuclear Physics (HINPw4), ed. A. Pakou, http://hinpw4.physics.uoi.gr
16. S. G. Nilsson, Binding states of individual nucleons in strongly deformed nuclei, Mat. Fys. Medd. K. Dan. Vidensk. Selsk. **29**, no. 16 (1955).
17. S. G. Nilsson and I. Ragnarsson, Shapes and Shells in Nuclear Structure (Cambridge University Press, Cambridge, 1995).
18. J. P. Elliott, Collective motion in the nuclear shell model I. Classification schemes for states of mixed configurations, Proc. Roy. Soc. Ser. A **245**, 128(1958).
19. J. P. Elliott, Collective motion in the nuclear shell model II. The introduction of intrinsic wave-functions, Proc. Roy. Soc. Ser. A **245**, 562 (1958).
20. J. P. Draayer, Y. Leschber, S. C. Park, and R. Lopez, Representations of U(3) in U(N), Comput. Phys. Commun. **56**, 279 (1989).
21. F. Iachello and A. Arima, *The Interacting Boson Model* (Cambridge University Press, Cambridge, 1987).
22. R. D. Ratna Raju, J. P. Draayer, and K. T. Hecht, Search for a coupling scheme in heavy deformed nuclei: The pseudo SU(3) model, Nucl. Phys. A **202**, 433 (1973).
23. Brookhaven National Laboratory ENSDF database http://www.nndc.bnl.gov/ensdf/
24. A. Bohr and B. R. Mottelson, Nuclear Structure, Vol. II: Nuclear Deformations (Benjamin, New York, 1975).
25. O. Castaños, J. P. Draayer, and Y. Leschber, Shape variables and the shell model, Z. Phys. A **329**, 33 (1988).
26. J. P. Draayer, S. C. Park, and O. Castaños, Shell-model interpretation of the collective-model potential-energy surface, Phys. Rev. Lett. **62**, 20 (1989).

Table 1. Comparison between SU(3) irreps for U(6), U(10), U(15), and U(21), obtained by the code UNTOU3 [20], contained in the relevant U(n) irrep for M valence protons or M valence neutrons. Above the U(n) algebra, the relevant shell of the shell model and the corresponding proxy-SU(3) shell are given. The highest weight SU(3) irreps, given in the columns labelled by hw, are compared to the SU(3) irreps with the highest eigenvalue of the second order Casimir operator of SU(3), given in the columns labelled by C. Irreps breaking the particle-hole symmetry in the hw columns are indicated by boldface characters. Taken from Ref. [12].

		8-20	8-20	28-50	28-50	50-82	50-82	82-126	82-126
		sd	sd	pf	pf	sdg	sdg	pfh	pfh
M	irrep	U(6)	U(6)	U(10)	U(10)	U(15)	U(15)	U(21)	U(21)
		hw	C	hw	C	hw	C	hw	C
0		(0,0)	(0,0)	(0,0)	(0,0)	(0,0)	(0,0)	(0,0)	(0,0)
1	[1]	(2,0)	(2,0)	(3,0)	(3,0)	(4,0)	(4,0)	(5,0)	(5,0)
2	[2]	(4,0)	(4,0)	(6,0)	(6,0)	(8,0)	(8,0)	(10,0)	(10,0)
3	[21]	(4,1)	(4,1)	(7,1)	(7,1)	(10,1)	(10,1)	(13,1)	(13,1)
4	[2^2]	(4,2)	(4,2)	(8,2)	(8,2)	(12,2)	(12,2)	(16,2)	(16,2)
5	[$2^2$1]	(5,1)	(5,1)	(10,1)	(10,1)	(15,1)	(15,1)	(20,1)	(20,1)
6	[2^3]	(6,0)	(0,6)	(12,0)	(12,0)	(18,0)	(18,0)	(24,0)	(24,0)
7	[$2^3$1]	**(4,2)**	(1,5)	(11,2)	(11,2)	(18,2)	(18,2)	(25,2)	(25,2)
8	[2^4]	(2,4)	(2,4)	(10,4)	(10,4)	(18,4)	(18,4)	(26,4)	(26,4)
9	[$2^4$1]	(1,4)	(1,4)	(10,4)	(10,4)	(19,4)	(19,4)	(28,4)	(28,4)
10	[2^5]	(0,4)	(0,4)	(10,4)	(4,10)	(20,4)	(20,4)	(30,4)	(30,4)
11	[$2^5$1]	(0,2)	(0,2)	**(11,2)**	(4,10)	(22,2)	(22,2)	(33,2)	(33,2)
12	[2^6]	(0,0)	(0,0)	**(12,0)**	(4,10)	(24,0)	(24,0)	(36,0)	(36,0)
13	[$2^6$1]			**(9,3)**	(2,11)	(22,3)	(22,3)	(35,3)	(35,3)
14	[2^7]			**(6,6)**	(0,12)	(20,6)	(20,6)	(34,6)	(34,6)
15	[$2^7$1]			**(4,7)**	(1,10)	(19,7)	(7,19)	(34,7)	(34,7)
16	[2^8]			(2,8)	(2,8)	**(18,8)**	(6,20)	(34,8)	(34,8)
17	[$2^8$1]			(1,7)	(1,7)	**(18,7)**	(3,22)	(35,7)	(35,7)
18	[2^9]			(0,6)	(0,6)	**(18,6)**	(0,24)	(36,6)	(36,6)
19	[$2^9$1]			(0,3)	(0,3)	**(19,3)**	(2,22)	(38,3)	(38,3)
20	[2^{10}]			(0,0)	(0,0)	**(20,0)**	(4,20)	(40,0)	(40,0)
21	[2^{10}1]					**(16,4)**	(4,19)	(37,4)	(4,37)
22	[2^{11}]					**(12,8)**	(4,18)	**(34,8)**	(0,40)
23	[2^{11}1]					**(9,10)**	(2,18)	**(32,10)**	(3,38)
24	[2^{12}]					**(6,12)**	(0,18)	**(30,12)**	(6,36)
25	[2^{12}1]					**(4,12)**	(1,15)	**(29,12)**	(7,35)
26	[2^{13}]					(2,12)	(2,12)	**(28,12)**	(8,34)
27	[2^{13}1]					(1,10)	(1,10)	**(28,10)**	(7,34)
28	[2^{14}]					(0,8)	(0,8)	**(28,8)**	(6,34)
29	[2^{14}1]					(0,4)	(0,4)	**(29,4)**	(3,35)
30	[2^{15}]					(0,0)	(0,0)	**(30,0)**	(0,36)
31	[2^{15}1]							**(25,5)**	(2,33)
32	[2^{16}]							**(20,10)**	(4,30)
33	[2^{16}1]							**(16,13)**	(4,28)
34	[2^{17}]							**(12,16)**	(4,26)
35	[2^{17}1]							**(9,17)**	(2,25)
36	[2^{18}]							**(6,18)**	(0,24)
37	[2^{18}1]							**(4,17)**	(1,20)
38	[2^{19}]							(2,16)	(2,16)
39	[2^{19}1]							(1,13)	(1,13)
40	[2^{20}]							(0,10)	(0,10)
41	[2^{20}1]							(0,5)	(0,5)
42	[2^{21}]							(0,0)	(0,0)

Table 2. Most leading SU(3) irreps [18,19] for nuclei with protons in the 50-82 shell and neutrons in the 82-126 shell. Nuclei are divided into five groups: 1) Nuclei with $R_{4/2} = E(4_1^+)/E(2_1^+) \geq 2.8$ are indicated by boldface numbers. 2) Nuclei with $2.8 > R_{4/2} \geq 2.5$ are denoted by *. 3) A few nuclei with $R_{4/2}$ ratios slightly below 2.5, shown for comparison, are labelled by **. 4) For any other nuclei with $R_{4/2} < 2.5$, no irreps are shown. 5) Nuclei for which the $R_{4/2}$ ratios are still unknown [23] are shown using normal fonts and without any special signs attached . Underlined irreps correspond to oblate shapes. Based on Ref. [12].

	Ce	Nd	Sm	Gd	Dy	Er	Yb	Hf	W	Os	Pt
Z	58	60	62	64	66	68	70	72	74	76	78
122	(18,14)	(20,14)	(24,14)	(20,16)	(18,18)	(18,16)	(20,10)	(12,18)	(6,22)	(2,22)	(0,18)
120	(20,20)	(22,20)	(26,16)	(22,22)	$\underline{(20,24)}$	$\underline{(20,22)}$	(22,16)	$\underline{(14,24)}$	$\underline{(8,28)}$	$\underline{(4,28)*}$	$\underline{(2,24)**}$
118	(24,22)	(26,22)	(30,18)	(26,24)	(24,16)	(24,24)	(26,18)	$\underline{(18,26)}$	$\underline{(12,30)}$	$\underline{(8,30)*}$	$\underline{(6,26)**}$
116	(30,10)	(32,10)	(36,6)	(32,12)	(30,14)	(30,12)	(32,6)	(24,14)	$\underline{(18,28)*}$	$\underline{\mathbf{(14,28)}}$	$\underline{(12,24)**}$
114	(38,14)	(40,14)	(44,10)	(40,16)	(38,18)	(38,16)	(40,10)	(32,18)	**(26,22)**	**(22,22)**	(20,18)**
112	(48,4)	(50,4)	(54,0)	(50,6)	(48,8)	(48,6)	(50,0)	**(42,8)**	**(36,12)**	**(32,12)**	(30,8)**
110	(46,12)	(48,12)	(52,8)	(48,14)	(46,16)	(46,14)	(48,8)	**(40,16)**	**(34,20)**	**(30,20)**	(28,16)*
108	(46,16)	(48,16)	(52,12)	(48,18)	(46,20)	(46,18)	**(48,12)**	**(40,20)**	**(34,24)**	**(30,24)**	(28,20)*
106	(48,16)	(50,16)	(54,12)	(50,18)	(48,20)	**(48,18)**	**(50,12)**	**(42,20)**	**(36,24)**	**(32,24)**	(30,20)*
104	(52,12)	(54,12)	(58,8)	(54,14)	**(52,16)**	**(52,14)**	**(54,8)**	**(46,16)**	**(40,20)**	**(36,20)**	(34,16)*
102	(58,4)	(60,4)	(64,0)	**(60,6)**	**(58,8)**	**(58,6)**	**(60,0)**	**(52,8)**	**(46,12)**	**(42,12)**	(40,8)*
100	(54,10)	(56,10)	(60,6)	**(56,12)**	**(54,14)**	**(54,12)**	**(56,6)**	**(48,14)**	**(42,18)**	**(38,18)**	(36,14)*
98	(52,12)	(54,12)	**(58,8)**	**(54,14)**	**(52,16)**	**(52,14)**	**(54,8)**	**(46,16)**	**(40,20)**	(36,20)*	
96	(52,10)	**(54,10)**	**(58,6)**	**(54,12)**	**(52,14)**	**(52,12)**	**(54,6)**	**(46,14)**	**(40,18)**	(36,18)*	
94	**(54,4)**	**(56,4)**	**(60,0)**	**(56,6)**	**(54,8)**	**(54,6)**	**(56,0)**	**(48,8)**	**(42,12)**	(38,12)*	
92	**(48,8)**	**(50,8)**	**(54,4)**	**(50,10)**	**(48,12)**	**(48,10)**	**(50,4)**	(42,12)*			
90	**(44,8)**	**(46,8)**	**(50,4)**	**(46,10)**	**(44,12)**	(44,10)*	(46,4)*	(38,12)*			
88	(42,4)*	(44,4)*									

Table 3. Same as Table II, but for nuclei with both protons and neutrons in the 50-82 shell. Based on Ref. [12].

	Ba	Ce	Nd	Sm	Gd	Dy	Er	Yb	Hf	W	Os	Pt
Z	56	58	60	62	64	66	68	70	72	74	76	78
78							(18,14)	(20,8)	$\underline{(12,16)}$	$\underline{(6,20)}$	$\underline{(2,20)}$	$\underline{(0,16)}$
76		(20,16)*	(22,16)*	(26,12)*	(22,18)*	(20,20)*	(20,18)	(22,12)	$\underline{(14,20)}$	$\underline{(8,24)}$	$\underline{(4,24)}$	$\underline{(2,20)}$
74	(24,12)*	(24,16)*	(26,16)*	(30,12)*	(26,18)*	**(24,20)**	(24,18)	(26,12)	$\underline{(18,20)}$	$\underline{(12,24)}$	$\underline{(8,24)}$	$\underline{(6,20)}$
72	(30,8)*	(30,12)*	**(32,12)**	**(36,8)**	(32,14)	(30,16)	(30,14)	(32,8)	(24,16)	$\underline{(18,20)}$	$\underline{(14,20)}$	$\underline{(12,16)}$
70	(38,0)*	**(38,4)**	**(40,4)**	**(44,0)**	(40,6)	(38,8)	(38,6)	(40,0)	(32,8)	(26,12)	(22,12)	(20,8)
68	**(36,6)**	**(36,10)**	**(38,10)**	(42,6)	(38,12)	(36,14)	(36,12)	(38,6)	(30,14)	(24,18)	(20,18)	(18,14)
66	**(36,8)**	**(36,12)**	(38,12)	(32,8)	(38,14)	(36,16)	(36,14)	(38,8)	(30,16)	(24,20)	(20,20)	(18,16)
64	**(38,6)**	**(38,10)**	(40,10)	(44,6)	(40,12)	(38,14)	(38,12)	(40,6)	(32,14)	(26,18)	(22,18)	(20,14)
62	**(42,0)**	(42,4)	(44,4)	(48,0)	(44,6)	(42,8)	(42,6)	(44,0)	(36,8)	(30,12)	(26,12)	(24,8)
60	(28,4)	(38,8)	(40,8)	(44,4)	(40,10)	(38,12)	(38,10)	(40,4)	(32,12)	(26,16)	(22,16)	(20,12)
58	(36,4)	(36,8)	(38,8)	(42,4)	(38,10)	(36,12)	(36,10)	(38,4)	(30,12)	(24,16)	(20,16)	(18,12)
56	(36,0)	(36,4)	(38,4)	(42,0)	(38,6)	(36,8)	(36,6)	(38,0)	(30,8)	(24,12)	(20,12)	(18,8)

Nuclear Physics Using Lasers

A. Bonasera

Cyclotron Institute, Texas A&M University, College Station, TX-77843, USA;
Laboratori Nazionali del Sud, INFN, via Santa Sofia, 62, 95123 Catania, Italy

Abstract. The plasma astrophysical S factor for the $^{3}He(d;p)^{4}He$ fusion reaction was measured for the first time at temperatures of few KeV, using the interaction of intense ultrafast laser pulses with molecular deuterium clusters mixed with ^{3}He atoms. The experiments were performed at the Petawatt laser facility, University of Texas, Austin-USA. Different proportions of D_2 and ^{3}He or CD_4 and ^{3}He were mixed in the gas target in order to allow the measurement of the cross section. The yield of 14.7 MeV protons from the $^{3}He(d;p)^{4}He$ reaction was measured in order to extract the astrophysical S factor at low energies.

Recent results obtained at the ABC-laser facility, ENEA-Frascati, Italy on the p+^{11}B, ^{6}Li+^{6}Li and d+^{6}Li systems will be discussed.

References

PRL 111, 082502 (2013); PRL 111, 055002 (2013); PHYS.REV. E 88, 033108 (2013); NIM A 720 (2013) 149–152; Progr.Theor.Phys. Supplement No. 154, 2004, 261
http://physics.aps.org/synopsis-for/10.1103/PhysRevLett.111.082502

EoS studies in heavy ion collisions: from Coulomb barrier to LHC

M. Veselsky[1], J. Klimo[1], G.A. Souliotis[2], Y.G. Ma[3], and M. Ploskon[4]

[1] Institute of Physics, Slovak Academy of Sciences, Bratislava, Slovakia
[2] National and Kapodistrian University, Athens, Greece
[3] Shanghai Institute of Applied Physics, Shanghai, China
[4] Lawrence Berkeley National Laboratory, Berkeley, USA

Abstract. Investigations of nuclear equation of state in nucleus-nucleus collisisons are presented in a wide range of incident energies, ranging from Coulomb barrier up to the ultra-relativistic energies at Large Hadron Collider at CERN. In particular, fusion probabilities in reactions leading to super-heavy elements will be investigated at beam energies close to Coulomb barrier and parameters of equation of state will be extracted. Transport model is employed at intermediate energies and flow observables are investigated. Multiplicity of charged particles will be investigated at ultra-relativistic energies and a relation of its trend to topology of phase space is demonstrated.

PACS. PACS-key discribing text of that key – PACS-key discribing text of that key

1 Introduction

Collisions of accelerated heavy ion beams with heavy nuclei (nucleus-nucleus collisions) lead to various reaction scenarios, depending primarily on the incident beam energy. At low energies, close to or just above the repulsive Coulomb barrier, the reaction scenario is governed by the nuclear mean-field generated mostly by nuclear matter close to the saturation density and one can observe either fusion of two colliding nuclei into a compound nucleus or exchange of nucleons in the damped binary collisions such as deep-inelastic transfer. As the incident energy grows the collisions of two nuclei lead to compression of nuclear medium to still higher densities. Also the two-body collisions between nucleons become still more important. Properties of nuclear matter become demonstrated in transport observables such as stopping and various types of flow observables. At very high beam energies the two-body nucleon-nucleon collisions become dominant, and large number of hadrons can be produced. Such medium can undergo phase transition into deconfined quark matter, and observables which can demonstrate such phase transition and location of eventual critical point are of great interest. Practically any information about nuclear equation of state is important for understanding of various astrophysical processes, related e.g. to supernovae and properties of neutron stars. For example, an important open question in nuclear astrophysics is the origin of the heavy nuclei observed in the Universe. At the present the most promising candidate appears to be the merger of two neutron stars, de-facto a collision of two huge nuclei, where the conditions, necessary for nucleosynthesis of heavy elements can be achieved.

In this contribution we show how nucleus-nucleus collisions at large span of beam energies from Coulomb barrier up to the LHC energies can be used to extract properties of nuclear equation of state.

2 Nucleus-nucleus collisions close to Coulomb barrier

In the last two decades of the past century, the heavy elements up to Z=112 were synthesized using cold fusion reactions with Pb, Bi targets in the evaporation channel with emission of one neutron [1]. The experimentalists had to face a rapid decrease of cross sections down to the picobarn level due to increasing fusion hindrance whose origin was unclear. Since the turn of millennium, still heavier elements with Z=113-118 were produced in the hot fusion reactions with emission of 3-4 neutrons using ^{48}Ca beams with heavy actinide targets between uranium and californium [2]. Again the increase of fusion hindrance was observed, caused by competition of the fusion process with an alternative process called quasi-fission. It is usually considered that the process of quasi-fission is governed by a complex dynamics of the projectile-target system, however, success of a simple statistical model of fusion hindrance, introduced in [13,14] suggests that the competition of fusion and quasi-fission could be dominantly driven by the available phase-space and hindrances originating in diabatic dynamics are not decisive. In the work [3] we employed the Boltzmann-Uehling-Uhlenbeck

(BUU) equation with the Pauli principle implemented separately for neutrons and protons and with the Coulomb interaction and demonstrated how various equations of state of nuclear matter implemented into such transport simulation influence the competition of fusion and quasi-fission. Based on available data on reactions, leading to production of super-heavy nuclei, we extracted most stringent constraints on the stiffness of the nuclear equation of state and on the density-dependence of the symmetry energy.

In order to describe theoretically the competition of fusion and quasi-fission at energies close to the Coulomb barrier, the evolution of nuclear mean field can be described by solving the Boltzmann equation. One of the approximations for the solution of the Boltzmann equation, the Boltzmann-Uehling-Uhlenbeck model is extensively used [4,5], which takes both the nuclear mean field and the Fermionic Pauli blocking into consideration. The simple single-particle mean field potential with the isospin-dependent symmetry energy term

$$U = a\rho + b\rho^{\kappa} + 2a_s(\frac{\rho}{\rho_0})^{\gamma}\tau_z I, \qquad (1)$$

was used, where $I = (\rho_n - \rho_p)/\rho$, ρ_0 is the normal nuclear matter density; ρ, ρ_n, and ρ_p are the nucleon, neutron and proton densities, respectively; τ_z assumes the value 1 for neutron and -1 for proton, the coefficients a, b and exponent κ represent the properties of symmetric nuclear matter, while the last term describes the influence of the symmetry energy, where a_s represents the symmetry energy at saturation density and the exponent γ describes the density dependence.

The in-medium nucleon-nucleon cross sections are typically approximated using the experimental cross sections of free nucleons (e.g. using the parametrization from Cugnon [6]). Alternatively, as shown in the work [7], in-medium nucleon-nucleon cross sections can be estimated directly using the equation of state.

We use the version of Van der Waals Boltzmann-Uehling-Uhlenbeck model which was developed by Veselský and Ma [7]. In a system constituting of nucleons, the proper (excluded) volume b' can be used to estimate its cross section within the nucleonic medium

$$\sigma = (\frac{9\pi}{16})^{1/3} b'^{2/3}, \qquad (2)$$

where b' can be expressed using single particle potential as

$$b' = \frac{b\kappa\rho^{\kappa} + 2\gamma a_s(\frac{\rho}{\rho_0})^{1+\gamma}\tau_z I}{(\frac{f_{5/2}(z)}{f_{3/2}(z)})\rho T + b\kappa\rho^{1+\kappa} + 2\gamma a_s\rho_0(\frac{\rho}{\rho_0})^{1+\gamma}\tau_z I}. \qquad (3)$$

where $z = exp(\mu/T)$ is the fugacity value of nucleons, with ρ being particle density, μ chemical potential and T is the temperature; and $\frac{f_{5/2}(z)}{f_{3/2}(z)}$ is a factor, a fraction of the Fermi integrals $f_n(z) = \frac{1}{\Gamma(n)}\int_0^{\infty}\frac{x^{n-1}}{z^{-1}e^x+1}dx$. Such cross section can be implemented into the collision term of the Boltzmann-Uehling-Uhlenbeck equation. In this way, both isospin-dependent mean-field and nucleon-nucleon cross sections, which are correlated to each other. This is a so-called VdWBUU equation. More details can be found in Ref. [7].

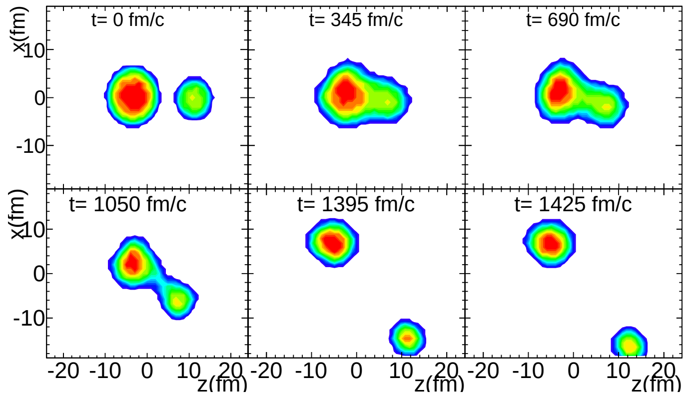

Fig. 1. Typical evolution of nucleonic density for the central collision ^{64}Ni+^{186}W at beam energy 5 MeV/nucleon, simulated using the soft equation of state with incompressibility $K_0 =$ 202 MeV and the soft density dependence symmetry energy with $\gamma = 0.5$. Weak surface tension is overcome by Coulomb interaction and quasi-fission occurs.

To account for Coulomb force, we complement the corresponding density-dependent force $\nabla_r U$ acting at a given cell of the cubic grid (with a mesh of 1 fm) with the summary force generated by the all remaining protons outside of a given cell. This approach avoids fluctuation of the Coulomb force due to interaction of protons at small distances inside the cell, and also avoids double counting since interaction of protons within the same cell is considered in the collision term. Specifically we consider only interaction with the protons of the same set of test particles.

In order to investigate the role of the equation of state of nuclear matter in the competition of fusion and quasi-fission in reactions leading to heavy and superheavy nuclei, we selected a representative set of reactions, where experimental data exists. As one of the heaviest systems, where fusion is still dominant, we use the reaction ^{48}Ca+^{208}Pb. This reaction was measured [8,9], and a typical dominant peak at symmetric fission was observed in the mass vs TKE spectra of fission fragments, with TKE consistent to fusion-fission proceeding through formation of the compound nucleus ^{256}Nb. Onset of quasi-fission was observed [10] in the reaction ^{64}Ni+^{186}W, leading to compound system ^{250}No, where a prominent fusion-like peak is not observed anymore, however symmetric fission, which can be attributed to fusion-fission, is still observed relatively frequently. Quasi-fission becomes even more dominant in the reaction ^{48}Ca+^{238}U, nominally leading to compound nucleus ^{286}Cn. Nevertheless, the symmetric fission events still amount to about 10 % of fission events [11]. Comparison with the reaction ^{64}Ni+^{186}W shows that the relative amount of symmetric events in reaction ^{48}Ca+^{238}U is twice lower than in the reaction ^{64}Ni+^{186}W, thus implying the relative amount of 20 % of symmetric fission for the latter reaction. In reactions ^{64}Ni+^{208}Pb [8], ^{48}Ca+^{249}Cf

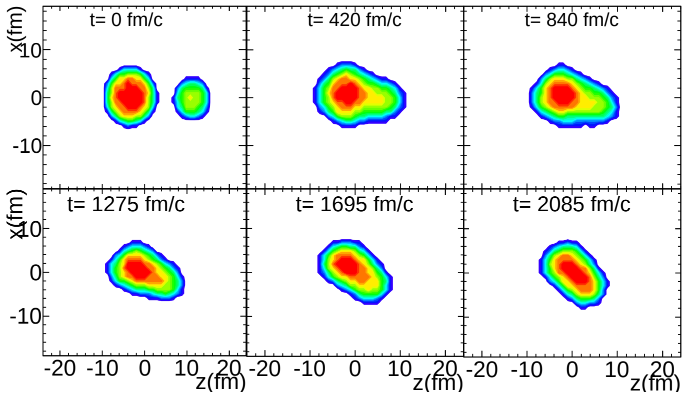

Fig. 2. Typical evolution of nucleonic density for the central collision ^{64}Ni+^{186}W at beam energy 5 MeV/nucleon, simulated using the soft equation of state ($K_0 = 202$ MeV) and the stiff density-dependence of symmetry energy ($\gamma = 1.5$). Despite weak surface tension the stiff density-dependence of symmetry energy prevents formation of a neck and quasi-fission is prevented.

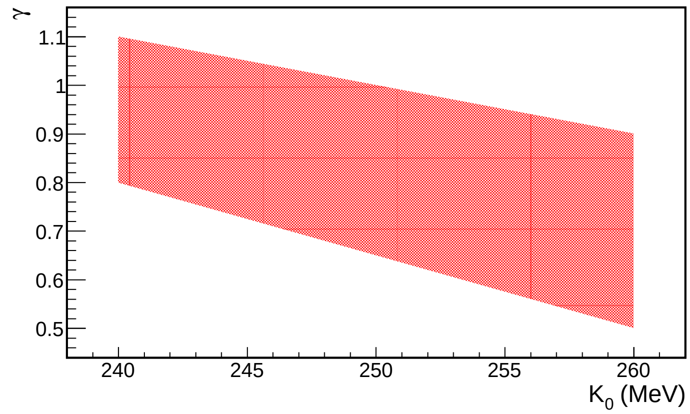

Fig. 3. Constraint on stiffness of symmetric nuclear matter (modulus of incompressibility) and on density-dependence of the symmetry energy (exponent γ from Eq. 1) derived from the simulations of competition between fusion and quasi-fission.

[2], and ^{64}Ni+^{238}U [12] the quasi-fission already dominates and fusion hindrance amounts to several orders of magnitude (10^{-3} - 10^{-5} [13,14]).

Simulations were performed at beam energy 5 AMeV, which is above the Coulomb barrier and in all cases corresponds to the nearest experimental point within few MeV. Since the angular momentum range where quasi-fission events are produced is not known precisely and also to assure that we won't observe deep-inelastic transfer, which occurs at peripheral collisions, we simulate the most central events, with impact parameter set to 0.5 fm (exactly central events practically do not occur in experiment). Simulations were performed up to the time 3000 fm/c, sufficient for formation of the final configuration in all investigated cases.

From the investigated reactions, the collisions of ^{64}Ni+^{186}W exhibit highest sensitivity to the parameters of the equation of state. Fig. 1 shows typical evolution of nucleonic density for the collision ^{64}Ni+^{186}W, simulated using the soft equation of state with incompressibility $K_0 = 202$ MeV and the soft density-dependence of symmetry energy $\gamma = 0.5$. One can see that the impinging projectile nucleus establishes contact with the target nucleus, however the weak surface tension, caused by the soft equation of state, is not sufficient to overcome Coulomb repulsion of the projectile and target which re-separate after approximately 1200 fm/c (scission time is comparable with other approaches [15–19]). Similar evolution was observed in all 20 simulated test particle sets. In the simulation of the same reaction with $K_0 = 300$ MeV and $\gamma = 0.5$ the stronger surface tension generated by the stiff equation of state allows to overcome the Coulomb repulsion and system undergoes fusion. Strong sensitivity to the stiffness of the equation of state is thus demonstrated. Fig. 2 shows the simulation with $K_0 = 202$ MeV and $\gamma = 1.5$. One can observe that increased stiffness of the density-dependence of symmetry energy can also prevent system from separating into two fragments. In this case the weak surface tension allows to form elongated configuration (similar to Fig. 1), however the stiffer symmetry energy prevents formation of a low-density neutron-rich neck and thus the contact between the two reaction partners is preserved until the surface tension finally overcomes the Coulomb repulsion. Figs. 1 - 2 demonstrate a strong sensitivity of the system ^{64}Ni+^{186}W to the parameters of the equation of state.

As a result of the analysis of competition between fusion and quasi-fission in all above mentioned reactions, it was possible to set a rather strict constraint on the incompressibility of the equation of state of nuclear matter $K_0 = 240 - 260$ MeV with softer density dependence of the symmetry energy with $\gamma = 0.5 - 1.0$ (see Fig. 3). This constraint is based on simulations of collisions, where maximum density reaches 1.4 - 1.5 times the saturation density. The shape of the constrained area reflects a trend of softening the density-dependence of the symmetry energy, necessary to balance increase of incompressibility. Such trend stems from competition of the surface tension, related to the stiffness of the equation of state of symmetric nuclear matter, with the Coulomb repulsion. This corresponds to the traditional picture of nuclear fission, where fissility of the system is defined as a ratio of the Coulomb repulsion to twice the surface energy. However, the present analysis goes beyond this simple macroscopic picture and elucidates the crucial role of the density-dependence of the symmetry energy in the dynamics of the system close to the scission point. In comparison with other methods, such as constraining the equation of state using the nuclear giant resonances [20–22] or the flow observables in relativistic nucleus-nucleus collisions [23], in the present analysis the effect of nuclear equation of state is manifested directly, and thus it is not affected by uncertainty related e.g. to description of underlying nuclear structure in the former or disentangling the effect of the two-body dissipation via nucleon-nucleon collisions in the latter case. Thus, by using a representative set of investigated reactions we provide a solid base for assumption that the extracted constraints do not depend critically on the effect of shell structure. In order to obtain even more strict constraints, in particular on the density-dependence of symmetry energy, more experimental data are necessary close to the onset of quasi-fission, where the sensitivity of the neck dynamics to the density dependence of the symmetry energy is highest.

3 Analysis of flow observables

The flow observables were introduced primarily as observables directly related to the equation of state of nuclear matter. Different flow observables can be identified with the coefficients of the Fourier expansion of the azimuthal angular distribution in transverse direction relative to the reaction plane.

The systematics of directed flow for protons observed in the semi-peripheral collisions (b=5.5-7.5 fm) of Au+Au at various beam energies was published in [24] and the systematics of elliptic flow for the protons observed in the semi-peripheral collisions of Au+Au at mid-rapidity was published in the work [25]. When combined, these two systematics provide a good set of experimental data for testing of the transport codes and for determination of the parameters of the equation of the state of nuclear matter.

As described above, the new variant of the transport code for simulation of the nucleus-nucleus collisions (VdWBUU) was introduced in the work [7]. At variance to previous methods used for the solution of the Boltzmann-Uehling-Uhlenbeck equation (BUU), the nucleon-nucleon cross sections used for evaluation of the collision term, are estimated directly from the equation of state used for evaluation of the mean-field potential. The method of estimation of the nucleon-nucleon cross sections is based on the formal transformation of the equation of state into the form of the Van der Waals equation of state and the cross sections is obtained from excluded volume after inverting the Van der Waals equation of state. Thus the whole calculation is based on a single equation of state and there is no need to use free or empirically estimated in-medium cross sections. Like in the work [7], particles are considered as emitted when they are separated in the phase-space from any other particle and separation is large enough to assure that two particles are not part of a cluster (a condition $\Delta\boldsymbol{p}\Delta\boldsymbol{r} > 2h$ is implemented).

For each simulation the emitted protons were selected as described above and the resulting flow observables were compared to the measured values. Since the measured values represent a compilation of results of many experiments, no specific filtering procedure, taking into account experimental angular and momentum coverage, was performed. It is simply assumed that if the calculated value, at least a maximum value of the negative elliptic flow at a given transverse momentum, approaches the measured value, the corresponding choice of the parameters of the equation of the state is considered as viable, while if neither the inclusive data nor the subset approach the measured value, the corresponding choice of the parameters of the equation of the state is considered as excluded by the measured data.

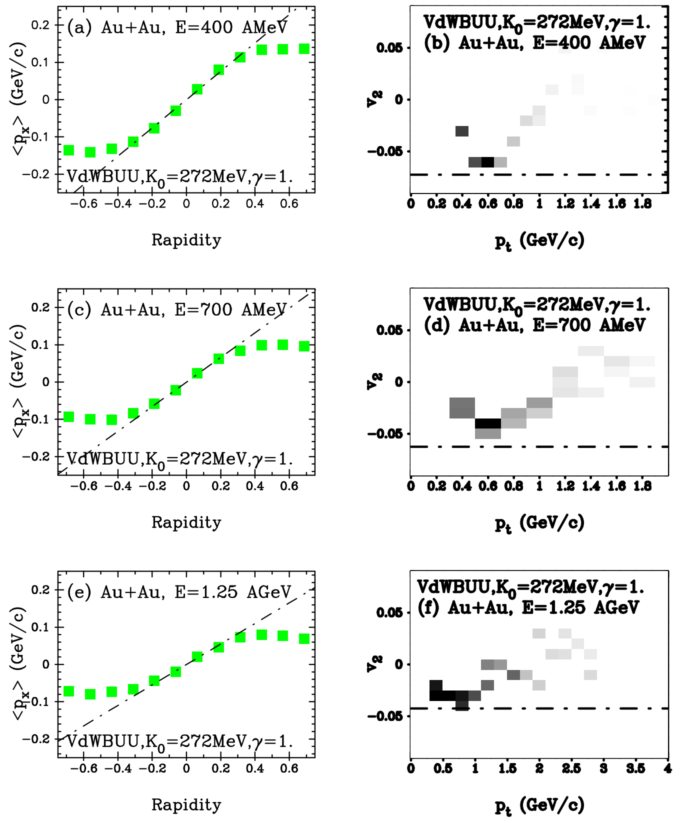

Fig. 4. Systematics of the proton directed flow (left panels, lines indicate experimentally observed slopes) and the momentum dependence of the calculated proton elliptic flow at mid-rapidity versus the experimental value (boxes and the dash-dotted line in right panels, respectively) in the collisions of Au+Au at beam energies ranging from 400 AMeV to 1.25 AGeV. Results were obtained using the VdWBUU simulation using the intermediate EoS with $\kappa = 3/2$ (K_0=272 MeV) and the symmetry energy density dependence with $\gamma = 1$.

In Figure 4 are shown the results of the simulations with the intermediate EoS (with incompressibility $K_0 =$ 272 MeV). This mode of simulations leads to reasonable agreement with the measured directed flow and also the agreement with the measured elliptic flow is within the limits preventing to disregard this variant. On the other hand, simulations with the soft EoS (with incompressibility $K_0 = 202$ MeV) fail to reproduce both the directed flow and also elliptic flow. The directed flow is not reproduced from the beam energy 700 AMeV and above, the slopes of the transverse momentum are much less steep and such a soft equation of the state appears as excluded by the measured data on directed flow. The situation concerning the elliptic flow is less dramatic, still the observed agreement is worse than in the case of stiffer equation of the state. Another interesting observation is that simulations with the stiff EoS $K_0 = 380$ MeV and stiffer parametrizations of the density dependence of the symmetry energy $\gamma = 1--2$ lead to results similar to Figure 4 and all these symmetry energy parametrizations can be considered as viable. It appears to signal that the such stiff equation

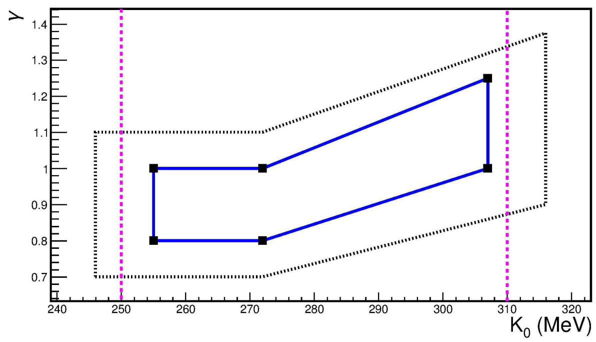

Fig. 5. The area marked by solid contour in the γ vs K_0 plot shows the values of the EoS and symmetry energy parameters, constrained by the analysis using the VdWBUU simulations (squares show the values where calculation was performed). Dotted contour shows the uncertainty where the values can not be conclusively excluded. Dashed lines shows the constrained values of K_0 from re-analysis of giant monopole resonance data [21].

of state limits the effect of the density dependence of the symmetry energy. It can be understood since especially at high densities the contribution of symmetry energy to the total value of single particle potential is only a small part of the term corresponding to the stiff equation of state. Thus the effect of the density dependence of the symmetry energy can be expected to be more prominent when using the softer equations of the state.

In an attempt to obtain more strict constraints we decided to explore also higher beam energies up to 10 AGeV. As mentioned above, the kinematics of the particles is treated fully relativistically, and thus the code can be used in principle. However, above 1 AGeV one can expect that non-elastic (non-nucleonic) channels will start to play role. Simulation, used in previous cases, considers only a dominant non-nucleonic channel, inelastic production and absorption of the Δ-resonance, with the corresponding cross sections as given in [6]. Besides Δ, ther potentially important hadronic channels are channels with production of strange Σ and Λ hyperons, along with production of strange K-mesons. These channels are introduced into our BUU simulation, using the calculated cross sections from work [26].

Results from the VdWBUU simulations show that the directed flow at 10 AGeV is not reproduced neither by the soft (K_0=202 MeV) nor by the stiff (K_0=380 MeV) equation of state. Only the intermediate EoS with K_0=272 MeV allows to reproduce the directed flow. The fBUU simulation with K_0=272 MeV and with nucleon-nucleon cross sections of Cugnon et al. [6]. results in directed flow at 10 AGeV which can not reproduce experimental value. Instead of the weakly positive directed flow a strong negative flow is observed, due to overestimation of stopping in the nuclear matter.

The results of the flow analysis are summarized in the Figure 5. The range of the possible stiffness of the EoS can be identified, based on the analysis presented here, as encompassing incompressibilities $K_0 = 245 - 315$ MeV, in agreement with the results of recent re-analysis of the data from giant monopole resonance [21], a process occuring close to saturation density, where the range of $K_0 =$ 250 - 310 MeV (shown as dotted area in Figure 5) was determined after modification of the fitting procedure, used to determine incompressibility, higher than earlier constrained softer values between 200 - 240 MeV. Thus the values of incompressibility obtained at different density ranges appear to be in agreement, Also the recent re-analysis of the determination of the neutron star radii appears to lead to larger radii with lower limit around 14 km [27] and thus to favor stiffer equation of the state. Furthermore, also the relatively thick neutron skin of ^{208}Pb, reported by the PREX experiment [28,29], appears to favor a stiffer equation of state [30].

4 Transition from three-dimensional to one-dimensional phase space as a signal of phase transition and rate of entropy production in ultra-relativistic heavy-ion collisions

Charged particle multiplicity data from nucleus-nucleus collisions obtained in last decades at SPS, RHIC and LHC show an interesting feature. The dependence of charged particle multiplicity on number of participating nucleons N_{part} does not change from $\sqrt{s_{\mathrm{NN}}} = 0.008$ TeV [31] to $\sqrt{s_{\mathrm{NN}}} = 5.02$ TeV [32]. Such trend suggests that despite large differences in centre-of-mass energy the production of particles is governed by similar underlying production mechanisms, characterized by N_{part}.

At lower energies below the onset of deconfinement, production of charged particles occurs via nucleon-nucleon collisions. E.g. when colliding two nuclei (in center of mass frame), the energy available for production of emitted particles in nucleon-nucleon collisions is proportional to beam energy in the c.m. frame $\sqrt{s_{\mathrm{NN}}}$. Thus it appears natural that their number will scale with beam energy. Of course also available phase space will play role, however such scaling is typical for statistical models, e.g statistical bootstrap model for hadron production [33,34]. This regime with N_π proportional to $\sqrt{s_{\mathrm{NN}}}$ can thus be expected for resonant hadronic gas.

Indeed, as shown in Fig. 6 the experimental data on $\mathrm{d}N_{\mathrm{ch}}/\mathrm{d}\eta$ tend to follow $\sqrt{s_{\mathrm{NN}}}$-scaling in the region below 7 GeV, for the AGS (E802/E917) [38,39] data up to the SPS [40,41] and low-energy RHIC [31]. We acknowledge the results from SIS by FOPI Collaboration [46] but we do not consider those as they are too close to pion emission threshold.

The observed $\sqrt{s_{\mathrm{NN}}}$ scaling validates the 3D phase space scenario described above. However, at higher energies, at about 10 GeV the $\sqrt{s_{\mathrm{NN}}}$-scaling clearly breaks down and experimental multiplicity starts to grow much slower. It appears, that scenario considering only two-body collisions is no longer valid there. As an alternative to two-body collision scenario it can be assumed,

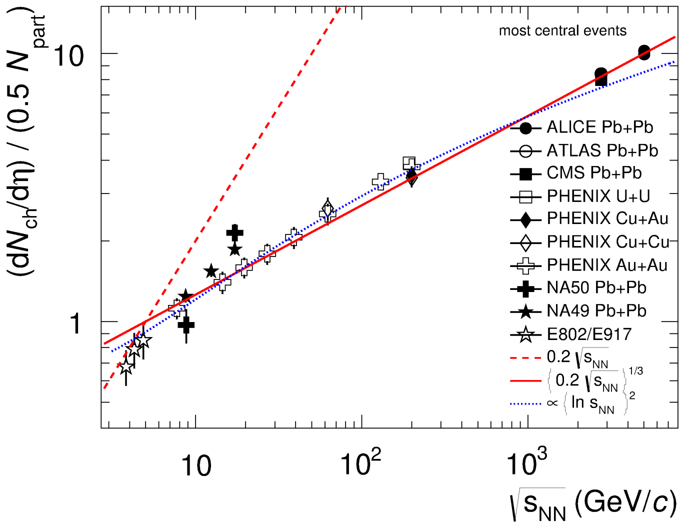

Fig. 6. Excitation function of pseudorapidity density of charged particles per participating nucleon pair in heavy-ion collisions [40,38,39,41,42,32,43–45,31]. Data points are for most central collisions. See text for more details.

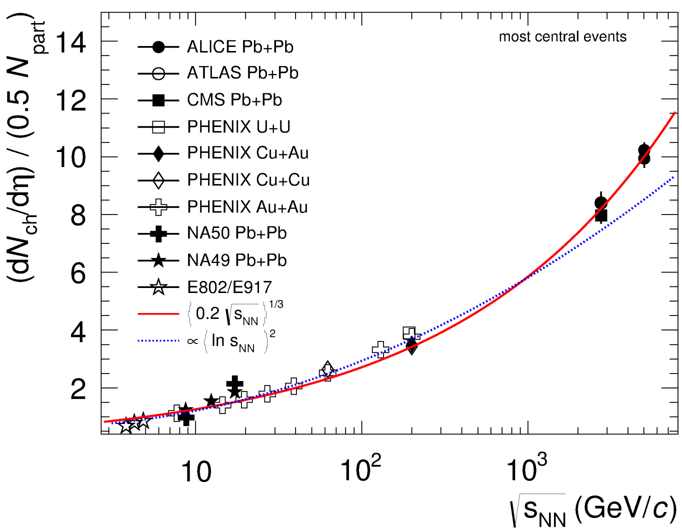

Fig. 7. Same as Fig. 6 but shown with linear multiplicity axis emphasizing the comparison of the parametrizations of the excitation functions at the LHC energies.

that at high energies pions are produced by fragmentation of strings between two participant quarks, in the fashion described e.g. by Lund model [35,36]. This implies that while available phase space does not change dramatically, it will be filled in a different way. The occupation of space in transverse directions is determined by the number of participating quarks, and only the direction parallel to the beam represents the available phase space. Then one can expect that number of pions will scale with $\sqrt{s_{\rm NN}}^{1/3}$. The above trend is indeed observed experimentally, as shown in Fig. 6 for most central collisions. The $\sqrt{s}^{1/3}$ scaling (solid line) is observed in the region ranging from the SPS, through RHIC, up to the data from the LHC. The agreement with the simple $\sqrt{s_{\rm NN}}^{1/3}$ scaling over the broad range of energies leads us to claim that the formation of QGP is present in collisions from $\sqrt{s_{\rm NN}} = 0.01$ TeV on. Moreover, the transition between the two, $\sqrt{s_{\rm NN}}$ and $\sqrt{s_{\rm NN}}^{1/3}$ regimes is correlated with the deconfinement phase transition. In Fig. 6 and Fig. 7 the function derived by the PHOBOS Collaboration proportional to $\ln\sqrt{s_{\rm NN}}^2$ [47] is fitted to data points from the PHENIX Collaboration [31], it however can not reproduce the data points obtained at LHC energies (see Fig. 7).

In Fig. 8 the PHENIX data points correspond to centrality selection of 35-40%. For CMS and ATLAS two points (for each) are shown: 30-35% and 35-40%, while for ALICE the centrality selection is 30-40%. The line for $f = 0.15$ (with negligible error) is a result of a fit to RHIC data for $\sqrt{s_{\rm NN}} > 20$ GeV. The line for $f = 0.1$ is to guide the eye - a good match at the LHC top energy. Grey dashed lines are to guide the eye and correspond to the lines for most central events shown in Fig. 6 and Fig. 7. It is apparent that $\sqrt{s_{\rm NN}}^{1/3}$ scaling is preserved also in semi-peripheral collisions.

Taking that entropy production is proportional to particle production, the $\sqrt{s_{\rm NN}}^{1/3}$ dependence of charged particle multiplicity seen in data implies that a limiting rate of entropy production was reached in high-energy heavy-ion collisions. In thermodynamics it is postulated that system evolves toward maximum entropy. For instance, statistical bootstrap model [33,34], leading to linear multiplicity dependence, corresponds to maximum entropy growth while temperature reaches limit. Instead, it is observed that the maximum achievable particle production and thus entropy grows considerably slower, possibly proportionally to time of expansion into freezeout volume in only one dimension. In this context we note that the transverse energy follows a trend, similar to $\sqrt{s_{\rm NN}}^{1/3}$ scaling [31]. The proportionality factor between $E_{\rm T}$ and N_π grows relatively slowly ($\sqrt{s}^{0.08}$) and thus increase of mean energy of emitted particles do not compensate for missing multiplicity. Thus the limitation on production of entropy appears real.

Moreover, we project that the search for the end-point at lower energies (E between 4 and 15 GeV) of the second order phase transition can benefit from studies of particle production between the multiplicity bins rather than from tedious variations of the beam energy. On the other hand, we claim that the most interesting region is at the crossing between the linear dependence and $\sqrt{s_{\rm NN}}^{1/3}$ of the multiplicity density. From our investigations it lies somewhere between $\sqrt{s_{\rm NN}} = 0.007$ TeV and $\sqrt{s_{\rm NN}} = 0.015$ TeV. Another interesting aspect is a prediction of particle production for the energies much larger than the LHC. Current considerations of a future accelerators, such as Future Circular Collider [48], consider energies of 40 TeV in the centre-of-mass. While such an increase in energy does not yet warrant existence of new type of QGP it will be most interesting how strongly the $dN_{\rm ch}/d\eta/N_{\rm part}/2$ differs from the $\sqrt{s_{\rm NN}}^{1/3}$ dependence.

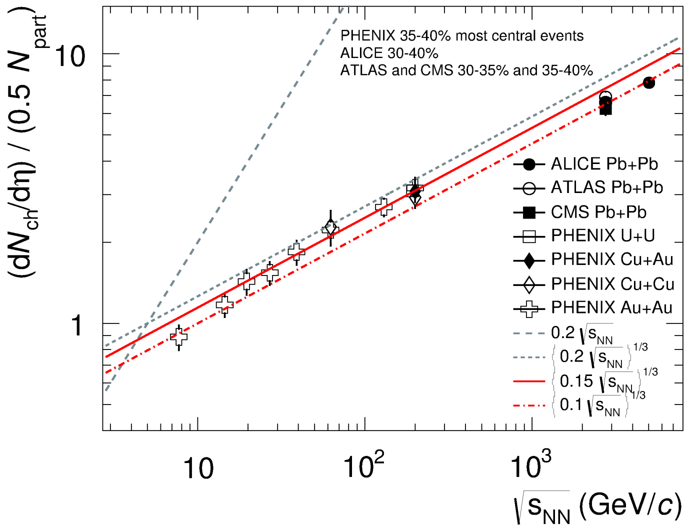

Fig. 8. Excitation function of pseudorapidity density of charged particles per participating nucleon pair in semi-central heavy-ion collisions [42,32,43,44,31]. See text for details.

Acknowledgements

This work is supported by the Slovak Scientific Grant Agency under contract 2/0129/17, by the Slovak Research and Development Agency under contract APVV-15-0225 (M.V.), in part by the Major State Basic Research Development Program in China under Contract No. 2014CB845400, the National Natural Science Foundation of China under contract Nos. 11421505 and 11520101004 (Y.G.M.), by ELKE account No 70/4/11395 of the National and Kapodistrian University of Athens (G.S.), and by the U.S. Department of Energy, Office of Science, Office of Nuclear Physics, under contract DE-AC02-05CH11231.

References

1. S. Hofmann, Rep. Prog. Phys. **61**, 639 (1998).
2. Yu. Ts. Oganessian and V. K. Utyonkov, Rep. Prog. Phys. **78**, 036301 (2015).
3. M. Veselsky, J.Klimo, Y.G. Ma and G.A. Souliotis, Phys. Rev. C **94**, 064608 (2016).
4. G.F. Bertsch, H. Kruse and S. Das Gupta, Phys. Rev. C **29**, 673 (1984).
5. H. Kruse, B. V. Jacak and H. Stöcker, Phys. Rev. Lett. **54**, 289 (1985).
6. J. Cugnon, T. Mizutani and J. Vandermeulen, Nucl. Phys. A **352**, 505 (1981).
7. M. Veselsky and Y.G. Ma, Phys. Rev. C **87**, 034615 (2013).
8. R. Bock et al., Nucl. Phys. A **388**, 334 (1982).
9. E. Prokhorova et al., Nucl. Phys. A **802**, 45 (2008).
10. G.N. Knyazheva et al., PEPAN Letters **5**, 91 (2008).
11. M.G. Itkis et al., Nucl. Phys. A **787**, 150c (2007).
12. E.M. Kozulin et al., Phys. Lett. B **686**, 227 (2010).
13. M. Veselsky, Acta Phys. Slovaca **49**, 101 (1999).
14. M. Veselsky, Phys. Atom. Nucl. **66**, 1086 (2003); Yad. Fiz. **66**, 1122 (2003).
15. G.G. Adamian, N.V. Antonenko and W. Scheid, Nucl. Phys. A **618**, 176 (1997).
16. V. Zagrebaev and W. Greiner, J. Phys. G **31**, 825 (2005).
17. Y. Aritomo et al., Phys. Rev. C **85**, 044614 (2012).
18. N. Wang, Z. Li, and X. Wu, Phys. Rev. C **65**, 064608 (2002).
19. C. Golabek and C. Simenel, Phys. Rev. Lett. **103**, 042701 (2009).
20. D. H. Youngblood, H. L. Clark, and Y.-W. Lui, Phys. Rev. Lett. **82**, 691 (1999).
21. J.R. Stone, N.J. Stone and S.A. Moszkowski, Phys. Rev. C **89**, 044316 (2014).
22. J. Piekarewicz, Eur. J. Phys. A **50**, 25 (2014).
23. B.A. Li, L.W. Chen, and C.M. Ko, Physics Reports **464**, 113 (2008).
24. N. Herrmann, J. P. Wessels, and T. Wienold, Ann. Rev. Nucl. Part. Sci. **49**, 581 (1999).
25. A. Andronic, J. Lukasik, W. Reisdorf, and W. Trautmann, Eur. Phys. J. **30**, 31 (2006).
26. G.Q. Li, and C.M. Ko, Nucl. Phys. A **594**, 439 (1995).
27. V. Suleimanov, J. Poutanen, M. Revnivtsev and K. Werner, Astrophys. J. **742**, 122 (2011).
28. S. Abrahamyan et al., Phys. Rev. Lett. **108**, 112502 (2012).
29. C. Horowitz et al., Phys. Rev. C **85**, 032501 (2012).
30. F.J. Fattoyev and J. Piekarewicz, Phys. Rev. Lett. **111**, 162501 (2013).
31. A. Adare et al. (PHENIX), Phys. Rev. C **93**, 024901 (2016).
32. J. Adam et al. (ALICE), Phys. Rev. Lett. **116**, 222302 (2016).
33. R. Hagedorn, Nuovo Cim. Suppl. **3**, 147 (1965).
34. S. Frautschi, Phys. Rev. D **3**, 2821 (1971).
35. B. Andersson, G. Gustafson, and C. Peterson, Zeitschrift fur Physik C Particles and Fields **1**, 105 (1979).
36. B. Andersson, The Lund Model, Cambridge University Press, 1998.
37. K. Aamodt et al. (ALICE), Phys. Lett. B **696**, 328, (2011).
38. L. Ahle et al. (E-802), Phys. Rev. C **59**, 2173 (1999).
39. L. Ahle et al. (E917, E866), Phys. Lett. B **490**, 53 (2000).
40. S. V. Afanasiev et al., Nucl. Phys. A **715**, 161 (2003).
41. M. C. Abreu et al. (NA50), Phys. Lett. B **530**, 43 (2002).
42. K. Aamodt et al. (ALICE), Phys. Rev. Lett. **106**, 032301 (2011).
43. G. Aad et al. (ATLAS), Phys. Lett. B **710**, 363 (2012).
44. S. Chatrchyan et al. (CMS),JHEP **08**, 141 (2011).
45. S. S. Adler et al. (PHENIX), Phys. Rev. C **71**, 034908 (2005).
46. W. Reisdorf et al. (FOPI), Nucl. Phys. A **612**, 493 (1997).
47. B. Alver et al. (PHOBOS), Phys. Rev. C **83**, 024913 (2011).
48. A. Dainese et al., (2016), arXiv:1605.01389 [hep-ph].
49. H. Fujii, and K. Itakura, Nucl. Phys. A **809**, 88 (2008).

Production of neutron-rich isotopes toward the astrophysical r-process path

G.A. Souliotis[a,*], A. Papageorgiou[a], Y.K. Kwon[b], K. Tshoo[b], M. Veselsky[c], A. Bonasera[d,e]

[a] Laboratory of Physical Chemistry, Department of Chemistry, National and Kapodistrian University of Athens, Athens, Greece
[b] The Rare Isotope Science Project (RISP), Institute for Basic Science, Daejeon, Korea
[c] Institute of Physics, Slovak Academy of Sciences, Bratislava, Slovakia
[d] Cyclotron Institute, Texas A&M University, College Station, Texas, USA
[e] Laboratori Nazionali del Sud, INFN, Catania, Italy

* Corresponding author. Email: soulioti@chem.uoa.gr

Abstract. The production cross sections of neutron-rich rare isotopes from collisions of ^{86}Kr projectiles with ^{64,58}Ni and ^{124,112}Sn targets at 15 and 25 MeV/nucleon are pre-sented. Our experimental data are compared with calculations employing a two-step approach. The dynamical stage of the projectile-target interaction was described with either the phenomenological deep-inelastic transfer (DIT) model or the mi-croscopic constrained molecular dynamics model (CoMD). For the de-excitation of projectile-like fragments, the statistical multifragmentation model (SMM) as well as the binary-decay code GEMINI were employed. A satisfactory agreement of the calculations with the experimental data was obtained. We conclude that our current understanding of the reaction mechanism at beam energies below the Fermi energy suggests that such nuclear reactions, involving peripheral nucleon exchange, can be exploited as an effective route to access extremely neutron-rich isotopes toward the r-process path and the neutron drip-line.

1 Introduction

The limits of the nuclear landscape toward the astrophysical r-process path and the neutron drip-line have recently received special attention by the nu-clear physics community (see, e.g., [1,2] and references therein). Closely related to this development is the efficient production of very neutron-rich nuclides which constitutes a central issue in current and upcoming rare isotope beam facilities (see, e.g., [3–12]).

Neutron-rich nuclides are mainly produced by spallation, fission and projectile fragmentation [13]. Spallation is an efficient mechanism to produce rare isotopes for ISOL-type techniques [14]. Projectile fission is appropriate in the region of light and heavy fission fragments (see, e.g., [15] for recent efforts on ^{238}U projectile fission). Finally, projectile fragmentation offers a universal approach to produce exotic nuclei at beam energies above 100 MeV/nucleon (see, e.g., [16,17]). This approach is, nevertheless, based on the fact that optimum neutron excess in the fragments is achieved by stripping the maximum possible number of protons (and a minimum possible number of neutrons).

To reach a high neutron-excess in the products, apart from proton stripping, it is necessary to capture neutrons from the target. Such a possibility is offered by reactions of nucleon exchange at beam energies from the Coulomb barrier [18,19] to the Fermi energy (20–40 MeV/nucleon) [20,21]. Detailed experimental data in this broad energy range are scarce at present [19,22,23]. In multinucleon transfer and deep-inelastic reactions near the Coulomb barrier [19], the low velocities of the fragments and the wide angular and ionic charge state distributions may limit the collection efficiency for the most neutron-rich products. The reactions in the Fermi energy regime combine the advantages of both low-energy (i.e., near and above the Coulomb barrier) and high-energy (i.e., above 100 MeV/nucleon) reactions. At this energy, the synergy of the projectile and the target enhances the N/Z of the fragments, while the velocities are high enough to allow efficient in-flight collection and separation.

Our initial experimental studies of projectile fragments from 25 MeV/nucleon reactions of ^{86}Kr on ^{64}Ni [20] and ^{124}Sn [21] indicated substantial production of neutron-rich fragments. Motivated by recent developments in several fa-cilities that will offer either very intense primary beams [5,8] at this energy range or re-accelerated rare isotope beams [4,5,8,9], we continued our experimental studies at 15 MeV/nucleon [24]. In this contribution, after a short overview of the experimental measurements, we present a systematic calculation of the production cross sections based on either the phenomenological deep-inelastic transfer (DIT) model or the microscopic constrained molecular dynamics model (CoMD). The good description of the experimental results with the CoMD code, as well as, with a properly modified version of the DIT code, suggest the possibility of using the present theoretical framework for the prediction of exotic nuclei employing radioactive beams that will soon be available in upcoming facilities. As an example, we present the production cross sections and the rates of neutron-rich nuclei using a radioactive beam of ^{92}Kr at 15 MeV/nucleon.

2 Outline of Results and Comparisons

A detailed presentation of the experimental results appear in [24] in which the mass spectrometric measurements of production cross sections of neutron-rich projectile fragments from the reactions of a 15 MeV/nucleon ^{86}Kr beam with ^{64}Ni, ^{58}Ni and ^{124}Sn, ^{112}Sn targets are given. We also note that the experimental results of the 25MeV/nucleon reactions and the relevant procedures are described in detail in our articles [20–23].

In Fig. 1 we present the experimental mass distributions of elements with Z 35–30 of the reaction ^{86}Kr(15 MeV/nucleon)+^{64}Ni [24] compared to the calculations with the CoMD code [25,26] combined with the de-excitation codes SMM [27] (solid line) and GEMINI [28] (dotted line), used for the de-excitation of the quasiprojectiles emerging after the dynamical stage. The results of the calculations are in overall agreement with the experimental data especially for the isotopes close to the projectile with Z = 35–32. We also observe that the microscopic CoMD model is able to describe even the rare neutron-rich products from this reaction that are the products for our main interest. The overestimation of the cross sections for the products with Z = 31,30 is related to issues of the excitation energy as calculated by CoMD and are currently under further investigation.

Subsequently, motivated by our previous studies [20,21], we employed Tassan-Got's phenomenological model of deep inelastic transfer (DIT) [29] coupled with SMM [27] or GEMINI [28]. The results of this standard version of DIT were not satisfactory. We thus proceeded with our modified version of the DIT model (DITm) [30] in which we have introduced a detailed description of the nuclear surface and the neutron skin of the involved nuclei. In Fig 2, we present the experimental mass distributions of elements with Z = 35–30 of the reaction ^{86}Kr(15 MeV/nucleon)+^{64}Ni [24] and compare them to the results of the modified DIT (DITm) calculations (dotted line) and to the results of the CoMD calculations (solid line) using SMM as the de-excitation code. From this figure we observe that the modified DIT code describes the experimental results rather well at these beam energies. Moreover, it can better describe the products further away from the projectile, that cannot be well described by CoMD, as we mentioned previously.

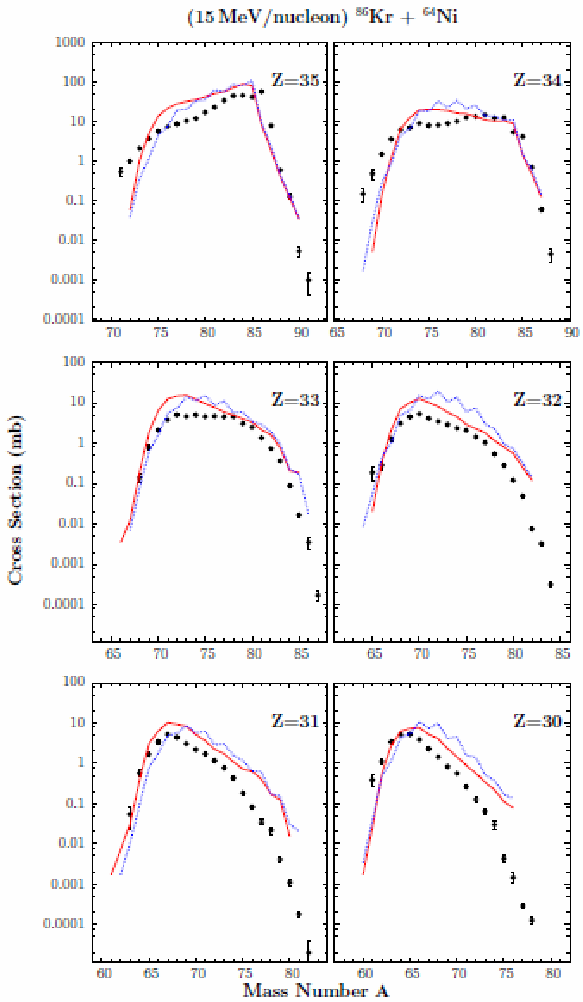

Fig. 1. Experimental mass distributions (symbols) of elements with Z= 35–30 observed in the reaction ^{86}Kr(15 MeV/nucleon)+^{64}Ni [24] compared to the results of CoMD/SMM calculations (solid red line) and CoMD/GEMINI calculations (dotted blue line).

We mention that a thorough comparison of the data with the calculations for the 15 MeV/nucleon, as well as the 25 MeV/nucleon reactions has been performed that appears in [31]. After this systematic comparison of the calculations with the experimental data of the stable ^{86}Kr beam, we proceeded to investigate what results we would obtain by using a neutron-rich radioactive beam, such as ^{92}Kr. In Fig. 3 we present again the experimental mass distributions (black symbols) of the reaction ^{86}Kr(15 MeV/nucleon)+ ^{64}Ni, the CoMD/SMM calculations for this reaction (solid line) and, furthermore, the CoMD/SMM calculations for the

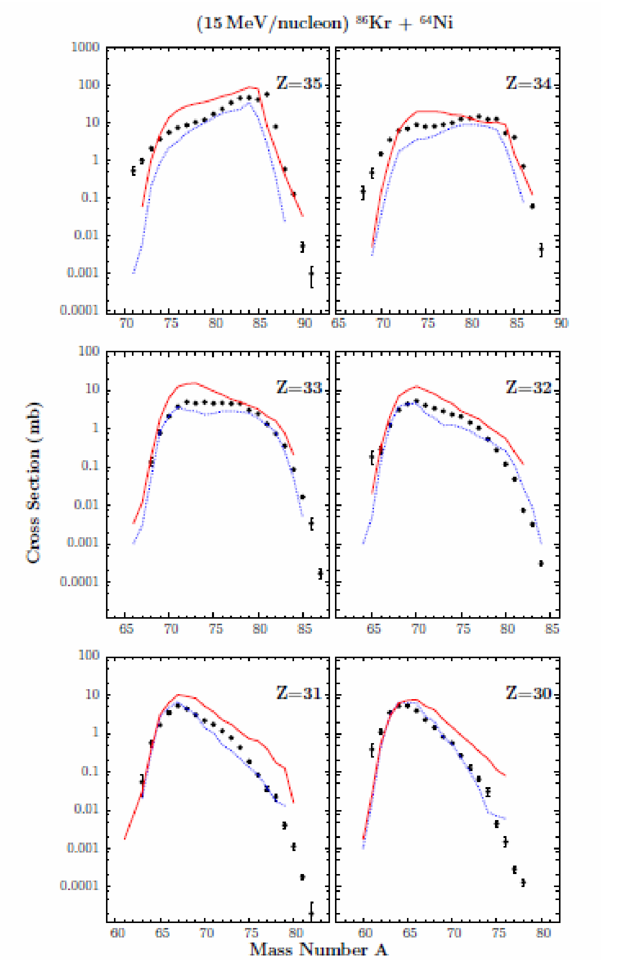

Fig. 2. Experimental mass distributions (symbols) of elements with Z=35–30 observed in the reaction ^{86}Kr(15 MeV/nucleon)+^{64}Ni [24] compared to the results of CoMD/SMM calculations (solid red line) and DITm/SMM calculations (dotted blue line).

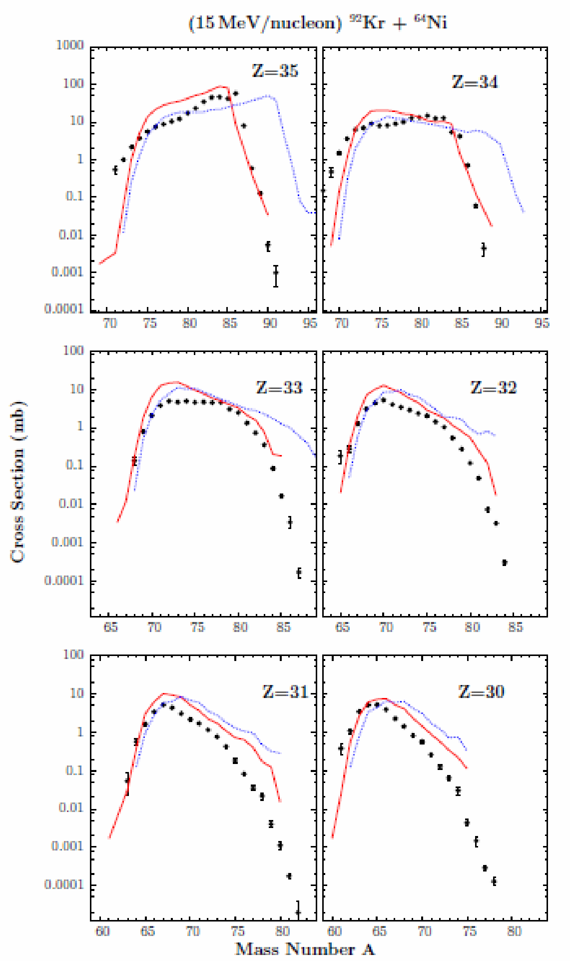

Fig. 3. Experimental mass distributions (symbols) of elements with Z = 35–30 observed in the reaction ^{86}Kr(15 MeV/nucleon)+^{64}Ni [24], calculations CoMD/SMM for the reaction ^{86}Kr(15 MeV/nucleon)+^{64} Ni (solid red line), calcula-tions CoMD/SMM for the reaction ^{92}Kr(15 MeV/nucleon)+^{64} Ni (dotted blue line).

reaction ^{92}Kr(15 MeV/nucleon)+^{64}Ni (dot-ted line). We observe that by using the neutron-rich radioactive beam of ^{92}Kr, we obtain more neutron-rich products. This is primarily true for the isotopes near the projectile. We point out that, e.g., for bromine (Z=35), isotopes that have up to 15 more neutrons (A = 96) than the corresponding stable isotope (A = 81) can be obtained. This observation indicates that by using neutron-rich radioactive beams, and through the mechanism of peripheral multinucleon transfer, we will have the possibility to produce even more neutron-rich nu-clides toward neutron drip line.

A comprehensive presentation of the CoMD/SMM calculated production cross sections of the projectile-like fragments from the above radioactive-beam re-action on the Z vs N plane is given in Fig. 4. In this figure, stable isotopes are represented by closed squares, whereas fragments obtained by the radioactive-beam reaction are given by the open circles (with sizes corresponding to cross-section ranges according to the figure key). The dashed (green) line gives the location of the neutron drip-line and the full (red) line indicates the expected path of the astrophysical rapid neutron-capture process (r-process). In the figure we clearly observe that the neutron pickup products from the ^{92}Kr pro-jectile reach and even exceed the path of the r-process near Z=30–36.

In Table I, we present the predicted cross-sections and the production rates of neutron rich isotopes from the reaction of the radioactive beam of ^{92}Kr (15 MeV/nucleon) with ^{64}Ni. For the rate calculations, the ^{92}Kr beam with intensity 0.5 pnA (3.1×10^9 particles/sec) is assumed to inter-

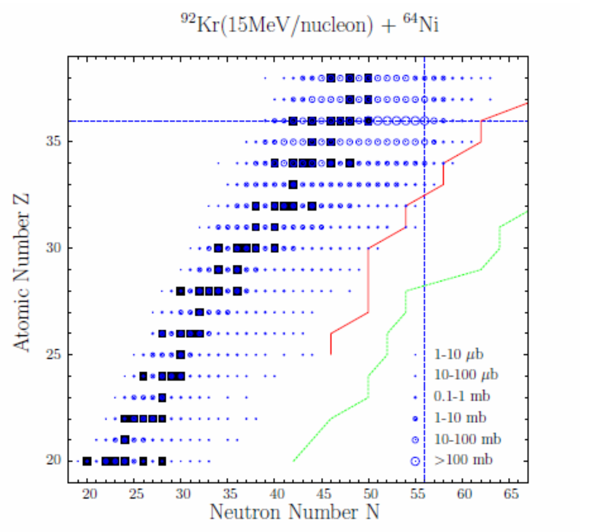

Fig. 4. Representation of CoMD/SMM calculated production cross sections of projectile fragments from the radioactive-beam reaction ^{92}Kr (15 MeV/nucleon) + ^{64}Ni on the Z–N plane. The cross section ranges are shown by open circles according to the key. The closed squares show the stable isotopes. The solid (red) line shows the astrophysical r-process path and the dashed (green) line shows the location of the neutron drip-line. The horizontal and vertical dashed lines indicate, respectively, the proton and neutron number of the ^{92}Kr projectile.

Table 1. Cross sections and rate estimates (last column) of very neutron-rich isotopes from the reaction ^{92}Kr (15 MeV/nucleon) + ^{64}Ni. For the rates, a radioactive beam of ^{92}Kr with intensity 0.5 pnA (3.1×10^9 particles/sec) is assumed to interact with a ^{64}Ni target of 20 mg/cm^2 thickness.

Rare Isotope	Reaction Channel	Cross Section (mb)	Rate (sec^{-1})
^{93}Kr	-0p+1n	18.8	1.1×10^4
^{94}Kr	-0p+2n	2.3	1.3×10^3
^{95}Kr	-0p+3n	0.63	3.8×10^2
^{96}Kr	-0p+4n	0.2	1.2×10^2
^{92}Br	-1p+1n	4.5	2.7×10^3
^{93}Br	-1p+2n	0.75	4.5×10^2
^{94}Br	-1p+3n	0.078	47
^{95}Br	-1p+4n	0.040	23
^{96}Br	-1p+5n	0.008	5
^{90}Se	-2p+0n	2.7	1.6×10^3
^{91}Se	-2p+1n	0.6	3.5×10^2
^{92}Se	-2p+2n	0.12	70
^{93}Se	-2p+3n	0.04	23

ract with a ^{64}Ni target of 20 mg/cm^2 thickness. We see that we have the possibility to produce extremely neutron-rich isotopes in these energies with the use of re-accelerated radioactive beams, such as ^{92}Kr, that will be available in upcoming rare-isotope facilities (e.g. [10,11]).

In this respect, we have plans to continue the present work at Texas A&M University (with the MARS separator) at LNS/Catania (using beams from the S800 Cyclotron and the MAGNEX spectrometer) and, in the future, at RISP/Korea (employing beams from the RAON accelerator complex and the KOBRA separator).

3 Summary and Conclusions

In summary, we performed a systematic study of the production cross sections of projectile-like fragments from collisions of ^{86}Kr projectiles with ^{64,58}Ni and Sn targets at 15 and 25 MeV/nucleon with emphasis on the neutron-rich isotopes. We noted that neutron pick-up isotopes (with up to 6-8 neutrons picked-up from the target) were observed with large cross sections. Our experimental data were compared with systematic calculations employing a two-step approach. The calculations for the dynamical stage of the projectile-target interaction were carried out using either the phenomenological deep-inelastic transfer (DIT) model or the microscopic constrained molecular dynamics model (CoMD). For the de-excitation of the projectile-like fragments, the statistical multifragmentation model (SMM) or the binary-decay code GEMINI were employed. An overall good agreement with the experimental results was observed. With the current understanding of the reaction mechanism at these beam energies, we suggest that these nuclear reactions, involving peripheral nucleon exchange, be exploited as an efficient route to access neutron-rich rare isotopes toward the r-process path and the neutron drip-line. Therefore, future experiments in several accelerator facilities [13] can be planned that will en-able a variety of nuclear structure and nuclear reaction studies in unexplored regions of the nuclear chart.

References

1. J. Erler et al, Nature **486**, 509 (2001).
2. J. Aysto, W. Nazarewicz, M. Pf`utzner, C. Signorini, eds, Proceedings of the Fifth International Conference on Exotic Nuclei and Atomic Masses (ENAM'08), Ryn, Poland, September 7–13 (2008); Eur. Phys. J. **A 42** (2009).
3. D. F. Geesaman, C. K. Gelbke, R. V. F. Janssens, B. M. Sherrill, Ann. Rev. Nucl. Part. Sci. **56**, 53 (2006).
4. FRIB main page: www.frib.msu.edu
5. GANIL main page: www.ganil.fr
6. GSI main page: www.gsi.de
7. RIBF main page: www.rarf.riken.go.jp/Eng/facilities/RIBF.html
8. ATLAS main page: www.phy.anl.gov/atlas/facility/index.html
9. EURISOL main page: www.eurisol.org
10. RISP main page: www.risp.re.kr/eng/pMainPage.do
11. K. Tshoo, Y. K. Kim, Y. K. Kwon et al, Nucl. Instrum. Methods **B 317**, 242 (2013).

12.K. Tshoo, H. Chae, J. Park, J.Y. Moon, Y.K. Kwon, G.A. Souliotis et al, Nucl. Instrum. Methods **B 376**, 188 (2016).
13.Y. Blumenfeld, T. Nilsson and P. Van Duppen, Phys. Scr. **T152** 014023 (2013).
14. A. Keli´c, M. V. Ricciardi, K. -H. Schmidt, BgNS Transactions **13**, 98 (2009).
15. H. Alvarez-Pol et al., Phys. Rev. **C 82**, 041602 (2010).
16. O. B. Tarasov et al., Phys. Rev. **C 80**, 034609 (2009).
17. S. Lukyanov et al., Phys. Rev. **C 80**, 014609 (2009).
18. V. V. Volkov, Phys. Rep. 44, 93 (1978).
19. L. Corradi, G. Pollarolo, S. Szilner, J. Phys. **G 36**, 113101 (2009).
20. G. A. Souliotis et al., Phys. Lett. **B 543**, 163 (2002).
21. G. A. Souliotis et al., Phys. Rev. Lett. **91**, 022701 (2003).
22. G. A. Souliotis et al., Nucl. Instrum. Methods **B 204**, 166 (2003).
23. G. A. Souliotis et al., Nucl. Instum. Methods **B 266**, 4692 (2008).
24. G. A. Souliotis et al., Phys. Rev. **C 84**, 064607 (2011).
25. M. Papa et al., Phys. Rev. **C 64**, 024612 (2001).
26. M. Papa et al, J. Comp. Phys. **208**, 403 (2005).
27. J. Bondorf et al., Phys. Rep. **257**, 133 (1995).
28. R. Charity et al., Nucl. Phys. **A 483**, 391 (1988); Phys. Rev**. C 58**, 1073 (1998).
29. L. Tassan-Got and C. Stephan, Nucl. Phys. **A 524**, 121 (1991).
30. M. Veselsky and G.A. Souliotis, Nucl. Phys. A **765**, 252 (2006).
31. P.N. Fountas, G.A. Souliotis, M. Veselsky and A. Bonasera, Phys. Rev. **C 90**, 064613 (2014).

Fission in High-Energy Proton-Induced Spallation Reactions: Recent Progress

Nikolaos G. Nicolis[1], A. Asimakopoulou[2] and G.A. Souliotis[2]

[1]Department of Physics, The University of Ioannina, Ioannina 45110, Greece
[2]Laboratory of Physical Chemistry, Department of Chemistry, University of Athens, Athens, Greece

Abstract. A number of projects of current interest such as transmutation of nuclear waste, neutron sources, radiation damage in space etc. require a detailed modeling of spallation reactions induced by high-energy protons. For a phenomenological description of spallation reactions, we couple the results of the intranuclear cascade model ISABEL with evaporation calculations performed with the statistical model codes SMM and MECO incorporating symmetric fission. Preliminary results of 200, 500 and 1000MeV protons on ^{208}Pb targets are compared with experimental data. Extension of our calculations to describe the reaction mechanism is discussed.

1 Introduction

The study of nucleon-induced spallation reactions is a topic of extensive experimental and theoretical studies due to their importance in basic and applied Nuclear Science. Spallation reactions have numerous applications in accelerator-driven systems (ADS), transmutation of nuclear waste, spallation neutron sources and the production of rare isotopes. Astrophysics and space research also benefits from this research due to implications in interaction of cosmic rays with interstellar bodies and radiation damage of electronic devices in space. Last but not least, this type of reactions provides a framework for testing high-energy nuclear reaction models in the bombarding energy range above 150-200 MeV [1].

A proton-induced spallation reaction (SR) proceeds in two stages. In the first stage, the incident particle interacts with the nucleons of the target in a sequence of collisions. As a result, we have the formation of an intranuclear cascade (INC) of high-energy (greater than 20 MeV) protons, neutrons and pions within the nucleus. This is a fast process lasting approximately 10^{-22}s. During the intranuclear cascade, some of these energetic hadrons escape from the target. Others deposit their kinetic energy in the nucleus leaving it in an excited state. In the second stage, the produced excited nuclear species deexcite. Sequential evaporation is assumed to be the dominant process with a typical time scale of 10^{-8}s – 10^{-6}s. Emission of nucleons, protons, alpha-particles and gamma-rays is dominant. Emission of heavier nucleon clusters in their ground or excited states is also possible. If the target is heavy enough, high-energy fission may compete with sequential evaporation. The deexcitation products of target-like and/or fission fragments may be radioactive. In the case of thick target experiments, the secondary high-energy particles produced in the INC phase move roughly in the same direction as the incident proton and induce secondary spallation reactions. In such a case, a hadronic cascade is observed as a result of an accumulation of all reactions initiated by the primary and secondary particles. In many applications it is desirable to have a reliable model description of the number of neutrons emitted in a spallation reaction, as well as associated observables like fission cross sections, mass and isotopic distributions of the reaction products.

In the present work we are concerned with the description of thin target experiments. Our objective is to describe proton-induced spallation reactions on ^{208}Pb at 200, 500 and 1000 MeV. We choose a phenomenological approach in which we couple the results of an INC code with an evaporation code extended to describe high-energy symmetric fission. The employed nuclear reaction codes are briefly discussed in Section 2. In Section 3, results of preliminary calculations are compared with experimental data consisting of fission cross sections, neutron multiplicities, mass and isotopic distributions of evaporation residues and fission fragments. The results of two evaporation codes coupled to the same INC code input are compared in Section 4. A summary of our results is given in Section 5.

2 Description of the nuclear reaction codes

For the description of the INC phase, we use the code ISABELE [2,3]. It is a well tested Monte-Carlo code with a long history of improvements. The target nucleus is simulated by a continuous medium bounded by a diffuse surface. Collisions between the incident nucleon and the nucleons of the target occur with a criterion based on the mean free path. Between successive collisions, linear trajectories are assumed. Free nucleon-nucleon cross sections are used. The code allows for elastic and inelastic N-N collisions. Furthermore, it takes full account of Pauli blocking i.e. interactions resulting in nucleon falling below the Fermi sea are forbidden. From a typical run we obtain the mass number (A), atomic number (Z) and excitation energy (E*) of the various nuclear species produced in the INC phase. The deexcitation stage is described with the codes SMM and MECO.

The SMM code [4,5,6] combines a description of sequential compound nucleus decay with a multifragmentation model. Equilibrium compound nucleus decay dominates at excitation energies E*<2-3 MeV/A. At higher energies, the importance of these processes diminishes and multifragment decay takes over. The fission decay channel is taken into account empirically, by producing fission fragment mass distributions with parameters adjusted to fit experimental data [6]. At E*>4 MeV/A, multifragmentation is expected to dominate. Thus, all possible decay processes occuring in the wide excitation energy range realized in a spallation reaction should be adequately taken into account.

The code MECO [7] is a multisequential binary decay code. It describes the equilibrium decay of excited nuclei as a sequence of binary division processes involving the emission of light particles, gamma rays and nucleon clusters in their ground, excited bound and unbound states. Emission of nucleons and progressively heavier clusters leading to symmetric mass divisions are calculated in a generalized Weisskopf evaporation formalism. The computational method is Monte-Carlo, thus allowing the simulation of experimental conditions. Also, it may accommodate any number of user-defined channels. MECO provides a complete description of compound nucleus decay of medium to low mass (A<100) systems and excitation energies E*<2-3 MeV/A.

In order to calculate the decay of heavy compound nuclei with MECO, we introduce a fission decay mode. At each decay step, we calculate the fission probability, as the ratio of the fission decay width over the sum of decay widths of all possible decay modes. We calculate the fission decay width according to the transition stage theory [8]. As a first approximation, we assume symmetric mass divisions. The employed fission barrier heights correspond to a liquid drop model calculation including the finite range of nuclear forces [9]. It is well known that the standard theory of fission, just described underestimates the pre-fission neutron multiplicities. For this reason, we introduce a fission delay to account for the slowing effects of nuclear dissipation [10]. Our Bohr-Wheeler decay width was multiplied by the Kramer's reduction factor. The reduction parameter gamma was set equal to 5, a value suggested from fission studies of heavy-ion induced reactions [10].

Fission fragment masses are selected from a Gaussian distribution with an excitation energy dependent width, parametrized from experimental data [11]. Each fragment is assumed to have the same N/Z ratio as the parent nucleus. From the conservation of energy and linear momentum we obtain the kinetic energies of the two fragments. The excitation energy of the parent nucleus is divided among the two fragments in proportion to each fragment's mass, i.e. assuming equal temperatures. Then, we follow the particle decay of each fragment.

3 Comparisons with experimental data

Figure 1 shows the mass distributions of evaporation residues and fission fragments in 500MeV p + ^{208}Pb spallation reactions. Experimental data (symbols) [12,13] are compared with calculations performed with the code ISABEL followed by SMM (open histogram) and MECO (solid line).

The ISABEL-SMM calculation describes well the plateau of the mass distribution of evaporation residues. However, it underpredicts the low-mass region of the distribution. The same calculation predicts two nearby broad mass peaks for the mass distribution of fission fragments, implying an excess of asymmetric fission. This is in contrast of the experimental data, which show a broad mass peak, centered at approximately A=97.

The ISABEL-MECO calculation, predicts a plateau for the evaporation residue mass distribution in agreement with the shape but a greater magnitude than the experimental data. It also underpredicts the low-mass region. For the mass distribution of the fission fragments, this calculation predicts a broad distribution with a centroid that agrees with experiment. This was expected, since the code takes only symmetric fission into account. However, the width of the experimental mass distribution is underestimated. Since the width of the mass distribution in MECO was calculated in accordance with systematics, this underprediction means that we need to consider the asymmetric mode of fission as well.

Comparing SMM with MECO, we realize a rough agreement between the two codes in the description of the evaporation residue mass distribution. However, the two codes disagree with each other and both fail to describe fully the fission fragment mass distribution. The SMM code needs a symmetric fission component and MECO needs an asymmetric one. Charge distributions of evaporation residues and fission fragments calculated with the two codes were found consistent.

In Figure 2 we show the mass distributions of evaporation residues and fission fragments in 1000MeV p + ^{208}Pb spallation reactions. The experimental data [14] are shown with symbols and compared with calculations performed with ISABEL-SMM (open histogram) and ISABEL-MECO (solid line).

The ISABEL-SMM calculation predicts well the plateau of the evaporation residue mass distribution but underestimates the low-mass region. The fission fragment

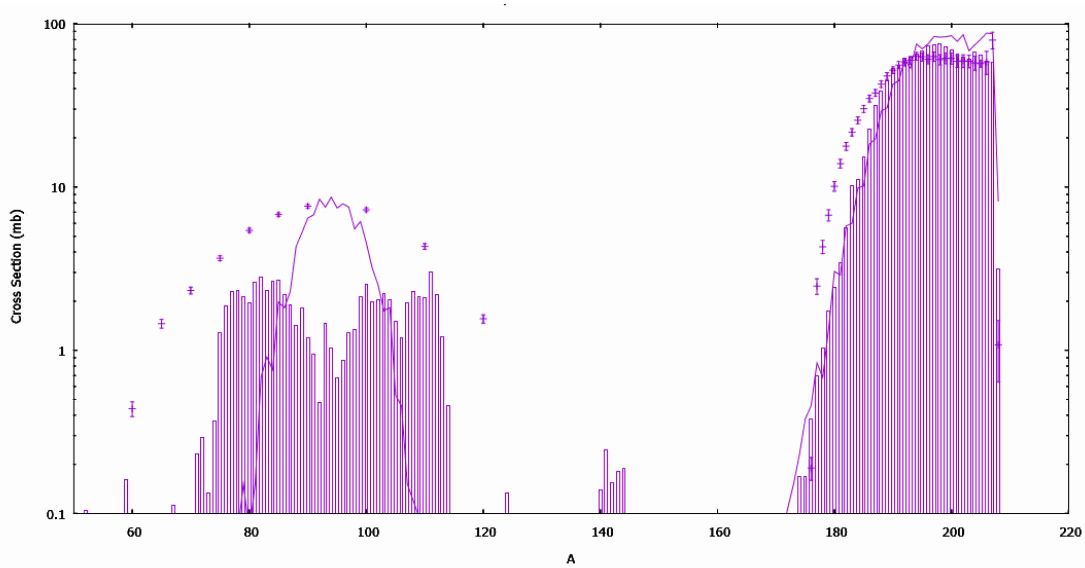

Fig. 1. Mass distributions of evaporation residues and fission fragments in spallation reactions of 500MeV p + ^{208}Pb. Experimental data (symbols) are compared with calculations performed with the code ISABEL followed by SMM (open histogram) and MECO (solid line).

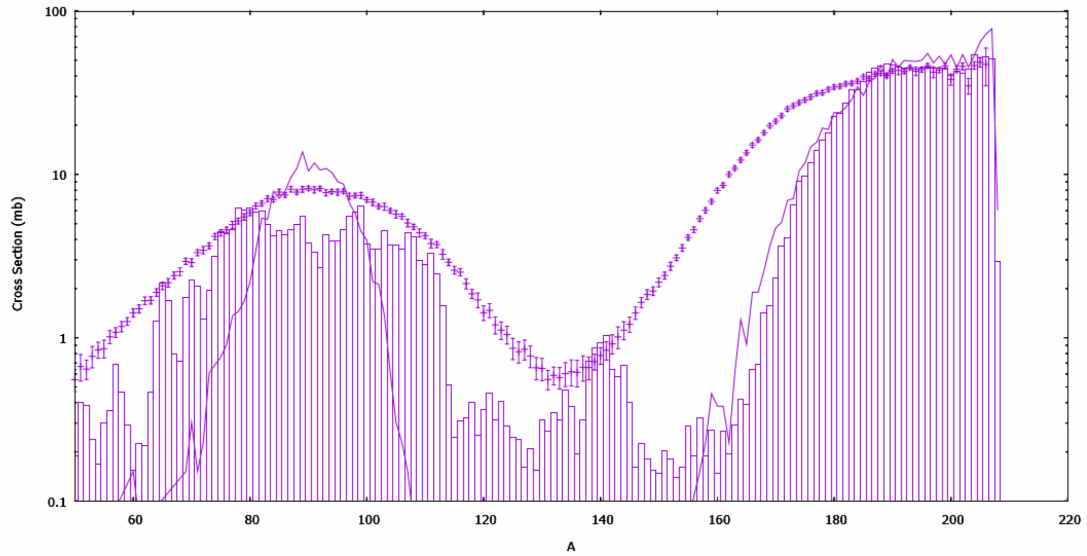

Fig. 2. Mass distributions of evaporation residues and fission fragments in spallation reactions of 1000MeV p + ^{208}Pb. Experimental data (symbols) are compared with calculations performed with the code ISABEL followed by SMM (open histogram) and MECO (solid line).

mass distribution is again predicted to have two peaks. However, its width is very broad and tends to approach the data. At this bombarding energy, we have a yield in the region between A=120 and A=150, filling the gap between the evaporation residue and the fission fragment mass distributions.

Comparing SMM with MECO at 1000MeV, we realize again a similarity in the description of the evaporation residue mass distribution. The two codes differ in the description of the fission fragment mass distribution, in a complementary way, as pointed out at 500MeV. A new feature of the SMM code at this energy is the appearance of masses in the A=120-150 range. Some analysis is needed in order to trace the origin of these events. Charge distributions of evaporation residues and fission fragments calculated with the two codes were found consistent.

In Figure 3, we show isotopic yields of various elements produced by p + ^{208}Pb at 500MeV. The symbols on the panels show the cross sections as a function of the mass number for elements with (Z=82)Pb, (Z=81)Th, (Z=80)Hg and (Z=79)Au. The ISABEL-SMM calculation is shown with the open histogram. For Z=82 and Z=80, it describes well the majority of cross sections. However, it overestimates the experimental cross sections most neutron-deficient isotopes for Z=81 and Z=82. For Z=80 we have a good agreement with the data. However, for Z=79 the calculation starts underestimating the cross sections of all isotopes. The ISABEL-MECO shown by the solid curve provides a better description of the isotopic yields for Z=80-82. For Z=79, the calculation underestimates the data at the same level as the SMM calculation.

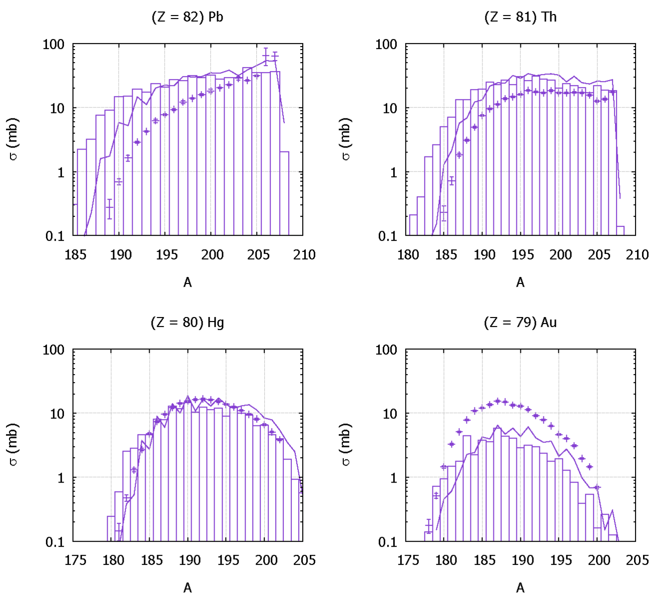

Fig. 3. Isotopic distributions in spallation reactions of 500MeV p + ^{208}Pb, for the indicated values of Z. Experimental data (symbols) are compared with calculations performed with the code ISABEL followed by SMM (open histogram) and MECO (solid line).

4 Summary and outlook

In the present work, we combined the intranuclear cascade code ISABEL with the code SMM as well as the sequential binary decay code MECO in an effort to study spallation reactions induced by high-energy protons. Preliminary calculations of p + ^{208}Pb at bombarding energies 500 and 1000MeV were compared with experimental mass and isotopic distributions. For the evaporation residue mass, charge and isotopic distributions our calculations with MECO are consistent with the predictions of the SMM code. They describe the heavy but underestimate the low-mass region of the evaporation residue mass distribution. Both codes require improvements for a succesful description of the experimental fission fragment mass distributions. From the point of view of the MECO code, the fission decay mode is expected to improve with an appropriate treatment of asymmetric and symmetric fission. Work in this direction is in progress.

References

1. J.C. David, *Spallation reactions. A successful interplay between modeling and applications*, Eur. Phys. J. A51, 68 (2015).
2. Y. Yariv and Z. Fraenkel, Phys. Rev. C20, 2227 (1979).
3. Y. Yariv and Z. Fraenkel, Phys. Rev. C24, 488 (1981).
4. J.P. Bondorf, A.S. Botvina, A.S. Iljinov, I.N. Mishustin and K. Swneppen, Phys. Rep. 257, 133 (1995).
5. A.S. Botvina, (INR, Moscow, Russia) *Role of multifragmentation in spallation reactions*, Proceedings of Joint ICTP-IAEA Advanced Workshop on Model Codes for spallation reactions, Trieste, Italy, 4-8th February 2008, arXiv:0806.3455 [nucl-th]
6. N. Eren, N. Buyukcizmeci, R. Ogul and A.S. Borvina, Eur. Phys. J. A49, 48 (2013).
7. N.G. Nicolis, Int. J. Mod. Phys. E17, 1541-1556 (2008).
8. N. Bohr and J.A. Wheeler, Phys. Rev. 56, 426 (1939).
9. A.J. Sierk, Phys. Rev. C33, 2039 (1986).
10. J.P. Lestone, Phys. Rev. C59, 1540 (1999).
11. G.D. Adeev *et al.*, Preprint INR 816/93, Moscow, 1993
12. L. Audouin *et al.*, Nucl. Phys. A768, 1-21 (2006).
13. J.L. Rodriguez-Sanchez, J. Benlliure *et al.*, Phys. Rev. C 91, 064616 (2015).
14. T. Enqvist *et al.*, Nucl. Phys. A 686, 481-524 (2001).

AMIAS: A Model Independent Analysis Scheme – From Hadronics to Medical Imaging

E. Stiliaris[1,2] and C.N. Papanicolas[1,2]

[1] Department of Physics, National and Kapodistrian University of Athens, Greece
[2] The Cyprus Institute, Nicosia, Cyprus

Abstract. AMIAS is a novel method for extracting physical parameters from experimental and simulation data. The method is based on statistical concepts and it relies on Monte Carlo simulation techniques. It identifies and determines with maximal precision parameters that are sensitive to the data. The method has been extensively studied and it is shown to produce model independent results. It is applicable to a wide range of scientific and engineering problems. The initial ideas on which the method relies and the further development of the model are presented. A brief review on the application of AMIAS in the analysis of experimental data in hadronic physics and of lattice QCD correlators, and most recently in the image reconstruction of tomographic data, are introduced here.

PACS. 02.30.Zz Inverse problems – 21.60.Ka Monte Carlo methods in nuclear structure – 13.40.Gp Nuclear form factors – 13.60.Le Photoproduction of mesons – 12.38.Gc Lattice QCD calculations – 87.57.nf Medical image reconstruction

1 Introduction

A principal task in experimental and computational physics concerns the determination of the parameters of a theory (model) from experimental or simulation data. Examples are abundant: the determination of the parameters of the Standard Model in Particle Physics, the multipole amplitudes in Nucleon Resonance excitation in Hadronic Physics, the determination of the spectrum from correlators in Lattice QCD calculations, the parameters of acoustic resonances in Cosmology, to mention a few.

The data from which information on parameters of the theory is to be extracted are characterized by statistical uncertainties and systematic errors, are typically of limited dynamic range and sensitive only to a few of the model parameters, rendering this task difficult and often intractable. Identifying which parameters of the model can be determined from the available data is often difficult to prejudge and their extraction without bias is often impossible. Particularly hard is the determination of the systematic and model uncertainties that ought to be assigned to the extracted values of the parameters.

We have addressed this problem via a method, which is known as the Athens Model Independent Analysis Scheme, "AMIAS" [1]. This method is capable of extracting theory (model) parameters and their uncertainties from a set of data in a rigorous, precise, and unbiased way. The methodology is first briefly presented and then subsequently applied to two problems in Hadronic Physics, namely the extraction of the multipole excitation amplitudes for the Nucleon resonances and in particular that of the first excited state of the Nucleon, the $\Delta(1232)$ resonance and secondly, the creation of the mass spectrum of hadrons from Euclidean time correlators in lattice QCD simulations. In addition, the image reconstruction problem in Medical Physics is also discussed in the framework of AMIAS.

2 AMIAS Methodology

The AMIAS method is applicable to problems in which the parameters to be determined are linked in an explicit way to the data through a theory or model. There is no requirement that this set of parameters are orthogonal; they can be subjected to constraints, e.g. by requiring that unitarity is satisfied. The method requires that a quantitative criterion for the "goodness" of a solution is chosen and thus far we have employed the χ^2 criterion.

For a given theory any set of values for its parameters, satisfying its symmetries and constraints, provides a solution having a finite probability of representing reality. This probability can be quantified through a comparison to the data being analyzed. Based on these concepts AMIAS can be formulated as follows:

A set of parameters $A_1, A_2, ..., A_N \equiv \{A_\nu\}$ which completely and explicitly describes a process within a theory, can be determined from a data set $\{V_k \pm \varepsilon_k\}$, produced by this process, by noting that any arbitrary set of values $\{a_\nu\}^j$ for these parameters constitutes a solution having a probability $P(j)$ of representing "reality" which is equal to:

$$P(j) = G[\chi^2(j), \{a_\nu\}^j] \tag{1}$$

where G is a function of the data and the parameters of the model and of χ^2, where,

$$\chi^2(j) = \sum_k \left\{ \frac{(U_k^j - V_k)}{\varepsilon_k} \right\}^2 \tag{2}$$

Thus $P(j)$ is a function of the χ^2 resulting from the comparison to the data $\{V_k \pm \varepsilon_k\}$ of the predicted, by the theory, values U_k^j by the $\{a_\nu\}^j$ solution.

In the case where we chose $G = e^{-\chi^2/2}$ the results obtained by AMIAS are related to those obtained by χ^2 minimization methods and widely used and implemented in a number of codes (e.g. MINUIT). The results become identical if correlations among the parameters of the theory are absent or ignored.

We call an ensemble Z of such a_ν^j solutions *Canonical Ensemble of Solutions*, which has properties that depend only on the experimental data set. Similarly a *Microcanonical Ensemble of Solutions* can be defined as the collection of solutions which are characterized by

$$\chi_A^2 \leq \chi^2 \leq \chi_B^2 \tag{3}$$

where χ_A^2 and χ_B^2 define a sufficiently narrow range in χ^2 space. A case of particular interest concerns the microcanonical ensemble near the minimum χ^2 value:

$$\chi^2 \leq \chi_{min}^2 + C \tag{4}$$

where C is usually taken to be the constant equal to the effective degrees of freedom of the problem.

The extraction of the model parameters $\{A_\nu \pm \delta A_\nu\}$ for a specific set of data can be accomplished by employing the following procedure:

– A canonical ensemble of solutions, is being constructed by randomly choosing values, $\{a_\nu\}^j$, for the set of parameters $\{A_\nu\}$ of the theory within the allowed physical limits and by imposing the required constraints. Each set $\{a_\nu\}^j$ constitutes a point in the ensemble which is labeled by the χ^2 value this solution generates when compared with the data. In the absence of constraints, any given model parameter A_ν will assume all allowed values with equal probability (equipartition postulate).
– To each point of the ensemble $\{a_\nu\}^j$ a probability is assigned, equal to $P(j)$. Following standard statistical concepts, the probability $\Pi(a_\nu)$ of a parameter A_ν assuming a specific value a_ν in the range $(a_\nu, a_\nu + \Delta a_\nu)$ is equal to:

$$\Pi(a_\nu) = \frac{\int\limits_{a_\nu}^{a_\nu + \Delta a_\nu} \sum_j dA_\nu^j \; P(j)}{\int\limits_{-\infty}^{+\infty} \sum_j dA_\nu^j \; P(j)} \tag{5}$$

This expression defines the Probability Distribution Function (PDF) of any parameter of the theory for representing "reality". It thus contains the maximum information that can be obtained from the given set of data. Having obtained the PDF, numerical results can be derived, usually moments of the distribution. The mean value is normally identified as the "solution" and the corresponding variance as its "uncertainty".

It is manifestly obvious that AMIAS has minimal assumptions and that it introduces no methodological bias to the solution. It determines the theory/model parameters that exhibit sensitivity to the data yielding PDFs that allow only a restricted range of values usually with a well defined maximum and a narrow width. If the data do not contain physical information to determine some of the parameters, then the resulting PDFs are featureless. The underlying stochastic approach allows easy scalability to a very large number of parameters even with limited number of data.

3 Multipole Extraction employing AMIAS

In applying AMIAS to the problem of multipole extraction in the $N \to \Delta$ transition the parameters to be extracted, $\{A_\nu\}^j$ in the general formulation, are the multipole amplitudes $M_{L\pm}$, and if the data allow, the isospin separated amplitudes $M_{L\pm}^{1/2}, M_{L\pm}^{3/2}$. The experimental observables (data) $\{O_i\}$ are typically cross section and polarization asymmetries. Furthermore, the parameters of our problem, the multipole amplitudes, are subjected to the constraint of unitarization, by imposing the Fermi Watson theorem.

The linkage of observables to multipoles in the case of nucleon resonances is based on the Chew-Goldberger-Low-Nambu (CGLN) amplitude composition via the functions $F_1 \ldots F_6$ [2]. In the demonstration case we will examine which concerns the Bates-Mainz data, the multipoles used refer to the $\pi^0 p$ charge channel which are connected to the $(A_p^{1/2},\ A_n^{1/2},\ A^{3/2})$ isospin-set through the relation:

$$A_{\pi^0 p} = A_p^{1/2} + \frac{2}{3} A^{3/2}$$

Following the standard practice of the field, we shall also consider the phases of the multipoles as known (from πN scattering) with extreme precision and therefore fixed. The above choices allow a meaningful comparison with previous analyses and model results; however they are not inherent to the scheme. It is quite easy to consider the phases, as experimental parameters characterized by uncertainties or even to perform a combined analysis of electroproduction and πN scattering data.

To demonstrate the capabilities of the method we reanalyzed the the $H(e, e'p)\pi^0$ measurements performed at $Q^2 = 0.127\ GeV^2/c^2$ and $W = 1232$ MeV [3]. This set consists of Bates and Mainz data with 31 data points, cross section results for the σ_{TT}, σ_{LT}, σ_0, σ_{E2} and the polarized beam cross section $\sigma_{LT'}$. Since the MAID model provides for this Q^2 a good description of the data set, the MAID-2003 multipoles are used as a starting point for the AMIAS method.

As commented earlier, the starting point can be arbitrary, however a good starting point provides easy convergence and considerable savings in computer time. A $L_{cut} = 5$ value was chosen, so that a sufficiently large number of background amplitudes are included in the computational exploration. Results are derived by uniformly varying the real and imaginary part of the input amplitudes of the model in the π^0 charge-channel after a reiterative selection of the phase volume to be explored. The unitary box width w_0 assigned to each of the input amplitudes was set to the $\pm 10\%$ of their central (MAID) value. Amplitudes in general were allowed to vary normally in a range of $20 \times w_0$; this range was reduced for the sensitive E_{1+} and L_{1+} amplitudes and particularly for the M_{1+} multipole.

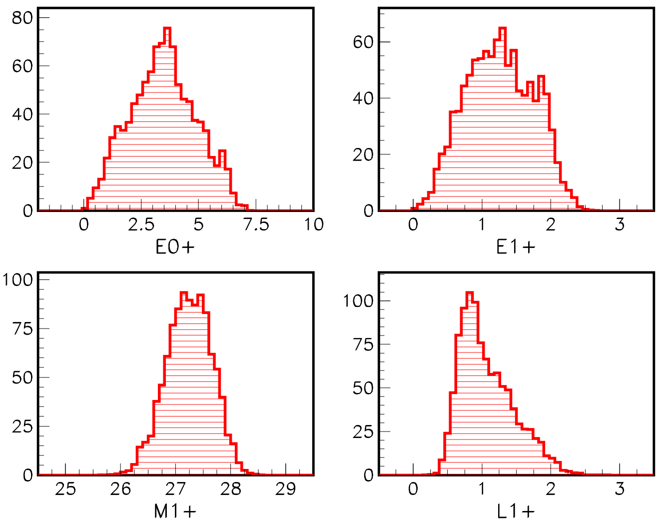

Fig. 1. Probability distributions for the norms of some of the sensitive amplitudes of the analyzed Bates/Mainz data set. The distributions allow the determination of the central value and corresponding uncertainty for each of the multipoles.

The resulting (non-normalized) probability distributions for some of the sensitive amplitudes are shown in Figure 1. The probability distributions allow the determination of both the value and the uncertainty of each of the sensitive multipoles. The extracted multipole values and (1σ confidence) uncertainties, of the Bates/Mainz data fit with the AMIAS method are presented in the Table 1.

The quoted uncertainties for the extracted multipoles include all experimental errors (statistical + systematic) and obviously contain no model error. The relative uncertainties, which can be considered as a measure of the sensitivity for each of the extracted multipoles, are also tabulated.

In Figure 2 the allowed region for partial cross sections for $Q^2 = 0.127\ GeV^2/c^2$ and $W = 1232$ MeV is shown in the shaded area (bands). These bands are defined through

Table 1. Extracted values and (1σ) uncertainties for the norm of the sensitive multipoles from the Bates/Mainz experimental data set using the AMIAS method. The results are presented with decreasing multipole sensitivity, which is reflected in the relative uncertainty. The MAID-2003model values are tabulated for comparison. The multipoles are in units of $10^{-3}/m_\pi$

.

Multipole	Extracted Value	Relative Error	MAID-2003
M_{1+}	27.24 ± 0.20	0.73 %	27.464
L_{1+}	$0.82\ ^{+0.20}_{-0.09}$	17.7 %	1.000
L_{0+}	2.23 ± 0.41	18.4 %	2.345
E_{0+}	3.44 ± 0.70	20.3 %	2.873
E_{1+}	$1.16\ ^{+0.32}_{-0.24}$	24.1 %	1.294

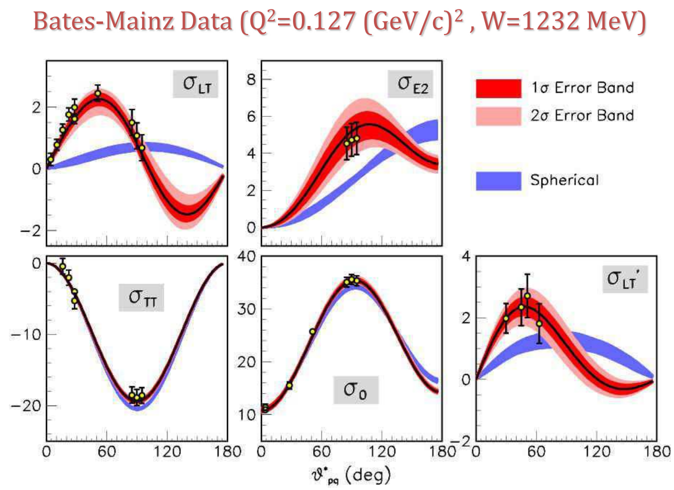

Fig. 2. The experimentally allowed region for the partial cross sections for $Q^2 = 0.127\ GeV^2/c^2$ and $W = 1232$ MeV, as determined by the analysis of the Bates/Mainz data by AMIAS: the red bands depict the allowed region with 1σ (dark red) and 2σ (light red) confidence. The blue shadowed region shows the "spherical" solutions.

the result of the AMIAS solution for the Bates/Mainz data set. The shaded band shows the envelope that accommodates all possible solutions that are compatible with the experimental data with 1σ or 2σ confidence level. These uncertainty bands are model independent.

Similar analyses for Photoproduction ($Q^2 = 0$)data [4] and for other kinematical values around the Δ-Resonance [5] have been performed.

4 Nucleon Excited States in Lattice QCD

The study of excited states within the framework of Quantum Chromodynamics on the lattice (LQCD) is difficult since it is based on the evaluation of Euclidean correlation functions for which the excited states are exponentially suppressed as compared to the ground state. The standard approach to study excited states is based on the variational principle, where one considers a number of interpolating fields as a variational basis and defines a generalized eigenvalue problem (GEVP) using the correlation matrix computed within the chosen variational basis [6].

In this section, the application of AMIAS for extracting the excited states from Euclidean correlators to study the nucleon spectrum is examined. A first analysis of the nucleon two-point function in Lattice QCD was carried out with promising results [7]. Here, the method is extended to analyze correlation matrices and compare the results with those obtained in recent study using the standard variational method. An advantage of AMIAS is that it can be applied to the correlation function at small separation times by allowing any number of states to contribute rather than to the large time-limit behavior typically done in the variational method. In fact, the merit of the method is that it determines the actual number of states on which the correlation matrix is sensitive on. Thus AMIAS does not rely on plateau identification of effective masses, which are usually noisy and thus difficult to determine, but instead it utilizes all the information encoded in the correlation function with the advantage of exploiting the small time separations where the statistical errors are small.

The quantity of interest in this work is a Euclidean two-point function computed at discrete times t_j. For Lattice QCD correlators the spectral decomposition of the hadron propagator is given by the equation:

$$C(t_j) = \sum_{n=0}^{\infty} A_n e^{E_n t_j} \tag{6}$$

where the parameters A_n and E_n are to be determined by AMIAS and the exponentials are ordered by the value of E_n ($E_0 < E_1 < E_2 \ldots$). For large values of the time the exponential with the smallest exponent dominates.

One of the significant advantages of AMIAS is that it determines unambiguously the parameters to which the data are sensitive on i.e. it determines n_{max} in the truncation of the infinite sum in Equation 6. The results obtained are then invariant under changes of n_{max}. The strategy is to increase n_{max} until there is no sensitivity to the additional exponentials and thus no observable change in the sampled spectrum. In Fig 3 an example of such an analysis for the nucleon correlator $C(t)$ is shown.

Another central issue that is properly treated in AMIAS, is the handling of correlations, since all possible correlations are accounted for. The sampling method allows all fit parameters to randomly vary and to yield solutions with all allowed values, including the insensitive exponential terms. The visualization of the dominant correlations can be accomplished by a two-dimensional contour plot in which the values of a selected pair of parameters is varied around the region of maximum probability, keeping all other parameters fixed.

Figure 4 presents such a correlation analysis, where the plane defined by the values of the parameters is color coded according to the χ^2-value. The top-left and bottom-left parts are examples where the parameters are correlated, while the right part is an example of uncorrelated

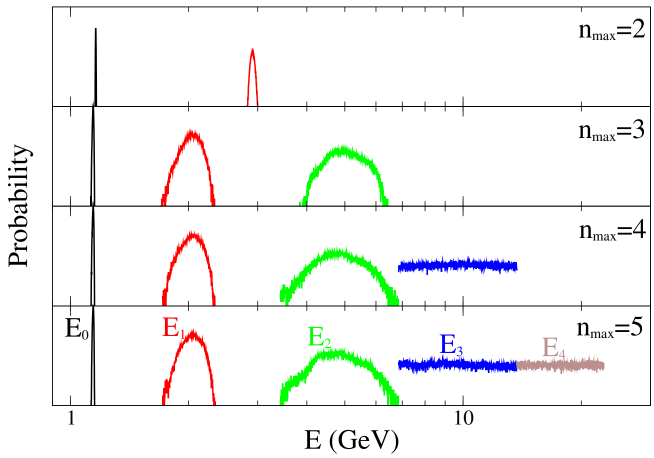

Fig. 3. The Probability Density Functions (PDFs) of E_n for different values of the truncation parameter n_{max}. A well defined distribution is only present for the parameters that contribute to the PDF. Parameters without any contribution lead to a uniform distribution.

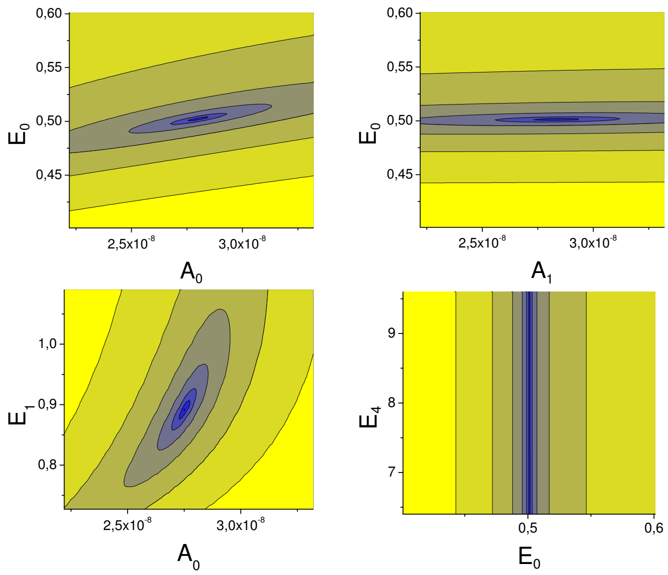

Fig. 4. Contour plots showing correlations among the parameters. The contours are color coded according to the χ^2-value.

parameters. In particular the bottom-right part is an example where sampling is insensitive to one of the parameters, namely E_4, indicating in this case the absence of a fourth state (compared with Fig. 3).

5 Tomographic Image Reconstruction

In the emission and absorbtion tomography, an image can be simply represented by a square matrix whose elements are proportional to the intensity of each pixel. Once this matrix is known, the projections in various angles θ, that is the sum of all cell contributions (Figure 5) along a certain ray R_i can be easily calculated. In tomography, we would rather interested in solving the inverse problem, that is to reconstruct the square matrix from its projections at different directions. By using the radiation emitted by an object, after the injection of radiopharmaceutical, we are able to obtain sectional (planar) images of the object. These projection data are then feeded into a reconstruction algorithm. The intensity of each ray R_i at

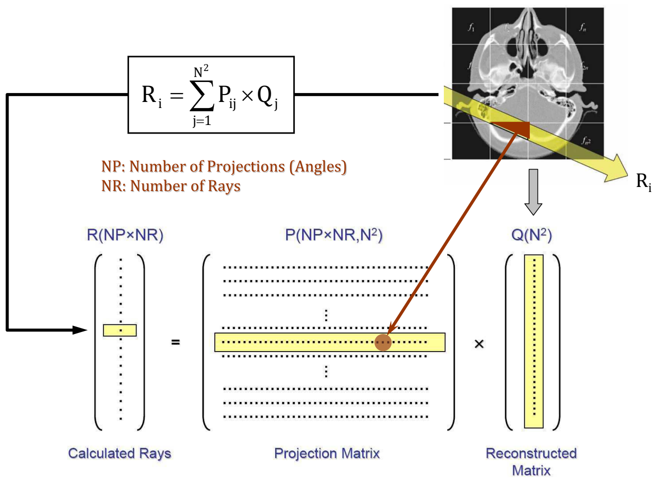

Fig. 5. Reconstruction of an $N \times N$ square matrix from its $NP \times NR$ projections.

a given angle can be calculated from the projection matrix P_{ij} and the reconstructed matrix Q_j. The projection matrix carries the information of how much the j^{th} element of the matrix Q contributes to the i^{th} ray. Let $N \times N$ be the dimension of the square matrix, NP the number of projections (angles) and NR the number of constant width rays per each projection; then the following expression holds:

$$R_i = \sum_{j=1}^{N^2} P_{ij} \times Q_j \quad \{i = 1 \cdots NP \times NR\} \tag{7}$$

Algorithmic aspects in Computed Tomography is still a very attractive field of investigations. Although the image reconstruction methodology from projections posses a variety of algorithmic techniques new approaches can be proven useful to specific problems. It is well known, that for finite projection sets characteristic of tomographic data, image reconstruction is an ill-posed inverse problem for which no unique solution exists.

The inverse problem, i.e. the reconstruction of the square matrix Q from the measured projections R (sinogram), is not a trivial procedure due to the large matrix dimensions. Although this problem is a well studied with a number of iterative techniques, like the Algebraic Reconstruction Technique (ART), many other stochastic approaches exist. Artificial Neural Networks have been shown to provide smart solutions especially to the problems that are otherwise difficult to model [8].

In this section an alternative method based on AMIAS for tomographic image reconstruction is presented. As it was mentioned previously, AMIAS requires the incorporation of a model to represent the physical characteristics of the problem. In order to achieve this task, parameters of size, location, orientation and intensity were modelled in the AMIAS framework to represent the imaged object. In this study [9], the imaged object is the distribution of a radiotracer in the physical space and it was modelled by using a series of 2-D Gaussian shapes, each one representing the presence of a emitting source in the absorbing material:

$$F_j = \sum_k A_k e^{-\frac{1}{2}\left(\frac{r_{jk}}{r^0_{jk}}\right)^2} \tag{8}$$

where A_k is the amplitude of the radiation intensity and r_{jk} is the distance between the j^{th} element of the image vector F_j from the center of the k^{th} source (x_0, y_0). The term r^0_{jk} is given by using the parametric equation of an ellipse:

$$r^0_{jk} = \frac{u \cdot v}{\sqrt{(v \cdot cos(\phi_{jk} - \theta))^2 + (u \cdot sin(\phi_{jk} - \theta))^2}} \tag{9}$$

where u and v are the major and minor axis of the ellipse respectively, and θ is the angle determining the orientation of the major axis in the tomographic plane.

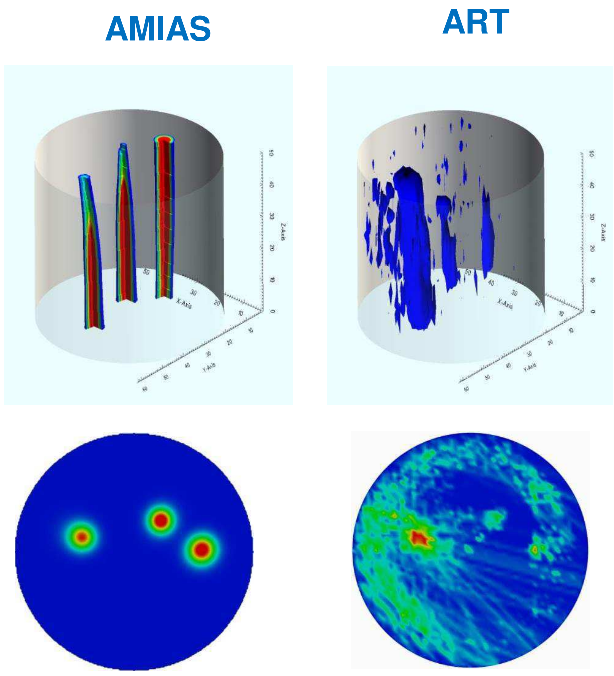

Fig. 6. AMIAS tomographic reconstruction of a real phantom consisting of three ^{99m}Tc capillaries embedded in a noisy water background. Results based on the Algebraic Reconstruction Technique (ART) are also shown for comparison.

A 3D AMIAS reconstruction example of a real phantom consisting of three capillaries filled with ^{99m}Tc solution and measured with a small-field high-resolution γ-Camera system is shown in Figure 6. The phantom is placed in a noisy water background. The AMIAS reconstruction result is compared with this of the Algebraic Reconstruction Technique (ART). In conditions of absorption, by which the conventional ART reconstruction technique is strongly affected, the AMIAS method was capable to produce a reliable representation of the phantom.

6 Summary

In summary, the AMIAS method of analysis is shown to offer significant advantages over existing methods in determining physical parameters from experimental or simulation data: it is computationally robust, it provides methodology independent answers with maximal precision in terms of the derived Probability Distribution Function for each parameter. The method has been successfully applied to extract in a independent way multipole excitation amplitudes for the Nucleon Δ-Resonance.

In the analysis of excited states within Lattice QCD, AMIAS is applied to study the spectrum of the nucleon. With the AMIAS methodology it is possible to determine the number of excited states, which can be extracted from the information that the lattice data encode. It takes advantage of the whole time dependence of the correlators not requiring identification of the large time asymptote that limits the accuracy of the determination of excited states.

The capabilities of the AMIAS data analysis method in the field of the Emission Tomography is also shown. The implementation of the AMIAS method in this field incorporates prior - information to formulate the physical characteristics of the imaging problem in a mathematical model. The ability of the method to extract the correlations between the modelled physical parameters is exploited in order to extract tomographic information from projection data. The method has been successfully applied to reconstruct the sectional images of various phantoms.

References

1. C.N. Papanicolas and E. Stiliaris: *A Novel Method of Data Analysis for Hadronic Physics*, http://arxiv.org/abs/1205.6505v1.
2. E. Amaldi, S. Fubini and G. Furlan: *Pion-Electroproduction: Electroproduction at Low Energy and Hadron Form Factors*, Springer Tracts in Modern Physics (Book **83**) (1979) Springer Verlag, ISBN: 978-3540089988.
3. E. Stiliaris and C.N. Papanicolas: *Multipole Extraction: A Novel, Model Independent Method*, AIP Proceeding "Shape of Hadrons", Vol. **904** (2007) 257–268.
4. L. Markou, C.N. Papanicolas and E. Stiliaris: *On Proton Deformation: A Model Independent Extraction of EMR from Recent Photoproduction Data*, These HINPw4 Proceedings (2017).
5. V. Hatzikos: *Experimental Data Analysis of the Proton Electroexcitation in the Kinematical Region of the Δ-Resonance with $W = 1232\ MeV$ and $Q^2 = 1.0\ (GeV/c)^2$*, MSc Thesis, Department of Physics, National & Kapoditrian University of Athens (2017).
6. C. Alexandrou, Th. Leontiou, C.N. Papanicolas and E. Stiliaris: *A Novel Analysis for Excited States in Lattice QCD – The Nucleon Case*, Phys. Rev. **D91** (2015) 014506.
7. C. Alexandrou, C.N. Papanicolas and E. Stiliaris: *A novel method for the determination of hadron excited states in Lattice QCD applied to the nucleon*, Proceedings of Science PoS (Lattice 2008) 099.
8. M. Argyrou, D. Maintas, Ch. Tsoumpas and E. Stiliaris: *Tomographic Image Reconstruction based on Artificial Neural Network (ANN) Techniques*, 2012 IEEE Nuclear Science Symposium and Medical Imaging Conference **M17-12** (2012) 3324–3327.
9. L. Koutsantonis, C.N. Papanicolas, A.-N. Rapsomanikis and E. Stiliaris: *AMIAS: A Novel Statistical Method for Tomographic Image Reconstruction – Application in Thermal Emission Tomography*, 2016 IEEE Nuclear Science Symposium and Medical Imaging Conference **M13A-4** (2016).

A model independent analysis of pion photoproduction data with the AMIAS

L. Markou[1], C. N. Papanicolas[1], and E. Stiliaris[1,2]

[1] The Cyprus Institute, Nicosia, Cyprus
[2] National and Kapodistrian University of Athens, Athens, Greece

Abstract. The Athens Model Independent Analysis Scheme (AMIAS) is a novel method for extracting physical parameters from experimental and simulation data. In this work it was applied for multipole extraction from state-of-the-art pion photoproduction data at a single energy at the $\Delta(1232)$. The data were created by randomizing the MAID07 solution as input. A methodology for a totally model independent analysis of the data was followed and the generating multipoles and EMR(%) were succesfully retrieved.

PACS. 25.20.Lj Photoproduction reactions – 05.10.Ln Monte Carlo methods

1 Introduction

Precision electromagnetic facilities around the world seek to fill in the details of the hadronic resonances picture and particulary of the resonances of the nucleon. An array of processes is studied such as pion photoproduction -and electroproduction- from a nucleon. Of immense importance to this program is the determination of reaction amplitudes from experimental observables. A well studied yet complex task of determining these reaction amplitudes is through multipole extraction.

Perhaps the most sought reaction in these experiments is the

$$\gamma N \to \Delta(1232) \to \pi N \tag{1}$$

transition. An important quantity derived at the $\Delta(1232)$ is the electric-to-magnetic ratio (EMR), as it serves as a gauge of the magnitude of the deformation of the nucleon. In the $\gamma N \to \Delta$ transition, $EMR = E2/M1$, where $M1$ is the dominant magnetic dipole due to a quark spin flip and E2 is the electric quadrupole amplitude which signals the non-zero angular momentum components in the nucleon and Δ. In the standard πN notation, $EMR = E_{1+}^{3/2}/M_{1+}^{3/2}$ where $M_{1+}^{3/2}$ and $E_{1+}^{3/2}$ are the resonant multipole amplitudes. Briefly, in the πN notation a multipole is noted as $X_{l_\pi \pm}^{I}$ where $X = E, M$ indicates the nature of the multipole - electric or magnetic, l_π is the angular momentum, "+" is used to distinguish whether the spin (s=1/2) is parallel to the angular momentum so that $J = l + s$ and "−" is used when it is antiparallel, J is the total angular momentum, and I is the isospin.

Since in the $\gamma N \to \pi N$ reaction the final state is a continuum, theoretically, there are an infinite number of possible multipoles [1]. Apart from the resonant multipoles, all other multipoles are considered as background coming primarily from Born terms and from the tails of higher resonances [2,3]. As an infinite number of parameters cannot be extracted the multipole series is truncated at a high enough l_{cut}, beyond which multipoles are expected to be negligible. The l_{cut} increases as the center of mass energy (W_{cm}) increases although which is the optimal l_{cut} for a given set of data is a matter of debate.

In general, multipole extractions from nucleon resonance data ([4–8]) may face any of the following shortcomings:

- A preconceived and somewhat arbitrary choice of the multipoles to be extracted is made as a rigorous way to assess the minimum l_{cut} at which the multipole series should be terminated is not used.
- The extracted values are biased by the model and therefore characterized by a hard to evaluate systematic model uncertainty. The bias, as shown in this work, affects both the multipoles' determined mean value and associated uncertainty.
- Multipole amplitudes to which the experimental data are only moderately sensitive are impossible to extract.

The nowadays readily available formidable computational power offers alternative ways of data analysis, more complete and more powerful, which would have been impossible to employ a few years ago in solving physical problems. Exploiting this computational power we employ the AMIAS ([9,10]) for multipole extraction from pion photoproduction data following a methodology which addresses the above concerns. The method is used for the analysis of the state-of-the-art pion photoproduction of ref. [11] where with no model input multipole amplitudes in accordance with the generator input are retrieved.

The AMIAS method is based on statistical concepts and relies heavily on Monte Carlo and simulation techniques, and it thus requires High Performance Computing as it is computationally intensive. It has been shown [10] that the method identifies and determines with maximal precision parameters that are sensitive to the data by yielding their Probability Distribution Function (PDF). The AMIAS is computationally robust and numerically stable. It uses a Monte Carlo routine to examine the whole parameter space and as it does not rely on any χ^2 minimization techniques it does not get trapped in any local minima. It has been successfully applied in the analysis of nucleon resonance data and lattice QCD ([10,12]).

2 The data

Pseudodata or simulation data are often used for the validation of analysis methods and methodologies [13,11,9]. Their great advantage is that the true solution to the problem they pose is known so results may be accepted or rejected based on this knowledge. The underlying statistical properties of the parameters can also be manipulated and therefore are known by the user.

In this work a selection of the pion photoproduction data at a single energy at the $\Delta(1232)$, from ref. [11], were analyzed. The data were created by randomizing the MAID07 solution as input and they contain all 16 single and double polarization observables. The data are characterized by a statistical precision that has become technically possible only very recently at the tagged photon facilities at ELSA (Univsersity of Bonn), CEBAF (Jefferson Laboratory) and MAMI (University of Mainz).

The dataset analyzed in this work consists of the differential cross section ($d\sigma_0$), the beam asymmetry ($\hat{\Sigma}$), the target asymmetry ($\hat{T}$), and the recoil baryon asymmetry ($\hat{P}$) of the $\gamma p \to p\pi^0$ reaction and $d\sigma_0$, $\hat{\Sigma}$ and $\hat{T}$ of the $\gamma p \to n\pi^+$ reaction. Each observables features 18 evenly spread angular measurements from 5° to 175°. Measurements at so high forward and backwards angles make the data very sensitive to multipole amplitudes with very high l_{cut}.

3 Methodology

The AMIAS has a minimal requirement that the parameters to be determined are linked in an explicit way to the measured experimental quantities. Multipole amplitudes, do not provide an orthogonal basis for describing the observables of photoproduction experiments, such as cross sections and polarization asymmetries, so we link them to the observables via the CGLN amplitudes [14,11].

Neutral pion photoproduction data are only sensitive to the charge amplitudes $A_{p\pi^0}$ of eq. (2) while positive pion photoproduction data are sensitive to the $A_{n\pi^+}$ amplitudes

$$\begin{aligned} A_{p\pi^0} &= A_p^{1/2} + \frac{2}{3}A^{3/2} \\ A_{n\pi^+} &= \sqrt{2}\left(A_p^{1/2} - \frac{1}{3}A^{3/2}\right) \end{aligned} \tag{2}$$

To access isospin multipoles one can either fix the background $A^{1/2}$ multipoles to a model and solve for the resonant amplitudes $A^{3/2}$ or simultaneously analyze data of two charge channels, for instance, $\gamma p \to p\pi^0$ and $\gamma p \to n\pi^+$. The first method is applied in cases where data from a single channel are available and unavoidably suffers from hard to evaluate model error. We employ the latter method since data measured at both proton target reactions are available.

Compton scattering, pion photoproduction, and pion-nucleon scattering are related by unitarity through a common S matrix and the Fermi-Watson [15] theorem requires the (γ, π) and (π, π) channels to have the same phase below the 2-pion threshold. Since our analysis takes place at the $\Delta(1232)$ it is subject to this theoretical constraint which, in essence, forces all multipoles with different character (electric or magnetic) but the same quantum numbers I, l, J to have the same phase $\pm n\pi$. The phases for this work were borrowed from the SAID πN analysis [16].

To employ the AMIAS for a model independent analysis we allowed multipole amplitudes to vary (fitted) while gradually increasing the l_{cut} until the χ^2_{min} reached and the yielded PDFs remained unchanged. In this way maximal information was derived from the data and the l_{cut} was not arbitrarily chosen but rather it was also determined by the data. At each step, all background amplitudes with $l > l_{cut}$ and up to all orders assumed their theoretically calculated Born values [17].

In single pseudoscalar production it has been established that at least eight independent measurements are required at each energy and at each angle to extract the four complex CGLN amplitudes up to an unmeasurable overall phase ([18]). In a truncated partial wave analysis multipoles can be obtained with even fewer observables and depending on the l_{cut} imposed ([19–21]). By imposing the F-W theorem, as in this work, the phase of each multipole is fixed and the unknown parameters of the problem are halved.

4 Extracted amplitudes

The AMIAS yields the Probability Distribution Function (PDF) of each parameter. While the method treats all parameters equally, parameters to which the data are highly sensitive exhibit well defined and narrow PDFs while non-sensitive parameters exhibit wider and featureless distributions. The shape of each PDF is not assumed, whether it is a Gaussian, a asymmetric Gaussian or a double solution depends solely on the data and the correlations between the extracted parameters.

Following the methodology described above adequate parameters were varied until convergence was reached; the

AMIAS analyses with $l_{cut} = 7$ and $l_{cut} = 8$ yielded identical results in terms of parameter PDFs. The probability distributions of the yielded amplitudes were fitted with a symmetric or asymmetric Gaussian so numerical results could be extracted.

Figure 1-above shows the χ^2_{min} reached as a function of the imposed l_{cut}. The χ^2_{min} corresponds to the solution with the minimum χ^2 value found in the AMIAS ensemble of solutions. It starts from a very high value at $l_{cut} = 1$ and rapidly drops for the $l_{cut} = 2$ and the $l_{cut} = 3$ analyses. It keeps decreasing as more amplitudes are allowed to vary until convergence of the amplitudes is reached. In the AMIAS framework the χ^2_{min} of each analysis does not assume the pivotal role it is attributed in standard χ^2 minimization techniques. The AMIAS requires a criterion to distinguish between solutions which have zero or some finite probability of being a solution to the problem. The χ^2 was chosen in this analysis as such criterion but other choices are possible [10].

Our criterion for convergence is the convergence of the yielded probability distribution functions which implies that maximal information is extracted from the data. Figure 1-below shows the (fitted) determined $EMR(\%)$ value of each l_{cut} analysis. The extracted EMR is in statistical agreement with the generator's value for all analyses with $l \geq 3$ and converges at $l_{cut} = 7$.

Figures 2 and 3 show the convergence of all extracted amplitudes characterized by $l < 3$ (S P and D multipole amplitudes). The green lines are the MAID07 solution which was used as the generator. As l_{cut} increases the determined uncertainty of the derived multipoles also increases until maximal information is extracted from the data. The determined amplitude values, mean value and uncertainty, converge to some value and remain stable when the $l = 8$ amplitudes are allowed to vary. The extracted amplitudes are in perfect agreement with the MAID07 values validating the method and methodology applied for the analysis of the data.

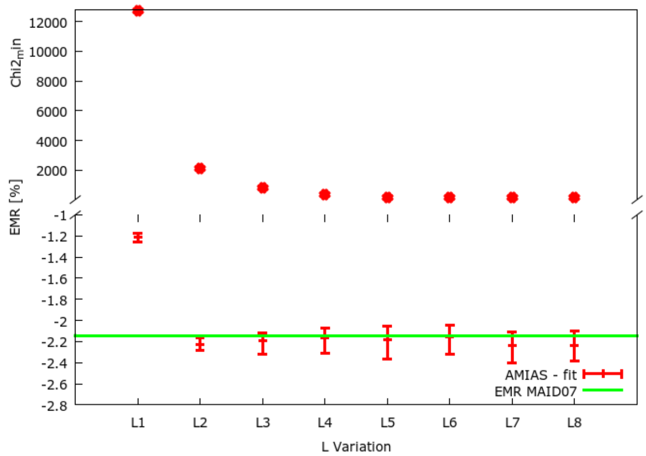

Fig. 1. (Color online) Above: χ^2_{min} reached for each l_{cut}. Below: The extracted $EMR(\%)$ as a function of l_{cut}. Both values converge for a variation of about $l = 7$ and higher.

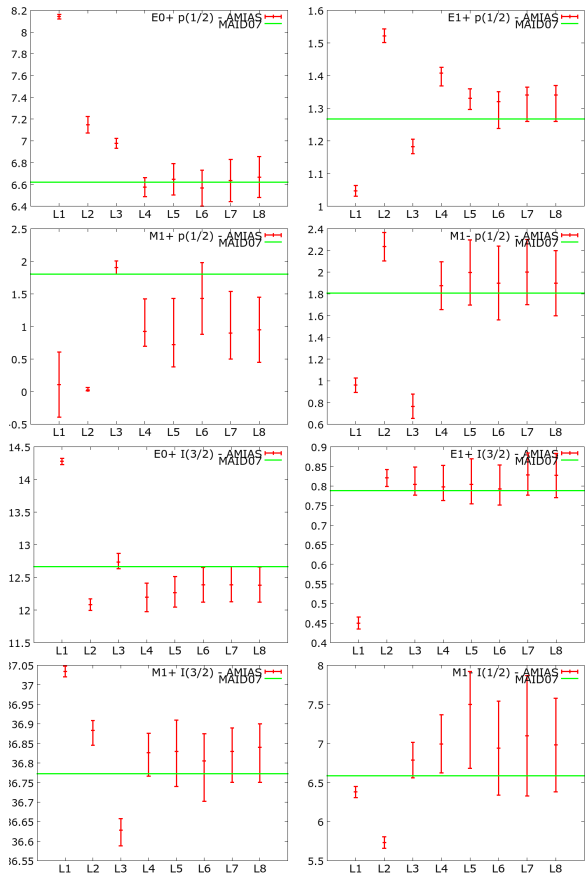

Fig. 2. Extracted values for all $l < 2$ multipole amplitudes as a function of l_{cut}. For each l_{cut} analysis higher amplitudes are set to zero. As more amplitudes are allowed to vary, determined mean values and their associated uncertainty approach the generator's value. Allowing amplitudes with $l > 7$ to vary does not affect the derived values therefore convergence is reached.

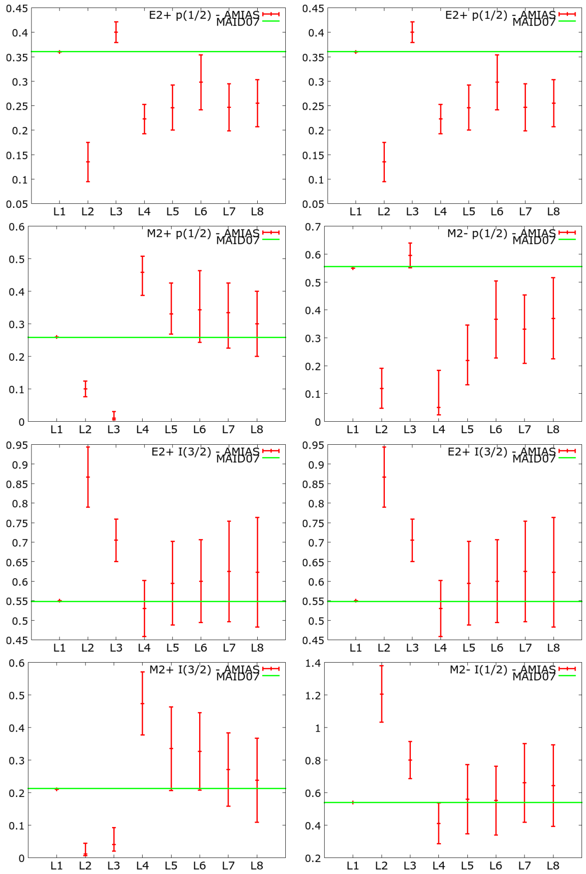

Fig. 3. Extracted values for all $l = 2$ multipole amplitudes as a function of l_{cut}. See caption of fig. 2 for more details.

A central issue in multipole extraction which is properly treated in the AMIAS method, is the handling of correlations. By examining the whole parameter space and considering all possible solutions, the method, captures all correlations between the parameters. Methods which treat insensitive amplitudes as frozen (fixed) exclude any possibility of determining them. As a consequence, they may underestimate the derived error and converge to shifted values for the fitted parameters.

5 Bands of allowed solutions

For a succesful AMIAS analysis the whole parameter space has to be sufficiently explored so that all solutions with non-zero probability of representing reality are accounted for. The histogram of the χ^2's of all solutions when weighted and normalized has the form of a (mathematical) χ^2-distribution with degrees of freedom equal to the number of varied parameters, as in fig. 4. In 4-a, all solutions which contribute to the distribution are binned. We may integrate the resulting distribution and capture all solutions within a certain confidence level (c.l.). These solutions may then be plotted one on top of the other to form bands around the data. In this way we may visuallize the spread of our solutions around the data exactly within the desired c.l.

For example, in fig. 4-b the weighted and normalized histogram of the χ^2's of the $l_{cut} = 3$ analysis was integraded to 68(%). Then, all solutions with χ^2 less or equal to that c.l. mark, were used to compute the 4 S-group $(d\sigma_0, \Sigma, T, P)$ and 4 DP-group observables $(E, F, G, H))$ for each of the two proton target reaction channels and a full 180° angular coverage. The result was plotted as bands shown in fig. 5 and 6 with blue color. The same procedure was used for the green and red bands where the results from the $l_{cut} = 2$ and $l_{cut} = 1$ analyses were used respectively.

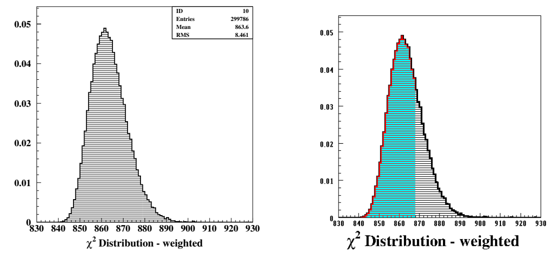

Fig. 4. Left: The weighted and normalized distribution of the χ^2's of the Ensemble of solutions for the $l_{cut} = 3$ analysis. All solutions with non-zero probability of being a good solution to the problem contributes to the distribution. Right: The same distribution integrated to 70(%).

For the analysis only $d\sigma_0/d\Omega$, Σ, T, and P observables of the $\gamma p \to p\pi^0$ reaction and $d\sigma_0/d\Omega$, Σ, and T observables of the $\gamma p \to n\pi^+$ reaction were used. The bands of allowed solutions can be plotted for all observables irrespectively if they were included in the analysis or not. As seen in fig. 5 and fig. 6 the bands are always centralized around the data (observables) which were included in the analysis. This is not always the case for observables not included in the analyzed dataset. For example, solutions are centralized around $\hat{E}$, but diverge in the case of $\hat{P}$ and $\hat{H}$. This precise visualization of the AMIAS ensemble of solutions allows us to make predictions whether an observable should be remeasured with more precision and at which angular region and which observables would benefit the analysis more if measured for the first time.

6 Conclusions

Pseudodata are widely used to validate methods and methodologies. In this work the numerically stable and robust AMIAS method [9,10] was employed for a model independent analysis of the state-of-the-art pion photoproduction data of ref. [11]. Multipole amplitudes were allowed to vary by gradually increasing l_{cut} until convergence of the extracted PDFs was reached and maximal information was extractted from the data. The determined multipole values and uncertainties were in complete agreement with the

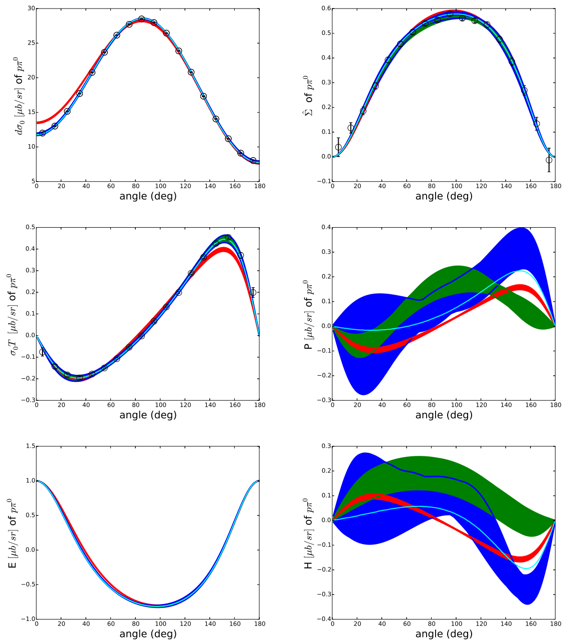

Fig. 5. Bands of allowed solutions for a 68(%) confidence level. Color coded as: Red for $l_{cut} = 1$, green for $l_{cut} = 2$ and blue for $l_{cut} = 3$ analyses. As more amplitudes are allowed to vary (l_{cut} increases), the bands give a much better description of the pion photoproduction observables.

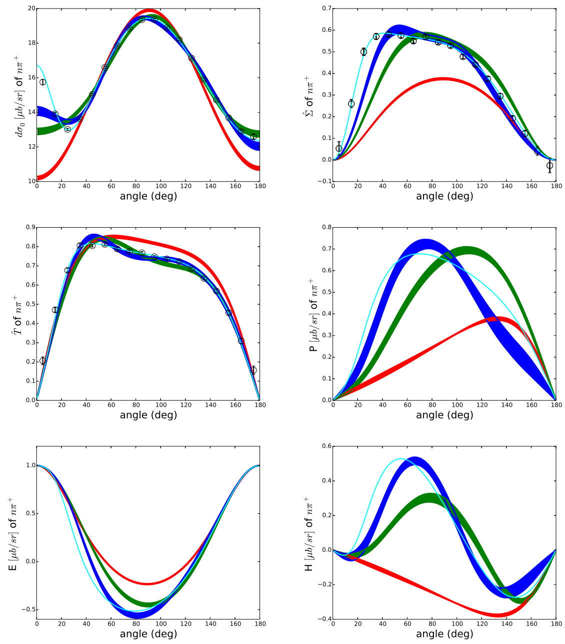

Fig. 6. Bands of allowed solutions for a 68(%) confidence level. Color coded as: Red for $l_{cut} = 1$, green for $l_{cut} = 2$ and blue for $l_{cut} = 3$ analyses.

generator. Bands of allowed solutions were created by exploiting the AMIAS's ensemble of solutions. These bands are useful for predictions regarding future experiments.

References

1. AM Bernstein, CN Papanicolas, Costas N Papanicolas, and Aron M Bernstein. Overview: The shape of hadrons. In *AIP Conference Proceedings*, volume 904, pages 1–22. AIP, 2007.
2. D Dreschsel and Lothar Tiator. Threshold pion photoproduction on nucleons. *Journal of Physics G: Nuclear and Particle Physics*, 18(3):449, 1992.
3. Alan Steven Raskin and T William Donnelly. Polarization in coincidence electron scattering from nuclei. *Annals of Physics*, 191(1):78–142, 1989.
4. F Kalleicher, U Dittmayer, RW Gothe, H Putsch, T Reichelt, B Schoch, and M Wilhelm. The determination of σ lt/σ tt in electro-pion-production in the δ-resonance region. *Zeitschrift für Physik A Hadrons and Nuclei*, 359(2):201–204, 1997.
5. V. V. Frolov, G. S. Adams, A. Ahmidouch, C. S. Armstrong, K. Assamagan, S. Avery, O. K. Baker, P. Bosted, V. Burkert, R. Carlini, R. M. Davidson, J. Dunne, T. Eden, R. Ent, D. Gaskell, P. Guèye, W. Hinton, C. Keppel, W. Kim, M. Klusman, D. Koltenuk, D. Mack, R. Madey, D. Meekins, R. Minehart, J. Mitchell, H. Mkrtchyan, N. C. Mukhopadhyay, J. Napolitano, G. Niculescu, I. Niculescu, M. Nozar, J. W. Price, P. Stoler, V. Tadevosian, L. Tang, M. Witkowski, and S. Wood. Electroproduction of the $\Delta(1232)$ resonance at high momentum transfer. *Phys. Rev. Lett.*, 82:45–48, Jan 1999.
6. Valery Victor Frolov, GS Adams, Abdellah Ahmidouch, CS Armstrong, Ketevi Assamagan, Steven Avery, OKeith Baker, Peter Bosted, Volker Burkert, Roger Carlini, et al. Electroproduction of the δ (1232) resonance at high momentum transfer. *Physical Review Letters*, 82(1):45, 1999.

7. C. Mertz, C. E. Vellidis, R. Alarcon, D. H. Barkhuff, A. M. Bernstein, W. Bertozzi, V. Burkert, J. Chen, J. R. Comfort, G. Dodson, S. Dolfini, K. Dow, M. Farkhondeh, J. M. Finn, S. Gilad, R. W. Gothe, X. Jiang, K. Joo, N. I. Kaloskamis, A. Karabarbounis, J. J. Kelly, S. Kowalski, C. Kunz, R. W. Lourie, J. I. McIntyre, B. D. Milbrath, R. Miskimen, J. H. Mitchell, C. N. Papanicolas, C. F. Perdrisat, A. J. Sarty, J. Shaw, S.-B. Soong, D. Tieger, C. Tschalær, W. Turchinetz, P. E. Ulmer, S. Van Verst, G. A. Warren, L. B. Weinstein, S. Williamson, R. J. Woo, and A. Young. Search for quadrupole strength in the electroexcitation of the $\Delta^+(1232)$. *Phys. Rev. Lett.*, 86:2963–2966, Apr 2001.
8. NF Sparveris, R Alarcon, AM Bernstein, W Bertozzi, T Botto, P Bourgeois, J Calarco, F Casagrande, MO Distler, K Dow, et al. Investigation of the conjectured nucleon deformation at low momentum transfer. *Physical review letters*, 94(2):022003, 2005.
9. E. Stiliaris and C.N. Papanicolas. Multipole extraction: A novel, model independent method. *arXiv preprint nucl-ex/0703031*, 2007.
10. C.N. Papanicolas and E. Stiliaris. A novel method of data analysis for hadronic physics. *arXiv preprint arXiv:1205.6505*, 2012.
11. R.L. Workman, M.W. Paris, W.J. Briscoe, L. Tiator, S. Schumann, M. Ostrick, and S.S. Kamalov. Model dependence of single-energy fits to pion photoproduction data. *The European Physical Journal A*, 47(11), 2011.
12. C Alexandrou, T Leontiou, CN Papanicolas, and E Stiliaris. Novel analysis method for excited states in lattice qcd: The nucleon case. *Physical Review D*, 91(1):014506, 2015.
13. J Friedrich and F Lenz. Elastic electron scattering from 208pb at moderate momentum transfers and model-independent description of the nuclear charge distribution. *Nuclear Physics A*, 183(3):523–544, 1972.
14. G. F. Chew, M. L. Goldberger, F. E. Low, and Y. Nambu. Relativistic dispersion relation approach to photomeson production. *Phys. Rev.*, 106:1345–1355, Jun 1957.
15. Kenneth M. Watson. Some general relations between the photoproduction and scattering of π mesons. *Phys. Rev.*, 95:228–236, Jul 1954.
16. INS Data Analysis Center.
17. O Hanstein. PhD thesis, Mainz, 1996.
18. Wen-Tai Chiang and Frank Tabakin. Completeness rules for spin observables in pseudoscalar meson photoproduction. *Physical Review C*, 55(4):2054, 1997.
19. RL Workman. Extracting amplitudes from photoproduction data. In *Journal of Physics: Conference Series*, volume 312, page 032019. IOP Publishing, 2011.
20. Yannick Wunderlich. Studies on a complete experiment for single pseudoscalar meson photoproduction. In *International Journal of Modern Physics: Conference Series*, volume 26, page 1460104. World Scientific, 2014.
21. RL Workman, L Tiator, Y Wunderlich, M Doering, and H Haberzettl. Amplitude reconstruction from complete experiments and truncated partial-wave expansions. *arXiv preprint arXiv:1611.04434*, 2016.

Employing a Novel Analysis Method in the field of Tomographic Image Reconstruction for Single Photon Emission Computed Tomography (SPECT)

L. Koutsantonis[1], C. N. Papanicolas[1], and S. Stiliaris[2]

[1] The Cyprus Institute, NICOSIA, Cyprus
[2] National and Kapodistrian University of Athens, ATHENS, Greece

Abstract. The quality of the tomographic image in Single Photon Emission Computed Tomography (SPECT) is strongly related to the radiation dose injected to the patient. Radiation reduction usually leads to noisy projection data which are further affecting the algorithms involved to reconstruct the inner distribution of radioactivity in the patient. To address this problem, we employ the Athens Model Independent Analysis Scheme (AMIAS), a well suited method for inverse scattering problems, in the field of Medical Image Reconstruction. The method was implemented in High Performance Computing (HPC) environment to be used in the reconstruction of SPECT projections characterised by low scintillation counts. Preliminary results have shown that the method leads to tomographic images of improved diagnostic accuracy in cases where few projections are available and/or characterised by noise and attenuation. A potential success of the method can be exploited to reduce the radiation dose which is injected into the patient and to minimise the duration of the clinical scan.

PACS. 87.57.uh SPECT – 87.57.C Image processing in medical imaging

1 Introduction

The diagnostic accuracy of the tomographic image obtained in Single Photon Emission Tomography (SPECT) is strongly related to the radiation dose. Last years, efforts have been made in the development of applications utilizing both hardware and software innovations to improve the quality of the obtained images in SPECT. In the same time, these developments are operating with lower scintillation counts, and therefore, require less amount of radiation dose injected into the patient. Furthermore, SPECT imaging is characterized by physical factors such as scatter, attenuation and the Poison statistics of photons' which degrade the quality of the obtained data. As a consequence, the planar information is limited and leads to tomographic images of reduced accuracy. It is straightforward that methods which are capable of providing accurate reconstruction results with the highest possible precision by planar projections characterized by low scintillation counts, scatter and attenuation can be involved in SPECT image reconstruction to reduce the duration of the scan and/or the radiation dose. A novel methodology implemented in the framework of SPECT tomographic image reconstruction is presented. The method, namely, the Athens Model Independent Analysis Scheme (AMIAS), has general applicability in inverse scattering problems, classical or quantum in nature. In this work, the AMIAS methodology is examined by reconstructing noisy planar projections simulated by using a software phantom.

2 The Athens Model Independent Analysis Scheme (AMIAS)

The Athens Model Independent Analysis Scheme (AMIAS) is based on statistical physics and relies on Monte Carlo techniques to extract the parameters of a model from a set of data. AMIAS is applicable in problems in which the parameters to be determined are linked with an explicit way to the set of data through a theory or model [1,2]. The method is exploiting the observation that for a given theory (or model) used to describe a dataset of observable quantities, any set of parameters values consist a solution with a finite probability of representing the real parameters values. This probability is quantified through a comparison to data of the predicted by the theory (or model) values as they are calculated by using the set of parameters values.

The χ^2 criterion is most often employed in AMIAS to quantify the goodness of each solution. Consider a set of observables $V_1, V_2, ..., V_M$ with standard deviations ϵ_i and a mathematical model f defined on a set of parameters

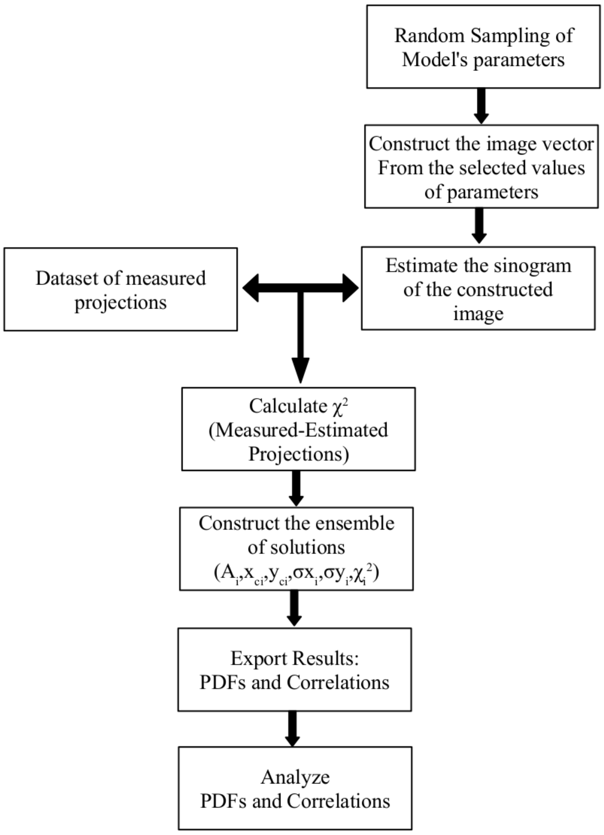

Fig. 1. Flowchart of the proposed algorithm for the statistical analysis of SPECT data by using the AMIAS method.

values $\mathbf{a} = (a_1, a_2, ..., a_N)$, the value of χ^2 is equal to:

$$\chi^2(i) = \sum_k \left(\frac{f_k(\mathbf{a}_i) - V_k}{\epsilon_k}\right)^2 \tag{1}$$

An ensemble of solutions is the whole set of solutions $\mathbf{a}_i$ which for a fixed number of parameters is called "Canonical Ensemble". The Micro-canonical Ensemble of solutions is defined as the subset of solutions $\mathbf{a}_i$ whose χ^2 value lies within the range $[\chi^2_A, \chi^2_B]$. Each solution in the Canonical Ensemble has a finite probability $P(i)$ of representing the real solution which is equal to:

$$P(i) = g(\chi^2(i), \mathbf{a}_i) \tag{2}$$

where g is a function of χ^2. Boltzmann equation ($P(i) = e^{-\chi^2(i)}$) is an example of such a probability function g and is widely used in data analysis with Monte-Carlo techniques.

Given a dataset of observables, the parameters values can be extracted by employing the following procedure:

- The model is chosen and expressed as a mathematical function of the parameters to be determined.
- The physical limits (range) of each parameter are determined. The space defined by parameters ranges is referred to as the phase space of the problem.
- A random sampling procedure is then used to choose the set of parameters values within the defined ranges. This procedure is repeated to generate the Canonical Ensemble of solutions.
- The value of χ^2 is calculated for each one of the solutions in the Canonical Ensemble by using Eq. 1.
- Having constructed the Canonical Ensemble of Solutions, the Probability Distribution Function (PDF) of each parameter can be extracted by summing the probabilities $P(i)$ of the Solutions a_i which lie in the interval $[a_j, a_j + \delta a_j]$ (this procedure is also known as histogram binning).

The principal benefit of the AMIAS is its ability to extract the maximum information in an unbiased way. Problems with complex topologies and multiple minima of χ^2 can be dealt with this method. AMIAS cannot be implemented without high level parallel computing, as it is computationally a demanding procedure. It has been suggested [1] from the very inception of AMIAS that is particularly well suited to solve inverse scattering problems, classical or quantum in nature. Medical Imaging reconstruction is an important class of problems that fall under this category.

The implementation of the AMIAS method in the framework of tomography requires a model representing the targeted distribution of radioactivity. This model is selected by utilizing prior-knowledge about the target. The model has to be a good approximation of the reality to extract results with a physical meaning. In this study, the model was constructed by taking into account the geometrical factors of the phantom. Parameters to be extracted are the position, the size and the orientation of the targeted "object". These parameters are formulated in 2D or 3D functions to represent the tomographic or volumetric image respectively, of the radiotracers' distribution.

In SPECT, the obtained data is the set of measured projections of the radiotracers' distribution. AMIAS generates the projections of the modelled target by implementing forward projection simulations.

3 Simulation Study

The capability of the method to provide reliable reconstruction results was examined by using generated data from computerized phantoms. This task was achieved by simulating 24 projections of a 64×64 phantom image as it is shown in Fig. 2. The methodology was examined on four different simulation studies. In each case, the simulated radioactivity of background was adjusted to produce different Target-to-Background (T:B) ratio. Each one of the sets of planar projections was randomized by using the Poison random distribution.

Reconstruction results of the phantom are shown in Fig. 3 as they were extracted with the AMIAS reconstruction methodology. The model parameters were derived from their Probability Distribution Functions (PDFs) and used to visualize the tomographic image of the phantom. Reconstruction results obtained by the Filtered Back Projection (FBP), the Algebraic Reconstruction Technique and the Maximum Likelihood Expectation Maximization

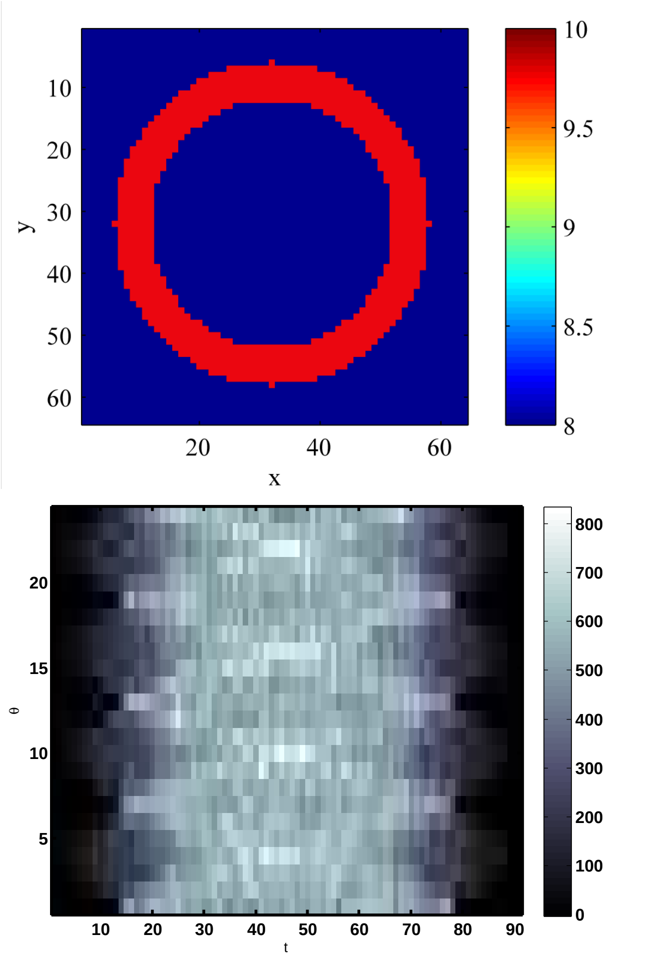

Fig. 2. The ring shaped computerized phantom was used to examine the capabilities of the AMIAS reconstruction methodology and the sinogram of the phantom, simulated by randomizing 24 planar projections with Poison noise.

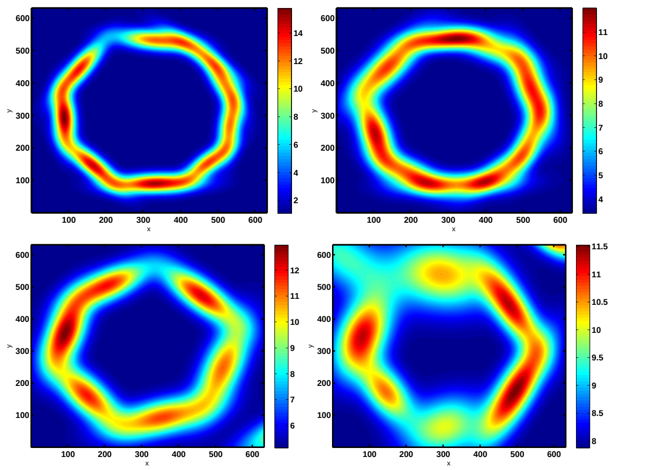

Fig. 3. Reconstructed images of the phantom as they were extracted by applying the AMIAS reconstruction methodology in the four different cases. Upper Left: T:B = 10 : 0, Upper Right: T:B = 7 : 3, Bottom Left: T:B = 1 : 1, Bottom Right: T:B = 1:4.

[5,3,4] are also shown in Fig. 4 for the case where the ratio T:B was equal to 1:4.

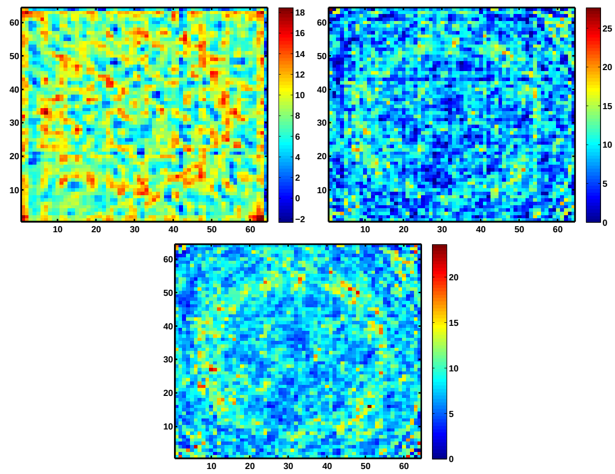

Fig. 4. Reconstructed images of the phantom as they were obtained from projection data characterized by T:B = 1 : 4 by using the FBP (upper-left), ART (upper-right) and MLEM (bottom) reconstruction techniques.

Compared to FBP and ART and MLEM the AMIAS methodology was capable of providing the most reliable reconstruction. The limited number of projections affects the reconstruction process with FBP which and degrades the quality of the image. ART and MLEM, as iterative reconstruction techniques, can provide reconstructions of better quality in such cases of small number of projections. However, the high level of background and subsequently the lower Signal-to-Noise ratio (SNR) characterizing the data hamper the reconstruction and leads to noisy images.

4 Conclusion

Methods that are used in SPECT Image Reconstruction to produce tomographic images from planar projections require sufficient number of photons' scintillation counts to provide reconstruction numerical results. The large degree of uncertainty in low statistics datasets impedes the reconstruction process and degrades the quality of the image. AMIAS, an analysis method based on a statistical mechanics and Monte Carlo simulation techniques is implemented in the framework of SPECT to analyse and reconstruct noisy dataset of projections characterized by low statistics. In order to extract the maximum possible information on the targeted distribution of radioactivity, AMIAS implements 2D or 3D mathematical models to simulate the morphology, the size and the location of target in the region of interest. The method is examined with projection data generated by computerized simulations. Initial numerical results are very promising as the application of AMIAS in image reconstruction was able to reconstruct the image of the phantom, even in the case where the Target-to-Background ratio was about 1:4. Compared to the results from conventional methods, commonly used in SPECT, AMIAS images provide the highest detectability of the targeting distribution.

References

1. C.N. Papanicolas and E. Stiliaris, A novel method of data analysis for hadronic physics. arXiv preprint arXiv:1205.6505, 2012.
2. E. Stiliaris and C.N. Papanicolas. Multiple extraction: A novel, model independent method. arXiv preprint nucl-ex/0703031, 2007.
3. L.A. Shepp and Y. Vardi. Maximum likelihood reconstruction for emission tomography. Med. Im., IEEE Trans., 1(2):113122, 1982.
4. D. Hwang and G. L. Zeng, Convergence study of an accelerated ML-EM algorithm using bigger step size, Phys. Med. Biol., vol. 51, no. 2, p. 237, 2006.
5. S. Angeli and E. Stiliaris, An accelerated algebraic reconstruction technique based on the Newton-Raphson scheme, in 2009 IEEE NSS/MIC, Oct 2009, pp. 33823387.

PhoSim: A Simulation Package Designed for Macroscopic and Microscopic Studies in the Time-Resolved Optical Tomography

A.-N. Rapsomanikis[1], A. Eleftheriou[1,*], M. Mikeli[1], Ch. Pafilis[1,2], M. Zioga[1], and E. Stiliaris[1,3]

[1] Department of Physics, National and Kapodistrian University of Athens, Greece
[2] EEAE, Greek Atomic Energy Commission, Agia Paraskevi, Attica, Greece
[3] Institute of Accelerating Systems & Applications (IASA), Athens, Greece

**Present address:* Institut für Pharmakologie und Toxikologie, University of Zurich, Switzerland

Abstract. *PhoSim* is an optical ray tracing Monte-Carlo simulator capable of reproducing the physical processes taking place in a tissue environment when illuminated by Near-Infrared radiation. From a macroscopic point of view this can be accomplished by the proper manipulation of the Henyey-Greenstein phase parameter g, which represents a simple and analytical solution for the fast generation of a random scattering angle photon distribution. Microscopically, the program can simulate certain biological structures by placing a proper density of subcellular organelles inside the volume of interest, proportional to the wavelength of the radiation used at the study ($\sim$ 750-1000 nm). The new version of this software package is able to create different type of phantoms in multi-layer environments and it is also equipped with a detailed Fate and Time of Flight information of each traveling photon. *PhoSim* is a simple and useful tool for Time-Resolved Optical Tomographic studies; its basic functions and capabilities with optical tomographic examples are presented in this work.

PACS. 87.57.Q- Medical imaging computed tomography – 87.19.lh Medical imaging optical – 42.15.Dp Ray tracing optical – 87.10.Rt Monte Carlo methods in biological physics

1 Introduction

It is well known that by implementing Near-Infrared radiation in biological tissues, absorption can be minimized and thus an anatomical investigation can be performed. Mie type of scattering however, is always present in this part of the electromagnetic spectrum causing most of the rays to loose their directional information. Despite this fact, an extremely small fraction of photons is capable of being scattered, totally or almost totally, forward (ballistic component) which can be used as a tomographic probe in this type of study. Therefore, by performing specific time-cuts to the accumulated data the anatomical structure of the diffused material under investigation can be studied, based on the fact that the early arriving events (nearly straight propagating rays) can be separated.

In the previous years, various attempts to implement several ray-tracing software packages suitable of providing the Time of Flight (ToF) information for studying Time-Resolved Optical Tomographic (TROT) modalities proved inadequate. While some of them were capable up to a point of producing a useful amount of data [1], due to their generic nature many questions left unanswered. For this reason and towards the generation of a prototype TROT system *PhoSim* was developed [2]. *PhoSim*, is a Monte Carlo simulator specifically dedicated to TROT modalities. It is a ray-tracing program with Time of Flight information for every event, which can resolve the Mie multiple scattering problem by utilizing the Henyey-Greenstein Phase Function (HGPF) [3,4]:

$$P(\theta) = \frac{1}{4\pi}\frac{1-g^2}{[1+g^2-2g\cos\theta]^{3/2}}$$

This is extremely useful from an algorithmic point of view, since it only depends on one parameter g ($-1 \leq g \leq 1$), that represents the average cosine of the scattering angle θ.

2 Latest Version of PhoSim

Macroscopically, the newest version of *PhoSim* is able to simulate certain tissue materials by manipulating the g parameter of the Henyey-Greenstein Phase Function (HGPF) along with the scattering and absorption length. In addition, it can create multi-layer materials resulting in more realistic situations. Moreover, spherical objects can be embedded in this environment having different optical properties as it will be described in this section.

2.1 Generation of a Multi-Layer Environment

The generation of multi-layer environment in *PhoSim* can be achieved by varying the g parameter of the HGPF and the Scattering Length (SL) for certain propagation areas of the medium along the Z-axis as it is depicted at the example in Figure 1. This is a simple but effective and

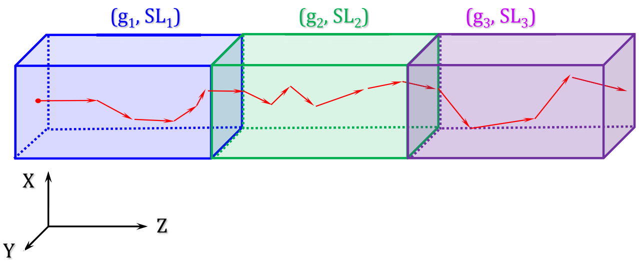

Fig. 1. An example of a 3-layered medium. Each colored area has a specific value of the Henyey-Greenstein parameter (g) and Scattering Length (SL).

also a computational "economic" way of creating realistic tissue structures which enables investigation of more complex scenarios.

2.2 Phantom Creation and Properties

Different optical type phantoms with spherical objects can be introduced inside the multi-layer areas defined in *PhoSim*. They can be (i) perfect reflectors, (ii) classical optical objects obeying Fresnel's rule of reflection and transmission for non-polarized photons, (iii) diffusers, following the Snell's law of deflection and refraction and which allow the rays either to be reflected in a cone of angle θ_0 or to be refracted (Figure 2). All these phantom objects are characterized by their own refraction index n_i.

The program calculates in a stochastic way the path of the light ray on each interaction point with the spherical object of the phantom. The Fresnel equation is a derivation of Maxwell's equation and calculates the reflectance R_s for s-polarized and R_p for p-polarized photons:

$$R_s = \left| \frac{n_a \cos\theta_\pi - n_b \cos\theta_\delta}{n_a \cos\theta_\pi + n_b \cos\theta_\delta} \right|^2$$

$$R_p = \left| \frac{n_a \cos\theta_\delta - n_b \cos\theta_\pi}{n_a \cos\theta_\delta + n_b \cos\theta_\pi} \right|^2$$

The probability for unpolarized light to be reflected is given by the mean value of these two components and can be expressed as a function of the incoming angle θ_π and the relative refraction index $n_{ba} = n_b/n_a$ in the following way:

$$R = \frac{1}{2} \left\{ \left| \frac{\cos\theta_\pi - n_{ba} \times \mathcal{F}}{\cos\theta_\pi + n_{ba} \times \mathcal{F}} \right|^2 + \left| \frac{\mathcal{F} - n_{ba} \cos\theta_\pi}{\mathcal{F} + n_{ba} \cos\theta_\pi} \right|^2 \right\}$$

with

$$\mathcal{F} = \sqrt{1 - \frac{1 - cos^2\theta_\pi}{n_{ba}^2}}$$

The previous expression for the calculation of the ray reflectance includes only the cosine of the incoming angle and the refraction index of the spherical object relative to the medium. Total reflection inside a phantom's object is possible; the fate of the ray is decided alone on a predefined maximum absorption length for the simulated path.

2.3 Ray Tracing and Time of Flight Information in PhoSim

PhoSim can ray-trace every event throughout the different simulated tissue materials (Figure 3) and can provide the

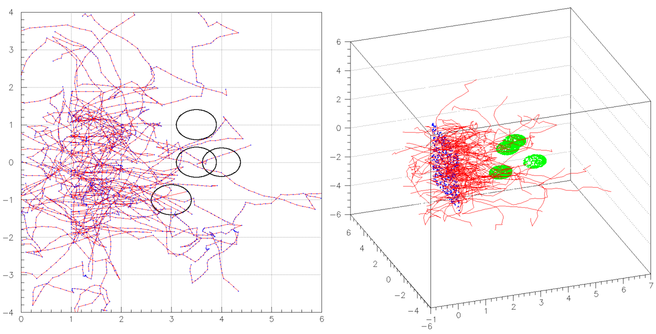

Fig. 3. *Left*: Profile image of Ray-Tracing (XZ-Plane) inside a multi-layer, scattering medium containing a phantom with four out-of-plane spherical objects. *Right*: 3D Ray-Tracing for the same phantom.

Fate (absorbed by the phantom, absorbed by the tissue, escaped, timed out, detected) on a event-by-event basis. However, the most important aspect of this algorithm is

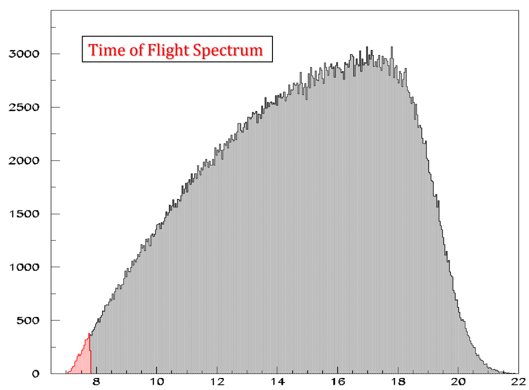

Fig. 4. The Time of Flight information (in arbitrary units) of a case study for all the detected photons. With red is indicated the ballistic component, which represents the forward scattered events. The vertical axis corresponds to the detected number of photons.

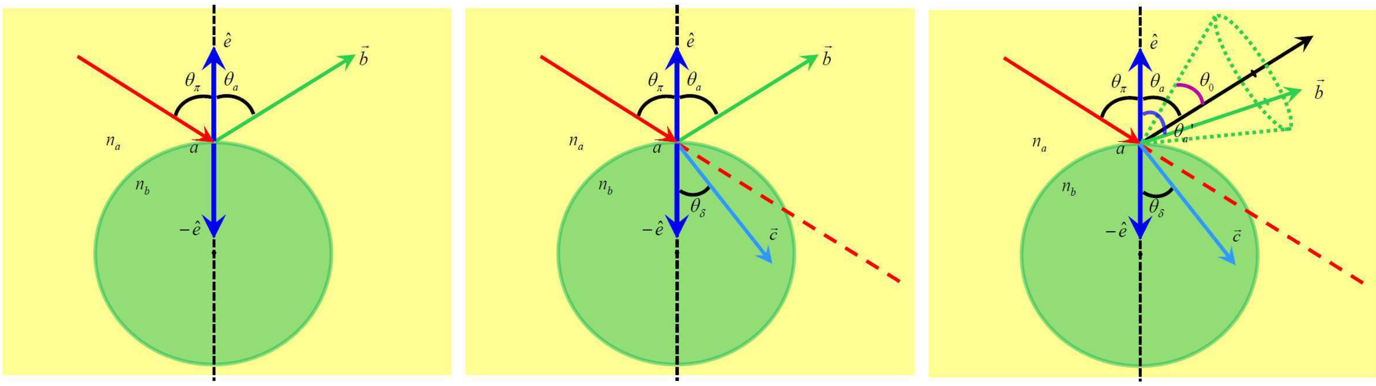

Fig. 2. The basic mechanisms for the light interaction with the phantom spherical objects incorporated in *PhoSim*. *Left*: A perfect reflecting spherical object ($\theta_\pi = \theta_\alpha$). *Middle*: A classic spherical optical object obeying the Snell law of reflection and refraction ($\theta_\pi = \theta_\alpha$ and $n_a \sin\theta_\pi = n_b \sin\theta_\delta$). *Right*: A diffusing spherical object which allows the reflected ray to be inside a cone of angle θ_0 and the refracted ray to follow Snell's law.

the ability to calculate the Time of Flight (ToF) information for each traveling photon using its optical path segments and the refraction index of the medium (Figure 4). This information is extremely useful; by applying proper time filtering on the collected data one can extract the important ballistic component, which provides the anatomical information of the simulated biological tissue.

2.4 Planar Imaging and Tomographic Capabilities

Since the Time of Flight information provided for simulated rays allows a proper event filtering, planar imaging detection can be achieved in *PhoSim*. This functionality is here demonstrated with a software phantom consisting of four out-of-plane and totaly absorbing spherical objects.

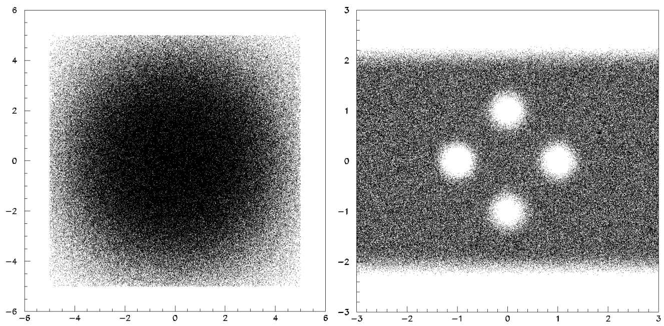

Fig. 5. *Left*: Detected raw image of a case study phantom in a three-layered medium with dimensions 10x10x5 in arbitrary length units. The phantom consists of four out-of-plane, totaly absorbing spherical objects with a diameter of 0.8 a.u. *Right*: Detected planar image of the phantom after proper time filtering.

This geometry was embedded in a three-layered, highly scattering medium and a collimated beam light, parallel to Z-axis, was utilized to probe the sample. The planar image of all the detected events without any filtering can be recorded, providing no anatomical information at all, as shown in the left part of Figure 5. However, the phantom's pattern can be obtained after performing the necessary time-cuts on the collected data. The right part of Figure 5 shows clearly the planar image profile of the phantom in the time-filtered image.

The clear structure of the planar images further allows a tomographic reconstruction of the phantom's geometry on the three-dimensional space. A total of 24 projections with a step of 15^o in the full angle range $0^o - 360^o$ were recorded. Results are obtained for each projection with time-filtering up to an optimal level. Every projection was sliced 80 times along the X-axis (the rotation axis) and further analyzed to reconstruct the tomographic images using iterative reconstruction algorithms developed in our laboratory, which are mainly based on accelerated algorithms within the Algebraic Reconstruction Technique (ART) [5].

Finally, all the two-dimensional tomograms (80 slices) were appropriately stacked and interpolated creating a 3D tomographic image in the form of an iso-surface plot. For the simulated phantom the reconstructed result is shown in Figure 6.

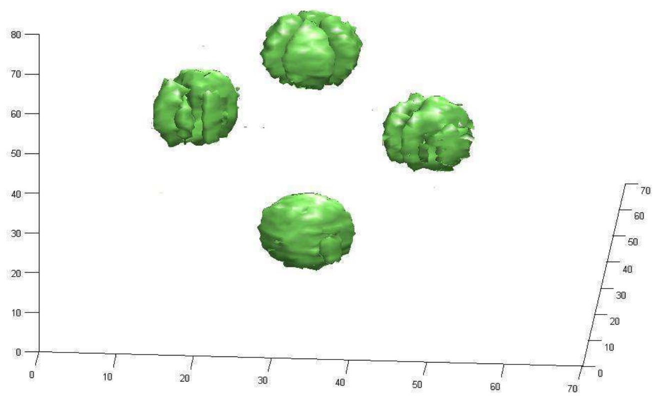

Fig. 6. The iso-surfaced 3D image of the original phantom after stacking all the sliced two-dimensional reconstructed tomograms.

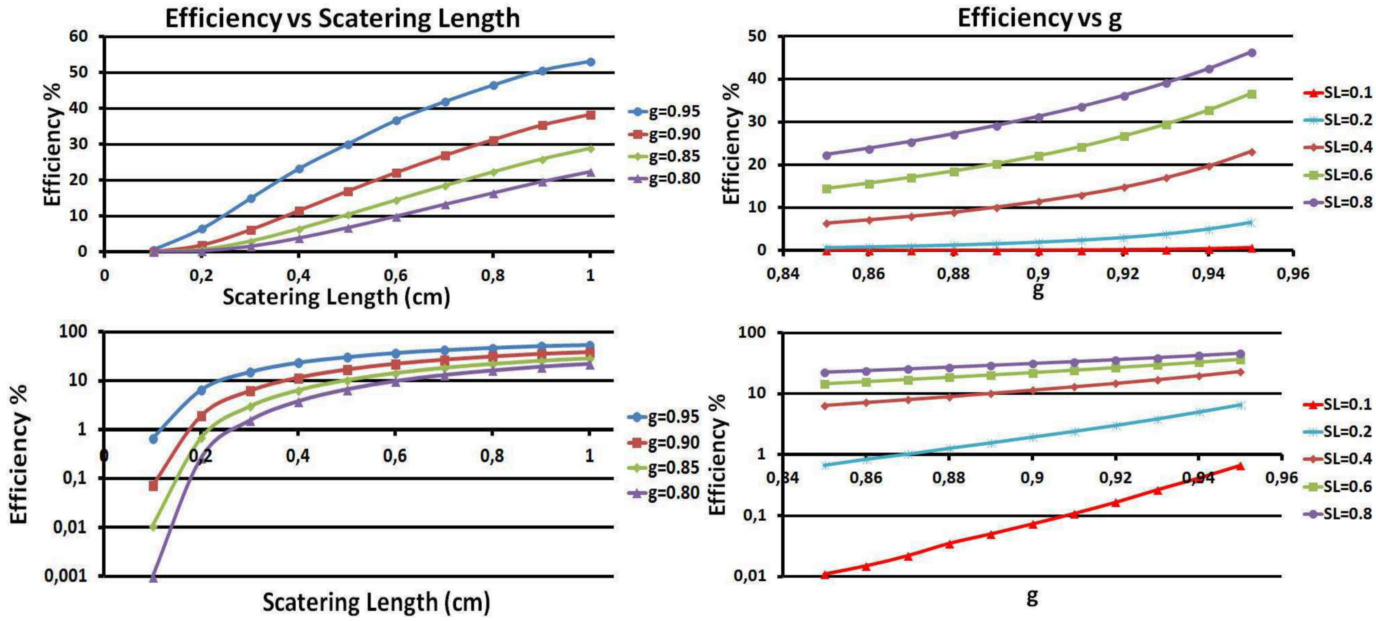

Fig. 7. *Left Row*: Detection efficiency as a function of the Scattering Length (SL) for different values of the Henyey-Greenstein g parameter in both linear and logarithmic scale. *Right Row*: Detection efficiency as a function of the Henyey-Greenstein g parameter for different Scattering Length (SL) values in both linear and logarithmic scale.

3 System Efficiency Validation

A highly diffused medium allows only a small part of the transmitted photons to be detected. For a simple tissue medium of specific dimensions 10x10x5 (in arbitrary length units) the response of the system was here studied. The ratio of the emitted photons from a point source to the number of the detected events defines the efficiency of the system:

$$\varepsilon = \frac{N_{detected}}{N_{initiated}}$$

This quantity was examined for two opposite cases. First, by maintaining constant the Scattering Length SL of the medium and varying the Henyey-Greenstein g parameter and second, by maintaining constant the g parameter and varying the Scattering Length SL. The g parameter is varying in the typical range $0.80 < g < 0.95$ covering realistic tissue values, while the Scattering Length SL varies in the range $0.1 < SL < 1.0$ of the arbitrary length unit. Results are depicted in the Figure 7.

In order to examine the effect of the ordering of the diffuse media in the system's detection efficiency, following case study has been performed. In this investigation, simple phantoms consisting of two different iso-volumetric materials were placed in contact; the efficiency was evaluated by commutating the two volumes for various combinations of g and Scattering Lengths SL. The results are summarized in the tables I and II.

The results indicate that, if a biological tissue is to be time resolve investigated, the efficient way to proceed is by illuminating first (if possible in a real case) the area of grater g parameter, larger Scattering Length SL or both at the same time and by detecting the arriving photons at the more diffusive area. This can be explained by considering the fact that the rays which begin to travel in a volume with lower scattering properties tend to keep their directional information longer than the ones in a turbit environment. Hence, it is less likely to loose that "knowledge" by entering a low scattering medium and exiting at a higher one, rather than following the opposite direction.

Table 1. Efficiency for g=0.95

Material 1 (au)	Material 2 (au)	Efficiency %
SL = 0.1	SL = 0.2	2.11
SL = 0.2	SL = 0.1	2.47
SL = 0.1	SL = 0.3	3.26
SL = 0.3	SL = 0.1	4.27
SL = 0.1	SL = 0.5	4.72
SL = 0.5	SL = 0.1	7.81
SL = 0.1	SL = 0.8	6.25
SL = 0.8	SL = 0.1	13.10

Table 2. Efficiency for SL=0.30 au

Material 1	Material 2	Efficiency %
g = 0.80	g = 0.99	8.06
g = 0.99	g = 0.80	11.52
g = 0.81	g = 0.98	7.17
g = 0.98	g = 0.81	9.64
g = 0.83	g = 0.96	6.32
g = 0.96	g = 0.83	7.83
g = 0.86	g = 0.93	5.86
g = 0.93	g = 0.86	6.53

4 Microscopic Mode in PhoSim

From a microscopic point of view *PhoSim* can introduce a specific density of subcellular organelles in the form of spherical objects in a cubic grid formation. The program allows for a given material the input of an externally calculated scattering angle spectrum based on the microscopic Mie theory. In addition, the canonically repeated stereometric structure can be described with software parameters allowing the creation of the proper environment suitable for microscopic studies. The diameter of the equidistant spherical objects must be of the same size as the wavelength of the Near-Infrared radiation used to probe the biological material under investigation. However, the computational time and processing power for a typical microscopic study is by far more time consuming compared to the Henyey-Greenstein Monte-Carlo approach.

5 Conclusions

It is clear that *PhoSim* in its current version can be used for Time-Resolved Optical Tomography (TROT) studies of complicated materials for biological purposes. Moreover, the characteristics of the software along with the aforementioned properties and its simplicity make it an attractive tool for investigating light transmission in a variety of turbit environments, such as atmospherical, oceanic or stelar. The future versions of *PhoSim* will extend to different phantom geometries (cones, cylinders, ellipsoids) in order to simulate organs as well as other, more complicated phantoms. They will be able to behave as diffusing structures following the same procedure as the outer tissue environment described earlier.

References

1. A.-N. Rapsomanikis, A. Eleftheriou, M. Mikeli, M. Zioga and E. Stiliaris: *Time Resolved Optical Tomographic Imaging: A Simulation Study*, 2014 IEEE Nuclear Science Symposium and Medical Imaging Conference **M19-95** (2014).
2. A.-N. Rapsomanikis, A. Eleftheriou, M. Mikeli, Ch. Pafilis, M. Zioga and E. Stiliaris: *A Monte Carlo Simulator Dedicated to a Time-Resolved Optical Tomographic Modality Based on Henyey-Greenstein Phase Function*, 2015 IEEE Nuclear Science Symposium and Medical Imaging Conference **M5BP-163** (2015).
3. L.G. Henyey and J.L. Greenstein: *Diffuse radiation in the galaxy*, Astrophys. J. **93** (1941) 70–83.
4. T. Binzoni, T.S. Leung, A.H. Gandjbakhche, D. Ruefenacht and D.T. Delpy: *The use of the Henyey-Greenstein phase function in Monte Carlo simulations in biomedical optics*, Phys. Med. Biol. **51** (2006) N313–N322.
5. S. Angeli and E. Stiliaris: *An Accelerated Algebraic Reconstruction Technique based on the Newton-Raphson Scheme*, 2009 IEEE Nuclear Science Symposium and Medical Imaging Conference **M09-323** (2009) 3382–3387.

Mastering Conic Sections for a Direct 3D Compton Image Reconstruction

M. Mikeli[1], M. Zioga[1], A. Eleftheriou[1,*], Ch. Pafilis[1,2], A.-N. Rapsomanikis[1], and E. Stiliaris[1,3]

[1] Department of Physics, National and Kapodistrian University of Athens, Greece
[2] EEAE, Greek Atomic Energy Commission, Agia Paraskevi, Attica, Greece
[3] Institute of Accelerating Systems & Applications (IASA), Athens, Greece

*Present address: Institut für Pharmakologie und Toxikologie, University of Zurich, Switzerland

Abstract. Given the complexity of the image reconstruction procedures for Compton Camera events, especially when a 3D image is required for distributed sources in space, a simple, direct algorithmic approach is presented in this work. The recently developed ComptonRec package carefully handles the geometry of the conic sections to accumulate ray density distribution in a user defined voxelized volume inside the specified field of interest. Prior to planar reconstruction, the event selection part of the program filters out misidentified coincidence events and other physical background events with unbalanced total energy or inverse interaction sequence with the cameras subsystems. For each accepted event a series of planar reconstructions is performed, where the density distribution is the accumulation product of the conic intersection with all the affected pixels. A 3D image is finally reconstructed by assembling the partial planar information and by taking into account volume effects. The efficiency of this reconstruction method is checked with a plethora of simulated phantoms and results are presented and discussed.

PACS. 87.57.Q- Medical imaging computed tomography – 34.50.-s Compton scattering in atoms – 07.85.Fv Gamma-ray detectors – 07.05.Tp Computer modeling and simulation – 87.64.Aa Spectroscopy in medical physics

1 Introduction

In Nuclear Medicine a general purpose γ-Camera device is commonly used. Since its introduction, it has become a standard choice for clinical *in vivo* tests. Mechanical collimation is used by the γ-Camera in order to localize the photon source. This unfortunately leads to intrinsic limitations in sensitivity and spatial resolution, which could be overcame by the equivalent usage of electronic collimation in the configuration of a Compton Camera [1]. This kind of collimation is able to define the locus of a γ-ray by using a geometrical interpretation of the Compton Scattering. One major drawback of the Compton Camera is the difficulty of its image reconstruction. The algorithmic approach presented in this work in the fashion of a standalone program, the ComptonRec package, is assuming to serve as a simple, direct geometrical solution based on the appropriate handling of the conic sections involved in the 3D image reconstruction of a Compton Camera.

2 Principle of Operation

A Compton Camera consists of two detectors that operate using time coincidence, the Scatterer and the Absorber, where the latter replaces the mechanical collimator [2] [3]. The Camera's functionality relies on the Compton Scattering effect. An initial photon of the source interacts with the first thin detector and then it is absorbed by the second thicker one. The interaction point at each detector and the energy deposited in the Absorber are detected for every single event.

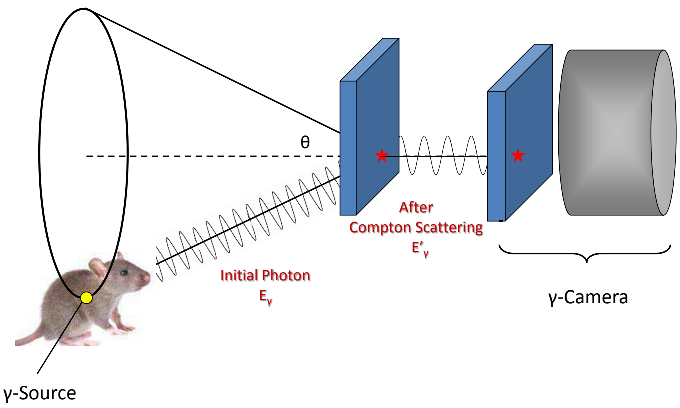

Fig. 1. Schematic explanation of the Compton Camera operation with a single layer Scatterer.

A conical surface (Figure 1) is formed with its vertex defined by the first interaction point, while its axis is determined by the two interaction location points in both detectors. The cone angle θ is determined by the Compton equation as

$$\theta = cos^{-1}\left[1 + m_0c^2\left(\frac{1}{E_\gamma} - \frac{1}{E'_\gamma}\right)\right] \qquad (1)$$

where E_γ is the initial gamma energy of the radiotracer and E'_γ the detected energy in the Absorber. This conical surface defines the locus of the emitted initial gamma photon from the source.

3 Reconstruction Techniques

As in conventional SPECT and PET, reconstruction algorithms for Compton Camera imaging may be broadly classified as either analytical or iterative methods. The most commonly used reconstruction algorithms show, not only for the Compton Camera modality, known and significant disadvantages.

- Analytical algorithms: Require large number of data and need to solve complex mathematical problems. They have proven to be unstable and also they can not handle complicated factors, present in the Compton Camera, mainly induced by the spatial intensity variation.
- Iterative algorithms: Need the use of spherical harmonics and due to the above mentioned variation are less efficient.

Compton Imaging in 3D is complicated by the fact that the point spread function varies from event to event, depending on the location of the interaction. Any reconstruction procedure for this modality is seeking to optimally determine the intersection points for all conical surfaces corresponding to all measured events [4]. In order to minimize computational time and to achieve optimum image quality an event based reconstruction technique is preferable.

4 The ComptonRec Program

A novel, simple and direct algorithmic approach, that masters conic sections in a user defined voxelized volume is here proposed. The main action in the event loop is the conical surface calculation for a selected event and its conic section with the corresponding Z plane inside the cameras Field of View (Figure 2). Accumulated information is stored pixelwise in each of the predefined Z planes. The final 3D image is assembled by taking into account volume effects. In order to reduce background events various cuts must be implemented.

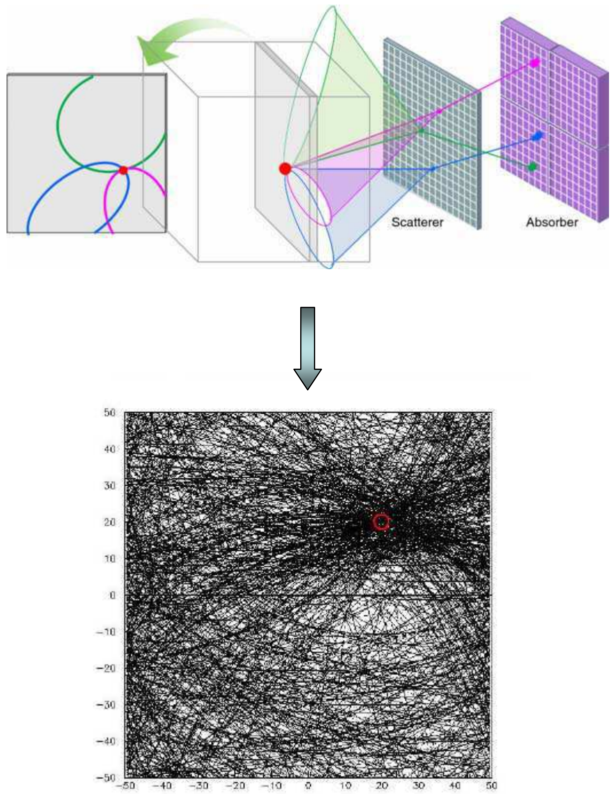

Fig. 2. Reconstruction of a point source in a planar Compton Camera image based on conical intersections.

4.1 Conic Sections

Supposing that the two interaction points in the Scatterer and the Absorber are defined by the coordinates (x_1, y_1, z_1) and (x_2, y_2, z_2) respectively as shown in Figure 3 and that through the measured energy deposition E'_γ in the Absorber the cone angle θ is reconstructed as in (1), the analytic equation for the associated conic section of this event with the projection plane Z_L can be found following next steps.

The basic analytic equation which defines the event cone is the scalar product

$$\boldsymbol{u} \cdot \boldsymbol{d} = |\boldsymbol{u}||\boldsymbol{d}|cos\theta \qquad (2)$$

where $\boldsymbol{u}$ is the vector which describes the location of all points on the event cone surface and $\boldsymbol{d}$ is the vector defined by the two measured interaction points:

$$\boldsymbol{u} = (x - x_1, y - y_1, z - z_1) \qquad (3)$$

$$\boldsymbol{d} = (x_1 - x_2, y_1 - y_2, z_1 - z_2) \qquad (4)$$

By squaring equation (2) the event cone definition through the inner product now reads:

$$(\boldsymbol{u} \cdot \boldsymbol{d})^2 - (\boldsymbol{u} \cdot \boldsymbol{u})(\boldsymbol{d} \cdot \boldsymbol{d})cos^2\theta = 0 \qquad (5)$$

and by taking into account that the conic section with a given plane $z = Z_L$ specifies the scalar products to the following expressions:

$$\begin{aligned}\boldsymbol{u}\cdot\boldsymbol{d} &= (x-x_1)(x_1-x_2)\\ &+ (y-y_1)(y_1-y_2)\\ &+ (Z_L-z_1)(z_1-z_2)\end{aligned}$$

which leads to the equation:

$$\boldsymbol{u}\cdot\boldsymbol{d} = x(x_1-x_2)+y(y_1-y_2)+\mathcal{CC}$$

with

$$\mathcal{CC} = x_1(x_2-x_1)+y_1(y_2-y_1)+(Z_L-z_1)(z_1-z_2)$$

Similarly,

$$\begin{aligned}\boldsymbol{u}\cdot\boldsymbol{u} &= (x-x_1)^2+(y-y_1)^2+(Z_L-z1)^2\\ \boldsymbol{d}\cdot\boldsymbol{d} &= (x_1-x_2)^2+(y_1-y_2)^2+(z_1-z_2)^2 = d^2\end{aligned}$$

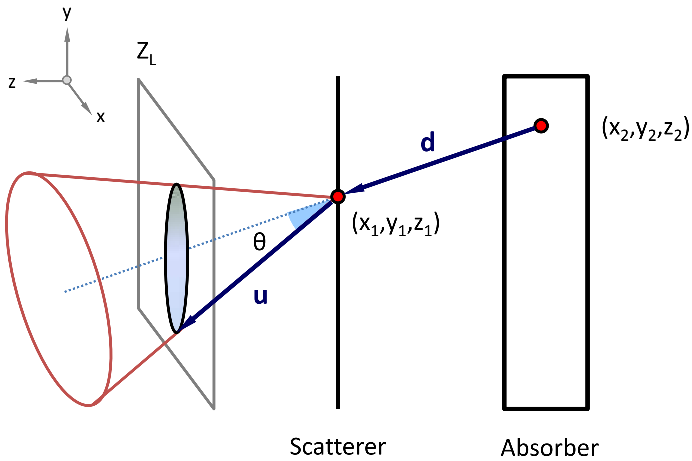

Fig. 3. The definition of the event geometry in a Compton Camera and the associated conic section (ellipse) of the formed event cone (with vertex the interaction point inside the Scatterer and opening angle θ) on the projection plane Z_L.

Finally, equation (5) after substitution of the inner products leads to the form of quadratic equation:

$$\begin{aligned}(\boldsymbol{u}\cdot\boldsymbol{d})^2-(\boldsymbol{u}\cdot\boldsymbol{u})(\boldsymbol{d}\cdot\boldsymbol{d})cos^2\theta &=\\ Ax^2+Bxy+Cy^2+Dx+Ey+F &= 0\end{aligned}\qquad(6)$$

where the set of the coefficients $\{A,B,C,D,E,F\}$ is defined for each event through the expressions:

$$\begin{aligned}A &= (x_1-x_2)^2-d^2cos^2\theta\\ B &= 2(x_1-x_2)(y_1-y_2)\\ C &= (y_1-y_2)^2-d^2cos^2\theta\\ D &= 2(x_1-x_2)\,\mathcal{CC}+2x_1d^2cos^2\theta\\ E &= 2(y_1-y_2)\,\mathcal{CC}+2y_1d^2cos^2\theta\\ F &= \mathcal{CC}^2-\left[x_1^2+y_1^2+(Z_L-z_1)^2\right]d^2cos^2\theta\end{aligned}$$

The quadratic equation (6) represents the conic section with the given plane Z_L for each of the measured events. It is easily calculable from the set of the above given coefficients based on the recorded values of the two interaction points and the kinematically reconstructed angle θ from (1) through the measured photon energy deposited in the Absorber E'_γ and the initial radiotracer photon energy E_γ. This is the conic section which is stored in a pixelated fashion in the matrix $[N_x,N_y]$ for a given plane vertically oriented to the Compton Camera's axis at the distance $z=Z_L$.

4.2 Event Selection Criteria

The Compton Camera modality shows a high number of background events. A need for an increase signal to noise ratio is obvious. This can be achieved by imposing specific criteria to each of the recorded events. The *Event Selection* component of the program, as shown in the Flow Diagram of Figure 4, rejects coincidence events that do not fulfill specific kinematical or energetic criteria.

There are two main categories in this event filtering routine:

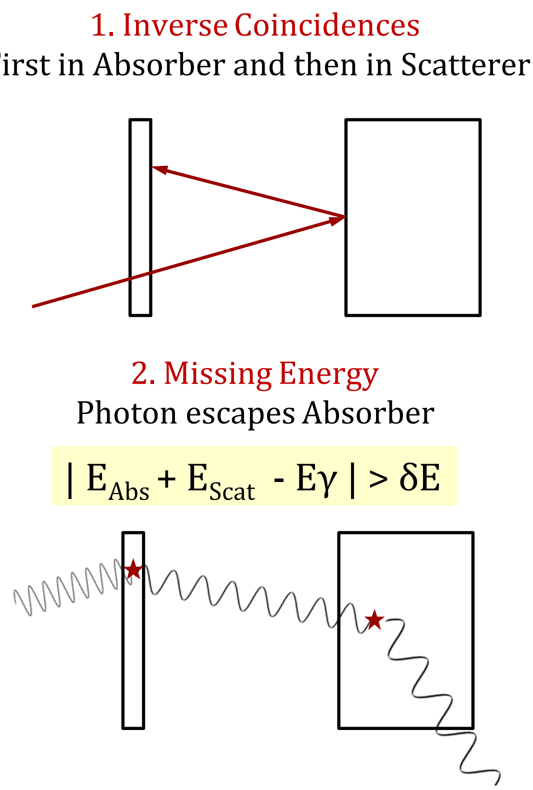

Fig. 5. Examples of rejected events: (1) Events that do not fulfill kinematical criteria and produce mathematically incorrect solutions ($|cos\theta| > 1$). The majority of them are traced back to an inverse scattering sequence in the detector's components. (2) Events that are not fully absorbed and they violate specific energy conservation criteria.

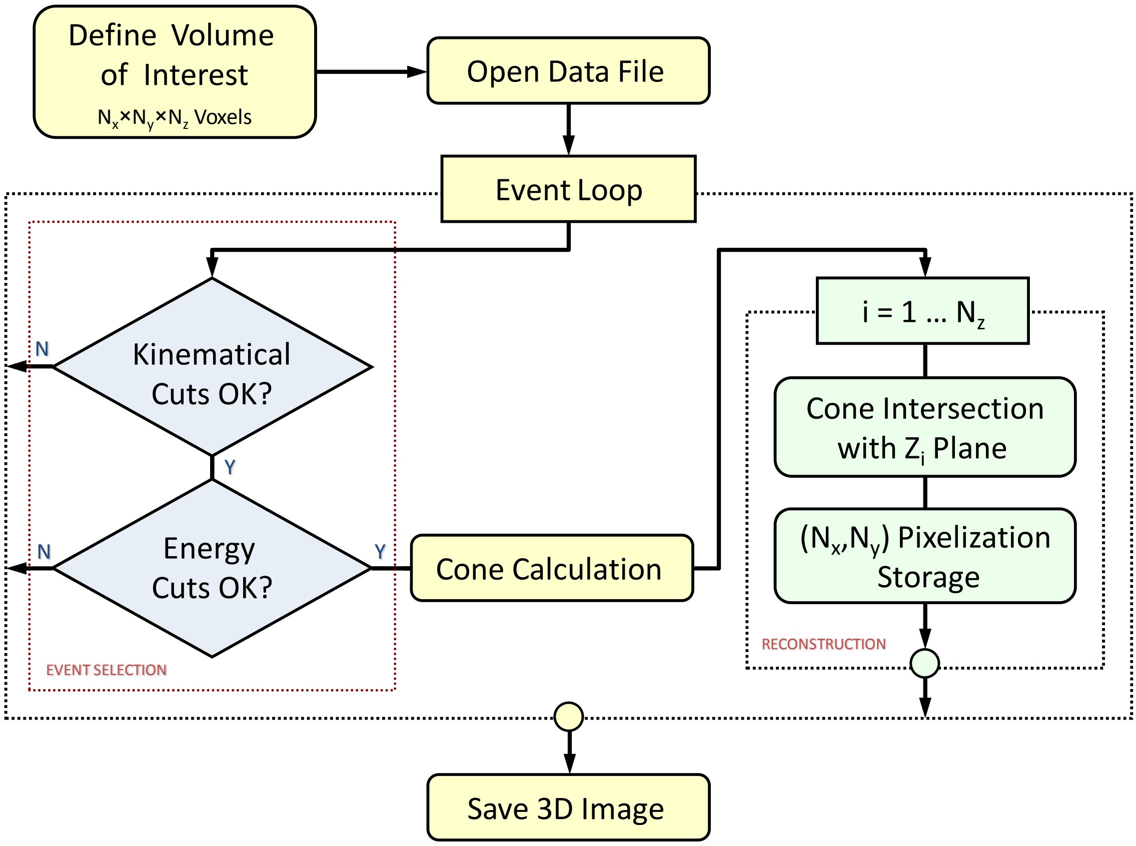

Fig. 4. Flow Diagram of the ComptonRec package with the various filtering and reconstruction components.

- *Kinematical Cuts:* This involves event rejection with inverse interaction sequence. These events are first scattered off the Absorber and then they interact with the Scatterer (see Figure 5.1). The majority of them produce a meaningless conical angle θ by incorrectly imposing $|cos\theta| > 1$.

- *Energetic Cuts:* The acceptance criterion fulfills the equation $E_{Abs} + E_{Scat} = E_\gamma \pm \delta E$. Here, E_{Abs} and E_{Scat} are the detected energy in the Absorber and Scatterer respectively. E_γ is the nominal energy of the radiotracer and δE the overall energy resolution of the detection system. Events that show an absolute deviation $|E_{Abs} + E_{Scat} - E_\gamma|$ larger than the predefined energy resolution δE are rejected and they are not further considered in the reconstruction procedure (see Figure 5.2).

Both criteria can be check in simulated events, where the exact information of the interaction location and time, as well as the energy deposition in every detector component, is stored. For real events, where normally only the E_{Abs} is measured, there is not a control mechanism to investigate possible escape of photons and violation of the energy criterion.

The user first defines the volume of interest in physical dimensions and then decides for the discretization of it by specifying the number of voxels $\{N_x, N_y, N_z\}$ to be used. For each of the vertical planes at $z_i = Z_{L_i}$, $i = 1...N_z$ a planar image reconstruction is performed, which is based on the pixelization of the conic solution for every of the stored events and the additive accumulation of the reconstructed ray density at each planar pixel $\{P_x, P_y\}$. By taking into account volume effects, a series of N_z planar images are finally stored from which a 3D image can be reconstructed. The flow diagram of the program ComptonRec is summarized in Figure 4.

5 Simulating the Compton Camera

The performance of the Compton Camera reconstruction algorithm ComptonRec is validated through GATE [5] simulations for various geometrical characteristics [6]. The most optimal detector configuration used in this study was a simple 1mm thick Silicon Scatterer in circular geometry followed by a cylindrical CsI Absorber with dimension $2'' \times 2''$. Various energy γ-ray sources have been used.

A typical reconstruction result of a simulated three-point source is shown in Figure 6. This phantom was simulated in the GEANT4/GATE environment in order to test the algorithm's efficiency, always taking into account the volume effects. The phantom consists of three spherical sources 1 mm in radius that form a triangle on the XY plane of the Compton Camera and it was placed

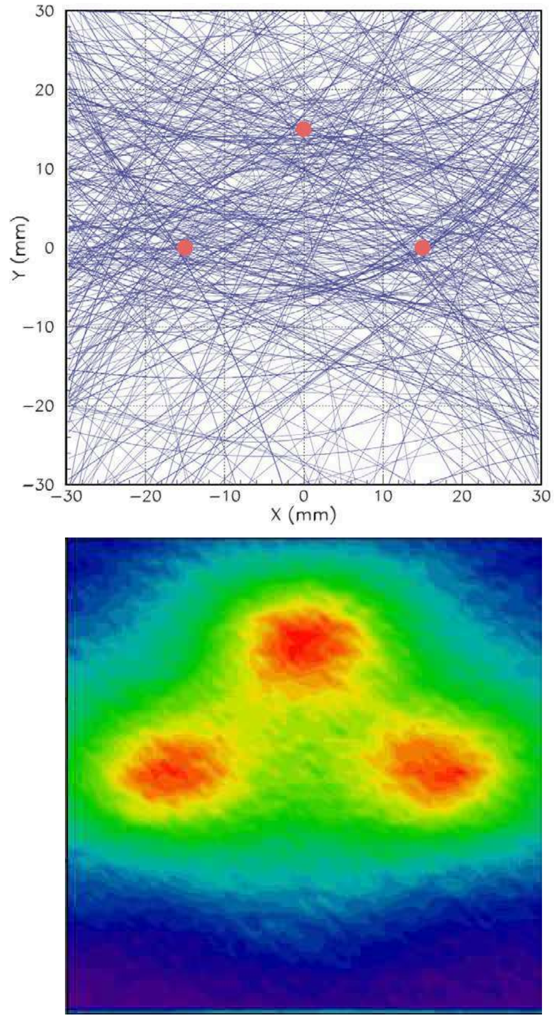

Fig. 6. Reconstruction with the ComptonRec program of a simple coplanar three-point source phantom. *Upper Part:* Intersection of the conical surfaces with the reconstruction plane for some of the accumulated events. The location of the three γsources is indicated with closed circles *Lower Part:* Contour plot of the reconstructed planar image for the same phantom with full statistics.

at a distance of 60 mm away from the Scatterer. The exact location of the three sources was $S_1(-15mm, 0)$, $S_2(+15mm, 0)$ and $S_2(0, +15mm)$. The reconstructed planar image with the ComptonRec package in the form of a contour plot is shown in the lower part of Figure 6.

However, the reconstructed image is normally affected by the strong solid angle variation with the distance of the Compton Camera system and thus characterized with deformation errors. In order to overcome these effects, the detection efficiency is extensively studied and a correction procedure to optimize the previously described reconstruction technique is proposed. It takes into account all possible factors that potentially cause the non-uniformity in the angular acceptance of the system and influence its performance, such as the interaction probability of the incoming γ-photon of a given energy with both detector subsystems.

6 The Correction Model

The basic methodology, how the non-uniformity in the angular acceptance of a simple Compton Camera is determined by means of a Monte Carlo study, is described in this section. The geometrical characteristics of the Scatterer and the Absorber define in a complicated way the angular acceptance of a Compton Camera. This complication enhanced by the angular dependence of the Compton Effect requires an extensive simulation of all electromagnetic interactions for a given detector geometry and for a fixed energy of the emitted photons [7].

6.1 A Membrane Source

A two stage Compton Camera is modeled using the GATE Monte Carlo simulation package. For reasons of simplicity, the Scatterer is simulated as a 2 mm thick Silicon homogeneous cylinder with a diameter of 50 mm. Similarly, the Absorber is a 50 mm × 50 mm CsI cylinder.

In order to investigate and quantify the detection efficiency of the system, a plane phantom source (membrane) with the same dimensions 50 mm × 50 mm as the detector window is simulated. This plane source, emitting isotropically photons of a constant energy E_γ, is placed at a distance D from the Scatterer. Due to the angular and physical acceptance of the system, the reconstructed planar image has no more a uniformly distributed intensity but it exhibits a symmetrical Gauss form. A sufficient number of simulation studies at different distances D which cover the whole area of interest inside the Field of View (FoV) of the system has been performed.

6.2 The Fitting Procedure

For a given distance D between the plane γ-source (membrane) and the head of the Compton Camera a matrix that contains the amount of the detected and accepted source photons is formed. Although the phantom source is of homogeneous nature, due to the angular variation of the efficiency mentioned above, this matrix exhibits a non-uniform but symmetrical character. This effect is clearly depicted in Figure 7, where the number of the detected source photons are shown in the form of a Lego plot.

The symmetric around the camera's axis intensity distribution in the (x,y)-plane can be approached by a two-dimensional Gaussian distribution in the form of:

$$I(x, y, D) = A(D)exp\left[-\frac{(R-R_0)^2}{2\sigma^2(D)}\right] \tag{7}$$

where, $R = \sqrt{x^2 + y^2}$ is the radial distance from the axis and $A(D)$ and $\sigma(D)$ are two free fit parameters depending on the distance D of the plane source. The parameter $A(D)$ corresponds to the maximum γ-ray intensity accumulated at the center of the image, while $\sigma(D)$ represents

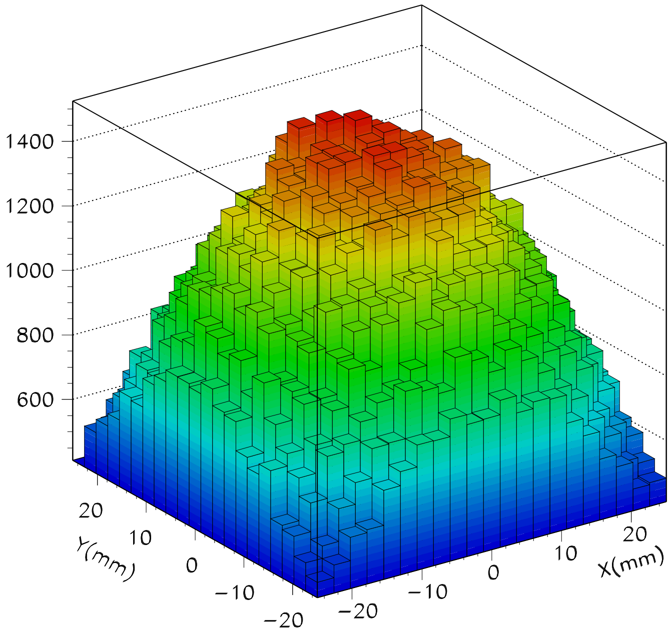

Fig. 7. XY-planar distribution of the detected photons from a homogeneous plane γ-source.

the standard deviation of the 2D symmetrical Gauss distribution. In all simulated cases $R_0 \simeq 0$.

It is obvious that this accumulated distribution can be considered as a correction matrix. Any planar image at a distance $z = D$ detected by the Compton Camera and reconstructed with the ComptonRec algorithm can be corrected by a simple element division with the value $I(x, y, D)$.

6.3 A Generalized Model for the Correction Matrix

The area of interest inside the FoV of the Compton Camera system has been covered by a series a plane source simulations followed by the fit procedure described in the previous section. In all simulations the number of the emitted from the source photons is kept constant, while the energy of the emitted photons is fixed at $E_\gamma = 511$ keV. The values of the two fit parameters are expected to be continuously varying numbers with the distance D. Results for $D \in \{10, 20, 30, ...110\}$ mm are shown in Figure 8.

In order to develop a generalized model for the correction of the reconstructed planar image at any given distance D, the exact values of the parameters $A(D)$ and $\sigma(D)$ are needed. Arithmetic evaluation of these parameters allows the analytic expression of Equation (7) to be directly applied as a correction function. Therefore, a global fit on these parameters $A(D)$ and $\sigma(D)$ is performed using the simple functions:

$$A(D) = A_0 e^{-A_1\sqrt{D}} \qquad (8)$$
$$\sigma(D) = \sigma_0 e^{+\sigma_1 D} \qquad (9)$$

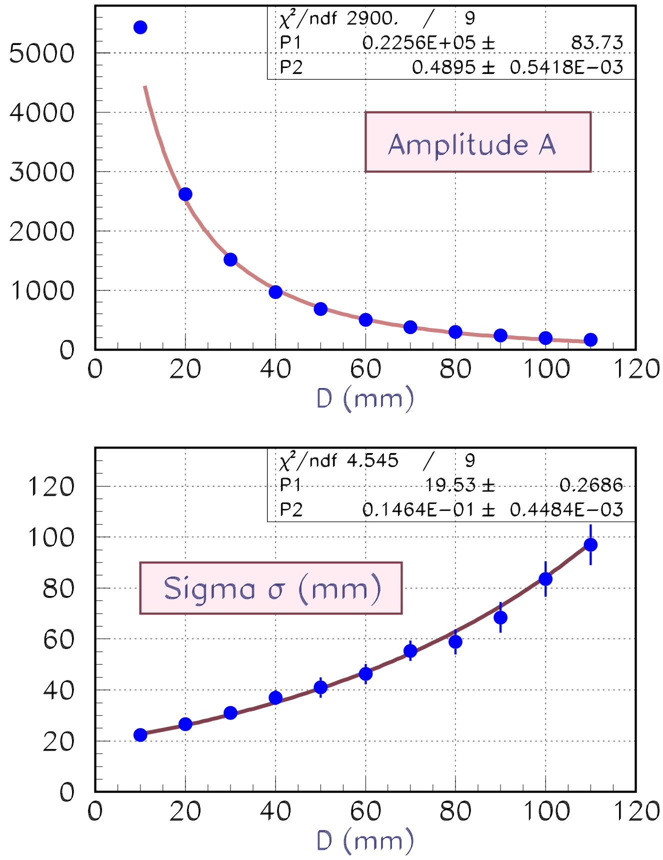

Fig. 8. A global fit of the 2D Gauss parameters $A(D)$ (amplitude) and $\sigma(D)$ (standard deviation) which are the simulation results for the plane source at different distances D.

The best description for the parameters is obtained for the values:

$$\begin{aligned} A_0 &= \ 22560\ (80)\ [a.u.] \\ A_1 &= 0.4895 \ \ (5)\ [mm^{-1/2}] \\ \sigma_0 &= \ \ 19.53\ (27)\ [mm] \\ \sigma_1 &= 0.0146 \ \ (4)\ [mm^{-1}] \end{aligned}$$

As shown in Figure 8 the amplitude $A(D)$ decays as the distance D increases while the standard deviation $\sigma(D)$ increases.

6.4 Optimized 3D Reconstruction

Having defined the general expression for the correction function $I(x, y, D)$, a 3D reconstruction can be now performed for any source distribution inside the FoV. As a typical example, a simple phantom consisting of three identical coplanar spherical sources with $E_\gamma = 511$ keV and radius r=2 mm is simulated and reconstructed. The (x,y)-position of the three spherical sources is taken $(0, 0)$, $(+15, +15)$, $(-15, 0)$, all distances in mm.

Reconstruction results are shown in Figure 9 in the form of 3D isosurface plots. Left are shown the reconstructed images with the ComptonRec algorithm for dis-

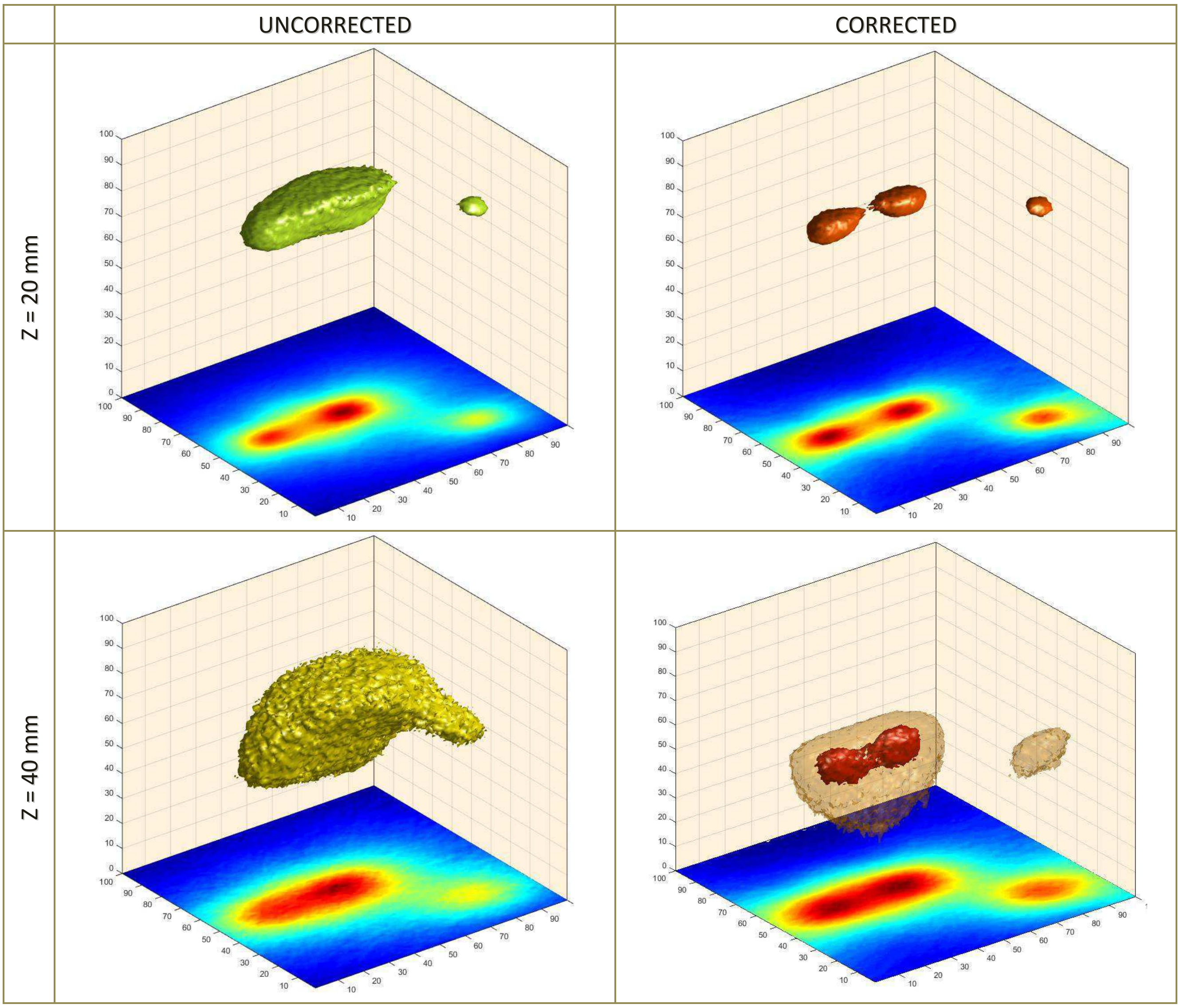

Fig. 9. 3D reconstruction results in the form of isosurface plots for the three coplanar spheres phantom without applying (left) and with the optimization procedure (right) described in this work. The correction algorithm has been implemented in the ComptonRec package used in the 3D reconstruction. Each grid dimension is $100 \times 100 \times 100$ units, where 1 mm $= 2$ grid units.

tances 20 mm and 40 mm from the Compton Camera entrance without applying any correction method. In the right are the same reconstruction images with the optimization procedure proposed in this work. The analytical expression for the $I(x, y, D)$ function with the best fit parameters is implemented in the reconstruction algorithm. The best result is obtained for the Z=20 mm distance.

7 Summary

In summary, the architecture and functionality of the package ComptonRec, which handles the geometry of the conic sections to accumulate ray density distribution in a user defined voxelized volume inside a specified field of interest for Compton Camera image reconstruction, is here presented. The planar image reconstruction is examined with GEANT4/GATE simulated γ-rays by filtering out misidentified coincidence or energetically mismatched events. Reconstruction results are shown for a typical simple geometry source configuration.

Non-uniformity of the system's efficiency caused by the angular acceptance and the angular dependence of the Compton Effect for distributed γ-sources is extensively studied and improved with a correction matrix expressed in the form of an analytical 2D symmetric Gauss function with parameters obtained from the analysis of the detected events of uniformly emitting homogeneous plane sources in space and covering the whole Field of View of the Compton Camera

References

1. R. Todd, J. Nightingale and D. Everett: *A proposed Gamma Camera*, Nature **251** (1974) 132–134.
2. J. Krimmer *et al.*: *Development of a Compton Camera for Medical Applications based on Silicon Strip and Scintillation Detectors*, Nucl. Instr. and Methods **A 787** (2015) 98–101.
3. M.A. Alnaaimi *et al.*: *Performance Evaluation of a Pixellated Ge Compton Camera*, Phys. Med. Biol. **56** (2011) 3473–3486.
4. A. Andreyev, A. Sitek and A. Celler: *Fast Image Reconstruction for Compton Camera using Stochastic Origin Ensemble Approach*, Med. Phys. **38** (2011) 429–438.
5. S. Jan *et al.*: *GATE: A Simulation Toolkit for PET and SPECT*, Phys. Med. Biol. **49** (2004) 4543–4561 and The OpenGATE Collaboration
6. M. Zioga, M. Mikeli, A. Eleftheriou, Ch. Pafilis, A.-N. Rapsomanikis and E. Stiliaris: ComptonRec*: Mastering Conic Sections for a Direct 3D Compton Image Reconstruction*, 2015 IEEE Nuclear Science Symposium and Medical Imaging Conference **M4CP-266** (2015).
7. M. Mikeli, M. Zioga, A. Eleftheriou, Ch. Pafilis, A.-N. Rapsomanikis and E. Stiliaris: *3D Reconstruction Optimization for Compton Camera Events*, 2015 IEEE Nuclear Science Symposium and Medical Imaging Conference **M4CP-210** (2015).

Nuclear and atomic techniques to the study of U- bearing formation of Epirus region[1]

I. T. Tzifas and P. Misaelides

Department of Chemistry, Aristotle University of Thessaloniki, GR-54124 Thessaloniki, Greece.

Abstract. Sedimentary Mesozoic rocks from Epirus region and particularly tectonized/re-processed organic rich limestones, were examined for their actinide content. Gamma-ray measurements using HPGe detector showed that the above geological materials exhibit enhanced radioactivity mainly attributed to the ^{238}U-series. Bulk geochemical analyses using ICP-OES/MS showed variable U concentrations with a notable value of 648 ppm in the case of dark organic-rich material hosted into the tectonized/reprocessed phosphatized limestones. SEM-EDS combined with XRD showed that the main phases were apatite (fluoroapatite and carbonate apatite) calcite and organic matter. Synchrotron radiation (μ-XRF) revealed uranium accumulation in areas of the material containing, among others, carbonate apatite and organic matter. Uranium-bearing carbonate apatite crystals were separated from the rock and characterized by Raman spectroscopy and microprobe analysis. The analysis of these crystals also indicated the presence of sodium and sulfur. The UL_{III}-edge of μ-XANES spectra showed that uranium is present in tetravalent form. The uranium presence in the crystals was also visualized, after neutron irradiation and etching, by the observation of the fission tracks. Epirus samples are classified among the richest U-bearing phosphatized limestones and/or sedimentary phosphorites in the world.

References

Tzifas, I.T., et al., "Uranium-bearing phosphatized limestones of NW Greece." *Journalof Geochemical Exploration* 143 (2014) 62.
Tzifas, I.T., et al., Uranium-bearing francolites present in organic-rich limestones of NW Greece: a preliminary study using synchrotron radiation and fission track techniques. *Journal ofRadioanalytical andNuclearChemistry*311 (2017) 465.

[1]Part of I.T. Tzifas' PhD Dissertation (in preparation)

Paleoseismology: Defining the seismic history of an area with the use of the OSL dating method

K.C. Stamoulis, I. Tsodoulos, C. Papachristodoulou, K.G. Ioannides

Department of Physics, The University of Ioannina, Ioannina 45110, Greece

Abstract. Paleoseismology is a supplementary method of the geological science which is used to define the seismological history of an area, in a span of few thousands of years. A crucial step in assessing the age of previous large seismic events is the dating of the geological patterns that appear on the walls of a trench, excavated along the fault under investigation. This can be accomplished by dating either carbon remains or human artifacts. In the absence of such findings, the Optically Stimulated Luminescence (OSL) dating method can be applied to provide absolute ages of the geological patterns and thus of the deformations that were produced from large seismic events in the past.

The present article gives an example of a paleoseismological investigation of a known fault at Gyrtoni, North East Thessaly, which revealed strong earthquakes in the past history of the area. Paleoseismological analysis of the trenches indicates evidence of three surface faulting events in the time span between 1.42 ± 0.06 ka and 5.59 ± 0.13 ka before present. The observed vertical displacement per event of ~0.50 m corresponds to an Mw 6.5 ± 0.1 earthquake. An average fault slip rate of 0.41 ± 0.01 mm/yr and an average recurrence of 1.39 ± 0.14 ka for earthquakes were estimated. Accordingly, documented the activity of the fault and as the return period from the most recent event (minimum age 1.42 ± 0.06 ka) has expired, the possibility for reactivation of this active structure in the near future could be taken into Seismic Hazard Assessment. This information can be proved very valuable for the area which is in the vicinity of the populated city of Larissa. Analogous results were obtain and in the case of Paleochori-Sarakina Fault near Grevena. Recurrence interval was found to be very high (ca. 30ka) and the slip rates were accordingly very low, about 0.01-0.03 mm/yr.

1 Introduction

Earthquakes are one of the most dangerous natural phenomena for the human life. Throughout human history, great seismic events led to the devastation of ancient civilizations. Thus, the study of evidences from ancient earthquakes buried into the earth crust could prove very valuable for the evaluation of the seismic hazard nowadays, especially in the vicinity of populated areas.

Paleoseismology is a supplementary method of the science of Geology that looks for ancient earthquakes' signs at geologic sediments and rocks at a depth from 2-8 m below the earth's surface. For this purpose, geologists look for geologic faults associated with large seismic events that occurred either in recent years or in historical times. The existence of a fault is evidenced by the fracture of the stratigraphy and the relative movement of the rocks along the fault. Over the downthrown blocks, new sedimentation may occur or material from the uplifted earth surface may move downwards creating colluviums at the base of the fault. Then a trench is excavated along the fault direction, about 2-4 m wide, 2-8 m deep and 10-30 m long. The walls are cleaned and scanned in order to log the stromatography and the deformations observed [1]. During the excavation, carbon-containing remains are collected for radiocarbon dating, as well as artifacts that could help to evaluate the age of each distinct sedimentary bed. The study of the chronological context of the fault regime can lead to the age estimation of ancient earthquakes and the time of recurrence. Other important features, such as the slip rate along the fault, the sedimentation rate of the area and the landscape degradation can also be estimated from the paleoseismological study of an area. In case no dateable remains or artifacts are found, the only method for dating the stratigraphy of the fault is the Optically Stimulated Luminescence (OSL) dating of sediment samples, collected from each distinct unit of the stratigraphic formations in the upthrown and downthrown sites of the fault. The surrounding soil is also sampled in order to estimate the annual dose rate through γ radiation spectroscopy. The age of each sample is subsequently calculated.

In the present study, faults at Gyrtoni, Larissa, Eastern

Thessaly, and at Paleochori-Sarakina, Grevena, Western Macedonia, where strong earthquakes occurred in the recent years, were investigated. Trenches were excavated along the faults and samples were collected and delivered at the Archaeometry Center of the University of Ioannina, to be processed and measured with the OSL method. The calculated ages were analyzed in order to estimate the age of ancient earthquakes, evidenced from the geological study of the trenches. Ages and mean recurrence time, as well as slip rates for the faults were estimated. The results are presented here.

2 Materials and Methods

Paleoseismological trenches were excavated perpendicular to the trace of the faults at Gyrtoni (Fig. 1) and Paleochori-Sarakina. The trench at Gyrtoni Fault was 30m long, 4m deep and 2m wide. The walls were cleaned, gridded with a 1 m x 1 m string grid and mapped in detail. The trench excavated near the village of Paleochori, was 17m long and 3m deep and was gridded in a similar way. Several soil cores were collected perpendicular to the trench walls and were brought to the Archaeometry Center of the University of Ioannina for OSL measurements. Special care was taken to collect samples from each of the stromatographic units revealed on the trench walls, in order to construct an accurate age context and to assess the age of ancient earthquakes, the evidences of which were observed.

The OSL dating method involves measurement of the luminescence signal of quartz grains and radioactivity measurements of the surrounding soils. In the first step, the dose that is absorbed was estimated. The sample preparation consists of drying and sieving, followed by chemical treatment in order to enrich the soil in quartz grains. The soil cores were unpacked under subdued red light and the outer 2 cm of the cores were discarded. Four to 8 cm of the inner parts was transferred to plastic containers, dried to 50^o C for a day, grounded and sieved. The 125-250 μm fractions of the grains were transferred to small tubes and were chemically treated. Solutions of HCl (8%) to eliminate carbonates, of H_2O_2 (30%) to eliminate organic content and finally of HF (40%) to dissolve feldspars and etch the quartz grains, were added to the selected fractions [2]. The last step of chemical treatment was performed to discard the surface of the grains at 20 μm depth where the α-particles energy is absorbed.

For each sample, a number of aliquots were prepared by pouring few mg of enriched quartz grains on stainless steel disks. The disks were measured for luminescence signal on a TL/OSL Reader (Riso model DA-20). The Single Aliquot Regenerative dose protocol (SAR) was used to measure the

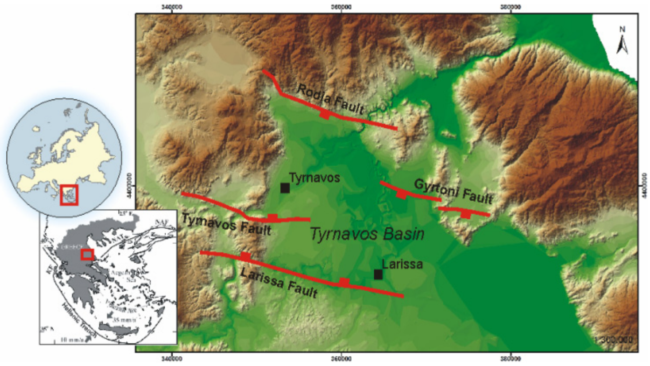

Fig. 1. Gyrtoni Fault near the city of Larissa.

dose absorbed by the quartz grains during the burial time, or since the time they were bleached, either exposed to sun or to high temperature heat [3, 4]. The protocol was slightly changed by adding a step of Infrared Stimulated Luminescence (IRSL) to check for feldspar impurities [5]. Each cycle of the protocol involved a natural dose (N) measurement under IRSL and OSL mode and an irradiation of the aliquot with a test dose (T) followed again by IRSL and OSL measurements. Following this first step, the aliquots were irradiated with raising doses and the same cycle for luminescence measurements was repeated to calculate the ratio of the given dose to test dose (L_i/T_i). Finally, the growth curves for each aliquot were constructed using the ratios L_i/T_i and N/T, was interpolated with the fit of the growth curve giving the equivalent dose ED or paleodose (see Fig. 2).

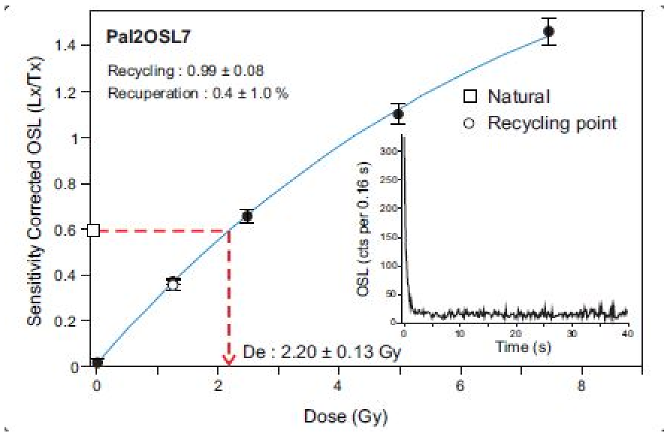

Fig. 2. Typical dose-response curve and natural OSL signal decay curve (inset) from sample Pal2OSL7 collected from the Paleochori -Sarakina trench.

Radioactivity of the environment was measured with γ spectrometry using a HPGe detector (BE3825, Canberra) with relative efficiency >26% and FWHM 1.9 keV, at 1.33 keV photo peak of ^{60}Co, and a digital spectrum analyzer (DSA-1000, Canberra). Soil samples were dried to steady weight at 105^{o} C, sieved and the <500 μm fraction was mounted in a standard geometry plastic container and measured for γ radioactivity. The photopeaks of the natural decay series of ^{238}U, ^{235}U, and ^{232}Th, as well as the photopeak of the ^{40}K isotope were analyzed and the annual dose rate delivered at the quartz grains was calculated using the appropriate conversion factors [6, 7].

The ages for each aliquot and the mean values for each sample were calculated using the equation:

$$\text{Age (years)} = \frac{\text{Paleodose (Gy)}}{\text{Annual Dose rate }\left(\frac{\text{Gy}}{\text{year}}\right)}$$

3 Results and Discussion

The age calculations of the core samples revealed ancient earthquakes of high magnitudes. A detailed description of the east wall of the trench at the Gyrtoni Fault, is given at Fig. 3. The corresponding paleodose assessements, dose rates and calculated ages are presented in Table 1. In the case of Gyrtoni Fault three strong earthquakes seem to have been occurred in the time span between 1.42 ± 0.06 ka and 5.59 ± 0.13 ka before present (see Fig. 3). The observed vertical displacement per event was found to be ~0.50 m, which corresponds to an Mw 6.5 ± 0.1 earthquake. An average fault slip rate of 0.41 ± 0.01 mm/yr and an average recurrence of 1.39 ± 0.14 ka for earthquakes were estimated. Accordingly, documented the activity of the fault and as the return period from the most recent event (minimum age 1.42 ± 0.06 ka) has expired, the possibility for reactivation of this active structure in the near future could be taken into Seismic Hazard Assessment.

In the case of the Paleochori-Sarakina Fault (see Fig. 4) the excavated trench revealed the recent earthquake in 1995, and other earlier seismic events, not well known. Preliminary results of OSL age calculations of some of the samples collected at this trench are given in Table 2. Ages show that the Paleochori–Sarakina Fault is very old given that the lowest units of the trench are about 130 ka old while ages of samples collected at the colluvial wedge of the fault show that new paleosoil horizons occur at about every 30 ka, indicating that the recurrence interval of strong seismic events in this fault is very high. Also, the elevation distance between the samples (~0.50 m) shows that the slip rate of the fault should be very slow at about 0.010-0.025 mm/a. These findings are in agreement with earlier investigations at the same fault by Chatzipetros et al. [8].

These results, revealed from the two excavated trenches at the Gyrtoni and Paleochori-Sarakina Faults, indicate that the OSL dating method could be of great value in the study

Table 2. Dose rates from the environment, paleodose assessements and age calculations of selected samples collected from the Paleochori-Sarakina trench.

No	Sample ID	Water Content (%)	Total dose rate (Gy/ka)	n	CAM De (Gy)	CAM age (ka)
1	Pal2OSL1	20.0	2.27±0.02	10	289.33±6.54	127.66±3.17
2	Pal2OSL3	13.7	2.13±0.02	10	171.66±13.17	80.66±6.25
3	Pal2OSL4	14.2	2.38±0.02	10	124.3±5.95	52.21±2.55
4	Pal2OSL5	13.5	2.63±0.02	10	53.24±3.09	20.23±1.19
5	Pal2OSL6	8.0	1.91±0.02	18	5.29±0.27	2.77±0.15
6	Pal2OSL7	11.0	1.71±0.02	24	1.45±0.07	0.85±0.04

Table 1. OSL measurements, equivalent doses, dose rates from the environment and age calculations of the samples collected from the Gyrtoni trench.

Sample no.	Sample position	Material	Depth (m)[a]	Water Content (%)[b]	^{238}U (Bq/kg)[c]	^{232}Th (Bq/kg)[c]	^{40}K (Bq/kg)[c]	External β dose rate (Gy/ka)[d]	External γ dose rate (Gy/ka)[d]	Cosmic dose rate (Gy/ka)[e]	Total dose rate (Gy/ka)[f]
Gyrtoni 1 trench											
Gyr1OSL_01	Upthrown block	Sediment	0.5	7.3	28.1 ± 1.3	16.3 ± 1.1	327.8 ± 25.3	0.98 ± 0.05	0.65 ± 0.02	0.21 ± 0.02	1.84 ± 0.06
Gyr1OSL_02	Upthrown block	Sediment	1.1	5.5	20.2 ± 0.9	12.7 ± 0.7	279.5 ± 20.0	0.82 ± 0.04	0.52 ± 0.02	0.18 ± 0.02	1.51 ± 0.05
Gyr1OSL_03	Upthrown block	Sediment	0.7	19.2	38.1 ± 1.5	30.3 ± 1.5	489.9 ± 34.6	1.29 ± 0.06	0.89 ± 0.03	0.19 ± 0.02	2.37 ± 0.07
Gyr1OSL_04	Upthrown block	Sediment	1.2	26.6	24.5 ± 1.2	31.6 ± 1.4	454.6 ± 32.2	1.05 ± 0.05	0.73 ± 0.02	0.18 ± 0.02	1.96 ± 0.06
Gyr1OSL_05	Upthrown block	Sediment	1.4	23.6	26.2 ± 1.1	21.5 ± 1.1	347.2 ± 23.8	0.87 ± 0.04	0.60 ± 0.02	0.17 ± 0.02	1.64 ± 0.05
Gyr1OSL_06	Upthrown block	Sediment	2.5	43.7	20.4 ± 0.8	21.7 ± 0.8	269.3 ± 18.0	0.58 ± 0.03	0.43 ± 0.01	0.15 ± 0.02	1.17 ± 0.03
Gyr1OSL_07	Fault zone	Sediment	1.8	17.1	20.0 ± 1.1	23.3 ± 1.2	349.3 ± 27.6	0.89 ± 0.05	0.61 ± 0.02	0.17 ± 0.02	1.67 ± 0.06
Gyr1OSL_08	Fault zone	Sediment	1.8	12.2	15.0 ± 0.9	19.0 ± 1.1	445.0 ± 30.7	1.05 ± 0.06	0.62 ± 0.03	0.17 ± 0.02	1.84 ± 0.07
Gyr1OSL_09	Fault zone	Sediment	2.2	14.9	29.4 ± 1.3	20.4 ± 1.1	369.6 ± 27.3	1.01 ± 0.05	0.68 ± 0.02	0.16 ± 0.02	1.85 ± 0.06
Gyr1OSL_10	Downthrown block	Sediment	0.7	12.6	29.1 ± 1.4	28.8 ± 1.4	499.3 ± 34.3	1.32 ± 0.07	0.87 ± 0.03	0.20 ± 0.02	2.38 ± 0.07
Gyr1OSL_11	Downthrown block	Pottery	0.7	13.8	28.9 ± 1.3	26.0 ± 1.3	498.2 ± 35.7	1.28 ± 0.07	0.83 ± 0.03	0.20 ± 0.02	2.31 ± 0.08
Gyr1OSL_12	Downthrown block	Pottery	1.0	9.7	27.2 ± 1.4	30.0 ± 1.6	504.2 ± 35.9	1.36 ± 0.07	0.89 ± 0.03	0.18 ± 0.02	2.43 ± 0.08
Gyr1OSL_13	Downthrown block	Pottery	1.0	14.6	33.0 ± 1.5	26.5 ± 1.4	505.9 ± 35.2	1.32 ± 0.07	0.86 ± 0.03	0.18 ± 0.02	2.37 ± 0.07
Gyr1OSL_14	Downthrown block	Pottery	1.0	13.5	26.2 ± 1.1	25.4 ± 1.1	512.1 ± 31.1	1.29 ± 0.06	0.81 ± 0.03	0.18 ± 0.02	2.28 ± 0.07
Gyr1OSL_15	Downthrown block	Pottery	2.0	16.5	29.8 ± 1.1	25.0 ± 1.1	464.5 ± 30.1	1.19 ± 0.05	0.78 ± 0.02	0.16 ± 0.02	2.13 ± 0.06

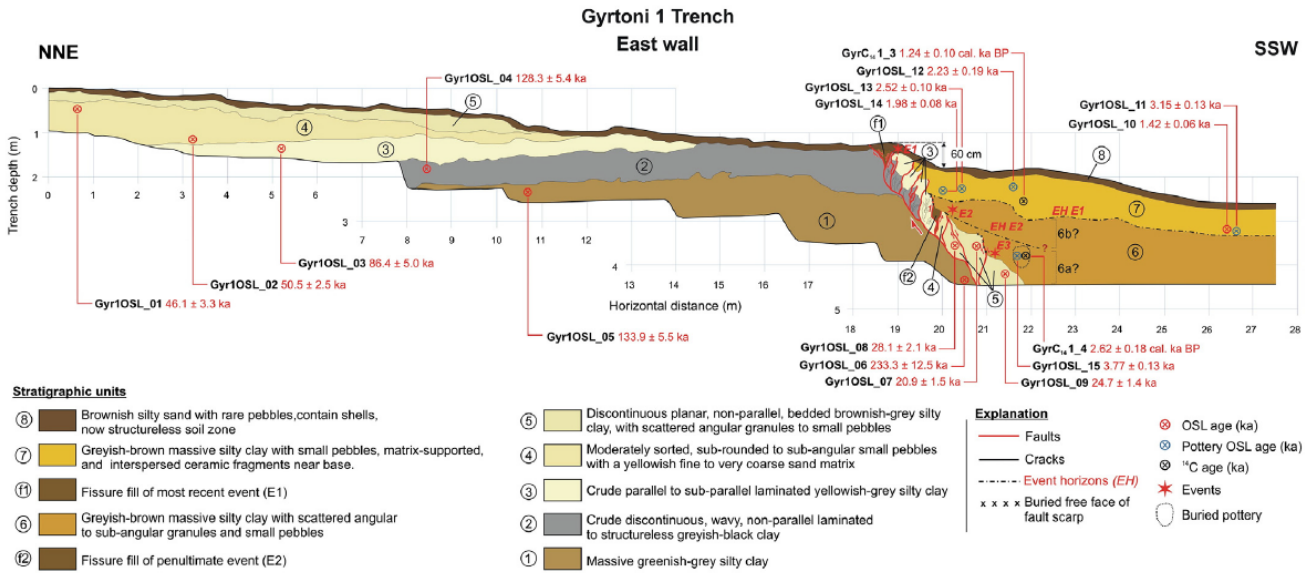

Fig. 4. Gyrtoni trench, east wall. The distinct units of the stratigraphy of the area are shown with different colors. The three paleoseismic events mentioned in the text are also presented (red stars and labels).

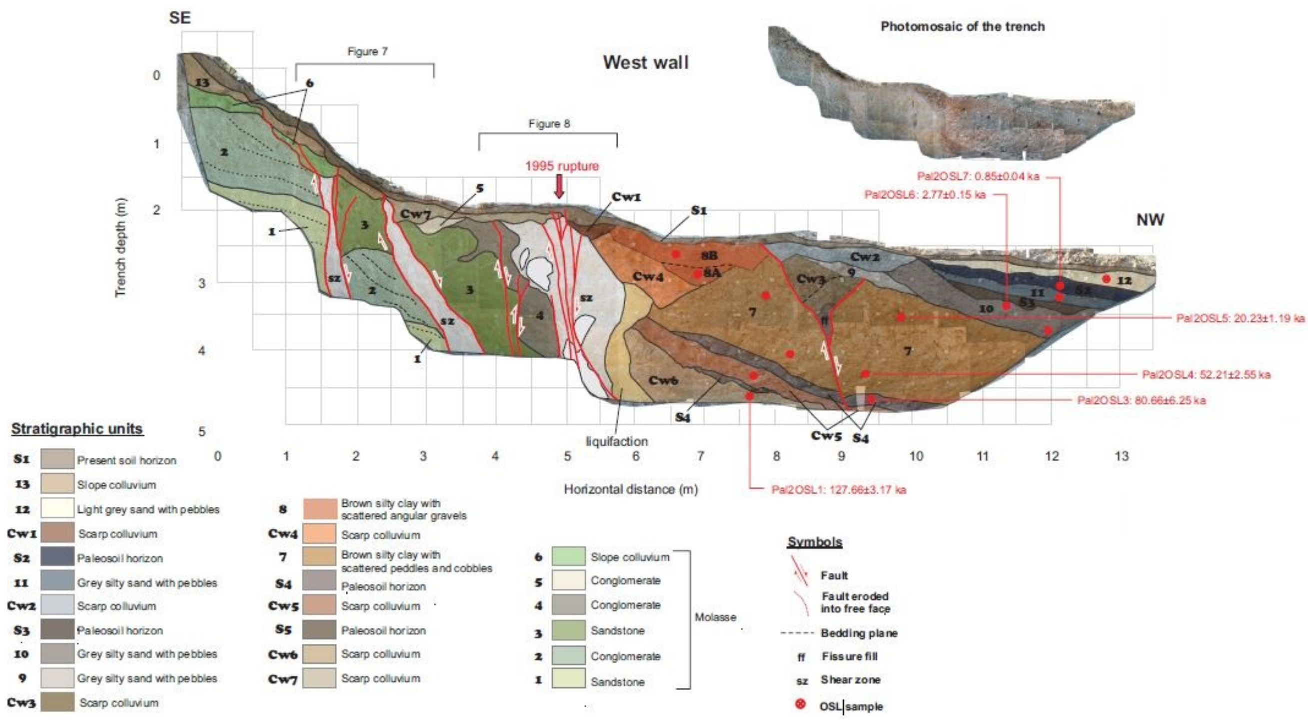

Fig. 3. Paleochori-Sarakina, west wall (preliminary interpretation). The paleoseismic events are noted with red lines.

of recurrence intervals and slip rates of ancient strong earthquakes. Improving our knowledge about the seismic history of an area could be very valuable for a better evaluation of the seismic hazard potential of the regions.

References

1. McCalpin J.P., 2009. Field techniques in paleoseismo-logy. Paleoseismology in extensional tectonic environ-ments. In: McCalpin, J.P. (Ed.), Paleoseismology. Academic Press, San Diego, pp. 161–269.
2. Aitken M. J., 1998. "An Introduction to Optical Dating". Oxford University Press, Oxford.
3. Murray A.S., Wintle A.G., 2000. Luminescence dating of quartz using an improved single-aliquot regenerative-dose protocol. Radiation Measurements 32, 57-73.
4. Murray A.S., Wintle A.G., 2003. The single aliquot regenerative dose protocol: potential for improvements in reliability. Radiation Measurements 37, 377–381.
5. Duller G.A.T., 2003. Distinguishing quartz and feldspar in single grain luminescence measurements. Radiation Measurements 37, 161-165.
6. Liritzis I., Stamoulis K., Papachristodoulou C., Ioannides K. A re-evaluation of radiation dose-rate conversion factors, Med. Archaeology and Archaeometry, 2013, V13, 3, 1-15.
7. Adamiec G., Aitken M.J., 1998. Dose-rate conversion factors: update. Ancient TL 16, 37-50.
8. Chatzipetros A.A., Pavlides S.B., Mountrakis D.M., 1998. Understanding the 13 May 1995 western Macedonia earthquake: a paleoseismological approach. J. Geodynamics 26, 327–339.

^{210}Pb and ^{7}Be concentrations in moss samples from the region of Northern Greece

Ch. Betsou[1,3], E. Tsakiri[2], J. Hansman[3], M. Krmar[3], and A. Ioannidou[1]

[1] Physics Department, Nuclear Physics Lab., Aristotle University of Thessaloniki, Thessaloniki, 54124, Greece
[2] Biology Department, Division of Botany, Aristotle University of Thessaloniki, Thessaloniki, 54124, Greece
[3] Physics Department, Faculty of Science, University of Novi Sad, Trg Dositeja Obradovica 4, Novi Sad, 21000, Serbia

Abstract. Terrestrial mosses obtain most of their nutrients directly from precipitation and dry deposition. They can be used for monitoring of airborne radionuclide depositions. Ninety five samples of Hypnum Cupressiforme were collected in Northern Greece during the end of summer 2016. After the preparation, mosses were measured in a low-background HPGe detector with relative efficiency 32%. The activity concentrations of ^{7}Be ranged from 69 to 1280 Bq kg^{-1}, and the concentrations of ^{210}Pb were between 147 and 1920 Bq kg^{-1}. Differences have been observed in the activity concentrations between the mosses collected from different surface types (ground surface, rocks, branches and near roots). No correlation between the concentrations of ^{7}Be and ^{210}Pb has been found.

PACS. 92.60.Mt Aerosols in atmosphere

1 Introduction

Using biological indicators is a quite interesting and reliable method for detecting radioactive contamination of an ecosystem [1]. Mosses have been used as bioindicators of atmospheric deposition of radionuclides and for atmospheric assessments since the late 1960s in Scandinavian countries [2-4]. Carpet-forming moss species can be used as biomonitors providing a number of advantages. Mosses obtain most of their nutrients directly from precipitation and dry deposition. The absence or strong reduction of the cuticle and thin leaves allows easy uptake from the atmosphere. Lack of an elaborate rooting system also means that uptake from the substrate is normally insignificant. These properties make mosses an ideal sampling medium for metals and airborne radionuclides deposited from the atmosphere, as they are accumulated by the moss, producing concentrations much higher than those in the original wet or dry deposition [5-6]. Another advantage of moss technique is that the sample collection is so simple, that a high sampling density can be achieved, in contrast to the conventional precipitation analysis and the air sampling. High resolution gamma spectrometry measurements can be carried out with the moss technique, without any chemical treatment of the samples. Naturally occurring radionuclides ^{7}Be and ^{210}Pb are useful tools in studying the environmental processes. It is expected that the content of radionuclides that are deposited from the atmosphere can vary from place to place, depending on several factors. ^{7}Be is formed by spallation reaction between cosmic rays and nuclei of oxygen and nitrogen in the stratosphere and upper troposphere [7-11]. After production, the ^{7}Be atoms are attached to aerosol particles and the fate of ^{7}Be will become the fate of the carrier aerosols. Since aerosol particles contain most of the air pollutants, the transport of the last ones can be investigated by tracking the ^{7}Be pathway. The production rate of cosmogenic isotopes depends on the intensity of the geomagnetic field. The concentrations of ^{7}Be in surface air are decreasing with the increase of latitude [12-14]. The radionuclide ^{210}Pb is widely found in the terrestrial environment and it is present in the atmosphere due to the decay of ^{222}Rn diffusing from the ground. The presence of ^{210}Pb in the atmosphere depends on the emanation rate of ^{222}Rn. The last one depends on different factors such as the geological properties of the ground, the ability of radon to leak from the ground and enters in the atmosphere and the conditions of the ground surface layer (the humidity of the soil, the presence or no of the snow cover, the thickness of the frozen soil crust) [15]. Once ^{210}Pb is formed in the atmosphere, it is attached to aerosol particles and follows their path. So it can be used for tracking the aerosols deposition and their residence time in the atmosphere. The aim of this study is to measure activities of the radionuclides ^{7}Be and ^{210}Pb in mosses and investigate their possible variabilities over different places in Northern Greece. The different meteorological conditions, the wind direction and precipitation can influence the deposition of airborne radionuclides, as well as their activities in mosses.

2 Sampling and measurements

Ninety five (95) samples of Hypnum Cupressiforme Hedw. were collected in the region of Northern Greece. The sampling sites were located from 39.97^o North to 41.65^o North and from 20.97^o East to 26.26^o East. The samples were collected from different altitudes, from 30 m to 1450 m above the mean sea level. All samples of fresh plant material were collected in a short time interval during the end of summer 2016. During the sampling there was no rain, thus avoiding the exposure to additional precipitation and extra component of airborne radionuclides by rain washing of the atmosphere [6]. The regions from where samples were collected were open regions far from treetops in most of the sampling sites. All sampling sites were selected avoiding possible contact of mosses with surface water. All the samples were collected according to the instructions of the Protocol of the European Survey ICP Vegetation [16], in which Greece is the first time that is included. After sampling, mosses were dried at 105 ^{o}C for 2 hours to a constant weight. Soil and all other mechanical impurities were removed manually. After the preparation, mosses were put in two cylindrical plastic containers, diameter 67 mm and height 31 mm. The minimum mass of dry moss was 8.9 g and the maximum was 58 g. Low-background extended range HPGe detector equipped with a Be window was used in order to get evidence about ^{210}Pb. Relative efficiency of detector is 32%. Background count was reduced by passive shield (18 cm of lead, 1 mm of tin and 1.5 mm of copper) which does not interfere with gamma photons emitted from samples. Gamma spectrum of each sample was collected until statistical uncertainty of the 477.6 keV ^{7}Be line up to 5% was achieved and statistical uncertainty of 46.5 keV ^{210}Pb line was up to 5%. The detection efficiency was established using NIST Standard Reference Material 4350B (Columbia River sediment) packed in same geometry. Accuracy of efficiency calibration was tested using IAEA source made from dry grass [6].

3 Results and discussion

In the gamma spectrum several prominent peaks appeared. After the subtraction of the background and peak analysis, the intensities of ^{7}Be (477.6 keV) and ^{210}Pb (46.5 keV) were obtained. The activity concentrations of the radionuclides ^{7}Be and ^{210}Pb were calculated and are presented in Table 1. The mean value of each radioisotope is presented in parenthesis in Table 1. The lowest measured value of ^{7}Be activity per unit mass of dry plant material is 69 Bq kg^{-1} and the highest one is 1280 Bq kg^{-1}. The activity concentrations of ^{210}Pb range between 147 and 1920 Bq kg^{-1}. The values of the activity concentrations of ^{210}Pb radionuclide referred in literature present great variability. ^{210}Pb concentrations measured in Belarus were between 141 to 575 Bq kg^{-1} (mean value 312 Bq kg^{-1}), while in Slovakia the activity concentration of ^{210}Pb ranged between 330 to 1521 Bq kg^{-1} (mean value 771 Bq kg^{-1}) [17]. The values of ^{210}Pb in Serbia were measured from 347 to 885 Bq kg^{-1} [5]. There are differences among ^{210}Pb concentrations due to the different soil characteristics and structure. Values of ^{7}Be activity concentrations measured in other surveys in Serbia show also variability depending on the season when moss samples were collected. In autumn, the lowest values of ^{7}Be were found between 95-360 Bq kg^{-1}, with mean value of 195 Bq kg^{-1} [18], while during the summer period ^{7}Be concentrations ranged between 201 to 920 Bq kg^{-1} [18]. The concentrations of ^{7}Be in this current survey are higher (the mean value is almost 20% higher) than those in Serbia during the summer period. This is due to the fact that the cosmogenic radionuclide ^{7}Be presents higher concentrations in regions with lower latitude than those with higher latitude [19]. There are seasonal variances in ^{7}Be activity concentrations for the same region (Serbia), but in the current survey the sampling was conducted only during the summer period, so this could not be observed.

Table 1. Activity concentrations of the radioisotopes ^{7}Be and ^{210}Pb in Bq kg^{-1} in moss samples collected from the region of Northern Greece during the summer of 2016.

Radionuclide	Range (mean value) Bq kg^{-1}
^{7}Be	69-1280 (388)
^{210}Pb	147-1920 (817)

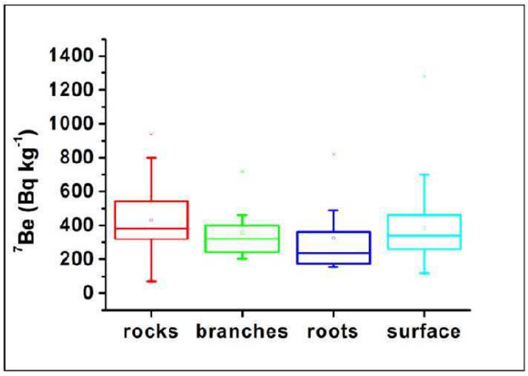

Fig. 1. Differences in the activity concentrations of the radioisotope ^{7}Be in moss samples collected from different surface types. .

Differences have been observed in the activity concentrations between mosses collected from different surface types such as ground surface, rocks, branches and roots (Fig.1 and Fig.2). ^{7}Be and ^{210}Pb activity concentrations are higher in moss samples from the ground surface and rocks than those near roots. The ratio of the activity concentrations of ^{7}Be between mosses collected from the surface and those collected near roots is around 1.5. This ratio is logical, if someone can expect that the majority of ^{7}Be should be found in mosses collected in open areas and not under trees.

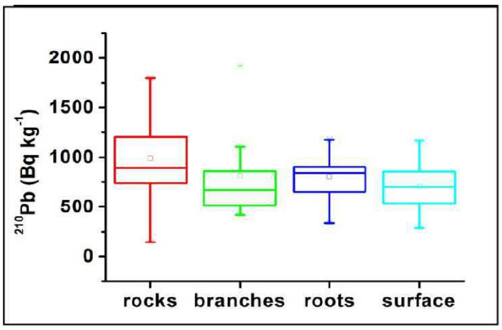

Fig. 2. Differences in the activity concentrations of the radioisotope ^{210}Pb in moss samples collected from different surface types.

There is no correlation between the concentrations of ^{7}Be and ^{210}Pb radionuclides. No special variances in the concentrations of ^{210}Pb and ^{7}Be due to different altitudes or meteorological conditions have been observed. The majority of ^{210}Pb in mosses has arrived through aerosol deposition (e.g. dust that contains ^{238}U daughters). The activity of ^{210}Pb in mosses can vary from region to region due to the different soil structure.

4 Conclusions

Mosses can be used as a sampling medium for the detection of ^{7}Be and ^{210}Pb radionuclides accumulated through some period, covering a high density of sampling points in differently sized areas [18]. A big number of sampling sites (95) was covered and the information obtained using mosses as biomonitors, provide a detailed spatial distribution of the above radionuclides over Northern Greece. Mapping of ^{7}Be and ^{210}Pb activity in mosses provide information about aerosols deposition and help tracking their pathway. The concentrations of ^{7}Be in mosses in Greece are higher than those in Serbia, due to the different latitude and probably due to the different existing meteorological conditions. The activity concentration of ^{210}Pb depends on the different soil properties and structure. The majority of ^{210}Pb and ^{7}Be is accumulated in mosses through aerosols deposition.

References

1. T. Sawidis, L. Tsikritzis, C. Tsigaridas Journal of Environmental Management 90, (2009) 2620-2627.
2. A. Rhling and G. Tyler Water, Air and Soil Pollution 2, (1973) 445-455.
3. L. Yurukova, E. Tsakiri, A. Cayir Bulletin of Environmental Contamination and Toxicology 83, (2009) 174-179.
4. L. Barandovski, M. Cekova, M. V. Frontasyeva, S. S Pavlov, T. Stafilov, E. Steinnes, V. Urumov Environmental Monitoring and Assessment 138, (2008) 107-118.
5. M. Krmar, D. Radnovic, D. T. Mihailovi, B. Lali, J. Slivka, I. Bikit Applied Radiation and Isotopes 67, (2009) 1139-1147.
6. M. Krmar, K. Wattanavatee, D. Radnovic, J. Slivka, T. Bhongsuwan, M. V. Frontasyeva, S. S. Pavlov Journal of Environmental Radioactivity 117, (2013) 45-48.
7. D. Lal and B. Peters In: Handbuch der Physik 46, (1967) 551612.
8. K. OBrien Journal of Geophysical Research 84, (1979) 423431.
9. J. Masarik and R. C. Reedy Earth and Planetary Science Letters 136, (1995) 381395.
10. D. Lal, P. K. Malhotra, B. Peters Journal of Atmospheric and Solar Terrestrial Physics 12, (1958) 306328.
11. N. Bhandari, D. Lal, Rama Tellus 18, (1966) 391405.
12. E. A. Bondietti, F. O. Hoffmann, I. L. Larsen J. Environ. Radioact. 1, (1984) 5-27.
13. C. Papastefanou, and A. loannidou Environment International 22 (Suppl. 1), (1996) S125-S130.
14. A. Ioannidou, E. Kotsopoulou, C. Papastefanou Journal of Radioanalytical and Nuclear Chemistry 289, (2011) 395400.
15. M. Krmar, D. Radnovi, J. Hansman Journal of Environmental Radioactivity 129, (2014) 23-26.
16. Harmens, H., Norris, D. and all the participants of the moss survey Spatial and Temporal Trends in Heavy Metal Accumulation in mosses in Europe (1990-2005). Programme Organization Centre for the ICP Vegetation. (2008) 12-14.
17. Yu. V. Aleksiayenak, M. V. Frontasyeva, M. Florek, I. Sykora, K. Holy, J. Masarik, L. Brestakova, M. Jeskovsky, E. Steinnes, A. Faanhof, K. I. Ramatlhape Journal of Environmental Radioactivity 117, (2013) 19-24.
18. M. Krmar, D. Radnovic,S. Rakic, M. Matavuly Journal of Environmental Radioactivity 95, (2007) 53-61.
19. A. Ioannidou and C. Papastefanou Journal of Environmental Radioactivity 85, (2006) 121-136.

Systematic study of proton-induced spallation reactions with microscopic and phenomenological models

A. Assimakopoulou[1], G.A. Souliotis[1,*], N. Nicolis[2], M. Veselsky[3] and A. Bonasera[4,5]

[1] Laboratory of Physical Chemistry, Department of Chemistry, National and Kapodistrian University of Athens, Athens 15771, Greece
[2] Department of Physics, The University of Ioannina, Ioannina 45110, Greece
[3] Institute of Physics, Slovak Academy of Sciences, Bratislava 84511, Slovakia
[4] Cyclotron Institute, Texas A & M University, College Station, Texas, USA
[5] Laboratori Nazionali del Sud, INFN, Catania, Italy

* Corresponding author. Email: soulioti@chem.uoa.gr

Abstract. Proton induced spallation reactions on 238U, 208Pb, 181Ta and 197Au targets at high energies were investigated using the microscopic Contrained Molecular Dynamics (CoMD) model and the phenomenological models INC and SMM. We have calculated the total fission cross sections, the ratio fission cross section to residue cross section, the mass yield curves and the excitation energy after the intranuclear cascade using the CoMD model and the INC/SMM phenomenological models. We made a comparison between the models and the experimental data from the literature. Our calculations showed satisfactory agreement with available experimental data and suggest further improvements in the models. Our study with the CoMD code represents the first complete dynamical description of the spallation process with a microscopic code based on an effective nucleon-nucleon interaction.

1 Introduction

Spallation reactions induced by high-energy protons are of importance for fundamental research and technical applications in nuclear physics, as for in- stance, medical physics applications and nuclear-reactor technologies. The most important applications of these reactions are the spallation neutron sources [1,2], energy production techniques based on accelerator driven systems (ADS) [3, 4], transmutation of radioactive wastes [5-7] and radiation shield design for accelerators and cosmic devices [8]. Other applications are the production of radioactive ion-beams [9], in ISOL-type facilities and radio- pharmacological production [10,11]. All these applications require the total fission cross section to be known with high accuracy in a wide proton energy range.

Many efforts have been made in providing experimental data on interactions in the energy range (100 –1000 MeV) protons and neutrons with targets that are used in the various applications. Because of the variety of target nuclei and the wide range of energy of the beam particles, theoretical models and nuclear-reaction codes are needed.

Since the available experimental data on spallation reactions are rather poor and fragmentary, an experimental and theoretical work started at GSI Darmstadt [12]. In particular, the production of individual nuclides from charged-particle induced spallation reactions were measured, using the inverse kinematics technique with the high resolution magnetic spectrometer FRS. Also improved codes, such as INCL [13], were developed. However, there are still uncertainties concerning measured total fission cross sections and other observables. Most of the models describe the spallation reaction as a two-stage process. A code that has been extensively used is the Liege Intranuclear Cascade Model, INCL++ [14], which describes the first (fast) stage of the intranuclear cascade. Another code that describes the intranuclear cascade is the Monte Carlo simulation code CRISP [17]. The second stage is described by an evaporation-fission model like GEMINI, GEMINI++ [15], ABRA07 [16] or the generalized evaporation model (GEM) [18]. Moreover, the Statistical Multifragmentation Model (SMM) [20–24] is a deexcitation code which com- bines the compound nucleus processes at low energies and multifragmentation at high energies.

In the present work we used the CoMD model, which is described in the references [25–29] and the phenomenological models INC [19] and SMM. With the CoMD model we obtained (p,f) cross sections, mass yield curves, fission to residue cross sections, and neutron multiplicities for the targets ^{238}U, ^{208}Pb, ^{181}Ta at 200, 500, 1000 MeV and ^{197}Au at 800 MeV. We chose these targets because they are important especially for accelerator-driven systems (ADS). For example tantalum alloys and leadbismuth eutectic are optimum materials for the construction of spallation neutron sources. In our work, we compared our CoMD calculations with experimental data taken from refs. [31, 32, 34, 35, 37– 40]. With the INC model we calculated the excitation energy of ^{208}Pb nucleus after the intranuclear cascade and with the combination of INC/SMM models we obtained the mass distributions of ^{208}Pb and ^{238}U targets as well as the total fission cross sections.

2 Theoretical Model

The Constrained Molecular Dynamics (CoMD) code is based on the gereral approach of molecular dynamics as applied to nuclear systems [29, 30]. The nucleons are assumed to be localized gaussian wavepackets in coordinate and momentum space. A simplified effective nucleon-nucleon interaction is implemented with a nuclear-matter compressibility of K=200 (soft EOS) with several forms of the density dependence of the nucleon-nucleon symmetry potential. In addition, a constraint is imposed in the phase space occupation for each nucleon, restoring the Pauli principle at each time step of the collision. Proper choice of the surface parameter of the effective interaction was made to describe fission.

In the calculations of the present work, the CoMD code was used essentially with its standard parameters. The soft density-dependent isoscalar potential was chosen (K=200). For the isovector part, two forms were used: the "standard" symmetry potential [red(solid)lines]andthe"soft"symmetry potential [blue (dotted) lines] in the figures that follow. These forms correspond to a dependence of the symmetry potential on the 1 and the 1/2 power of the density, respectively [26]. The surface term of the potential was set to zero to describe fission. For a given reaction, a total of approximately 5000 events were collected. For each event, the impact parameter of the collision was chosen in the range b = 0–7 fm, following a triangular distribution. Each event was followed up to 15000 fm/c and the phase space coordinates were registered every 100 fm/c. At each time step, fragments were recognized with the minimum spanning tree method [25, 28] and their properties were reported. Thus, information on the evolution of the fissioning system and the properties of the resulting fission fragments were obtained. In this way, the moment of scission of the deformed heavy nucleus could be determined. We allowed 5000 fm/c after scission for the nascent fission fragments to deexcite and we reported and analyzed their properties. We mention that the effective nucleon-nucleon interaction employed in the code has no spin dependence and thus the result- ing mean field has no spin-orbit contribution. We are exploring possibilities of adding such a dependence on the potential to give us the ability to adequately describe the characteristics of fission at lower excitation energies i.e. $E^* < 50$ MeV.

3 Results and Comparisons

The present work was based on the use of the microscopic CoMD model and the combination INC and SMM models in order to simulate the p-induced spallation reactions at intermediate and high enegies on heavy targets (^{238}U, ^{208}Pb, ^{181}Ta and ^{197}Au). In the following, we present the excitation energy distribution of ^{208}Pb nucleus, the mass yield curve of the reaction p (1000 MeV) + ^{208}Pb and p (1000 MeV) +^{238}U, the total fission cross section of ^{208}Pb and finally the ratio fission to residue cross section for the targets ^{238}U, ^{208}Pb, ^{181}Ta and ^{197}Au. We compare our theoretical calculations with available experimental data as it is shown on the corresponding figures.

In Fig. 1, we present the excitation energy distribution as a function of the cross section after the intranuclear cascade for the ^{208}Pb target at 200, 500 and 1000 MeV, calculated with the INC model. We also calculated the mean excitation energy, which is about 55 MeV at E_p=200 MeV, about 85 MeV at E_p=500 MeV and about 130 MeV at E_p=1000 MeV.

In Fig. 2, we show the mass distribution of proton induced spallation of ^{208}Pb at 1000 MeV. We compare our theoretical results with the experimental data of [37], which are indicated with black triangles. The (red) solid circles with the solid

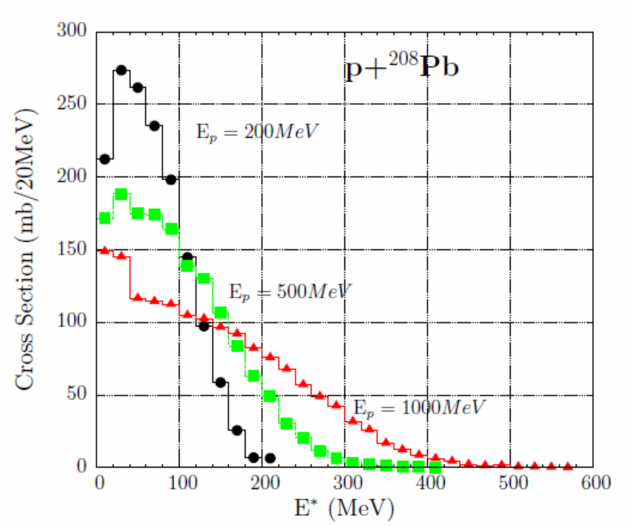

Fig. 1. Excitation energy distribution as a function of the cross section for 208Pb target at 200, 500 and 1000 MeV calculated with the INC model. The solid circles represent the Ep=200 MeV, the solid squares represent the energy beam at 500 MeV and the solid triangles represent the energy beam at 1000 MeV.

line represent the standard symmetry potential from the CoMD code while the grey (green) open circles represent the INC calculations. On this figure we distinguish two regions of fragments. One region has the heavy residues with larger mass numbers, close to the target and the other region has the fission fragments with the smaller mass numbers. We can observe that in the region with the fission fragments, the CoMD calculations and the INC/SMM calculations are in overall agreement with the experimental data. In the heavy residues region, the CoMD calculations and the INC/SMM calculations have a discrepancy with the data.

In Fig. 3 we display the mass distribution of proton induced spallation of ^{238}U at 1000 MeV. We compare our theoretical results with the experimental data of [35, 36, 46, 47]. The (red) solid circles represent the standard symmetry potential from the CoMD code, the (green) open circles represent the INC/SMM calculations and the experimental data are represented with the (pink) open squares, open (black) triangles and solid (black) triangles. The green points represent the Intermediate Mass Fragments. Similarly, we have two regions of fragments, the heavy residues region and the fission fragment region. We can observe, that in the fission fragments region, the CoMD calculations and the INC/SMM calculations are in overall agreement with the experimental data and in the heavy residues region there is a discrepancy between the data and our theoretical results.

In Fig. 4, we present the total fission cross sections calculated with the CoMD code and the INC/SMM models for ^{208}Pb target at 200, 500, 1000 MeV as a function of the proton energy. Our calculations are compared with experimental data and we also present predictions obtained with the systematics established by Prokofiev [33]. The (red) points with the solid line represent the standard symmetry potential and the (blue) points with the dashed line the soft symmetry potential from the CoMD code, while the (green) solid diamonds present the INC/SMM calculations. At 1000 MeV our calculations are in some agreement with the systematics of Prokofiev [33] and the measurements of T. Enqvist et al. [37]. At 500 MeV the CoMD calculations appears to be in moderate agreement with the data by B. Fernandez et al. [34], J.L. Rodriguez et al. [43] and with K.-H. Schmidt et al. [44], while the INC/SMM calculations underestimate both the data and CoMD calculations. Finally, at 200 MeV there is a large discrepancy between the CoMD and the INC/SMM calculations.

In Figure 5, we show the ratio of the fission cross section to the heavy-residue cross section as a function of the proton energy for ^{238}U, ^{208}Pb and ^{181}Ta, calculated with the CoMD code and INC/SMM models at 200, 500 and 1000 MeV and ^{197}Au at 800 MeV. We compare the calculations with the indicated experimental data, which are presented with black points. The (red) solid points with the solid line represent the standard symmetry potential and the (blue) open points with the dashed line the soft potential from the CoMD code, while the grey (green) triangles present the INC/SMM calculations for ^{208}Pb target and the grey (yellow) point the INC/SMM calculations for ^{197}Au at 800 MeV. At first, we can observe that the ratio of ^{238}U is about 8, which of course indicates that it is a high fissile nucleus. This value means that it has much higher possibility to undergo fission than evaporation.

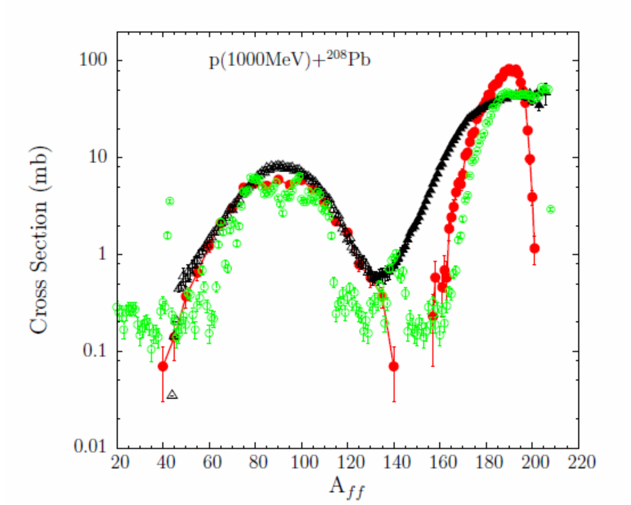

Fig. 2. Normalized mass distributions of fission fragments and heavy residues for p (1000 MeV) +208Pb. Experimental data: solid (black) trinagles [37]. The solid (red) circles represent the CoMD calculations and the open (green) circles the INC/SMM calculations.

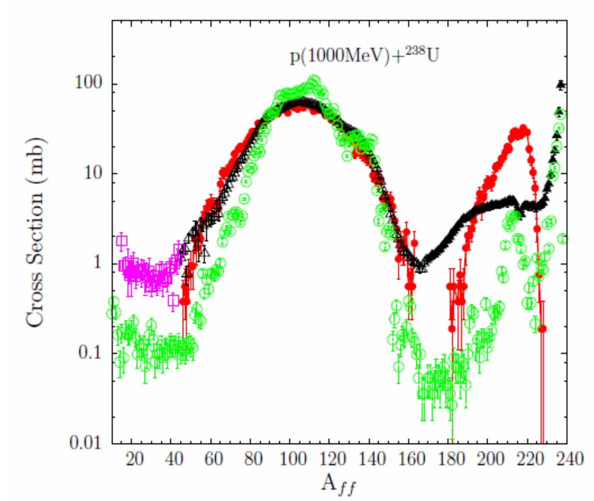

Fig. 3. Mass distributions of fission fragments and heavy residues for the reaction p(1000 MeV) + 238U. Experimental data: open (pink) squares [46], open (black) triangles [35] and solid (black) triangles [47]. The solid (red) circles represent the CoMD calculations and the open (green) circles the INC/SMM calculations.

We notice also that the CoMD calculations at 1000 MeV are in good agreement with the data of Bernas et al. [35]. The ratio of

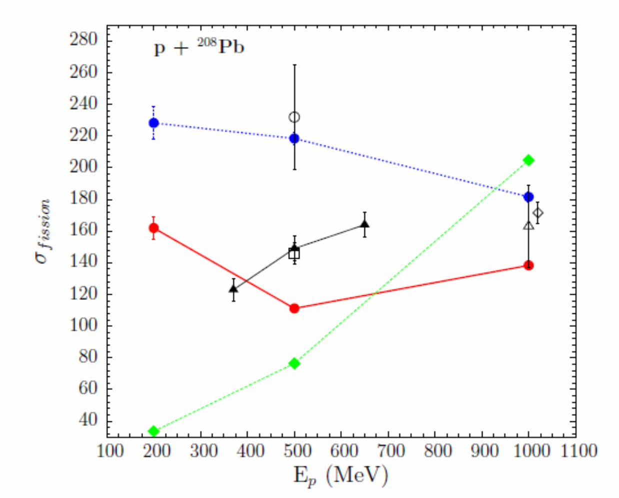

Fig. 4. Fission cross section as a function of the proton energy at 200, 500 and 1000 MeV for 208Pb target. Experimental data: solid triangle [43], open triangle [37], open square [44], open circle [44], open circle [34] and open diamond [33]. CoMD calculations: standard symmetry potential full (red) circles with solid line and soft symmetry potential full (blue) circles with dashed line. INC/SMM calculations: solid (green) diamonds.

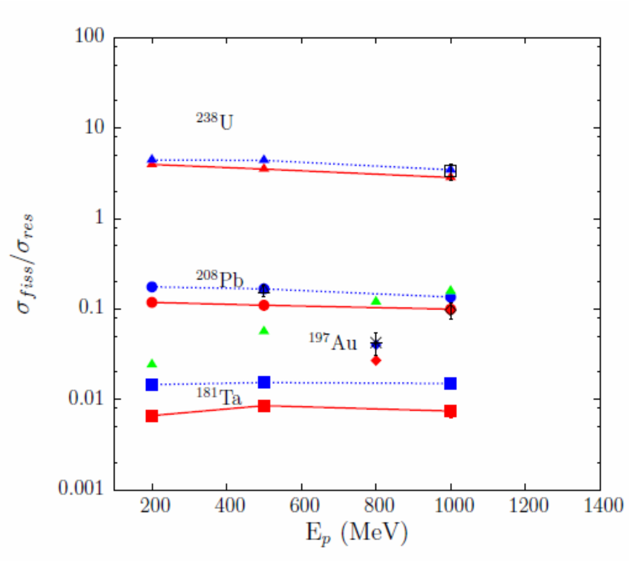

Fig. 5. Ratio of the fission to residue cross section as a function of the proton energy at 200, 500 and 1000 MeV for the targets 238U, 208Pb, 181Ta and 197Au at 800 MeV. Experimental data: open square [35], open triangle [34], rhombus [37], star [38, 39] CoMD calculations: standard symmetry potential full (red) points and soft symmetry potential full (blue) points. INC/SMM calculations for 208Pb target: solid (green) triangles.

fission cross section to residue cross section for ^{208}Pb calculated with the CoMD calculations is about 10%. This indicates that the lead target has a modest fissility. It appears that our calculations are in good agreement with the data of Fernandez et al. [34] at 500 MeV, especially our results with the soft symmetry potential. At 1000 MeV, the CoMD calculations with the standard potential are in good agreement with the data of Enqvist et al. [37]. Next, we present the ratio of ^{197}Au at 800 MeV which is 4%. This suggests an intermediate fissility in relation with tantalum and lead. We also compare our results with experimental data [38, 39] for ^{197}Au, which are displaced by 20 MeV for viewing purposes. The CoMD calculations with the soft symmetry potential are in very good agreement with the data. For ^{181}Ta, the ratio is only about 1%, as calculated from the CoMD. This low value suggests that ^{181}Ta has a low fissility and thus, has a tendency to undergo mostly evaporation. In general, we observe that the CoMD calculations with the soft potential are higher than the standard potential.

4 Discussion and Conclusions

In the present work we employed the semi-classical microscopic code CoMD to describe proton induced spallation in a variety of energies on ^{238}U, ^{208}Pb, ^{197}Au and ^{181}Ta nuclei. In addition we used the phenomenological models INC and SMM in the standard two-stage scenario. In our study we chose these nuclei because of the availability of recent literature data and because of their significance in current applications of spallation. We observe that the fission of ^{208}Pb and ^{238}U target is symmetric due to the high excitation energy at which the shell effects are fully washed out [48]. Also we reproduced well the total fission cross sections and the ratio of fission over residue cross sections. In general, we point out that the CoMD code gives results that are not dependent on the specific dynamics being explored and, thus, offers valuable predictive power for the different modes of fission. A comparison of our calculations with some of the available experimental data from the literature showed satisfactory agreement. It appears that the microscopic code CoMD is able to describe the complicated N-body dynamics of the fission/spallation process. In closing, we suggest the systematic study of the above observables of spallation reactions and further comparison with experimental data. Moreover, apart from the microscopic CoMD code, we used the phenomenological models INC and SMM. Both the microscopic CoMD and the two phenomenological models decribe well the fission process, while it seems that the spallation/evaporation process they cannot describe it well. We are planning to use the statistical model MECO for better description of the evaporation process and we will compare the models with each other.

Acknowledgements

We are thankful to M. Papa for his version of the CoMD code, and to Hua Zheng for his rewritten version of the CoMD. We are also thankful to W. Loveland for his enlighting comments and suggestions on this work and G.Giuliani for discussions on recent CoMD implementations.

References

1. K.N Clausen, in Proceedings of the 16th Meeting of the International Collaboration on Advanced neutron Sources, ICANS-XVI, edited by G.Mank and H.Conrad (Forshungszentrum Jlich GmbH,Jlich, Germany, 2003), Vol. 1,2 and 3.
2. The European Spallation Source Study, The ESS Technical Study, Vol.III, 1996, Report ESS-96-53-M.
3. H. Daniel, Y. Petrov, Subcritical fission reactor driven by the low power accelerator, Nucl. Instrum. Methods Phys. Res.A 373, (1), 131-134 (1996)
4. H. Nifenecker, S. David, J. Loiseaux, A. Giorni, Prog. Part. Nucl. Phys. 43, 683-827 (1999)
5. C.D. Bowman, Ann. Rev. Nucl. Part. Sci.48, 505 (1998).
6. C. Rubbia et al., CERN report,1995, CERN/AT/95-44(ET).
7. H. Nifenecker et al., Nucl. Instrum. Methods A 463, 428 (2001).
8. A.J. Koning, J.-P.Delaroche, and O. Bersillon, Nucl. Instrum. Methods Phys. Res. A 414, 49 (1998).
9. M. Lewitowicz, J. Phys.:Conf. Ser.312, 052014 (2011).
10. W. Uyttenhove, P. Baeten, G.V. den Eynde et al., Ann. Nucl. Energy 38 (7), 1519-1526 (2011).
11. K. Abbas, S. Buono, N. Burgio et al., Nucl.Instrum. Methods Phys. Res.A 601 (3), 223-228 (2009).
12. https://www-win.gsi.de/charms.
13. A. Boudard, J. Cugnon, S. Leray, and C. Volant, Phys. Rev. C 66, 044615 (2002).
14. A. Boudard et al., Phys. Rev. C 87, 014606 (2013).
15. D. Mancusi, R.J. Charity, J. Cugnon, Phys. Rev. C C 82, 044610 (2010).
16. A. Kelic et al., in: D. Filges et al.(Eds.), Proceedings of the Joint ICTP-IAEA Advanced Workshop on Model Codes for Spallation Reactions, ICTP Trieste, Vienna, Italy, 4-8 February 2008,IAEA report INDC(NDS)-530,2008,p.181.
17. A. Deppman et al., Phys.Rev. C 88, 024608 (2013).
18. S. Furihata, Nucl.Instrum. Methods B 171, 251 (2000).
19. Y. Yariv, Z. Fraenkel, Phys. Rev. C 24, 488-494 (1981).
20. N. Eren, N. Buyukcizmeci, R. Ogul, and A.S. Botvina, Eur. Phys.J. A 49, 48 (2013).
21. J. Bondorf et al., Phys. Rep. 257, 133 (1995).
22. A.S. Botvina and I. N. Mishustin, Phys Rev. C 63, 061601 (2001).
23. G.A. Souliotis et al. Phys. Rev. C 75, 011601 (2007).
24. N. Buyukcizmeci, R. Ogul, and A. S. Botvina, Eur. Phys. J. A 25, 57 (2005)
25. M. Papa et al., Phys. Rev. C 64, 024612 (2001).
26. M. Papa, Phys. Rev. C 87, 014001 (2013).
27. N. Vonta, G. A. Souliotis, M. Veselsky, A. Bonasera, Phys. Rev. C 92, 024616 (2015).
28. M. Papa et al, J. Comp. Phys. 208, 403 (2005).
29. J. Aichelin, Phys. Rep. 202, 233 (1991).
30. A. Bonasera, F. Gulminelli, J. Molitoris, Phys. Rep. 243, 1 (1994).
31. J.L. Rodriguez-Sanchez, J. Benlliure et al., Phys. Rev. C 91, 064616 (2015).
32. L. Audouin et al., Nucl. Phys. A 768, 1-21 (2006).
33. A. V. Prokofiev, Nucl. Instrum. and Methods in Phys. Res. A 463, 557-575 (2001).
34. B. Fernandez et al., Nucl. Phys. A 747, 227-267 (2005).
35. M. Bernas et al., Nucl. Phys. A 725, 213-253 (2003).
36. M. Bernas et al., Nucl. Phys. A 765, 197 (2006).
37. T. Enqvist et al., Nucl. Phys.A 686, 481-524 (2001).
38. J. Benlliure, P. Armbruster et al., Nucl. Phys. A 700, 469-491 (2002).
39. F. Rejmund et al., Nucl. Phys. A 683, 540-565 (2001).
40. S. Leray et al., Phys. Rev.C 65, 044621 (2002).
41. J. Benlliure, P. Armbruster et al., Nucl. Phys. A 683, 513-539 (2001).
42. Y. Ayyad, J. Benlliure et al., Phys. Rev. C 89, 054610 (2014).
43. J. L. Rodriguez et al., Phys. Rev. C 90, 064606 (2014).
44. K. -H. Schmidt et al., Phys. Rev. C 87, 034601 (2013).
45. A. A. Kotov et al. Phys. Rev.C 74, 034605 (2006).
46. M. V. Ricciardi et al., Phys. Rev.C 73, 014607 (2006).
47. J. Taieb et al., Nucl. Phys. A 724, 413-430 (2003).
48. A. Chaudhuri et al., Phys. Rev. C 91, 044620 (2015).

Microscopic description of neutron-induced fission with the Constrained Molecular Dynamics (CoMD) Model: Recent Progress

S. Papadimitriou[1], G.A. Souliotis[1*], M. Veselsky[2] and A. Bonasera[3,4]

[1] Laboratory of Physical Chemistry, Department of Chemistry, National and Kapodistrian University of Athens, Athens 15771, Greece
[2] Institute of Physics, Slovak Academy of Sciences, Bratislava 84511, Slovakia
[3] Cyclotron Institute, Texas A & M University, College Station, Texas, USA
[4] Laboratori Nazionali del Sud, INFN, Catania, Italy
[*] Corresponding author. Email: soulioti@chem.uoa.gr

Abstract. The microscopic description of the mechanism of nuclear fission still remains a topic of intense nuclear research. Understanding of nuclear fission, apart from the theoretical many-body point of view, is of practical importance for energy production, as well as for the transmutation of nuclear waste. Furthermore, nuclear fission is essentially the process that sets the upper limit to the periodic table of the elements and plays a vital role in the production of heavy elements via the astrophysical rapid neutron-capture process (r-process). In the present work, we initiated a systematic study of neutron-induced fission reactions using the code CoMD (Constrained Molecular Dynamics) of A. Bonasera and M. Papa [3-5]. In this paper, we present preliminary results of neutron-induced fission on ^{235}U at neutron energies 10, 20, 50, 70 and 100 MeV. Calculated mass and energy distributions will be shown and compared with the recent experimental data of W. Loveland group [1, 2].It appears that the microscopic code CoMD is able to describe the complicated many-body dynamics of the n-induced fission process. Proper adjustment of the parameters of the effective interaction and possible improvements of the code will be implemented to achieve a satisfactory description of the experiment data.

1 Introduction

The study of the mechanism of nuclear fission, that is, the transformation of a single heavy nucleus into two receding fragments, has been a long journey of fruitful research and debate and, still today, is far from being complete. Motivated by the present state of affairs regarding fission research, in this work we initiated a study of neutron induced fission based on on the semi-classical microscopic N-body constrained molecular dynamics (CoMD) model of A.Bonasera and M.Papa [6]. In CoMD code the nucleons are considered as gaussian wavepackets which interact with a phenomenological effective interaction. The code implements an effective interaction with a nuclear-matter compressibility of K=200 (soft EOS) with several forms of the density-dependence of the nucleon symmetry potential. In addition, CoMD imposes a constraint in the phase space occupation for each nucleon restoring the Pauli principle at each time step of the collision). Proper choice of the surface parameter of the effective interaction has been made to describe fission. In addition, in order to introduce the fermionic nature of the system the code implies the Pauli principle through a proper constraint in the phase space.

2 Results and Discussion

In this work, we implement a special treatment of the surface parameter of the effective interaction in order to describe fission. The study of the preliminary stage of the process until the scission point was performed with a configuration of the ground state which has surface parameter C_s=-2, so the values of the radius and of the binding energy were close to the experimental ones. However, with this configuration the system does not undergo fission, only evaporation. In order to study the fission process, we performed calculations with surface parameter C_s=0. The problem with this choice is that the value of binding energy deviates from the experimental value. So, we introduced a time dependent surface parameter, in order to start with the correct configuration of the ground state and also drive the system into fission. For time t=0 fm/c the initial value of the surface parameter is $C_{s,o}$=-2 and for time=300 fm/c the final value of the surface parameter is $C_{s,f}$=0. The value of the C_s parameter in every time step during these 300 fm/c is given by the linear function:

$$C_s(t) = C_{s,o} + C_{s,f} - C_{s,o}/t_f - t_f \qquad (1)$$

It is important to mention that in every step of the process we ensure the energy conservation of the system, by converting the change of potential energy into kinetic energy.

For a given reaction, a total approximately 2000 events were collected. For each event the impact parameter was chosen in the range b=0–7.5 fm, following a triangular distribution. Each event was followed up to 15000 fm/c and the phase space coordinates were registered every 100 fm/c. At each time step, fragments were recognized and their properties were reported.

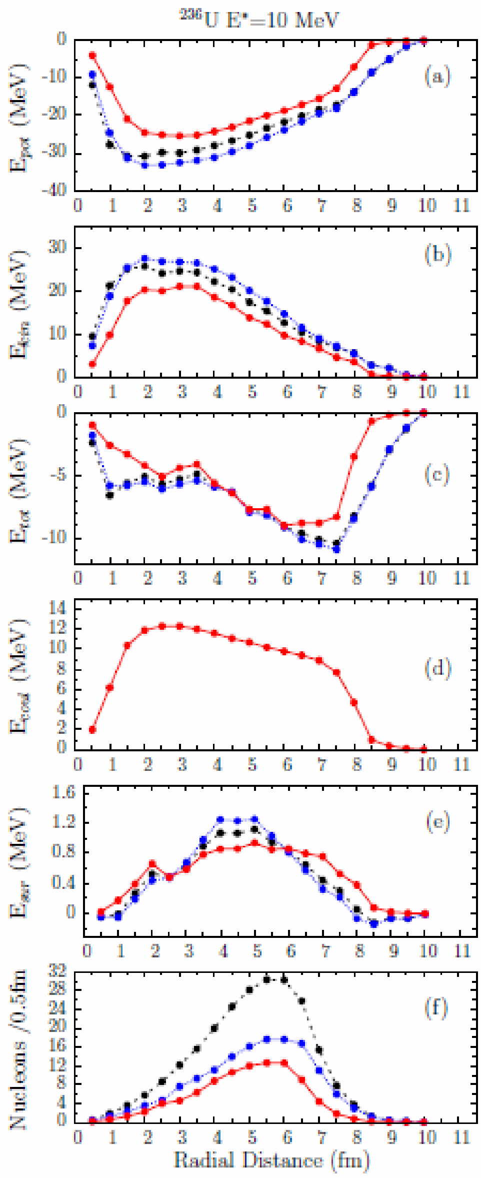

Fig. 1. Calculated energy terms per nucleon versus radial distance. Red line: protons. Blue line: neutrons. Black line: nucleons. a) Potential energy per nucleon. b) Kinetic energy. c) Total energy. d) Energy Coulomb. e) Surface energy. f) Nucleons/0.5 fm

In this presentation, we discuss preliminary results of fission for the reaction n+^{235}U at low and intermediate energies. In Fig. 1, we present the energy per nucleon as a function of the radius. In Fig. 1a) profile of the potential energy of the nucleons is shown, where protons are above neutrons because of the Coulomb interaction. In Fig. 1b) we show the distribution of the kinetic energy where neutrons seem to be above protons. This happens because the nucleus ^{235}U has more neutrons than protons that occupy the same volume, rendering the density of neutrons larger than that of the protons. In Fig. 1c) we present the total energy of the nucleus which has a local minimum at 2 fm and a total minimum at 7 fm. Fig. 1d) is pictured the variation of Coulomb interaction and in Fig. 1e) evolution of the surface term. The surface term has a maximum at about 4 fm, whereas for distance values greater than 4fm the term behaves repulsively. Finally, in Fig. 1f) we show the number of neutrons, protons and nucleons versus radius. The maximum number of nucleons is found at a distance of 6 fm.

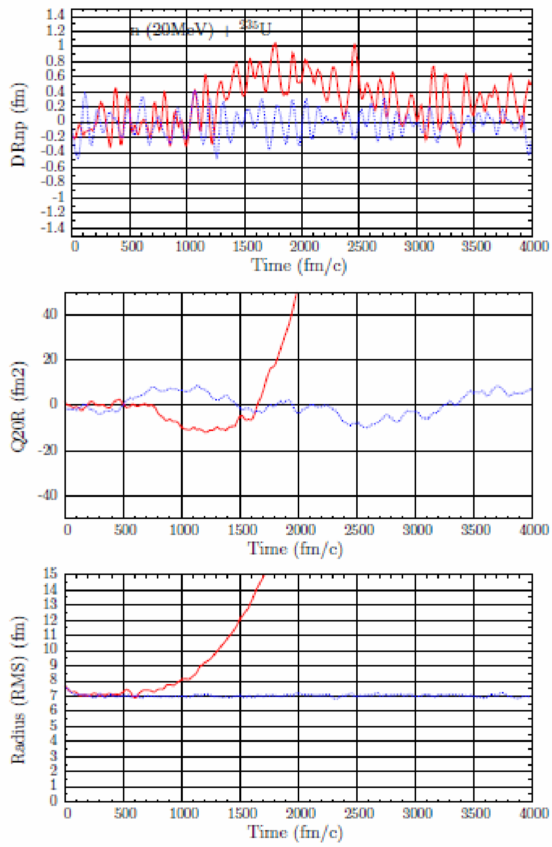

Fig. 2. CoMD calculations on important macroscopic quantities of the nucleus versus time for the reaction n(20MeV)+^{235}U. Red continuous line: Calculation with C_s=0. Blue dotted line: Calculation with C_s=-2. a) Relative distance between the centres of mass of protons and neutrons (GDR). b) Time evolution of the quadrupole moment(GQR). c) Time evolution of the radius(GMR).

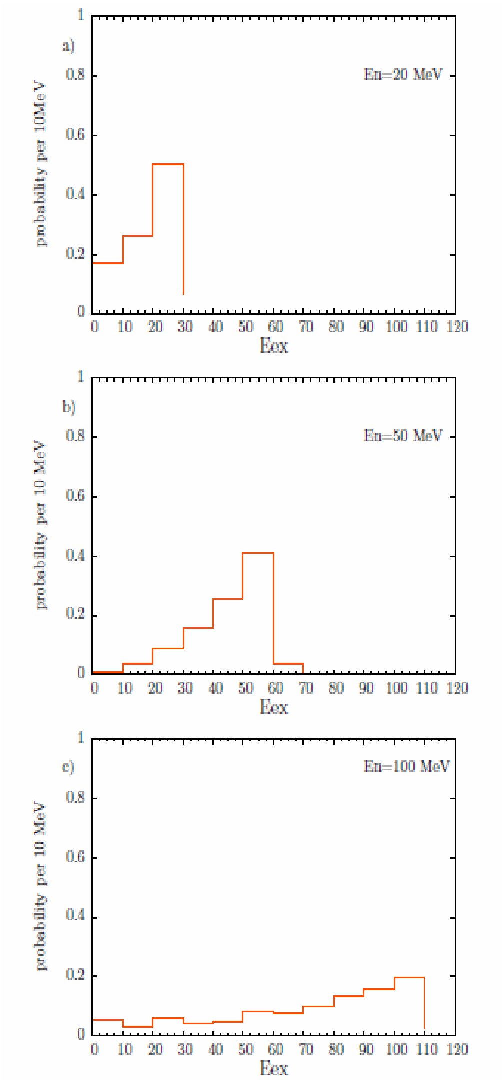

Fig. 3. CoMD calculations on the distribution of the excitation energy of the compound nucleus at 3000 fm/c. a) probability of the excitation energy for the reaction n(20 MeV)+^{235}U. b) probability of the excitation energy for the reaction n(50 MeV)+^{235}U. c) probability of the excitation energy for the reaction n(100MeV)+^{235}U.

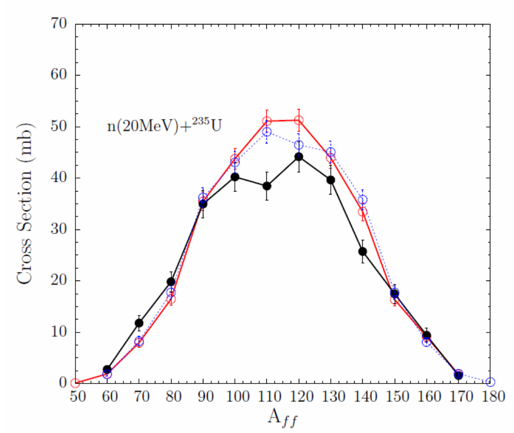

Fig. 4. CoMD calculated yield curves for the fission reaction n(20MeV)+^{235}U. Open red points: CoMD calculations with standard symmetry potential and C_s=0 . Open blue points: CoMD calculations with standard symmetry potential and C_s=0. Full black points: CoMD calculations with standard symmetry potential and C_s=-2.

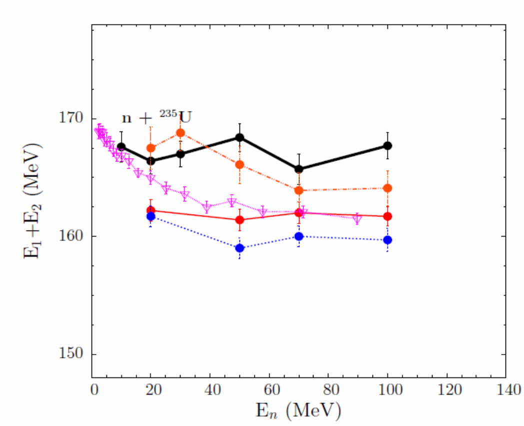

Fig. 5. CoMD calculations on average total energy of fission fragments with respect to incident neutron energy. Red points connected with thin dotted lines: CoMD calculations with standard symmetry potential and C_s=0. Blue points connected with dotted line: CoMD calculations with soft symmetry potential and C_s=0. Black points: CoMD calculations with standard symmetry potential and C_s=-2. Pink open triangles: experimental data of the Loveland group [1].

In Fig. 2, we present the evolution of three moment of the nucleus as a function of time for the reaction n(20MeV)+^{235}U. The continuous red line corresponds to the calculation with surface parameter C_s=0 and the dashed blue line to the calculation with surface parameter C_s=-2. In Fig. 2a) we show the distance between the centres of mass for the Fermi gases of protons and neutrons on z-axis of the nucleus. The blue line with C_s=-2 oscillates harmonically around the center of mass of the system, while the red line curve with C_s=0 shows an abrupt increase. Similar pattern is observed in the time evolution of the radius of the nucleus, as we see in Fig. 2c). The distributions in Fig. 2b) and 2c) indicate that with C_s=0, the system undergoes fission, while with C_s=-2 the only way of de-excitation is the evaporation.In Fig. 3, we display the distribution of the excitation energy of the nucleus at 3000 fm/c taken as a representative time before fission. We performed calculations with three different neutron energies: 20, 50 and 100 MeV. In Fig. 3a) and 3b) which correspond to the calculations with 20 and 50 MeV, respectively, the most probable excitation energy is near the projectile energy.In the calculation at 100 MeV [Fig. 3c)] the excitation energy shows a broad distribution, due to particle emission of the compound nucleus before the scission point.

In Fig. 4, we show the calculated mass distributions for the reaction n(20MeV)+^{235}U. The distributions with open symbols connected with dotted (blue) and solid (red) lines have surface parameter C_s=0 and show a quite symmetric fission [7]. The calculations shown by the full points connected with black line have time dependent surface parameter $C_s(t)$ and suggest a rather asymmetric fission as expected for this low-energy fission reaction [2].

In Fig. 5 we present the total kinetic energy of the fission fragments versus the kinetic energy of the neutron projectile. Our calculations with the CoMD model were performed with the soft and the standard symmetry potential and they were compared with the experimental data at the corresponding energies of Loveland and al. [1]. The calculation with time dependent surface parameter $C_s(t)$ describe better the experimental data at low energies, while the calculations with C_s=0 describe better the experimental values for higher neutron energies.

3 Conclusions

In the present work we employed the semi-classical microscopic code CoMD to describe neutron induced fission, at several energies on ^{235}U. We intend to study systematically the neutron induced fission by calculating a number of representative observables such as: mass yield curves, cross sections, energy distributions, the fission time scale and the pre-fission and post-fission neutron and proton emission. We mention that the code does not include the effect of spin-orbit interaction in the mean filed, as a result of the absence of spin dependence in the effective nucleon-nucleon interaction. We intend to add such a dependence in order to improve our ability to examine low energy fission.

References

1. R. Yanez, W. Loveland, J. Kind, J.S. Barett, Total kinetic energy release in the fast neutron induced fission of ^{235}U arXiv:1605.09690v2 [nucl-ex] (2016)
2. W. Loveland, J. King, Total kinetic energy release in the fast neutron induced fission of ^{232}Th and ^{235}U, arXiv:1702.01790v1 [nucl-ex] (2017).
3. M. Papa, T. Maruyama, and A. Bonasera, Constrained Molecular dynamics approach to fermionic systems, Phys. Rev. **C64**, (2001) 024612.
4. M.Papa, G.Guluilani, and A. Bonasera, Constrained Molecular Dynamics II: a N-body approach to fermionic systems, J. Comp. Phys. **208** (2005) 403.
5. A. Bonasera, M. Bruno, C.O. Dorso and P.F. Mastinu, Critical phenomena in nuclear fragmentation, Riv. Nuovo Cimento **23** (2000) 1.
6. M. Papa, Many-body in semiclassical molecular dynamics and Skyrme interaction, Phys. Rev. **C87** (2013) 014001.
7. N.Vonta, G.A. Souliotis, M. Veselsky, and A. Bonasera, Microscopic dynamical description of proton induced fission with the constrained molecular dynamics model, Phys. Rev. **C 92** (2015) 024616.

Neutron-rich rare isotope production with stable and radioactive beams in the mass range A ~ 40-60 at 15 MeV/nucleon

A. Papageorgiou[1], G.A. Souliotis[1*], Y.K. Kwon[2], K. Tshoo[2], A. Bonasera[3,4], M. Veselsky[5]

[1] Laboratory of Physical Chemistry, Department of Chemistry, University of Athens, Athens 15771, Greece.
[2] The Rare Isotope Science Project (RISP), Institute for Basic Science, Daejeon 305-811, Korea.
[3] Cyclotron Institute, Texas A&M University, College Station, Texas, USA.
[4] Laboratori Nazionali del Sud, INFN, via Santa Sofia 62, I95123 Catania, Italy.
[5] Institute of Physics, Slovak Academy of Sciences, Bratislava, Slovakia.
[*] Corresponding author. Email: soulioti@chem.uoa.gr

Abstract. This work reports on our continued efforts to study the production of rare isotopes with heavy-ion beams at energy 15 MeV/nucleon. Our calculations are based on a two-step approach: the dynamical stage of the collision is described with either the phenomenological Deep-Inelastic Transfer model (DIT) [1], or with the microscopic Constrained Molecular Dynamics model (CoMD) [2,3,4]. The de-excitation of the hot heavy projectile fragments is performed with the Statistical Multifragmentation Model (SMM) [4]. We first present experimentally acquired production cross sections of neutron-rich nuclides from collisions of a ^{40}Ar stable beam with targets of ^{58}Ni, ^{64}Ni and ^{27}Al [5] and we compare them with our calculations. Then we performed calculations for the same beam (15 MeV/nucleon) with other neutron rich targets such as ^{48}Ca and ^{238}U and find that the multinucleon transfer mechanism leads to very neutron-rich nuclides in mass range A ~ 40-60. Motivated by the high production cross section of target ^{238}U, we performed calculation with beam of ^{48}Ca (15 MeV/nucleon). We found that we can produce radioactive beams of ^{46}Ar and ^{54}Ca which can be separated and hit another target of ^{238}U, participating in reactions of multinucleon transfer which can produce extremely neutron-rich and even new isotopes.

1 Introduction

The study of the nuclear landscape toward the astrophysical r-process path and the neutron drip-line have received special attention by the nuclear physics community (see, e.g., [1]). To reach a high neutron-excess in the products, apart from proton stripping, capture of neutrons may be necessary from the target. Such a possibility is offered by reactions of nucleon exchange at beam energies from the Coulomb barrier [2,3] to the Fermi energy (20-40 MeV/nucleon) [4,5].

In this section we present the results of the calculation of peripheral heavy ion reactions. We compare our results with experimental data from the reaction ^{40}Ar + ^{64}Ni at beam energy 15 MeV/A, which were acquired as described in [6], as well as from the reactions ^{40}Ar + ^{181}Ta [7] and ^{48}Ca + ^{181}Ta [8] found in the literature. The calculation were performed with the phenomenological model DIT [9] and the microscopic CoMD [10], which describe the dynamical stage of the nucleon exchange, and the statistical de-excitation model SMM [11].

2 Calculations for stable beams of ^{40}Ar and ^{48}Ca at 15 MeV/A

In Fig. 1, we show the calculated mass distributions of projectile-like fragments with Z=12-19 from the reaction ^{40}Ar (15 MeV/A) + ^{64}Ni performed by CoMD/SMM (dashed red line) and DIT/SMM (solid green line) compared with the experimental data (black points). We observe that in the isotopes close to the projectile (Z=16-19), the results of the two models are almost identical, while they are in good agreement with the data. Subsequently, the largest part of the calculations will be performed with the DIT model, as it can conduct results of higher statistics in less time than the CoMD model.

After the presentation of the comparisons between our calculations with the experimental data, we can feel certain that the results of both DIT and CoMD can be considered as valid. Hence, they can be used to predict the results of reactions that have not taken place yet.

Motivated by these results, we performed calculations with a beam of the same mass range, but far more neutron

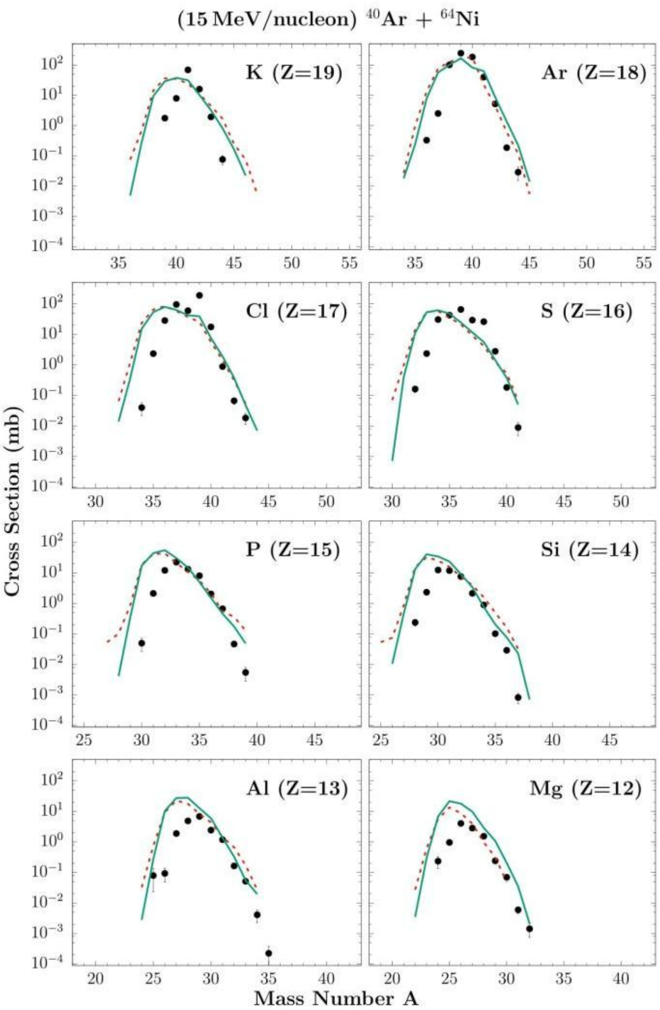

Fig. 1. Calculated mass distributions of projectile-like fragments with Z=12-19 from the reaction ^{40}Ar (15 MeV/A) + ^{64}Ni performed by CoMD/SMM (dashed red line) and DIT/SMM (solid green line) compared with the experimental data (black points) [6].

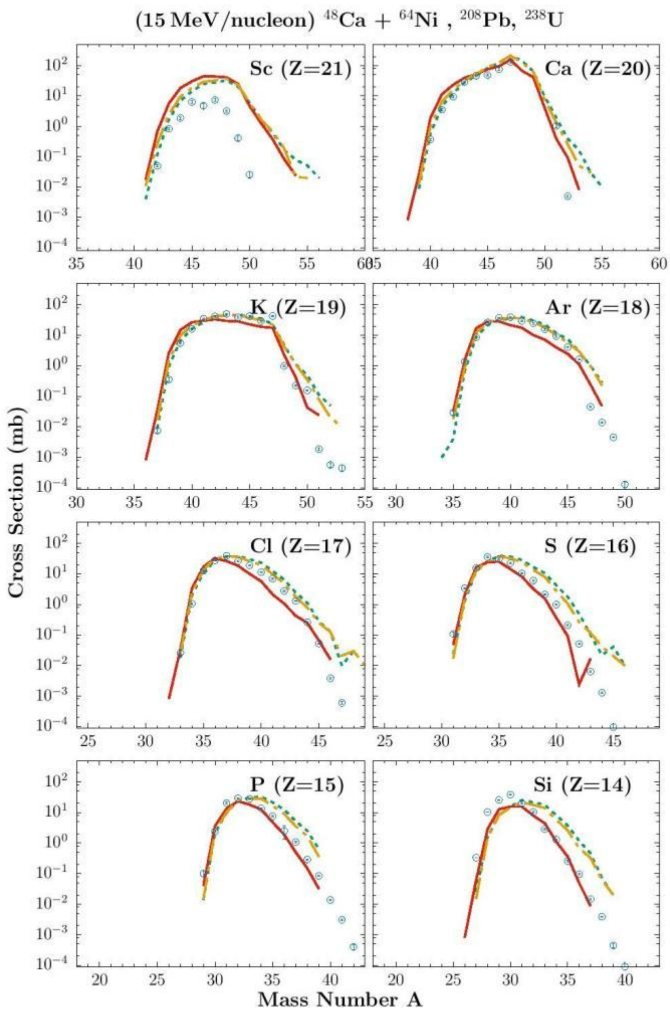

Fig. 2. Calculations for the reactions ^{48}Ca (15 MeV/A) + ^{64}Ni (solid red line), ^{48}Ca (15 MeV/A) + ^{238}U (dashed green line) and ^{48}Ca (15 MeV/A) + ^{208}Pb (dashed-dotted yellow line) compared with the data we found in the literature from the reaction ^{48}Ca (140 MeV/A) + ^{181}Ta [3] (open blue points).

rich, ^{48}Ca (15 MeV/A). In Fig. 2, we show our calculations for the reactions ^{48}Ca (15 MeV/A) + ^{64}Ni (solid red line), ^{48}Ca (15 MeV/A) + ^{238}U (dashed green line) and ^{48}Ca (15 MeV/A) + ^{208}Pb (dashed-dotted yellow line) compared the data we found in the literature from the reaction ^{48}Ca (140 MeV/A) + ^{181}Ta [8] (open blue points). Our calculations for the low energy reactions seem to favor the production of neutron-rich isotopes in contrast with the data of the high energy reaction, where neutron capture is rather unlikely to happen. If we examine the distribution of the calcium isotopes we can see that with the use of ^{238}U as a target, we can produce nuclei that have captured up to 6-7 neutrons, like ^{54}Ca.

3 Calculations for radioactive beam (RIB) of ^{54}Ca (15 MeV/A)

Radioactive beams are a very useful tool in the investigation of reaction mechanisms and nuclear stability. By using them, we are able to produce very rare isotopes near the neutron drip line. Motivated by the relatively high production cross section of the ^{54}Ca isotope from the reaction ^{48}Ca (15 MeV/A) + ^{238}U, we decided to perform calculations with this RIB. In Fig. 3, we show the DIT/SMM calculations for the reactions ^{54}Ca (15 MeV/A) + ^{64}Ni (solid red line) and ^{54}Ca (15 MeV/A) + ^{238}U (dashed green line). These calculations are, in our opinion, the most

Table 1. Predicted cross sections and production rate estimates of some isotopes from the reaction ^{48}Ca (15 MeV/A) + ^{238}U

Rare isotope	$t_{1/2}$	Reaction Channel	Cross Section (mb)	Rates (s^{-1})
^{54}Ca	0.09 s (expt)	-0p+6n	0.03	4.6×10^{3}
^{46}Ar	8.4 s (expt)	-2p-0n	2.88	4.4×10^{5}
^{55}Sc	0.09 s (expt)	+1p+6n	0.051	7.8×10^{3}
^{52}K	105 ms (expt)	-1p+5n	0.05	17.6×10^{3}

Table 2. Predicted cross sections and production rate estimates of some isotopes from the reaction ^{54}Ca (15 MeV/A) + ^{238}U

Rare isotope	$t_{1/2}$	Reaction Channel	Cross Section (mb)	Rates (s^{-1})
^{57}Ca	7 ms (expt)	-0p+3n	0.59	1.4×10^{-4} (12 day^{-1})
^{58}Ca	12 ms (theo)	-0p+4n	0.16	3.75×10^{-5} (3 day^{-1})
^{59}Ca	6 ms (theo)	-0p+5n	0.04	9.75×10^{-6} (6 week^{-1})
^{60}Ca	4 ms (theo)	-0p+6n	0.008	1.9×10^{-6} (1 week^{-1})
^{54}K	10 ms (expt)	-1p+1n	0.58	1.4×10^{-4} (12 day^{-1})
^{55}K	4 ms (expt)	-1p+4n	0.04	9.4×10^{-6} (6 week^{-1})

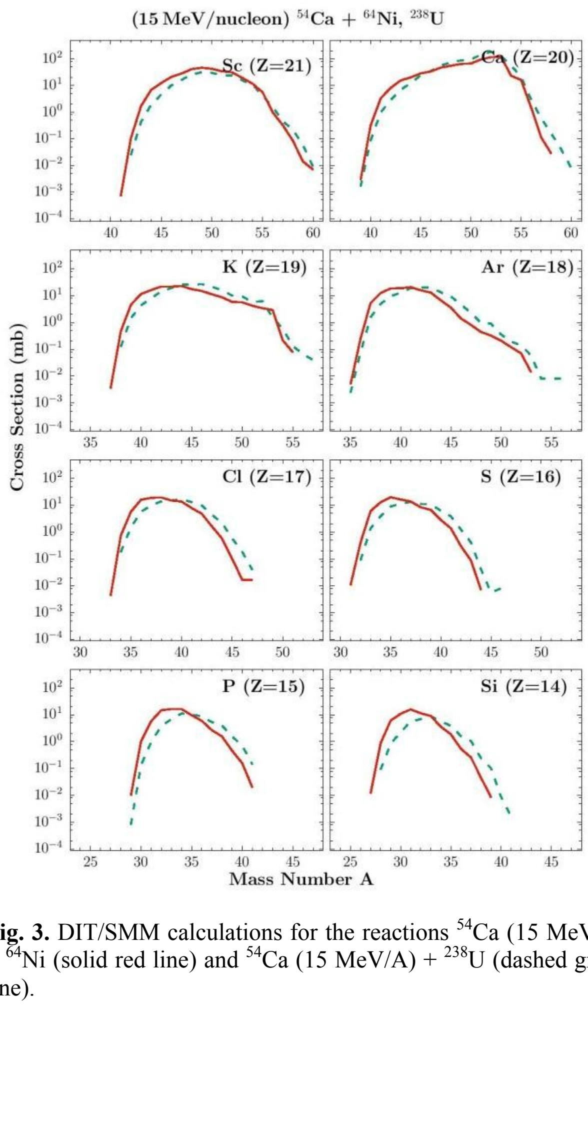

Fig. 3. DIT/SMM calculations for the reactions ^{54}Ca (15 MeV/A) + ^{64}Ni (solid red line) and ^{54}Ca (15 MeV/A) + ^{238}U (dashed green line).

interesting result of this work, as it seems that with this RIB and this neutron-rich target we can produce very rare and even new isotopes up to ^{60}Ca, or even beyond.

After the presentation of the yields, we proceed to the presentation of the production rates of some important isotopes. In Table 1, we show the predicted cross sections and production rate estimates of some isotopes from the reaction ^{48}Ca (15 MeV/A) + ^{238}U. We have assumed a relatively high beam intensity of 500 pnA (3x10^{12} particles/s) and target thickness 20 mg/cm^2. In this table we report the cross sections and production rates of the radioactive isotopes ^{46}Ar and ^{54}Ca, which were used as RIB. Also, we show the experimentally measured (expt) or theoretically predicted (theo) half life time [12,13] of each isotope.

In Table 2, we show the predicted cross sections and production rate estimates of some isotopes from the reaction ^{54}Ca (15 MeV/A) + ^{238}U. As before, we have assumed that the beam intensity is the production rate of ^{54}Ca from the reaction ^{48}Ca (15 MeV/A) + ^{238}U, which is about 4600 particles/s, and a target thickness of 20 mg/cm^2. We see that production of very rare and even new isotopes, like ^{59}Ca and ^{60}Ca, is predicted in peripheral low energy collisions of the radioactive beam ^{54}Ca.

4 Summarry and conclusions

In this work we performed a series of calculations of cross sections of projectile fragments from peripheral heavy ion reactions with beam energy 15 MeV/A. More specifically, we presented calculation for the reactions with the stable beams ^{40}Ar (15 MeV/A) and ^{48}Ca (15 MeV/A) + ^{64}Ni, ^{208}Pb, ^{238}U and with the radioactive beam ^{54}Ca (15 MeV/A) + ^{64}Ni, ^{238}U, using the phenomenological model DIT [9], the microscopic model CoMD [10] and the statistical de-excitation model SMM [11]. We saw that our calculations came to a satisfactory agreement with the available experimental data. Then, we predicted the production of very rare and even new isotopes toward the region of ^{60}Ca, which has not been produced yet.

References

1. J. Erler et al, Nature **486**, 509 (2011).
2. V. V. Volkov, Phys. Rep. **44**, 93 (1978).
3. L. Corradi, G. Pollarolo, S. Szilner, J. Phys. G **36**, 113101 (2009).
4. G. A. Souliotis et al., Phys. Lett. B **543**, 163 (2002).
5. G. A. Souliotis et al., Phys. Rev. Lett. **91**, 022701 (2003).
6. G.A. Souliotis, M. Veselsky, S. Galanopoulos *et al.*, Approaching neutron rich nuclei toward the r-process path in peripheral heavy ion collisions at 15 MeV/nucleon, Phys. Rev. C **84,** 064607 (2011).
7. Mashiro Notani, Projectile Fragmentation reactions and

production of nuclei near the neutron drip line, University of Tokyo (Phd thesis).
8. M. Mocko *et al.*, Projectile fragmentation of ^{40}Ca, ^{48}Ca, ^{58}Ni and ^{64}Ni at 140 MeV/nucleon, Phys. Rev. C **74**, 05612 (2006).
9. L. Tassan-Got and C. Stefan, Deep inelastic transfers. A way to dissipate energy and angular momentum for reactions in the Fermi energy domain, Nucl. Phys. A **524**, 121 (1991).
10. M. Papa *et al.,* Constrained molecular dynamics approach to fermionic systems, Phys. Rev. C **64**, 024612 (2001).
11. J.P Bondorf *et al.,* Statistical multifragmentaition of nuclei, Phys. Rep. **257**, 133 (1995).
12. P. Moller, J.R. Nix *et al.,* Nuclear ground state masses and deformations, Atomic Data Nucl. Data Tables **59**, 185-381 (1995).
13. P. Moller, J.R. Nix *et al.,* Nuclear properties for astrophysical applications, Atomic Data Nucl. Data Tables **66**, 131-345 (1997).

Study of the ^{7}Be + ^{28}Si at near barrier energies: Elastic scattering and alpha production

O. Sgouros[1], A. Pakou[1], D. Pierroutsakou[2], M. Mazzocco[3,4], L. Acosta[5,6], X. Aslanoglou[1], Ch. Betsou[1], A. Boiano[2], C. Boiano[7], D. Carbone[8], M. Cavallaro[8], J. Grebosz[9], N. Keeley[10], M. La Commara[2,11], C. Manea[4], G. Marquínez-Durán[12], I. Martel[12], N. G. Nicolis[1], C. Parascandolo[2], K. Rusek[13], A. M. Sánchez-Benítez[12,14], C. Signorini[15], F. Soramel[3,4], V. Soukeras[1], C. Stefanini[3], E. Stiliaris[16], E. Strano[3,4], I. Strojek[10], and D. Torresi[3,4]

[1] Department of Physics and HINP, The University of Ioannina, Ioannina, Greece
[2] INFN, Sezione di Napoli, via Cinthia, Napoli, Italy
[3] Dipartimento di Fisica e Astronomia, Universita di Padova, via Marzolo 8, Padova, Italy
[4] INFN, Sezione di Padova, via Marzolo 8, Padova, Italy
[5] Instituto de Fisica, Universidad Nacional Autonoma de Mexico, Mexico D.F, Mexico
[6] INFN, Sezione di Catania, via Santa Sofia 64, Catania, Italy
[7] INFN, Sezione di Milano, via Celoria 16, Milano, Italy
[8] INFN Laboratori Nazionali del Sud, via Santa Sofia 62, Catania, Italy
[9] The Henryk Niewodniczanski Institute of Nuclear Physics (IFJ PAN), Krakow, Poland
[10] National Centre for Nuclear Research, ul. Andrzeja Soltana 7, Otwock, Poland
[11] Dipartimento di Scienze Fisiche, Universita di Napoli Federico II, Napoli, Italy
[12] Departamento de Ciencias Integradas, Universidad de Huelva, Huelva, Spain
[13] Heavy Ion Laboratory, University of Warsaw, Pasteura 5a, Warsaw, Poland
[14] Centro de Fisica Nuclear da Universidade de Lisboa, Lisboa, Portugal
[15] INFN, LNL, viale dell' Universita 2, Legnaro, Italy
[16] Institute of Accelerating Systems and Applications and Department of Physics, University of Athens, Athens, Greece

Abstract. The ^{7}Be + ^{28}Si system was studied at four near barrier energies: 13.2, 17.2, 19.8 and 22.0 MeV. Angular distribution measurements for the elastically scattered ^{7}Be ions as well as the α and ^{3}He reaction products were performed with the multidetector array EXPADES. The elastic scattering data were analyzed in a double-folding framework and the energy evolution of the Optical Potential was deduced. The reaction data were analyzed in both statistical model and Distorted Wave Born Approximation frameworks (DWBA) in order to disentangle the degree of competition between direct and compound channels. The energy evolution of the ratio of direct to total reaction cross section was mapped in comparison with similar data for ^{6}Li and ^{7}Li projectiles on a ^{28}Si target, indicating larger transfer contributions for ^{7}Be and ^{7}Li that in the ^{6}Li case. Fusion cross sections for the system under study were deduced and were found to be compatible with systematic. Comparison with previous fusion data for ^{6}Li and ^{7}Li indicate fusion hindrance for ^{7}Li and ^{7}Be compared to ^{6}Li, starting from the barrier and below it. This hindrance is attributed to the existence of large transfer channels.

PACS. 25.70.Bc Heavy-ion reactions – 24.10.Ht Optical and diffraction models – 24.10.Eq Coupled-channel methods – 24.10.Lx Nuclear reaction models

1 Introduction

Over the past decades, elastic scattering has been established as the traditional tool for probing the Optical Potential. In this respect, many studies have been devoted so far to study the energy dependence of the Optical Potential through elastic scattering measurements. For tightly bound projectiles, it was well demonstrated that the imaginary part of the Optical Potential sharply decreases at barrier and the real part connected with it via dispersion relations develops a localized peak. This anomalous behavior was named potential Threshold Anomaly (TA) [1–3]. On the other hand, the situation for weakly bound encounters is very different with an imaginary part exhibiting either an increasing trend approaching the barrier from higher to lower energies or a decreasing one but which occurs well below barrier. Elastic scattering measurements with ^{6}Li and ^{7}Li on low mass targets (^{27}Al, ^{28}Si) have shown that their energy dependence of the Optical Potential deviates from the standard TA but also that, the situation is different for the two ions [4–8]. While for ^{6}Li an increasing trend of the imaginary potential approaching the barrier from higher to lower energies is met, for ^{7}Li the energy dependence resembles more the one seen for well bound projectiles but where the flat imaginary potential persist till very low sub-barrier energies. In principle the variations of TA for the Optical Potential should be connected with variations in reaction mechanisms appearing strong at near and below barrier. Investigations of collisions involving weakly bound nuclei create an interesting field to study reaction mechanisms and coupling effects, since direct reactions like breakup or transfer are enhanced. In this respect several studies on inclusive and exclusive measurements of light reaction products has been undertaken. Amongst them outstanding role hold the studies for the determination of fusion cross sections and the evolution of competition between direct and compound nucleus formation. Into this context, we have proposed the present study involving the radioactive projectile ^{7}Be on a ^{28}Si target. This system was chosen because comprehensive studies already exist for the related systems ^{6,7}Li + ^{28}Si and it will be an interesting point to investigate simiarities between weakly bound but stable projectiles with a radioactive one. Further on it will be interesting to investigate whether the ^{7}Be resembles more its mirror nucleus, ^{7}Li, or the ^{6}Li one, using the information from both elastic as well as reaction channels.

2 Experimental details and data reduction

The ^{7}Be secondary beam was produced at the EXOTIC facility [9–12] at the Laboratori Nazionali di Legnaro (LNL), Italy, by means of the In Flight (IF) technique and the ^{1}H(^{7}Li,^{7}Be)n reaction. The ^{7}Li^{+3} primary beam was delivered by the LNL XTU Tandem Van de Graaff accelerator with an intensity of ∼150 pnA and energies of 26 to 33 MeV. The primary beam was directed onto a 5 cm long gas cell with 2.2 m thick Havar foil windows filled with H_2 gas at a pressure of ∼1000 mbar and a temperature of 93 K, corresponding to an effective thickness of 1.35 mg/cm^2. The ^{7}Be beam was produced at 4 energies namely 13.2, 17.2, 19.8 and 22.0 MeV and it was impinged on a silicon target placed in the middle of the scattering chamber. The various ejectiles were collected by six ΔE-E telescopes of the detector array of the EXOTIC facility, EXPADES (EXotic PArticle DEtection System) [12], placed at symmetrical position to balance any beam divergence and to improve the statistics of the measurement. The ΔE stage of the telescopes was a Double Sided Silicon Strip Detector (DSSSD) (45-60)μm thick, while the E stage was a DSSSD ∼300μm thick. Also, our experimental setup included two X-Y position sensitive Parallel Plate Avalanche Counters (PPAC's) [12] for monitoring the secondary beam profile and providing information for an event by event reconstruction of the beam particle trajectories.

The elastically scattered ^{7}Be ions were stopped in the first stage of the telescope and therefore, the identification of the elastic peak was performed by analyzing single energy spectra. Furthermore, the reduction of the elastic scattering events was performed by means of an event by event code [13] which developed for the needs of the present study. This code handles the information provided by the two PPAC's and the DSSSD detectors in order to define in a more accurate way the scattering angle for each event. Briefly we can refer on that as following. Experimentally the coordinates for each beam particle are determined in two places via the information collected by the two PPAC's. This information is implemented in our code and via analytic geometry, the beam particle trajectories are reconstructed. In this respect, the reaction position on the target is defined for each event. Subsequently, the DSSSD telescopes provide the position of each elastically scattered particle, since each event is detected in a unique pixel of the detector. By using the coordinates of the reaction position on the target together with the coordinates of the events detected in the DSSSDs, the scattering angle for each event can be determined.

Data concerning both the elastic scattering of ^{7}Be on ^{28}Si and ^{208}Pb, the last used for the determination of the detector solid angles, were treated in an event by event framework. Events with the same angle or with an angle inside an angular range corresponding to a particular strip of each EXPADES detector ($\Delta\theta\sim 2^o$) were summed up. The ratios $\sigma/\sigma^{Si}_{Ruth}$ were deduced according to the following expression:

$$Ratio \equiv \frac{\sigma}{\sigma^{Si}_{Ruth}} = \frac{N_{Si}}{N_{Pb}} * K \tag{1}$$

where N_{Si} and N_{Pb} are the event by event counts corresponding to every strip collected with the silicon and lead targets respectively and the constant K corresponds to

$$K = \frac{T_{Pb}\Phi_{Pb}}{T_{Si}\Phi_{Si}} \frac{\sigma^{Pb}_{Ruth}}{\sigma^{Si}_{Ruth}} \tag{2}$$

where T_{Si} and T_{Pb} are the scattering centers of the silicon and lead targets respectively, Φ_{Si} and Φ_{Pb} are the beam fluxes during the runs with the silicon and lead targets respectively and σ^{Si}_{Ruth} and σ^{Pb}_{Ruth} are the calculated Rutherford cross sections for the elastic scattering of ^{7}Be on ^{28}Si and ^{208}Pb respectively. The constant K is determined assuming that at small scattering angles the ratio $\sigma/\sigma^{Si}_{Ruth}$ between elastic scattering cross sections and Rutherford cross sections is 1.0. This assumption is valid only at the lowest energy of 13.2 MeV. For the rest of the energies the ratio was assumed to be closed to 1, according to the theoretical calculations. The results of this analysis are also reported in Ref. [14].

The reaction products, that is the α and ^{3}He particles which are under study in this work, were well separated by the ΔE-E technique and their yield was obtained by applying the appropriate energy windows on the two dimensional ΔE-E plots. Missing counts, due to the energy threshold of each telescope where retrieved by comparing the experimental energy spectra with simulated ones.

Simulated energy spectra were obtained with the contribution of all processes direct and of compound nucleus origin, normalized appropriately in a best fit. Compound nucleus energy spectra were produced via the well known code PACE2 [15]. Alpha energy spectra due to direct processes where generated using a Monte Carlo simulation code starting from angular distributions in the center of mass system obtained in the DWBA framework via code FRESCO [16], for the production of ^{8}Be, ^{6}Be and ^{4}He. In case of the breakup reaction, the angular distributions in the center of mass system were obtained in a CDCC approach via code FRESCO. The appropriate transformations from the center of mass system to the laboratory system were obtained adopting the prescription of Olimov et al. [17]. Direct and compound nucleus spectra were summed up under various ratio assumptions of direct versus compound contributions and fitted to the data. A comparison between simulated and experimental alpha energy spectra is presented in Figure 1. After correcting for missing counts, the α-particle differential cross sections in the laboratory reference frame were evaluated via the following expression:

$$\frac{d\sigma}{d\Omega} = \frac{N_\alpha}{N_{Pb}} * K' \tag{3}$$

where N_α is the ^{4}He yield for each strip, N_{Pb} are the counts for each strip collected from ^{7}Be elastic scattering to the lead target and the constant K' corresponds to

$$K' = K * \sigma^{Si}_{Ruth} \tag{4}$$

with K being a constant determined by the elastic scattering data and σ^{Si}_{Ruth} is the calculated Rutherford cross section in the laboratory reference system for the elastic scattering of ^{7}Be on ^{28}Si. The results of this analysis are also reported in Ref. [18].

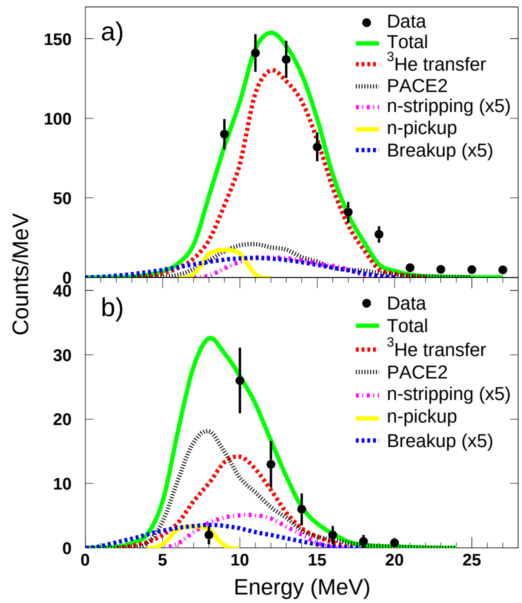

Fig. 1. Decomposition of the simulated alpha energy spectra at the energy of 22.0 MeV for a telescope set at (a) forward angles and (b) middle angles due to compound nucleus process, designated with the dotted black line, and direct processes as follows: The dashed red line indicates the spectrum due to ^{3}He stripping, the dashed blue line due to breakup, the dotted-dashed magenta line due to neutron stripping and the solid yellow line due to neutron pickup. The multiplication factors are arbitrary values for the purpose of presenting the different processes only.

3 Results and discussion

The elastic scattering data were analyzed within the Optical Model framework following the same method as the one adopted previously for ^{6,7}Li + ^{28}Si [4,5], and the elastic scattering calculations were performed with the code ECIS [19]. The Optical Model calculations were performed taking into account a BDM3Y1 interaction [20] for both the real and imaginary part of the Optical Potential but with two different normalization factors, N_R and N_I respectively, which were fitted to the angular distribution data. The deduced best fit angular distributions are compared with the data in Figures 2 and 3, while the energy evolution of the best fit Optical Potential parameters is presented in Figure 4. The energy evolution of the Optical Potential parameters is also compared with previous results of ^{7}Li on ^{28}Si [5]. Although the uncertainties in the determination of the potential parameters for the ^{7}Be + ^{28}Si system are large, the trend of the energy evolution seems to be the same for both projectiles pointing out to a similarity between the two mirror nuclei. In particular, the trend seems to be compatible with a standard threshold anomaly at least in what concerns the imaginary part, with a decreasing magnitude as we approach the barrier from higher to lower energies. The agreement of the present data with a dispersion relation cannot be confirmed, as in the critical position of the real potential, where a peak should appear, we possess only one datum.

The Optical Model analysis for the system ^{7}Be + ^{28}Si, leads also to total reaction cross sections which are included in Table 1. In the same Table are also included total reaction cross sections obtained from the analysis of the α-particle production for the same system, total reaction cross sections obtained with the phenomenological prediction as deduced for light targets in [21] and also total reaction cross sections calculated in a CDCC approach. All results are found in very good agreement, supporting our present Optical Model analysis, since total reaction cross sections are used as a traditional tool to restrict the imaginary part of the Optical Potential.

Moving to the reaction mechanism data, the α-particle yields for each strip, therefore for each angle, were transformed to cross sections using Equation 3. The obtained angular distributions are presented in Figure 5. In order to disentangle the compound from direct part, we follow a standard technique as applied previously for ^{6,7}Li +

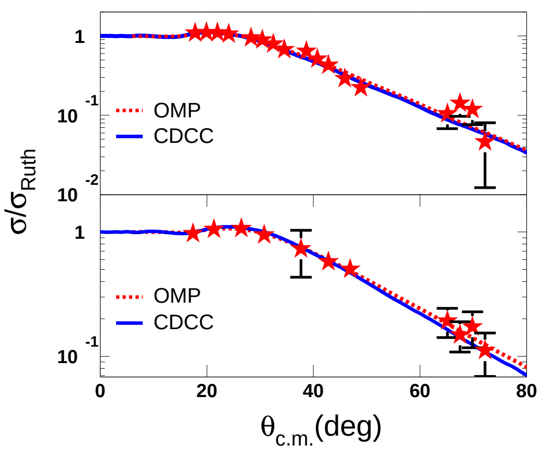

Fig. 2. Top panel: Present angular distribution data for the elastic scattering of ^{7}Be + ^{28}Si at the energy of 22.0 MeV, designated with the red stars, are compared with our best fit Optical Model calculation denoted with the dashed red line as well as with a CDCC calculation denoted with the solid blue line. Bottom panel: Same but for the energy of 19.8 MeV.

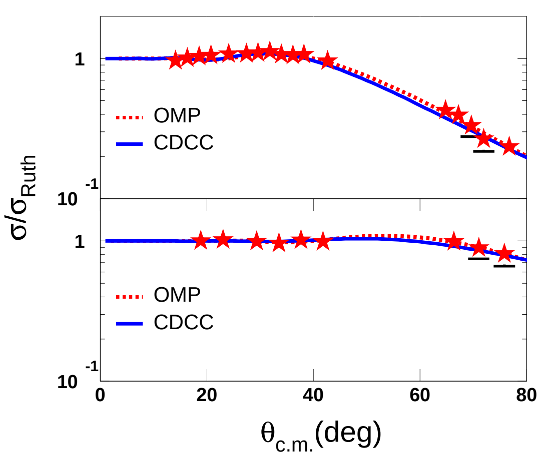

Fig. 3. Top panel: Present angular distribution data for the elastic scattering of ^{7}Be + ^{28}Si at the energy of 17.2 MeV, designated with the red stars, are compared with our best fit Optical Model calculation denoted with the dashed red line as well as with a CDCC calculation denoted with the solid blue line. Bottom panel: Same but for the energy of 13.2 MeV.

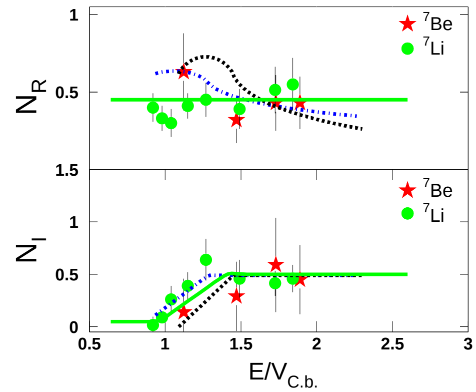

Fig. 4. The energy evolution of the Optical Potential parameters, N_R and N_I, obtained in a BDM3Y1 framework for the ^{7}Be + ^{28}Si - present data, designated with the red stars, are compared with Optical Potential parameters for the system ^{7}Li + ^{28}Si - previous data [5], designated with the green circles. The dotted-dashed blue line corresponds to a dispersion relation analysis performed previously for ^{7}Li [5], while the dashed black line corresponds to a dispersion relation analysis performed for the ^{7}Be. The solid green lines correspond to the results of a barrier distribution analysis for ^{7}Li [6], where an energy independent real potential is suggested, without obeying dispersion relations.

Table 1. Total reaction cross sections for ^{7}Be + ^{28}Si obtained in the present work via an Optical Model analysis, σ_{opt}, are compared with values deduced in the α-production analysis [18], σ_α, as well as with a theoretical value extracted from our CDCC calculations, σ_{cdcc} and a phenomenological prediction for light targets, σ_p, outlined in Ref. [21]. The first column includes projectile energies incident in front of the target, E_{lab}.

E_{lab} (MeV)	σ_{opt} (mb)	σ_α (mb)	σ_{cdcc} (mb)	σ_{pred} (mb)
22.0	1124±148	1206±195	1130	1118
19.8	1072±163	1103±242	1020	990
17.2	738±190	-	831	779
13.2	355±95	250±63	401	347

^{28}Si [22,23]. For that we have calculated in a statistical model approach, via code PACE2, the angular distribution of evaporated α particles, which was renormalized to the backward detectors data. Both angular distributions, the total (experimental) and of compound nucleus origin (theoretical renormalized to experimental data), were integrated. The so obtained compound nucleus α-particle production cross sections were transformed to fusion cross sections taking into account the α-particle multiplicities deduced from our statistical model approach. The fusion cross sections, for the system under study, were considered in a systematic involving other, stable, weakly bound and radioactive projectiles on the same or similar mass targets (^{27}Al, ^{28}Si). All the data sets were reduced to the so called fusion functions according to the prescription presented in Ref. [24]. Looking at Figure 6, we may see that all data sets show good consistency between each other as well as the Universal Fusion Function [24] (UFF) to within an uncertainty band of 10% to 20%. Variations between the data and the UFF are expected since the experimental values for fusion, are given, in principle, at least with an error $\sim 10\%$.

In order to investigate further the similarity between ^{7}Be with ^{6}Li or ^{7}Li, ratios of fusion functions for ^{6}Li to those for ^{7}Li and ^{7}Be were formed. Comparisons of previously measured data for ^{6,7}Li + ^{24}Mg [25], ^{28}Si [23], ^{28}Si [26], ^{59}Co [27] and ^{64}Zn [28] with present results are shown in Figure 7. It is seen that hindrance of fusion cross sections for ^{7}Li with respect to those of ^{6}Li, starts near barrier (already at $\sim$ E= 1.1V$_{C.b.}$, R= 1.5) and it reaches the order of $\sim 70\%$ well below barrier. The same trend is also met for the present data indicating a similarity between ^{7}Be and ^{7}Li rather than ^{6}Li.

The direct part of the α-particle production was obtained by subtracting from the experimental (total) cross sections the renormalized compound values at each angle. The obtained angular distributions are presented in Figure 8 where, the data are compared with theoretical calculations for the n-stripping, n-pickup and the breakup processes. The sum of the three processes is unable to describe the magnitude of the experimental data. The remaining part was attributed to the ^{3}He stripping process, but which cannot be quantified by DWBA calculations due to the lack of the appropriate spectroscopic factors.

For the ^{3}He-particle production, the only two contributing mechanisms are the ^{4}He stripping and the breakup. However, due to the low statistics and the geometrical efficiency of our detector setup, coincidence events between ^{3}He and ^{4}He particles, a clear signature of an exclusive breakup event, were not recorded. In Figure 9, experimental data for the ^{3}He-particle production are compared with theoretical angular distributions for the ^{4}He stripping and the breakup. The sum of the two processes underestimates the data in absolute magnitudes. However, taking into account that according to CDCC calculations, which described in a very good way the elastic scattering data, the contribution of the breakup channel is small, and also that the spectroscopic factors which are introduced in the calculation for the ^{4}He stripping are ambiguously determined, we can say that the bulk of the ^{3}He production is attributed to ^{4}He stripping process.

Finally, having obtained cross sections for the ^{3,4}He production due to direct mechanisms and fusion cross sections, total reaction cross sections were deduced by summing these two components. To avoid double summing the breakup channel, present in both ^{3}He and ^{4}He-particle production, we have subtracted the breakup cross section estimated via the CDCC calculations. Also, to avoid double counting of α's from the decay of ^{8}Be (n-pickup reaction) which breaks into two α particles, we have subtracted the cross section estimated via the DWBA calculations. Both these contributions are very small and do not significantly affect the final result. Subsequently, ratios of direct to total reaction cross section, R=direct/total were formed and are compared in Figure 10 with previous results for ^{6,7}Li on the same target. The ratio for all three projectiles

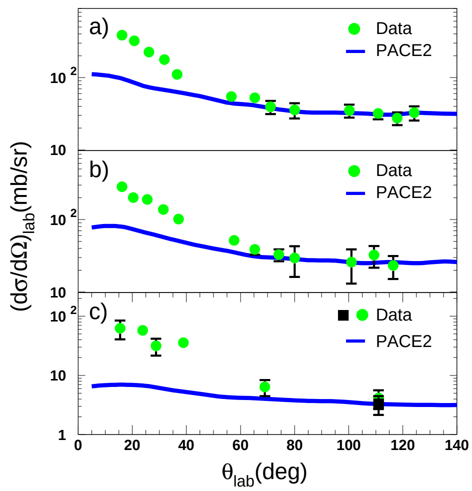

Fig. 5. Present angular distribution data for the ^{4}He particle production at the energies of a) 22.0 MeV, b) 19.8 MeV and c) 13.2 MeV. The solid blue line represents a calculation with the evaporation code PACE2 renormalized to the backward angle data. For the energy of 13.2 MeV, the black square represents the experimental datum minus the estimated contribution from direct processes, since in that case we expect significant direct contribution.

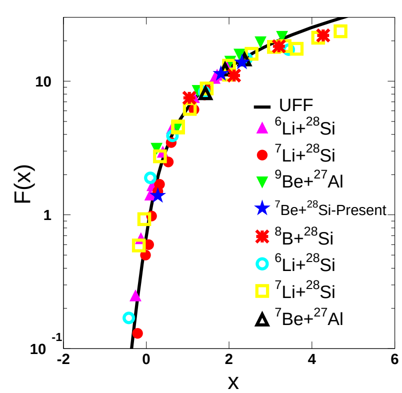

Fig. 6. Reduced fusion cross sections for various stable and weakly bound (stable or radioactive) projectiles incident on ^{27}Al and ^{28}Si targets as a function of parameter x (reduced energy). The reduction was made according to Ref. [24]. The solid black line represents the Universal Fusion Function, UFF, defined in [24].

presents an increasing trend approaching the barrier from higher to lower energies. However, our data follow closer in magnitude those of ^{7}Li and not those of ^{6}Li, indicating larger transfer contribution for the two mirror nuclei at barrier and below it. This may be the reason for the fusion hindrance mentioned above.

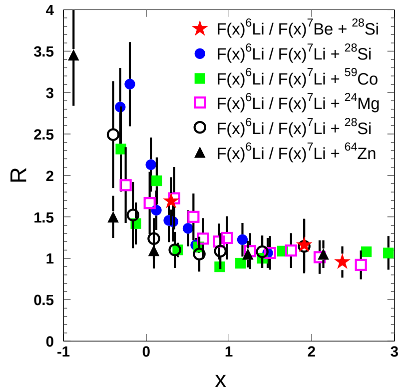

Fig. 7. Ratios of fusion functions for ^{6}Li + ^{28}Si versus ^{7}Li + ^{28}Si compared with ratios of fusion functions for ^{6}Li + ^{28}Si versus ^{7}Be + ^{28}Si as a function of parameter x (reduced energy). Other ratios for ^{6}Li versus ^{7}Li on various low and medium mass targets are also included.

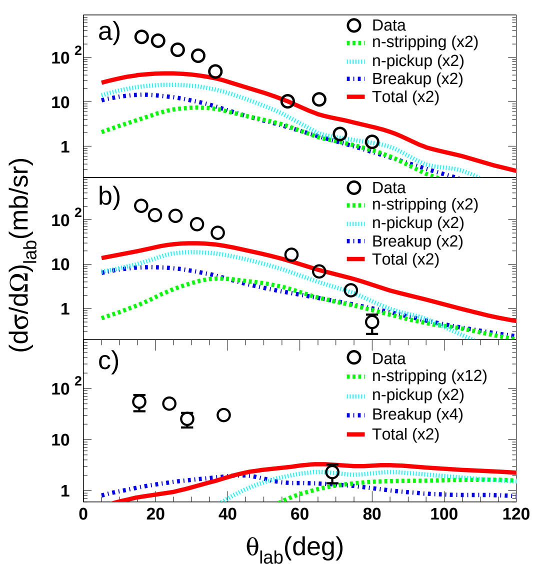

Fig. 8. Angular distributions for α-particle production due to direct processes at (a) 22.0 MeV, (b) 19.8 MeV and (c) 13.2 MeV. Experimental data are denoted with the black open circles, DWBA calculations for neutron stripping with the dashed green line and for neutron pickup with the dotted cyan line, while CDCC calculations for the breakup are denoted with the dotted-dashed blue line. The sum of the three processes is depicted with the solid red line. The remaining part may be attributed to ^{3}He stripping. The multiplication factors are arbitrary for a better display of the various processes. Errors in the data are solely due to the experimental uncertainties of total α production.

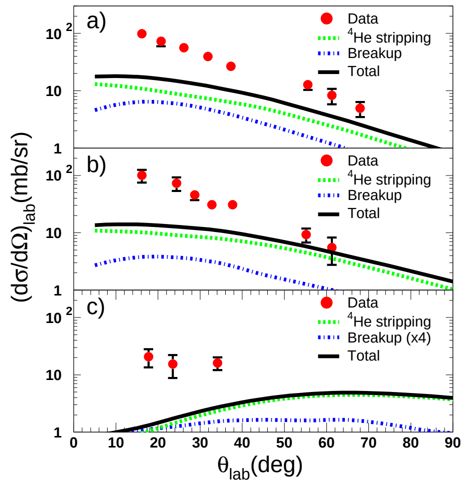

Fig. 9. Angular distributions for ^{3}He-particle production at (a) 22.0 MeV, (b) 19.8 MeV and (c) 13.2 MeV. Experimental data are denoted with the red circles, DWBA calculations for the ^{4}He stripping with the dashed green line and CDCC calculations for the breakup are denoted with the dotted-dashed blue line. The sum of the two processes is depicted with the solid black line. The multiplication factor (panel c) for breakup is arbitrary, for a better visual view.

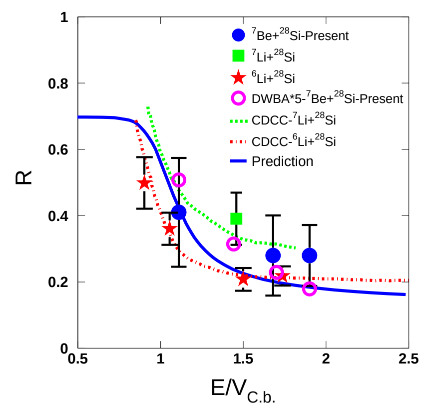

Fig. 10. Energy evolution of ratios, R, of direct to total reaction cross sections. The present results for ^{7}Be + ^{28}Si are compared with previous results for ^{6,7}Li + ^{28}Si [5]. They are also compared with a phenomenological prediction for ^{7}Be + ^{28}Si, outlined in Ref. [21]. Previous calculated ratios for ^{6}Li + ^{28}Si and ^{7}Li + ^{28}Si are also shown as the dotted-dashed red line and dotted green line, respectively [23]. The open circles correspond to the present DWBA calculations, multiplied by 5 to match the data.

4 Summary

The energy dependence of the Optical Potential was sought for the system ^{7}Be + ^{28}Si at near barrier energies via elastic scattering measurements. Comparisons between ^{7}Be -present data and ^{7}Li -previous data on the same target showed that, ^{7}Be resembles its mirror nucleus and not the ^{6}Li one. The behavior of imaginary part of the Optical Potential is compatible with the standard threshold anomaly, while the real part cannot be definitely interpreted into dispersion relations framework, due to the limited data points around Coulomb barrier. It should be noted that the similarity between ^{7}Be and ^{7}Li is also validated from the analysis of fusion data, where fusion hindrance is indicated below barrier for both ^{7}Be and ^{7}Li nuclei. This may be related to the large transfer cross sections, observed for the two mirror nuclei, which act at expense of the fusion ones. In our case, the bulk of the transfer cross sections is attributed to ^{3}He and ^{4}He stripping reactions.

References

1. M. A. Nagarajan, C. C. Mahaux and G. R. Satchler, Phys. Rev. Lett. **54**, 1136 (1985).
2. C. Mahaux, H. Ngo, G. R. Satchler, Nucl. Phys. A **449**, 354 (1986).
3. G. R. Satchler, Phys. Rep. 199, **147** (1991).
4. A. Pakou, N. Alamanos, A. Lagoyannis et al., Phys. Lett. B **556**, 21 (2003).
5. A. Pakou, N. Alamanos, G. Doukelis et al., Phys. Rev. C **69**, 054602 (2004).
6. K. Zerva, A. Pakou, N. Patronis et al., Eur. Phys. Journal A **48**, 102 (2012).
7. J. M. Figueira, D. Abriola, J. O. Fernandez Niello et al., Phys. Rev. C **73**, 054603 (2006).
8. J. M. Figueira, J. O. Fernandez Niello, D. Abriola et al., Phys. Rev. C **75**, 017602 (2007).
9. V. Z. Maidikov, T. Glodariu, M. La Commara et al., Nucl. Phys. A **746**, 389c (2004).
10. D. Pierroutsakou, B. Martin, T. Glodariu et al., Eur. Phys. J. Special Topics **150**, 47 (2007).
11. F. Farinon, T. Glodariu, M. Mazzocco et al., Nucl. Instr. and Meth. B **266**, 4097 (2008).
12. D. Pierroutsakou, A. Boiano, C. Boiano et al., Nucl. Instr. and Meth. A **834**, 46 (2016).
13. O. Sgouros, *PhD thesis*, University of Ioannina, 4 May 2017 (http://hinp.physics.uoi.gr/Theses.htm).
14. O. Sgouros, A. Pakou, D. Pierroutsakou et al., Phys. Rev. C **95**, 054609 (2017).
15. A. Gavron, Phys. Rev. C **21**, 230 (1980).
16. I. J. Thompson, Comput. Phys. Rep. **7**, 167 (1988).
17. K. K. Olimov, K. Olimov, V. V. Lugovoi et al., Int. Jour. Mod. Phys. E **25**, 1650021 (2016).
18. O. Sgouros, A. Pakou, D. Pierroutsakou et al., Phys. Rev. C **94**, 044623 (2016).
19. J. Raynal, Phys. Rev. C **23**, 2571 (1981).
20. D. T. Khoa and W. von Oertzen, Phys. Lett. B **342**, 6 (1995).
21. A. Pakou, D. Pierroutsakou, M. Mazzocco et al., Eur. Phys. Journal A **51**, 55 (2015).
22. A. Pakou, K. Rusek, N. Alamanos et al., Phys. Rev. C **76**, 054601 (2007).
23. A. Pakou, K. Rusek N. Alamanos et al., Eur. Phys. Journal A **39**, 187 (2009).
24. L. F. Canto, P. R. S. Gomes, J. Lubian et al., Nucl. Phys. A **821**, 51 (2009).
25. M. Ray, A. Mukherjee, M. K. Pradhan et al., Phys. Rev. C **78**, 064617 (2008).
26. M. Sinha, H. Majumdar, P. Basu et al., Eur. Phys. Journal A **44**, 403 (2010).
27. C. Beck, F. A. Souza, N. Rowley et al., Phys. Rev. C **67**, 054602 (2003).
28. A. Di Pietro, P. Figuera, E. Strano et al., Phys. Rev. C **87**, 064614 (2013).

A global study of the ^{6}Li+p system at near barrier energies in a CDCC approach

V. Soukeras[1], A. Pakou[1], F. Cappuzzello[2,3], L. Acosta[4,5], C. Agodi[2], N. Alamanos[6], S. Calabrese[2,3], D. Carbone[2], M. Cavallaro[2], A. Cunsolo[2], A. Di Pietro[2], J. P. Fernandez-Garcia[2], P. Figuera[2], M. Fisichella[2], A. Foti[3,5], N. Keeley[7], G. Marquinez-Duran[8], I. Martel[8], M. Mazzocco[9,10], D. Pierroutsakou[11], K. Rusek[12], G. Santagati[2,3], O. Sgouros[1], E. Stiliaris[13], E. Strano[9,10], D. Torresi[9,10], and K. Zerva[1]

[1] Department of Physics and HINP, The University of Ioannina, Ioannina, Greece
[2] INFN Laboratori Nazionali del Sud, via S. Sofia 62, Catania, Italy
[3] Dipartimento di Fisica e Astronomia, Universita di Catania, via S. Sofia 64, Catania, Italy
[4] Instituto de Fisica, Universidad Nacional Autonoma de Mexico, Mexico D. F., Mexico
[5] INFN-Sezione di Catania, via S. Sofia 64, Catania, Italy
[6] CEA-Saclay, DAPNIA-SPhN, Gif-sur-Yvette, France
[7] National Center for Nuclear Research, A. Soltana 7, Otwock Warsaw, Poland
[8] Departamento di Fisica Aplicada, Universidad de Huelva, Huelva, Spain
[9] Departimento di Fisica e Astronomia, Universita di Padova, via Marzolo 8, Padova, Italy
[10] INFN-Sezione di Padova, via Marzolo 8, Padova, Italy
[11] INFN -Sezione di Napoli, via Cinthia, Napoli, Italy
[12] Heavy Ion Laboratory, University of Warsaw, Pasteura 5a, Warsaw, Poland
[13] Institute of Accelerating Systems and Applications and Department of Physics, University of Athens, Greece

Abstract. Elastic scattering measurements have been performed for the ^{6}Li+p system in inverse kinematics at the energies of 16, 20, 25 and 29 MeV while exclusive breakup measurements have been performed for the same system at the two highest energies. In both cases, the heavy ejectile was detected by the large acceptance MAGNEX spectrometer at the Laboratori Nazionali del Sud (INFN-LNS) in Catania, Italy. The experimental data are considered in a global study within the Continuum Discretized Coupled Channel (CDCC) framework. Good agreement between data and theory is observed, interpreted as evidence for strong coupling to the continuum. The direct and sequential (via the first 3^+ resonance) breakup cross sections are found to be equally large at the higher incident energies, but the dominant effect on elastic scattering is due to coupling to the sequential breakup. This is true also for the lowest energy at 16 MeV, despite the negligible cross section for excitation of the resonance at this energy.

PACS. 24.10.Eq Coupled-channel and distorted-wave models – 25.40.Cm Elastic proton scattering – 25.70.Mn Projectile and target fragmentation – 27.20.+n $6 \leq A \leq 19$

1 Introduction

Investigations of collisions involving weakly bound nuclei at near barrier energies create an interesting field to study reaction mechanisms and coupling effects, since direct reactions like breakup are enhanced for such nuclei [1]. Especially the effect of breakup on elastic scattering of various weakly bound nuclei, stable or radioactive, was thoroughly investigated in the past via Continuum Discretized Coupled Channel Calculations (CDCC) [1].

A comprehensive study in the CDCC framework requires not only the measurement of elastic scattering channel but also the measurement of the breakup and the other reaction channels. Into this spirit, we consider here systematic elastic scattering measurements for the system ^{6}Li+p in their own rights as well as together with the breakup and the ^{6}Li+p $\rightarrow$ ^{4}He+^{3}He reaction channels. The results of the analysis of the elastic scattering and breakup channels in the CDCC framework were reported in Refs. [2–4], while the ^{6}Li+p $\rightarrow$ ^{4}He+^{3}He data obtained under the same experimental conditions, were reported in Ref. [5,6].

2 Experimental Details and Data Reduction

The experiment was performed at the MAGNEX facility of Istituto Nazionale di Fisica Nucleare - Laboratori Nazionali del Sud (INFN - LNS) in Catania, Italy. Details of the measurement can be found in Refs. [2–4] and briefly we will give some points here. Beams of $^{6}Li^{3+}$ were accelerated by the TANDEM accelerator for elastic scattering measurement at energies of 16, 20, 25 and 29 MeV and impinged on a 240 μm/cm^2 CH_2 target. The elastically scattered lithium ions were momentum analyzed by the MAGNEX spectrometer [7] whose optical axis was set at $\theta_{opt}=4^o$, subtending an angular range between 2^o to 10^o and were detected by its focal plane detector (FPD) [8,9].

The exclusive breakup measurements were performed at the two highest energies, namely 25 and 29 MeV, requiring a coincidence between alpha fragments detected in MAGNEX and deuterons recorded in a silicon detector set at 5^o. The detector was masked with tantalum foils of appropriate thicknesses such as to stop the elastical scattered lithium ions but to allow deuterons to go through. Exclusive yields were determined for pairs of angles every 0.5° for alpha particles observed in MAGNEX over the angular range 0° to 10°, combined with deuterons observed in the fixed angle detector at 5°. A representative two-dimensional spectrum for the 25 MeV run, displaying the energy of alpha particles recorded in MAGNEX versus the energy of deuterons or recoiling protons detected in the 5° detector, is shown in Fig. 1. A representative one-dimensional coincidence spectrum from the 5° detector is shown in Fig. 2 for the same energy. It is evident that the recoiling protons are well discriminated from the deuterons while, the background due to carbon was less than 15 % and hardly affected the main breakup measurement. It should be also pointed out that, due to the specific experimental conditions, events with energies corresponding to the second kinematical solution were not observed and the angular range of the measurement was limited to forward angles.

The exclusive yields were transferred to laboratory double differential cross sections ($d^2\sigma/d\Omega_\alpha\ d\Omega_d$) using a detection efficiency estimated through a Monte Carlo simulation code based on the CDCC binning of the continuum, details of which are presented in Refs. [3,4,10–12]. The results of our simulation for the energy distributions are presented in Figs. 1 and 2. The very good agreement between the experimental data and the simulation based on the CDCC binning of the continuum confirms the realistic "philosophy" behind this theoretical approach. It should be noted that another process which could contribute to α-d and α-p coincidences is the neutron-stripping reaction: ^{6}Li + $p \rightarrow$ ^{5}Li + $d \rightarrow \alpha + p + d$, with a Q value of -3.44 MeV, which, however, according to preliminary calculations is expected to have very low probability. The result of a simulation of this process is shown on Fig. 2 with the dashed blue line and it does not affect greatly our breakup data.

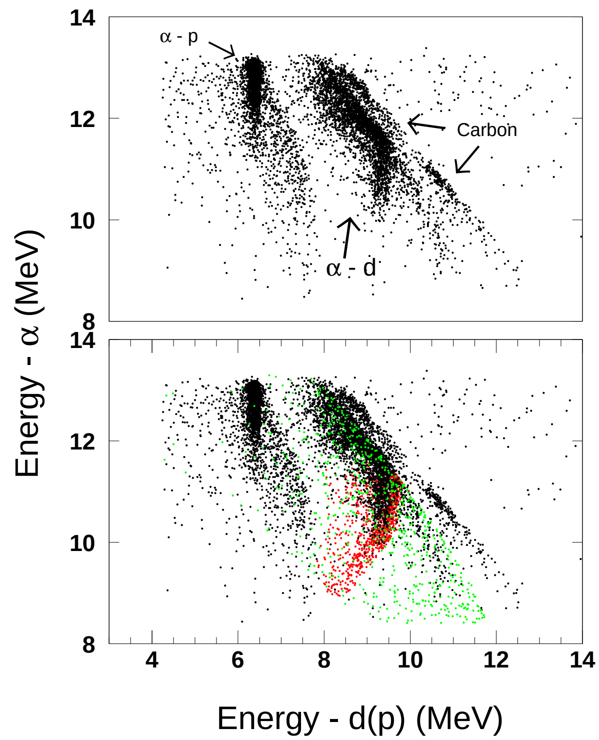

Fig. 1. Top Figure: Representative two dimensional plot of the measured energy of alpha particles (Energy - α) versus measured energy of deuterons or protons (Energy - d(p)) at the beam energy of 25 MeV (4.17 MeV/u). The observed loci for α - p coincidences, α - d coincidences due to breakup of ^{6}Li on hydrogen and α - d coincidences due to breakup on carbon are indicated in this Figure. Bottom Figure: Superimposed on the experimental top spectrum, designed in black, simulated events of the first kinematical solution for the resonant and direct breakup can be observed, designated with red and green dots respectively.

3 Theoretical Details: CDCC Calculations

Continuum Discretized Coupled Channel (CDCC) calculations were performed in order to explain the present experimental data in a global framework. For these calculations we follow the same technique as in [13], where CDCC calculations were presented for the same system at 155 MeV (25.8 MeV/u).

A cluster α + d model of ^{6}Li was adopted, with all the parameters of the model including discretization and truncation described in detail in Refs. [2,3,14]. The relative orbital angular momentum between the α particle and the deuteron was limited to the values L= 0, 1, 2 [14–16]. The first 3^+ resonance was taken into account and was treated as a momentum bin, with a width of 100 keV. Other resonant states were not taken into account since the available energy was such that it was not possible to excite them.

The central part of the entrance potentials for α - p and d - p, was derived as previously [13] from empirical p - α and p - d potentials by means of a single - folding method. The empirical potentials were obtained from p + d and p + α elastic scattering studies at E = 2.52 to 5

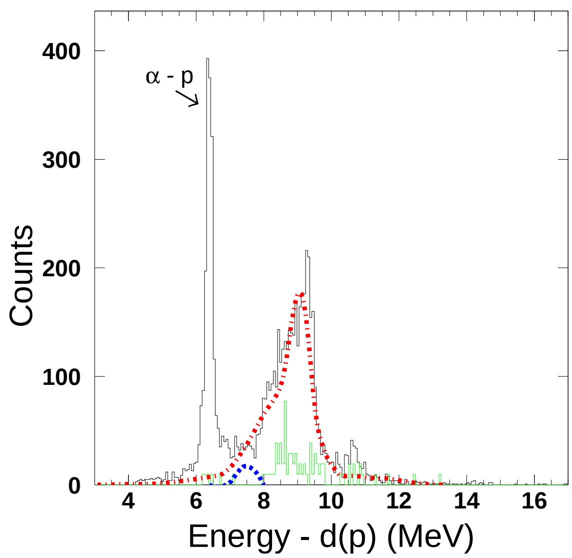

Fig. 2. Representative exclusive breakup spectrum, acquired in the 5^o silicon detector with the CH_2 target at 25 MeV (α-d or α-p coincidences). Simulations for the first kinematical solution for α - d coincidences, are given with the red dotted-dashed line. The peak at the left corresponds to α - p coincidences. The spectrum in green, represents an exclusive spectrum acquired with the carbon target, appropriately normalized. Last, the peak designated with a blue dashed line, represents a simulation for the reaction ^{6}Li + p $\rightarrow$ ^{5}Li + d $\rightarrow$ α + p + d arbitrarily normalized.

MeV/u performed previously [17–23]. These p + d and p + α elastic scattering data were fitted by simple Woods Saxon form factors for both real volume and imaginary volume parts for the p + α system and a real volume and a surface imaginary term for the p + d system. A spin-orbit term was necessary for the best fit of the data but, it was not possible to be used in the CDCC calculation as a part of p + d or p + α interaction. Instead of that, a spin-orbit potential of Thomas form with parameters V_{so}=4.26 MeV, r_{so}=1.10 fm and α_{so}=0.35 fm was added to the diagonal ^{6}Li + p Watanabe folding potentials. Further on, the potential binding the deuteron to α particle core was assumed to have a Woods - Saxon shape as it was described in Ref. [14]. Subsequently, all the potentials mentioned above were fed to a FRESCO calculation [24]. This calculation gives in detail angular distributions for both elastic scattering and breakup modes as well as absorption cross sections and total reaction cross sections.

4 Results and Discussion

In a global interpretation of the data within the CDCC approach, our study included comparisons between theory and simultaneous measurements of elastic scattering and breakup angular distributions as well as total breakup and absorption cross sections. Overall, the interpretation of the data in this framework was found to be satisfactory.

In more detail, the elastic scattering results are compared with the experimental data in Figs. 3-6 where we also present one-channel (no coupling) calculations and calculations with coupling to direct excitation of the continuum only, omitting coupling to the first 3^+ resonance. As can be seen, in general coupling to the continuum (resonant and non-resonant) is strong while the full CDCC calculations describe the elastic scattering reasonably well at all energies. Moreover, we find that coupling to direct breakup makes a slight change from the one-channel calculation and therefore the important coupling is that to the sequential breakup via the first resonance at 2.186 MeV. This is in accordance with similar findings for medium and heavy mass targets [25,26].

The breakup results are compared with the data in Figs. 7 and 8 for the energies of 25 and 29 MeV, respectively. They are in satisfactory agreement, although the general trend for the calculations is to underestimate the data. The experimental breakup cross sections, obtained by integration of the experimental angular distributions extended to all angles assuming the CDCC calculation shape, are given in Table 1. From an inspection of this table, where in the third column we present total breakup cross sections and in parentheses sequential breakup cross sections via the first 3^+ resonance, we can conclude that the sequential breakup accounts for $\sim$ 50 % of the total breakup for the highest two energies, $\sim$ 38 % at 20 MeV and almost zero for the lowest energy, 16 MeV. However, the importance of the influence of breakup coupling on the elastic scattering is not correlated with the magnitude of the breakup cross section. For example, at the lowest energy of 16 MeV, the coupling to the sequential breakup via the 3^+ resonance had the strongest influence, while the cross section for this breakup mode was almost zero, thus presenting an example of a "virtual" coupling effect. Such a striking situation was met with for the elastic scattering of ^{7}Li from a proton target [12]. In that case the cross section for excitation of the first $(7/2^-)$ $\alpha + t$ resonance was determined to be $\sim$ 0.5 mb compared a total breakup of 66 mb, while the coupling to resonant breakup was found to be dominant.

It is also important to make comparisons with other quantities deduced from the CDCC calculations such as absorption cross section. In Table 1, the calculated absorption cross sections are compared with experimental values for the ^{6}Li + p $\rightarrow$ ^{4}He + ^{3}He reaction, the only other available reaction channel at these energies, measured simultaneously with the breakup but reported in Ref. [5]. It is obvious that the agreement with the data is very good, giving further support to a global interpretation of the ^{6}Li + p reaction in the CDCC framework and the validity of the experimental data.

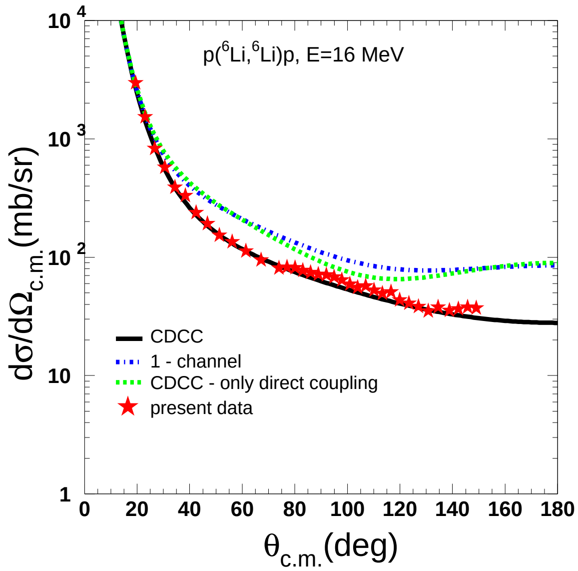

Fig. 3. Present elastic scattering data for ^{6}Li+p at 16 MeV (2.67 MeV/u). The data are compared with full CDCC calculations (solid black line), one-channel calculations (dotted-dashed blue line), and calculations with coupling only to direct breakup (dashed green line).

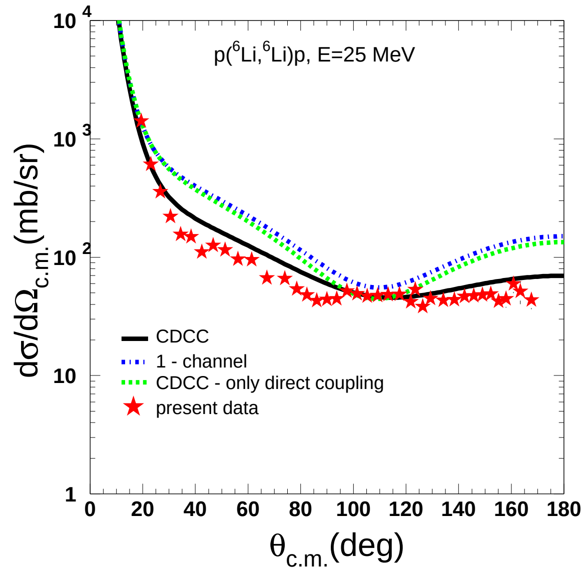

Fig. 5. Same as in Figure 3 but at the energy of 25 MeV (4.17 MeV/u).

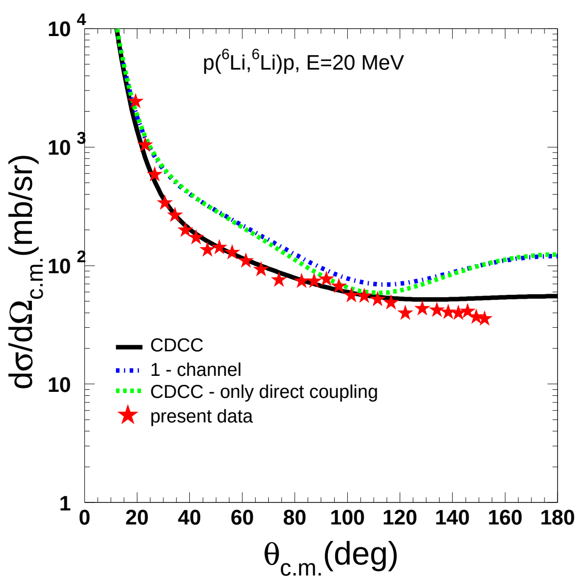

Fig. 4. Same as in Figure 3 but at the energy of 20 MeV (3.33 MeV/u).

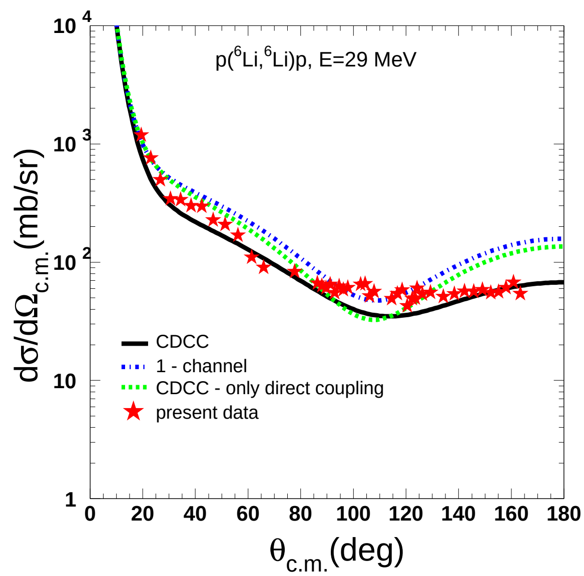

Fig. 6. Same as in Figure 3 but at the energy of 29 MeV (4.83 MeV/u).

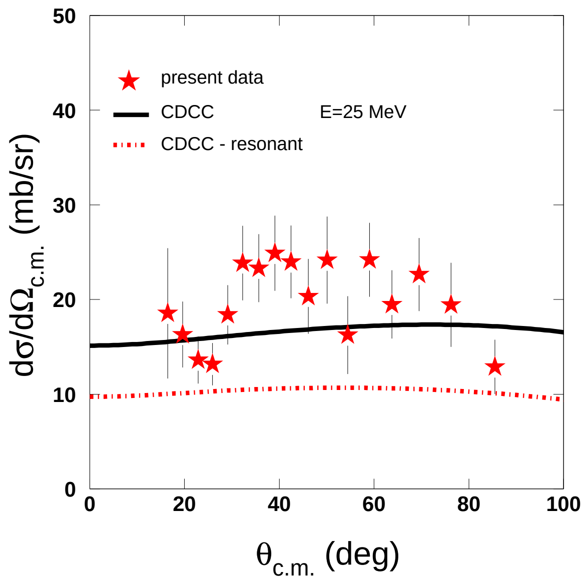

Fig. 7. Experimental and theoretical angular distributions in the center of mass frame, for the breakup of ^{6}Li on proton target at 25 MeV (4.17 MeV/u). The experimental data, referring to the first kinematical solution, are designated with red stars. The black solid line represents a full CDCC calculation while the red dotted-dashed line represents a CDCC calculation taking account coupling only to the first 3^+ resonance at 2.186 MeV.

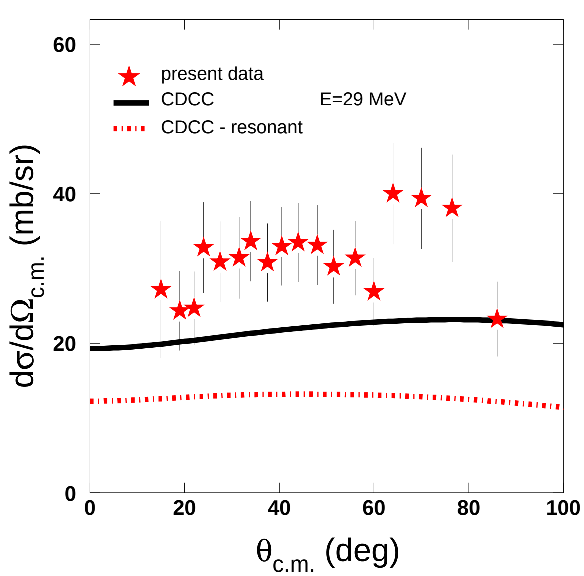

Fig. 8. Same as in Figure 7 but at the energy of 29 MeV (4.83 MeV/u).

Table 1. Reaction cross sections for the ^{6}Li+p system: Experimental breakup cross sections, σ_{break} , CDCC breakup cross sections (in parentheses the sequential breakup cross section via the first 3^+ resonance), σ^{CDCC}_{break} , absorption cross sections according to CDCC, σ^{CDCC}_{abs} , experimental absorption cross sections measured via the ^{6}Li+p $\rightarrow$ ^{4}He+^{3}He reaction, σ_{abs} [5].

E (MeV)	σ_{break}	σ^{CDCC}_{break}	σ^{CDCC}_{abs}	σ_{abs}
29	370±64	269.4 (143.3)	109.5	95±2
25	235±46	200.0 (117.0)	133.0	131±6
20	-	102.9 (37.5)	162.0	140±8
16	-	69.7 (0.03)	130.7	111±2

5 Summary

In summary, exclusive breakup measurements for the ^{6}Li + p $\rightarrow$ α + d + p process, performed for the first time at near barrier energies ($\sim$ 5 x $V_{C.b.}$), considered together with elastic scattering and reaction cross sections measurements, performed in the same experiment, present in total a very good agreement with CDCC calculations. The cross sections for sequential breakup via the first 3^+ resonance at 2.186 MeV are strong for ^{6}Li incident energies of 29, 25 and 20 MeV and coupling to this breakup mode has the most important effect on the elastic scattering. The direct excitation to continuum is substantial and likewise its effect on elastic scattering but only for the highest energy. As we go lower in energy this effect is reduced and becomes negligible at the lowest energy of 16 MeV ($\sim$ 2.7 MeV/u). At this lowest energy we find an example of a “virtual” coupling effect, where although the sequential breakup cross section is almost zero it remains the dominant coupling influence on the elastic scattering. Furthermore, the calculated absorption cross sections were compared with experimental values for the ^{6}Li + $p \rightarrow$ ^{4}He + ^{3}He reaction, the only other available reaction channel with significant cross section, measured simultaneously with the breakup. The excellent agreement between theory and experimental data gives further support to a global interpretation of the ^{6}Li + p reaction in the CDCC framework. Finally, it should be noted that our technique is well-established both experimentally and theoretically allowing the study of similar systems with stable weakly bound or radioactive projectiles on proton/deuteron targets, with the MAGNEX spectrometer.

References

1. N. Keeley, N. Alamanos, K. W. Kemper, K. Rusek, Prog. in Part. Nucl. Phys. **63**, (2009) 396; N. Keeley, R. Raabe, N. Alamanos, J. L. Sida, Prog. in Part. Nucl. Phys. **59**, (2007) 579; N. Keeley, K. W. Kemper, K. Rusek, Eur. Phys. J A **50**, (2014) 145.
2. V. Soukeras, A. Pakou, F. Cappuzzello et al., Phys. Rev. C **91**, (2015) 057601.

3. V. Soukeras, A. Pakou, F. Cappuzzello et al., Phys. Rev. C **95**, (2017) 054614.
4. V. Soukeras, PhD thesis, University of Ioannina, (2017) (http://hinp.physics.uoi.gr/Theses.htm)
5. Ch. Betsou, A. Pakou, F. Cappuzzello et al., Eur. Phys. J. A **51**, (2015) 86.
6. Ch. Betsou, MSc thesis, University of Ioannina, (2015) (http://hinp.physics.uoi.gr/Theses.htm)
7. F. Cappuzzello, C. Agodi, D. Carbone, M. Cavallaro, Eur. Phys. J. A **52**, (2016) 167.
8. M. Cavallaro, F. Cappuzzello, D. Carbone et al., Eur. Phys. J. A **48**, (2012) 59.
9. D. Carbone, F. Cappuzzello, M. Cavallaro, Eur. Phys. J. A **48**, (2012) 60.
10. O. Sgouros, PhD thesis, University of Ioannina, (2017) (http://hinp.physics.uoi.gr/Theses.htm)
11. O. Sgouros, V. Soukeras, A. Pakou, Multip : A Multi Purpose simulation programme for two and three body reaction kinematics, submitted for publication.
12. A. Pakou, O. Sgouros, V. Soukeras et al., Phys. Rev. C **95**, (2017) 044615.
13. K. Rusek, K. W. Kemper, R. Wolski, Phys. Rev. C **64**, (2001) 044602.
14. K. Rusek, P. V. Green, P. L. Kerr, K. W. Kemper, Phys. Rev. C **56**, (1997) 1895.
15. K. Rusek, N. M. Clarke, R. P. Ward, Phys. Rev. C **50**, (1994) 2010.
16. Y. Hirabayashi, Phys. Rev. C **44**, (1991) 1581.
17. R. Sherr, J. M. Blair, H. R. Kratz et al., Phys. Rev. **72**, (1947) 662.
18. F. Lahlou, R. J. Slobodrian, P. Bricault et al., J. Phys. France **41**, (1980) 485.
19. D. C. Kocher, T. B. Clegg, Nucl. Phys. A **132**, (1969) 455.
20. A. S. Wilson, M. C. Taylor, J. C. Legg, G. C. Phillips, Nucl. Phys. **130**, (1969) 624.
21. K. Sagara, H. Oguri, S. Shimizu et al., Phys. Rev. C **50**, (1994) 576.
22. G. Freier, E. Lampi, W. Sleator and J. H. Williams, Phys. Rev. **75**, (1949) 1345.
23. P. D. Miller and G. C. Phillips, Phys. Rev. **112**, (1958) 2043.
24. I. J. Thompson, Comput. Phys. Rep. **7**, (1988) 167.
25. J. P. Fernandez-Garcia, M. Zadro, A. Di Pietro et al., Phys. Rev. C **92**, (2015) 054602.
26. A. Gomez Camacho. A. Diaz-Torres, P. R. S. Gomes, J. Lubian, Phys. Rev. C **93**, (2016) 024604.

IN HONOR OF PROFESSOR ATHENA PAKOU

Honor plaque awarded to professor Athena Pakou

by the Hellenic Institute of Nuclear Physics

N. Alamanos' closing speech

Dear Athena,

I was delighted to participate in the HINPW4 conference and express during my talk and later on during the lecture of my notes, my deep appreciation for your scientific achievements. I was also happy to come a day before and discuss with Akis and Vassilis and have a first presentation of their thesis.

I hope that this early arrival did not disturb your plans.

My participation to the conference was also a testimony to our old friendship.

Before leaving Ioannina, I would like to send you the "Hokusai-Athena" text that I have read during the lecture of my notes. When he was seventy-four, he wrote:

> "*At seventy-three years, I partly understood the structure of animals, birds, insects and fishes, and the life of grasses and plants. And so, at eighty-six I shall progress further; at ninety I shall even further penetrate their secret meaning, and by one hundred I shall perhaps truly have reached the level of the marvelous and divine. When I am one hundred and ten, each dot, each line will possess a life of its own*".

I think that this sentence could be adapted to Athena's scientific carrier. Her work and publications are getting better and better. In the near future, she will further penetrate the secret meaning of the reactions with exotic nuclei and in the far future, she will reach the level of the marvelous and divine.

I would like to wish to Athena a marvelous continuation of her scientific career.

Athena, I wish you a brilliant continuation of your scientific career. If time allows, I will continue reading with interest your future articles.

My warmest regards

Nicolas Alamanos

LIST OF PARTICIPANTS

INVITED SPEAKERS

Alamanos Nicolas
IRFU/CEA/Saclay, FRANCE
alamanos@cea.fr

Bonasera Aldo
Texas A&M University, USA
abonasera@comp.tamu.edu

Cappuzzello Francesco
Istituto Nazionale di Fisica Nucleare - Laboratori Nazionali del Sud (INFN-LNS), Catania, ITALY
cappuzzello@lns.infn.it

Keeley Nicholas
National Center for Nuclear Research (NCNR), POLAND
nicholas.keeley@ncbj.gov.pl

Pierroutsakou Dimitra
Istituto Nazionale di Fisica Nucleare (INFN) - Sezione di Napoli, ITALY
pierroutsakou@na.infn.it

Ring Peter
Technical University of Munich (TUM), GERMANY
peter.ring@tum.de

Rusek Krzysztof
Heavy Ion Laboratory, University of Warsaw, POLAND
rusek@slcj.uw.edu.pl

Veselsky Martin
Institute of Physics, Slovak Academy of Sciences (SAS), SLOVAKIA
Martin.Veselsky@savba.sk

PARTICIPANTS

Alexandropoulou Matina
University of Ioannina (UOI), GREECE
matinagucci@gmail.com

Aslanoglou Xenofon
University of Ioannina (UOI), GREECE
xaslanog@cc.uoi.gr

Asimakopoulou Aggeliki
National and Kapodistrian University of Athens (NKUA), GREECE
angie.asim@yahoo.com

Assimakis Ioannis
National Centre for Scientific Research (NCSR) "Demokritos", GREECE
ioasimakis@gmail.com

Betsou Chryssoula
Aristotle University of Thessaloniki (AUTH), GREECE
Chrysam28@hotmail.com

Bonatsos Dennis
National Centre for Scientific Research (NCSR) "Demokritos", GREECE
bonat@inp.demokritos.gr

Eleme Zinovia
University of Ioannina (UOI), GREECE
ph06458@cc.uoi.gr

Gaitanos Theodoros
Aristotle University of Thessaloniki (AUTH), GREECE
tgaitano@auth.gr

Georvassili Stefania
University of Ioannina (UOI), GREECE
stefania_3@windowslive.com

Georgali Efstathia
University of Ioannina (UOI), GREECE
efi.gew9199@gmail.com

Hatzikos Vassileios
National and Kapodistrian University of Athens (NKUA), GREECE
vhatzikos@gmail.com

Ioannides Konstantinos
University of Ioannina (UOI), GREECE
kioannid@cc.uoi.gr

Karakatsanis Konstantinos
Aristotle University of Thessaloniki (AUTH), GREECE
kokaraka@physics.auth.gr

Koutsantonis Loizos
The Cyprus Institute (CyI), CYPRUS
l.koutsantonis@cyi.ac.cy

Lalazissis Georgios
Aristotle University of Thessaloniki (AUTH), GREECE
glalazis@auth.gr

Lykiardopoulou Marilena
National and Kapodistrian University of Athens (NKUA), GREECE

Margaritis Chryssovalantis
Aristotle University of Thessaloniki (AUTH), GREECE
chmargar@gmail.com

Markou Lefteris
The Cyprus Institute (CyI), CYPRUS
l.markou@cyi.ac.cy

Martinou Andriana
National Centre for Scientific Research (NCSR) "Demokritos", GREECE
amartinou@hotmail.com

Mikeli Maria
National and Kapodistrian University of Athens (NKUA), GREECE
mmikeli@phys.uoa.gr

Misaelides Panagiotis
Aristotle University of Thessaloniki (AUTH), GREECE
misailid@chem.auth.gr

Moustakidis Charalampos
Aristotle University of Thessaloniki (AUTH), GREECE
moustaki@auth.gr

Nikolis Nikolaos
University of Ioannina (UOI), GREECE
nnicolis@cc.uoi.gr

Pakou Athena
University of Ioannina (UOI), GREECE
apakou@cc.uoi.gr

Papachristodoulou Christina
University of Ioannina (UOI), GREECE
xpapaxri@cc.uoi.gr

Papadimitriou Sofia
National and Kapodistrian University of Athens (NKUA), GREECE
sofiapap1993@hotmail.gr

Papageorgiou Athanassios
National and Kapodistrian University of Athens (NKUA), GREECE
than-pap@hotmail.com

Patronis Nikolaos
University of Ioannina (UOI), GREECE
npatronis@cc.uoi.gr

Rapsomanikis Aristotelis-Nikolaos
National and Kapodistrian University of Athens (NKUA), GREECE
anrapso@phys.uoa.gr

Sarantopoulou Smaragda
National Centre for Scientific Research (NCSR) "Demokritos", GREECE
smaragda40poulou@yahoo.gr

Sgouros Onoufrios
University of Ioannina (UOI), GREECE
onoufriossgouros@yahoo.gr

Soukeras Vasileios
University of Ioannina (UOI), GREECE
soukerasb@yahoo.gr

Souliotis George
National and Kapodistrian University of Athens (NKUA), GREECE
soulioti@chem.uoa.gr

Stamoulis Konstantinos
University of Ioannina (UOI), GREECE
kstamoul@cc.uoi.gr

Stiliaris Efstathios
National and Kapodistrian University of Athens (NKUA), GREECE
stiliaris@phys.uoa.gr

Zerva Konstantina
University of Ioannina (UOI), GREECE
kzerva@staffmail.ed.ac.uk

Zioga Maria
National and Kapodistrian University of Athens (NKUA), GREECE
mzioga@phys.uoa.gr

AUTHOR INDEX